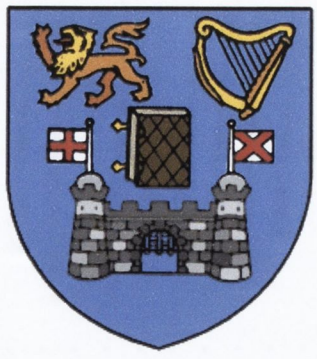

Nonlinear Optical Extinction in Polymer-Carbon Nanotube and Phthalocyanine Systems

By

Seán Martin O'Flaherty

A thesis submitted for the degree of
Doctor of Philosophy
in the
University of Dublin

Department of Physics
Trinity College Dublin

September 2003

Declaration

I declare that the work in this thesis has not been previously submitted as an exercise for a degree to this or any other university.

The work described herein is entirely my own, except for the assistance mentioned in the acknowledgements and the collaborative work mentioned in the list of publications.

I agree that Trinity College Library may lend or copy this thesis upon request.

Seán O'Flaherty

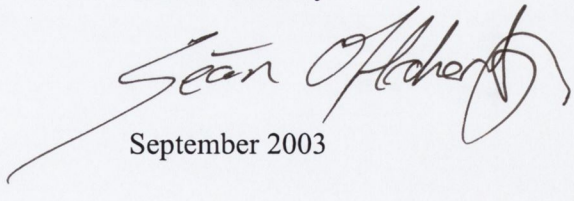

September 2003

"Science is the great antidote to the poison of enthusiasm and superstition"

Adam Smith
Economist and Philosopher

1723 - 1790

Acknowledgements

The foremost expression of gratitude that I would like to assert is for Prof. Werner Blau. During the period of my studies under his guidance he always freely shared his enthusiasm, knowledge and inspiration. Second only to him, I extend recognition to Dr. Jonathan Coleman for many donations of scientific insight to my research, and for perpetually being in the mood for "just the one in the Pav". Their support and friendship was always welcomed, accepted and well appreciated.

I would also like to pay tribute to the other members of 'Group Bu'. The older members there from when I started or soon after, past and present, are Adam, Andrew, Anna, Bernd, Brendan, Brian, Catriona, Christian, Colin, Gavin, Grace, Jean-Edouard, Johnny, Kevin, Manuel, Margaret, Marie-L, Martin, Michael, Patrick, Rebekah, Rob, Sandy, Stefanie, Stephanie, Stephen, Takeyuki, Valerie and Werner. From 'Materials Ireland' I would like to mention Keith. To the newer additions, Cathal, Ciara, David, Dennis, Éimhín, Eveann, Gordon, Jimmy and Valeria I wish you the best of luck with your future. For all sorts of administrative help, thanks Jeannette. Thank you all for your friendship and all things scientific and otherwise.

Many people produced the materials studied in this thesis and their contribution is acknowledged: thanks to Martin Cadek (TCD) for 'MWNTs', Anna Drury (TCD) for 'PmPV' and Stefanie Maier (TCD) for '*m*-PNV'. Thanks to our network partners Prof. M. Hanack and Dr. Y. Chen from the Universität Tübingen, Prof. T. Torres and E. Garcia-Frutos from the Universidad Autónoma de Madrid and Prof. M. Cook and A. Auger from the University of East Anglia who produced the phthalocyanine molecules used in these studies. Thanks to Stephanie Hold for assistance in the lab and to Rob Murphy for the EPR measurements in Chapter 5. I thank Johnny Coleman and Sandy Fleming for access to and useful discussions regarding their unpublished SWNT concentration dependent studies. For proof

reading of this thesis I thank Colin Belton, Johnny Coleman, Rebekah D'Arcy, Rob Murphy and Werner Blau; although I accept complete responsibility for any remaining errors! Thank you all.

The administrative and technical staff of the Department of Physics has been helpful whenever I have needed them over the last few years. I thank especially Tom Burke and John Kelly for guiding me through the college bureaucracy when it was necessary. Thanks also to Michelle and Susan.

For financial support I thank Enterprise Ireland for providing me with a scholarship. Finally, I extend sincere thanks to my parents for instilling in me at an early age the desire to learn and an appreciation of knowledge, priceless gifts for which I am forever grateful.

Abstract

The work presented in this thesis is based on experimental measurements of nonlinear optical extinction or optical limiting of nanosecond laser pulses by phthalocyanine and polymer-carbon nanotube systems. The nonlinear optical experiments were performed using open aperture z-scan with 6 ns Gaussian pulses at 532 nm from a frequency doubled Q-switched Nd:Yag laser.

Optical limiting resulting from reverse saturable absorption in forty one structurally different modified metallo-phthalocyanine and metallo-naphthalocyanine compounds are investigated where the response exhibited by the materials are theoretically fitted using electronic rate equations applied in a static state approximation. The compounds are modified with the addition of various groups to the peripheral of the macrocyclic systems and with the incorporation of various metals such as Zn, Pb, Co, Cu, Ni, In and Ga into the central cavity of the compounds. The effects on the nonlinear optical response of the basic phthalocyanine compound as a result of varying the central metal and the peripheral functional groups are investigated. The existence of molecular design rules linking the nonlinear optical properties with the molecular structure is also investigated.

Two distinctly different polymer and carbon nanostructure composite materials dispersed in solution are investigated. The polymer poly(para-phenylenevinylene-co-2,5-dioctyloxy-meta-phenylenevinylene) was used to form exclusive multi-walled carbon nanotube and polymer composites. The polymer poly(9,9-di-n-octylfluorenyl-2,7'-diyl) was used to form composites consisting of multi-walled carbon nanotubes, other clearly defined carbon nanoparticles and polymer. The fabrication technique and material characterisation steps are described, where it was found that the carbon nanostructures were stably dispersed in the polymer matrix in both cases. A range of each of these composites was prepared

and varied according to carbon nanostructure mass content. Furthermore, the scattering of high intensity light from the materials was qualitatively probed and its angular dependence investigated. The nature of the carbon nanostructure inclusions in each material was found to significantly influence the scattering response of the composites.

Further investigations of composite dispersions composed of polymer and single-walled carbon nanotubes are conducted using concentration dependent optical extinction. The breaking up of single-walled carbon nanotube bundles through thermal dissociation is detected using nonlinear optical extinction as the probe. Novel scaling laws linking the nonlinear response to the geometrical structure of the nanotube bundles are revealed.

Table of Contents

Table of Figures

Chapter 1

Introduction

1.1 Setting the Scientific Scene

The field of Nonlinear Optics was given birth in 1960 with the development by Maiman[1] of the first operational laser. Prior to this the usual sources of light available for optical investigations or experimentation tended to be weak, broadband and incoherent. Shortly after the development of the laser, Franken *et al.*[2] reported on the first experimental observation of second harmonic generation (SHG), where they produced the second harmonic line of the fundamental from a Ruby laser operated at 694 nm. Activity in the field escalated from this point on and larger intensity sources were developed with the realisation of Q-switching and short-pulsed mode-locked lasers. The avenues of investigation opened up by these breakthroughs allowed unprecedented levels of interest and research into the nonlinear optical nature of materials.

It was soon recognised that the possibility of producing coherent laser light of almost any wavelength and pulse-width was attainable through the use and manipulation of nonlinear optical properties of different materials. The development of electro-optic modulators greatly influenced and assisted the evolution of the technique of Q-switching, which in turn allowed the high-energy shorter pulsed lasers to be developed. These developments led to the development of nanosecond

regime lasers. Picosecond and femtosecond lasers are commonly used today and realisation of pulses in these time regimes required the development of the technique of mode-locking. Modelocked lasers of high intensity required materials that behaved as Saturable Absorbers. Saturable Absorption is effectively a resonant nonlinear optical process by which, due to optical interactions in the excited states of a material, the material becomes more transmitting under the influence of high intensity light. The newly attainable high intensities were then used to generate SHG with high efficiency in materials such as potassium dihydrogen phosphate (KDP).

In 1965 Moore[3], then head of Research and Development at Fairchild Semiconductor, prepared an article for the 35th anniversary of 'Electronics' magazine. He discovered that over the period 1959-65, the number of components (e.g., transistors) on a chip roughly doubled every year. This trend suggested that processing power would rise exponentially and at a fast rate, leading to a computing revolution. Moore predicted: "Integrated circuits will lead to such wonders as home computers - or at least terminals connected to a central computer, automatic controls for automobiles, and personal portable communications equipment." It is now a well-known fact that in electronics technology the limitations are rapidly being approached. Continued advancement relies on further device miniaturisation and increased processing speed. However, in electronics, which is the basis of current technology, the boundaries for these improvements are quickly being reached. The field of 'Photonics' provides an intriguing alternative approach to solving these problems. Photonics is analogous to electronics in that it describes the technology in which photons instead of electrons are used to acquire, store, transmit and process information[1]. There are advantages with photonics over electronics, the most obvious being that photonics enables processing of information at the speed of light.

The realisation of photonics technologies depends on two main factors; the existence and understanding of appropriate optical techniques and suitable optical materials for the fabrication of optical 'circuits', interconnects and devices. The first factor has been already realised with the development of the laser and the theory of nonlinear optics. The second factor required for photonic technologies are suitable materials, which can facilitate efficient nonlinear optical interactions of high conversion efficiency, and which can be fabricated into useful devices. Thus, currently research in this area involves the design and optimisation of suitable

materials to perform nonlinear optical processes under laser irradiation. As candidates, organic materials have many positive attributes including; their ability to support considerable nonlinear optical interactions and hence produce large and ultra fast nonlinear responses, their architectural flexibility, high optical damage thresholds, and ease of fabrication as well as low production cost.

Combined with the development of high-intensity laser light sources and the many desirable reasons for the development of photonic technologies it has been recognised that optical instruments, especially for example the human eye, could easily be damaged by accidental or intentional irradiation by these light sources. This has given rise to the field of optical limiting. Optical limiting is the name given to the process of high suppression or extinction of high intensity potentially damaging light while allowing the high transmission of low photonic energy ambient light irradiation. The need for optical limiters has thus generated much interest in the development of new nonlinear optical materials and devices.[4] Generally an optimal optical limiting material has a high dissipative optical nonlinearity, an inherently fast response time, a large dynamic range and a broadband spectral response. A schematic of the ideal response exhibited by an optical limiting material is sketched in Figure 1.1. At low intensity it can be seen that the transmission is perfectly linear, no different from everyday experiences. At a certain threshold the incident intensity

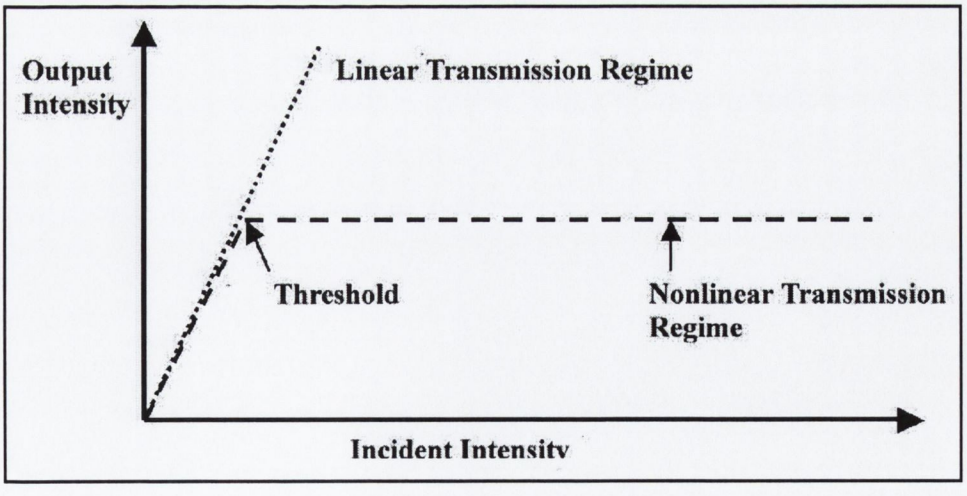

Figure 1.1 Schematic response of an ideal optical limiter, where the limiting response begins at the threshold point, which is below the damage value of the target that is being protected.

can be seen to be large enough to excite the dissipative nonlinearity and from this point forward to higher incident intensities it can be seen that the nonlinearity effectively clamps the output at a fixed intensity. A limiter would be designed so that the maximum output intensity is lower than the intensity required to damage the target that is being protected. The large number of different environments and the large amount of different optical elements that may conceivably require protection make it highly unlikely that any one optical limiting material will ever suit all requirements and consequently, research into optical limiting materials continues on a broad front spanning the traditionally isolated disciplines of physics, materials science and chemistry.

1.2 Thesis Outline

This thesis has at its subject matter the investigation of dissipative optical nonlinearities in two distinctly different organic materials or systems: namely these are the carbon nanotube and the phthalocyanine. Optical limiting is the central underlying theme that is under investigation and discussion throughout the entire body of this work, however its application is not the single motive behind the direction. Wherever possible the effect is used as a tool to shed light on other properties of the materials that are being investigated, and the possibilities of using the effect as a spectroscopic tool for other potential applications, other than laser light attenuation, is discussed wherever applicable.

Carbon nanotubes can be considered as rolled graphene sheets that are seamlessly joined into tubular-like structures. The phthalocyanine is an organic dye commonly used in the colorant industry. The carbon nanotubes investigated are incorporated into composite type materials where they form the inclusions in otherwise homogeneous polymer hosts and the phthalocyanines that are investigated are chemically modified in many different ways, with the incorporation of different organic and metallic components to the basic structure.

The thesis structure will take the following form: Chapter 2 will outline the formal introduction to nonlinear optics the origin of which will be discussed in terms of the classical 'Lorentz Model'. This will be followed with a general introduction to organic material and to why they are particularly suitable for nonlinear optical processes. The chapter will conclude with a general discussion and description of

the allowable optical transitions that are generally observed within the organic system using an orbital model under light irradiation.

Chapter 3 will be concerned with the description of the specific materials that will be subsequently investigated and the experimental techniques that will be employed to undertake these investigations. The structural and electronic properties of the phthalocyanine and carbon nanotube entity will be reviewed and followed by descriptions of the optical experimental techniques. This will involve mathematical discussions of the propagation of focused Gaussian beams and the 'Z-scan' technique, the understanding of which are of paramount importance to this work.

The subject matter of Chapter 4 will be the experimental measurements of optical limiting in the phthalocyanine system. Forty one structurally different phthalocyanines, substituted with different organic and metallic components, are under investigation and the principle aim of this chapter is to link the nonlinear response exhibited to the structural properties of the phthalocyanine molecule.

Chapter 5 deals with the experimental measurements of optical limiting exhibited by the carbon nanotube in polymer, inclusion in host, system. Two distinctly different polymer-nanotube composites are fabricated, materially investigated and optically characterised in the linear and nonlinear regimes. Again, the principle aim of the chapter is to link the nonlinear response to the structural nanoscale properties of the different composite materials.

The final experimental chapter, Chapter 6, is again concerned with the polymer-nanotube composite system. The composites in this chapter are investigated using concentration dependent optical extinction as a tool to probe the chemical kinetics of carbon nanotube bundles in the system. The principle aim of this chapter is to use the knowledge developed in the previous chapters to provide insight into the equilibrium conditions of the polymer-nanotube system.

Finally, a summary of the overall relevance and significance of the work that constitutes this thesis will be given in the concluding section, Chapter 7.

References

1 T. H. Maiman, Nature **187,** 493 (1960).

2 P. A. Franken, A. E. Hill, C. W. Peters, and G. Weinreich, Physical Review Letters **7,** 118 (1961).

3 G. Moore, Electronics **38**, 114-117 (1965).

4 L. W. Tutt and T. F. Boggess, Progress in Quantum Electronics **17,** 299-338 (1993).

Chapter 2

Nonlinear Optics and Organic Material

2.1 The Nonlinear Interaction of Light with Matter

2.1.1 Introduction

This chapter will outline the formal introduction to nonlinear optics the origin of which will initially be discussed in terms of a classical anharmonic oscillator a model generally known as the Lorentz Model. This model describes the classical response of an electron to excitation by a light wave. The electron is considered to be bound to a nucleus and the interaction between them considered to be simple harmonic as for a mass on a spring. If an incident light field exciting the electron is then considered, and providing the excitation is not too large, the electron exhibits simple harmonic motion at the frequency of the excitation. This is exactly analogous to a driven simple harmonic oscillator and results in the light field being re-radiated.

The Lorentz Model lacks the sophistication of a quantum mechanical treatment of light-matter interactions and despite this it proves successful in describing linear optical processes such as dispersion, birefringence and scattering, all of which are related to the refractive index. In order to account for phenomena associated with light dissipation, or absorption, it is necessary to introduce an empirical damping term into the simple harmonic oscillator model. This damping term manifests as the imaginary component of the refractive index. In the absence of any optical dissipation the refractive index is thus purely real.

Considering the anharmonic response of the electron oscillator model will follow this and the corresponding implications for nonlinear optics will be discussed. The nonlinear polarisation will then be introduced as a perturbation mathematically described using a Taylor series of the linear case. It will then be seen that this nonlinear polarisation may give rise to the generation of new frequencies from material interactions with the fundamental excitation.[1]

2.1.2 The Lorentz Model

The foundation for the fields of electromagnetism and optics require a mathematical method of describing the fundamental interactions between electromagnetic waves and matter. Such formalism was introduced in the work of James Clerk Maxwell (1831-1879) and is generally expressed by Oliver Heaviside's (1850-1925) version of the original Maxwell theory (developed in about 1888) where the resultant equations are known as 'Maxwell's Equations'. An appreciation of their significance is crucial for a full comprehension of electromagnetic theory and phenomena. If a neutral dielectric in a non magnetic regime is considered then the equation may be expressed as:

$$\underline{\nabla}.\underline{D} = 0 \tag{2.1}$$

$$\underline{\nabla}.\underline{B} = 0 \tag{2.2}$$

$$\underline{\nabla} \times \underline{E} = -\frac{\partial \underline{B}}{\partial t} \tag{2.3}$$

$$\underline{\nabla} \times \underline{H} = \frac{\partial \underline{D}}{\partial t} \tag{2.4}$$

where $\underline{E}$ and $\underline{H}$ represent the electric and magnetic field strength vectors respectively, and $\underline{B}$ and $\underline{D}$ represent the magnetic and electric displacement vectors defined as:

$$\underline{B} = \mu_0 \underline{H} \tag{2.5}$$

$$\underline{D} = \varepsilon_0 \underline{E} + \underline{P} \tag{2.6}$$

where μ_0 is the magnetic permeability of free space and ε_0 is the permittivity of free space. $\underline{P}$ is the polarisation or the electric dipole moment per unit volume and is the only term in Maxwell's equations that is directly related to the medium.

It is possible to perform some simple differential operations and rearranging of Equations (2.1)-(2.6) to derive the following equation

$$\underline{\nabla}^2 \underline{E} - \frac{1}{c^2}\frac{\partial^2 \underline{E}}{\partial t^2} = \mu_0 \frac{\partial^2 \underline{P}}{\partial t^2} \tag{2.7}$$

where c is speed of light in a vacuum. This is the inhomogeneous wave equation and is the fundamental equation for classical electromagnetic field propagation and light-matter interactions. It can be seen that the polarisation term is a source term and its significance will be discussed later.

For free space propagation the polarisation term can be neglected and Equation (2.7) reduces to the homogenous wave equation. This can be shown to support only transverse wave solutions, which propagate with phase velocity c. One such solution is the plane wave expressed as:

$$E(z,t) = pE_0 \cos(\omega t - kz) \tag{2.8}$$

where p is the polarisation of the wave, ω is the frequency of the wave and k is a propagation constant and obeys the following dispersion relation.

$$k^2 = \frac{\omega^2}{c^2} \tag{2.9}$$

As already stated, the polarisation induced in a medium under the influence of an electromagnetic field is a property of the medium in which the electric field propagates. It is thus directly related to how a material will respond to excitation by a light field and has enormous significance for nonlinear optics. In order to discuss this link in more detail it is necessary to develop a model for light-matter interactions.

One of the first successful models to describe such interactions was the electron oscillator model proposed by Hendrick A. Lorentz (1853-1928) around 1900, and frequently is referred to as the 'Lorentz Model'. In this description the interaction of light with matter is treated in terms of one-electron atoms. The electrons are assumed to reside at the equilibrium position of the potential well associated with the atoms and whenever subjected to a perturbation, which displaces them from equilibrium, they experience a restoring force due to the potential. This is analogous to the restoring force experienced, $\underline{F}_R$ by a mass on a spring that has been strained where the restoring force generally obeys Hooke's Law.

$$\underline{F}_R = -k\underline{x} \tag{2.10}$$

where k in this case represents the spring constant, and $\underline{x}$ is the strain displacement.

Lorentz considered the interaction of the electromagnetic wave as providing

the necessary perturbation to excite and displace the electrons. The force the electron experiences in this instance is the Lorentz Force, F_L,

$$\underline{F}_L = e\left(\underline{E} + \underline{v} \times \underline{B}\right), \tag{2.11}$$

where $\underline{v}$ is the velocity. However, the magnetic contribution to the force may be ignored, as the velocities of the charges involved do not normally approach relativistic magnitudes. Thus using Newtons second law the equation of motion for the electron can be described as:

$$\frac{\partial^2 \underline{x}}{\partial t^2} + \omega_0^2 \underline{x} = \frac{e\underline{E}}{m}, \tag{2.12}$$

where the natural frequency of oscillation of the electron has been defined as $\omega_0 = (k/m)^{1/2}$, with m representing the electronic mass. If the incident field is assumed to have the form of Equation (2.8) then Equation (2.12) has the particular solution:

$$\underline{x}(z,t) = p\frac{eE_0}{m(\omega_0^2 - \omega^2)}\cos\left(\omega t - kz\right) \tag{2.13}$$

This expression then describes the displacement from equilibrium that an electron is forced to have upon interaction with an electromagnetic field. This may then be used to determine the polarisation induced in the medium. Since the polarisation has already been defined as the dipole moment per unit volume and the dipole moment is simply the product of the electronic charge and its displacement the polarisation can thus be expressed as:

$$\underline{P} = Ne\underline{x} = p\frac{Ne^2E_0}{m(\omega_0^2 - \omega^2)}\cos\left(\omega t - kz\right), \tag{2.14}$$

where N is the number density of the electrons. This is then the source term for the polarisation which may be substituted back in to the right hand side of Equation (2.7). Doing so, and following the same procedure as before enables the determination of a new dispersion relation for the propagation constant given by

$$k^2 = n^2(\omega)\frac{\omega^2}{c^2}, \tag{2.15}$$

where $n(\omega)$ is the frequency dependent refractive index and may be expressed as:

$$n(\omega) = \sqrt{1 + \frac{Ne^2}{m\varepsilon_0(\omega_0^2 - \omega^2)}} \tag{2.16}$$

The Lorentz Model finds most success in predicting the response of plasmas and conducting metals, which have low density of free electrons such as the alkali

metals. It has limited accuracy for glass and high density metals where screening effects set up local fields which modify the local behaviour of the material.

The polarisation introduced above may also be expressed in the form:

$$\underline{P} = \varepsilon_0 \chi \underline{E} \tag{2.17}$$

where χ is the electric susceptibility and is a tensor parameter whose symmetry properties will reflect those of the medium that is describes.

In describing the expression for the polarisation in terms of the displacement the restoring force was assumed to be linear in the displacement. This is an approximation much the same way that in deriving the equations describing the simple harmonic motion executed by a perturbed mass on a spring, the restoring force was assumed to be linear the extension. Should the extension, however, exceed some elastic limit the restoring force will exhibit some dependence on higher order quadratic and cubic terms. In much the same manner, if the electromagnetic excitation is strong enough it is no longer adequate to approximate the restoring force of the electrons in the Lorentz Model to first order in the displacement. In this case higher order terms in the restoring force can be considered:

$$\underline{F}_R = -k\underline{x} - \tfrac{1}{2}k'\underline{x}^2 - \tfrac{1}{3}k''\underline{x}^3 - \ldots \tag{2.18}$$

These terms are expressed as a Taylor expansion of the restoring force about the equilibrium position in the displacement and can be seen to correspond to a potential energy function of the form:

$$U(x) = -\int \underline{F}_R d\underline{x} = \tfrac{1}{2}k\underline{x}^2 + \tfrac{1}{6}k'\underline{x}^3 + \ldots \tag{2.19}$$

These anharmonic terms can then be incorporated into the analysis to determine the response of the electrons to strong excitation. A typical anharmonic potential compared to a harmonic potential are plotted in Figure 2.1. Initially for simplicity the discussion will be limited to a first order correction in the restoring force. The equation of motion describing the system then becomes

$$\frac{\partial^2 \underline{x}}{\partial t^2} + \omega_0^2 \underline{x} + b\underline{x}^2 = \frac{e}{m}\varepsilon E_0 \cos(\omega t - kz) \tag{2.20}$$

where the coefficient in the quadratic correction term has been rewritten as 'b'. One can assume that the nonlinear correction is small compared to the linear terms except for when the displacement is very large.

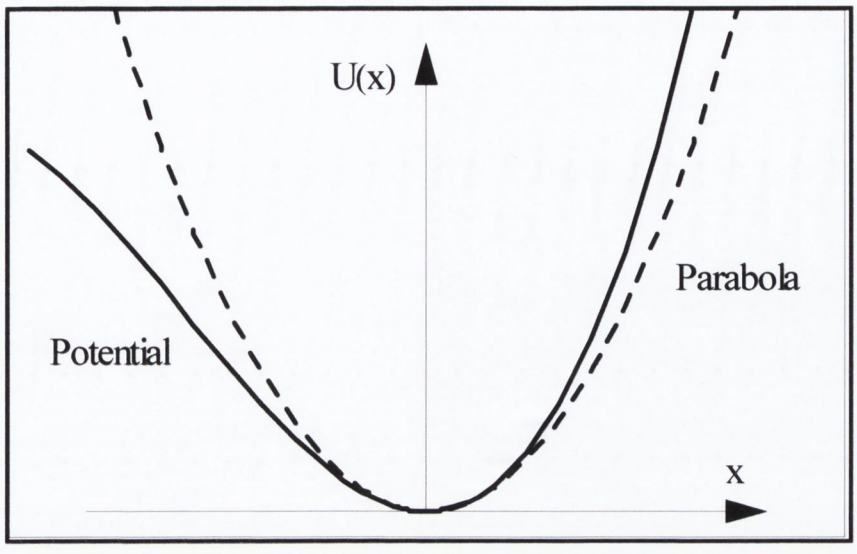

Figure 2.1 Potential energy function for a noncentrosymmetric medium calculated from Equation 2.19 where the deviation from the harmonic parabolic potential (dashed line) to the actual potential with the anharmonic correction (solid line) is clearly evident.

This can then be solved by initially assuming an approximate solution $\underline{x}^{(1)}(t)$ of the form of Equation 2.13 and then substituting this back into Equation 2.20. A better approximation to $\underline{x}(t)$ denoted $\underline{x}^{(2)}(t)$ can then be obtained and is expressed for the steadily driven case as:

$$\underline{x}^{(2)}(t) = \left(\frac{e}{m(\omega_0^2-\omega^2)}\right)E_0\cos(\omega t-kz) - \frac{b}{2\omega_0^2}\left(\frac{e}{m(\omega_0^2-\omega^2)}\right)^2 E_0^2 - \frac{b}{2}\left(\frac{1}{\omega_0^2-4\omega^2}\right)\left(\frac{e}{m(\omega_0^2-\omega^2)}\right)^2 E_0^2\cos(2\omega t-kz) \tag{2.21}$$

It can be thus seen that the solution contains a DC term and a term oscillating at twice the driving frequency. The significance of the anharmonic term manifests itself as adding an oscillatory term to the displacement at the second harmonic of the driving frequency. Since the polarisation is dependent upon the electron displacement through the dipole moment it can be seen that the polarisation now also includes a term oscillating at 2ω. When this form for the polarisation is introduced into the wave equation it acts as a source of electromagnetic radiation, which has its origin in the anharmonic response of the electrons to a perturbation in the Lorentz model. It can also be shown that the inclusion of higher order correction terms in the restoring force can lead to polarisation components of the same order.

2.1.3 Nonlinear Polarisation

The optical response of a material is usually formally presented by defining the polarisation vector $\underline{P}$. Under low irradiation intensity, this polarisation, is linearly dependent on the electric field strength, $\underline{E}$, and under high intensity the linear dependence can be series expanded and expressed as:

$$\underline{P} = \underline{P}_0 + \varepsilon_0 \left(\chi^{(1)} \underline{E} + \chi^{(2)} \underline{E}.\underline{E} + \chi^{(3)} \underline{E}.\underline{E}.\underline{E} + \ldots \right) \qquad (2.22)$$

where $\underline{P_0}$ is the linear polarisation, ε_0 is the permitivity of free space, $\underline{E}$ is the electric field strength of the incident optical field, $\chi^{(1)}$ denotes the linear susceptibility of the material and is a second rank tensor and $\chi^{(m)}$ for $m > 1$ denotes the m^{th} order nonlinear susceptibility tensors or rank $m+1$. The symmetry relationship $\underline{P(E)}=\underline{P(-E)}$ means that even order susceptibilities do not feature in materials with centrosymmetry as is the case for the materials studied in this thesis.[3] Thus, the third order susceptibility, $\chi^{(3)}$ is first nonlinear term and has no symmetry restrictions. It involves the interaction of three photons to produce a fourth and is of interest since it is responsible for several important phenomena including Self Phase Modulation (SPM), Phase Conjugation, Two Photon Absorption and Self Focusing and Defocusing

In general the susceptibilities are complex and the real part of the susceptibility defines parametric processes, which implies that the initial and final quantum mechanical states involved in the multiphoton interactions are the same and photon energy is conserved, while the imaginary part of the susceptibility implies damping of the optical wave in the medium resulting from the exchange of energy between the optical field and the nonlinear medium. These non-parametric processes can occur under resonant or non-resonant conditions and involve the redistribution of electrons among the electronic states.[4]

2.1.4 Effective Susceptibilities

Nonlinear absorption originating from other sources other that those of $\chi^{(3)}$ is also possible. These are generally due to either nonlinear scattering or more commonly excited state transitions, where under sufficiently large optical pumping a significant proportion of the samples' population is excited into a state of higher energy. Specific types of excited state absorption, namely saturable and reverse saturable absorption, are discussed mathematically later in Chapter 4. However, the total

absorption coefficient (α_{Total}) can be considered as consisting of both linear and nonlinear terms and can be expressed as:

$$\alpha_{Total} = \alpha_0 + \alpha_{NL} \tag{2.23}$$

where α_0 is the linear and α_{NL} is the nonlinear absorption coefficient. If the nonlinear absorption coefficient is considered as a summation of functions of the irradiation intensity then the expression can be rewritten as:

$$\alpha_{Total} = \alpha_0 + f(I) + O(I^2) + O'(I^3) + \ldots \tag{2.24}$$

where $f(I)$ represents an intensity dependent nonlinear absorption and there may be terms of orders of I^n in the expansion also, $O(I^n)$. If it is assumed that the dominant nonlinearity is described by $f(I)$ then under certain conditions, such as for example low intensity, it may be possible to expand $f(I)$ as a term linearly dependent on I. The total absorption coefficient then becomes:

$$\alpha_{Total} = \alpha_0 + bI \tag{2.25}$$

where b is constant. One can consider the material behaving as an effective $\chi^{(3)}$ material and relate the nonlinear absorption coefficient b to an effective imaginary third order susceptibility $Im\{\chi^{(3)}_{eff}\}$. The $Im\{\chi^{(3)}_{eff}\}$ coefficient can be used to compare the material with other 'true' parametric $\chi^{(3)}$ responses exhibited by other materials in terms of the magnitude of the observed optical dissipation.

Practically one can consider the response of a saturable absorber, which will be discussed in greater detail in Chapter 4. The light intensity at which the material saturates is termed I_{Sat}, and if optical pumping $I << I_{Sat}$ is considered then the total absorption coefficient can be described as:

$$\alpha_{Total} = \frac{\alpha_0}{1 + I/I_{Sat}} \approx \alpha_0 \left(1 - I/I_{Sat}\right) = \alpha_0 - \frac{\alpha_0}{I_{Sat}} I \tag{2.26}$$

The nonlinear term is then linearly dependent on the intensity and the response can be described as an effective $\chi^{(3)}$ response.

2.2 Optical Interactions in Organic Material

2.2.1 Basic Concepts of Organic Materials

The term organic material is used to refer to all materials where their chemistry is determined by their carbon atoms. They encompass a vast range of materials, from methane to polymers, dyes to fullerenes, and most biological materials. The materials

used in this thesis consist of phthalocyanines, carbon nanotubes, and specifically chosen conjugated polymers.

Carbon is unique in that it can form many different bond arrangements, both in carbon-carbon bonds, and in bonding to other materials. For example, simple hydrocarbons of two carbons can form several different arrangements, e.g. ethane (C_2H_6), or ethylene (C_2H_4) (Figure 2.2a and 2.2b respectively). The reason for this is due to the difference

(a) **(b)**

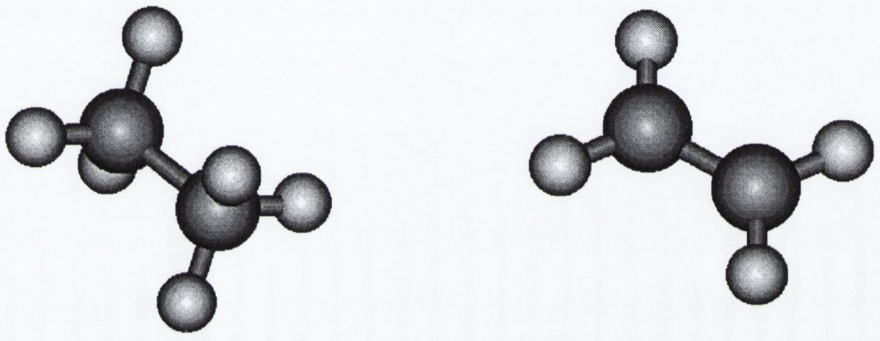

Figure 2.2 Structure for **(a)** ethane (C_2H_6) and **(b)** ethylene (C_2H_4)

in the carbon-carbon bonds in these materials. The electron configuration of a single carbon atom is $1s^2\ 2s^2\ 2p^2$. Because of this, carbon would be expected to exhibit a valence of two and would form structures such as CH_2, which would be similar to the bonding structure of H_2O. However, because of the small difference between the $2s^2$ and $2p^2$ energy levels, compared to the binding energy of chemical bonds, the wave functions of these four electrons can easily mix with each other in a process called hybridisation. For example in ethane, the 2s and 2p electron orbitals mix, creating four equivalent degenerate orbitals, arranged around the nucleus. These orbitals are sp^3 hybrid orbitals. Three of these combine with the 1s electron of the hydrogen atoms to form a filled orbital, a C-H bond. The fourth one combines with an sp^3 orbital from the other carbon atom to form a final filled orbital, a C-C bond. All the electrons in this molecule are then tightly bound in σ bonds. The end structures have a tetrahedral orientation and a bonding angle of approximately 109.5°. Due to the high bonding energy of these bonds, it takes a large amount of energy to excite these electrons, and these bonds are therefore relatively inert. Because of this, excitation of these bonds tends to be accompanied by chemical reaction of the molecule. This sp^3 bonding is the type of bonding that carbon forms in most common polymers used

in industrial applications, e.g. PVC (poly vinylene chloride), as well as diamond, and explains the highly insulating and inert nature of these materials.[5]

Ethylene (C_2H_4) has a much different bond structure, which is essential to understanding the nature of conjugated molecules, polymers and nanotubes. In ethylene, two s and one p electrons combine to form three sp^2 hybrid orbitals. These are arranged in a plane around the nucleus, separated by 120^0. Two of these bond with hydrogen atoms, one with another carbon atom, leaving one electron on each atom in the unhybridised p_z orbital. The p_z orbitals are arranged in a dumbbell shape out of plane. The electrons in these orbitals overlap to form a final filled bonding molecular orbital, a π bond. These bonds are weaker and much more delocalised, and therefore require much less energy to excite. In addition, excitations of these electrons leave the molecular structure relatively unperturbed. The bonding structure of ethylene is depicted in Figure 2.3.

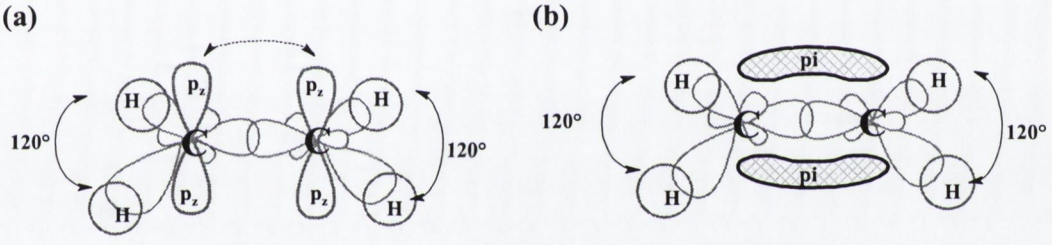

Figure 2.3 Bonding structure of Ethylene showing **(a)** p_z orbitals and **(b)** π bond molecular bonding orbitals.

The p_z orbitals perpendicular to the molecular plane can be seen in Figure 2.3a. It can be seen from Figure 2.3b that such delocalisation of the electrons in p_z orbitals results in an effective electron cloud equally probable above and below the plane of the molecule. What are important about these π bonds are their delocalisation from the molecular plane, and their relatively low energy. These highly delocalised π electrons require a much lower energy of excitation compared with electrons held in σ bonds.[6]

2.2.2 Conjugated Organic Systems and Colour

If two double bonds are separated by a single bond, the bonding system is said to be conjugated. Conjugated systems can be extended to a large amount of alternate double and single bounds and the resulting π electrons can be delocalised over the entire system. For example, in benzene (Figure 2.3a), one of the simplest cyclic

conjugated system containing six carbon atoms (six p_z orbitals), three double bonds and three single bonds, the π electrons are delocalised and form two cyclic orbitals one above and the other below the carbon ring (Figure 2.3b). This delocalisation reduces the energy of the system causing benzene to absorb at approximately 260 nm, compared to ethylene, which absorbs at 171 nm and ethane which absorbs at wavelengths below 160 nm.

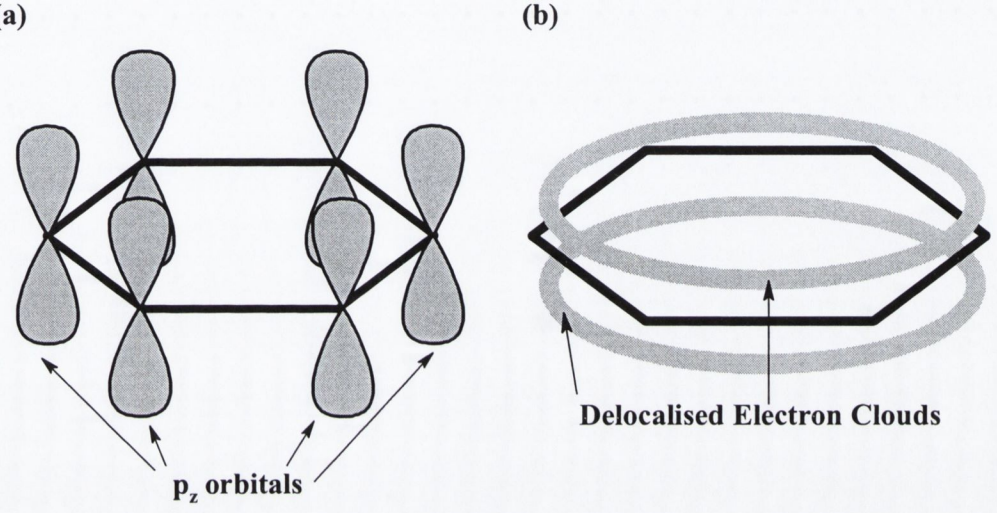

Figure 2.4 **(a)** Sketch of p_z orbitals in benzene **(b)** These delocalised electrons form cyclic electron clouds in conjugated systems, such as benzene, where the electrons are delocalised over the entire system.

Conjugated double bonds are the basic mechanism responsible for visible light absorption in compounds such as dyes that absorb at wavelengths above 200 nm. Conjugated systems or molecules can contain many different bonds apart from pure double bonded carbon. For example one can consider the azo group (-N=N-), the thio group (=C=S), and the nitroso group (-N=O). These groups are also called chromophores. Chromophores control colour in the sense that they alter the electronic structure of the remainder of the conjugated system and thus they function by altering the energy of the delocalised electrons. This alteration results in the compound absorbing radiation from within the visible range instead of outside this region. Groups called auxochromes may intensify the colour of a conjugated system. These are generally polar atoms or groups favouring the separation of electrical charge in the molecule. The function of the auxochromes is to increase the stability of the alternative resonance forms. They do so because they can retain electrical charge more readily than carbon atoms can. Common auxochromes groups are for

example amine ($-NH_2$), nitro ($-NO_2$), methyl ($-CH_3$), hydroxyl (-OH), bromide (-Br), and chloride (-Cl).[7, 8]

Cyclic conjugated carbon systems, or aromatic systems, are an immensely interesting family of molecules especially where nitrogen atoms replace some of the carbon atoms. The most basic example is chlorophyll, an 18 π electron derivate of the standard porphyrin, which is responsible for the green colour in plants. Myoglobin and haemoglobin, also 18 π systems, cause the red colour in muscles and blood. As will become clear later phthalocyanines studied in this work are also a member of the 18 π electrons family of conjugated systems. Thus, conjugated systems are ideal candidates for applications involving visible light.

2.3 Photophysical Processes in Conjugated and Aromatic Systems

2.3.1 Introduction

A photophysical process is one that results from the electronic excitation of a molecule or system of molecules by non-ionising electromagnetic radiation, and does not in the first instance involve a chemical change in the molecule though it may be the initiation step in one. There are several processes that will be of concern in the following chapters and they can be generally divided into radiative excitation and relaxation transitions and non-radiative transitions. However, before discussing these transitions it is necessary to discuss the environment in which they occur and for this a generalised electronic structure for polyatomic systems will be employed.

The electronic states of a diatomic molecule, for example, may be described in terms of a Morse potential energy function of the form:

$$E(r) = E_B\left(e^{-2a(r-r_0)} - 2e^{-a(r-r_0)}\right) \qquad (2.22)$$

where E_B is the binding energy, r the intermolecular separation r_0 is the natural separation of the diatomic bond and a is an arbitrary constant. Sample potential energy curves created with this equation are depicted in Figure 2.5 with three energy levels in the system. The energy here refers to the total energy, which includes both vibrational and electronic contributions. These and such curves are good approximations to the anharmonic oscillator model (Lorentz Model) for diatomic molecules presented earlier in this chapter. Considering this as a good starting point a similar set of levels can be used for the qualitative discussion of more complex polyatomic molecules, such as those systems that form conjugated units. In this case

the nuclear separation parameter has to be replaced by a nuclear configuration coordinate. It can be seen in Figure 2.5 that the molecular electronic levels were divided into singlet and triplet levels, the lowest or ground state being a singlet level and the next highest state generally being a triplet state in accordance with Hund's Rule which states that terms with greatest multiplicity lie lowest.

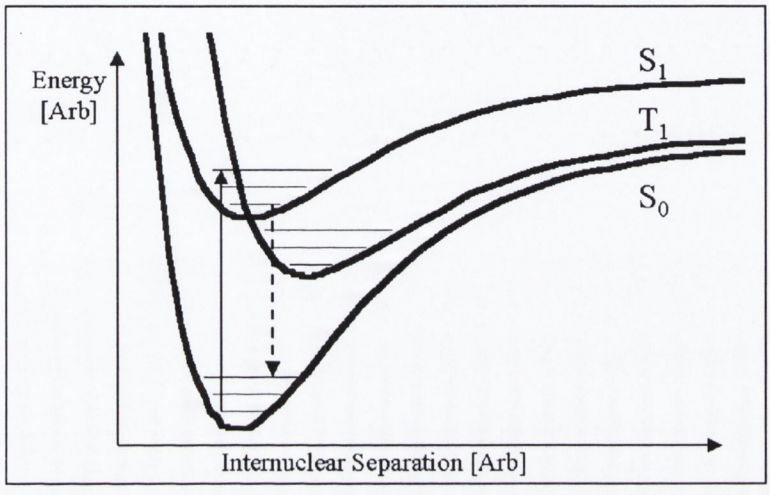

Figure 2.5 Potential energy curves of lowest singlet and triplet states. The solid arrow implies an excitation and the dashed arrow implies a radiative transition.

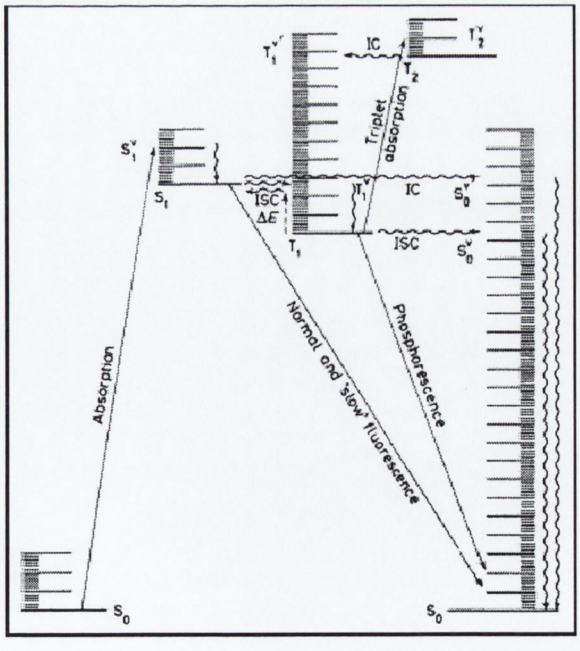

Figure 2.6 Jablonski diagram showing absorption and emission processes.

It can also be seen that each of the electronic levels are further sub-divided into vibrational and rotational levels whose extent is much greater and highly more complex than the representative three levels per electronic level depicted in Figure 2.5. High vibronics of the ground state can even occur at the same energy as higher excited singlet and triplet states. The various transitions that can take place between the electronic and vibronics levels can be presented schematically in a Jablonski diagram such as that in Figure 2.6. In this figure the possible excitation absorptions and radiative and non-radiative transitions can be seen.

2.3.2 Absorptive Excitation Transitions

If one considers an ensemble of molecules at room temperature the Boltzmann distribution shows that almost all of these are in the lowest vibrational level of the ground state S_{00}, with a small fraction in higher vibrational levels such as S_{01} or S_{02} etc. Thus the vast majority of excitations from the ground state take place from the S_{00} level. The most familiar form of an absorptive excitation is that of ground state absorption where a molecule is excited from its lowest ground state into a vibrational level in the first excited state. Since excitation occurs from only one level in the ground state to any or all of the vibrational levels in the excited state, dependent upon the wavelength of the excitation, an absorption spectrum hence yields information on the vibrational energy distribution in the excited state.

Absorptive processes occur on a time scale of $\sim 10^{-15}$ s, which is much too rapid too allow time for nuclear motion and hence there is no change in the nuclear coordinate for an electronic transition. This corresponds to the case of maximum overlap between the ground state vibrational wave function and that of the excited state. This is in accordance with the Frank-Condon Principle which simply states that the nuclear coordination remains stationary during an electronic transition. In Figure 2.5 this effect was sketched by representing the excitation as a vertical line.[9]

The envelope of the vibronic bands within an absorption band is referred to as the Frank-Condon envelope and its maximum corresponds to the Frank-Condon maximum. This approximates to the position of the most intense vibronic absorption band. If this corresponds to the a transition between the two lowest vibronics levels as in the $S_{00} \rightarrow S_{10}$ absorption, this indicates that the mean nuclear configuration of the excited state is similar to that of the ground state.

Subsequent absorption is also possible out of excited states and this form of absorptive transition is termed excited state absorption. This could be for example absorption of the form $S_{10} \rightarrow S_{xy}$ which represents an absorption excitation from S_{10} level to the y^{th} vibronic level of x^{th} excited electronic state. Excited state absorption is one of the principal effects under investigation in this work and its mathematical treatment and development in left until Chapter 4 where it is applied to phthalocyanine systems. The incidence of such excitations is rare except under high radiant fluences which appreciably deplete the ground state population and where the incident light has a spectral component that may couple to a higher energy level.

2.3.3 Vibrational Relaxations

Subsequent to a molecule being excited into an excited vibronic level of an excited state its energy is composed of three components, its electronic energy E_0, its zero point vibrational energy and its higher order vibrational energy. In a condensed medium, such as a liquid, the molecule will rapidly cascade down the vibrational manifold, losing its vibrational energy to establish thermal equilibrium with its surroundings. This process which is one of simple thermal relaxation occurs on a timescale of $\sim 10^{-13}$ s.

2.3.4 Fluorescence

A molecule that has been excited and subsequently undergone a vibrational relaxation to the lowest vibronic level of the excited state, may then relax radiatively to the ground state vibrational manifold. If both states have the same multiplicity this process is known as fluorescence. It is a spin allowed process and generally occurs over a lifetime of 1-100 ns (Figure 2.6). Since emission proceeds from the lowest vibrational level in the first excited state to the vibrational levels of the ground state, a fluorescence spectrum yields information concerning the vibrational energy level distribution in the ground state. Due to the thermal relaxation, which ensues after the initial excitation, the molecule looses energy. This manifests itself as a red shift in the emission spectrum compared to that of the absorption spectrum and is termed the Stokes shift. Thus, both spectra due to the complimentary nature of the transitions should share approximate mirror symmetry though in condensed media such as solvents the two states may be solvated differently and the symmetry

may not be so obvious. Such mirror symmetry is also taken to denote a similar nuclear configuration in the ground and excited states.

The quantum yield, φ_F, is defined as the ratio of the number of molecules excited to the number of molecules which subsequently fluoresce in a system and is an important parameter in the discussion of fluorescence. Thus this parameter is the ratio of absorbed to reemitted photons. There are many other processes that may compete with this radiative de-excitation such as internal conversion, intersystem crossing and other quenching mechanisms. Accounting for these the quantum yield of fluorescence may be redefined as the ratio of fluorescence to the total rate of all de-excitation of relaxation processes.

$$\varphi_F = \frac{k_F}{k_F + k_{ISC} k_{IC} + k_Q} \tag{2.22}$$

In this equation k_F, k_{ICS}, k_{IC} and k_Q are the rate constants for fluorescence, intersystem crossing, internal conversion and quenching mechanisms respectively.

The radiative lifetime τ_F is the reciprocal of the radiative transition probability and is equal to the Einstein A coefficient summed over the complete fluorescence spectrum.

$$\frac{1}{\tau_F} = \mathrm{k_F} = A_l = \sum_m A_{uo \to lm} \tag{2.23}$$

This is related to the B coefficient through the relation

$$A_{uo \to lm} = \frac{8\pi n h\nu^3}{c^3} B_{u0 \to lm} \tag{2.24}$$

where n, h, υ and c are the refractive index, the Plank constant the excitation frequency and the speed of light respectively. $B_{u0 \to lm}$ is related to the absorption spectrum through the relation

$$B_{lu} = \frac{2303c}{hnN} \int \frac{\varepsilon(\nu)}{\nu} d\nu \tag{2.25}$$

and this allowed the re-defining of k_F as

$$k_F = \frac{8\pi\, 2303 n_F^3}{c^2 N n_A} \langle \nu^{-3} \rangle \int \frac{\varepsilon(\nu)}{\nu} d\nu \tag{2.26}$$

where n_F, and n_A are the averaged refractive indices over the fluorescence and absorption bands respectively. This expression thus relates the radiative lifetime to the integrated absorption spectrum and is known as the 'Strickler-Berg Equation'.

2.3.5 Internal Conversion

If one considers a molecule that has been photo-excited to an energy level S_{2x} and has subsequently relaxed to S_{20} via vibrational relaxation it may transfer to a high vibronic level of S_{0x} through an isoenergetic process known as internal conversion. This can be considered in terms of Vavilov's Law, which states that the fluorescence quantum efficiency is independent of the excitation wavelength. Adherence to this rule implies the existence of some form of intramolecular radiationless transition whereby a molecule excited into S_{mx} for $m \geq 2$ relaxes into the first excited singlet state from which it fluoresces. Thus, any fluorescence will be as if the molecule was excited into S_{1x} only.

There does exist exceptions to Vavilov's rule, for example azulene which exhibits $S_{20} \rightarrow S_{0x}$ emission. The failure to observe radiative emission from higher excited states led to the formulation of Kasha's rule which states that in complex molecules all emission occurs from the lowest excited electronic state of a given multiplicity.

2.3.6 Intersystem Crossing

If a molecule undergoes an isoenergetic spin forbidden transition from an excited singlet state to a triplet state the process is termed intersystem crossing. It may originate from the zero point vibrational level of S_1 or a thermally populated vibrational level. The transition may be into any vibrational excited levels of the triplet levels with comparable energy. Some of the systems explored in this thesis exhibit this phenomenon and it is discussed mathematically in Chapter 4.

2.3.7 Phosphorescence

In the lowest lying vibronic level of the triplet state a molecule may radiatively relax to the ground state through a process known as phosphorescence. This process since it involves a change of multiplicity, unlike fluorescence, is forbidden and thus it regularly occurs on millisecond timescales when it is observed. The emission is generally weak as there is ample time for other more rapid competing processes to quench the triplet exciton. Spin forbidden transitions, such as phosphorescence or intersystem crossing, are made possible through spin-orbit coupling between the

states of different multiplicity.

References

1 R. W. Boyd, *Nonlinear Optics*, (Academic Press Inc., Boston, 1992).

2 J. Callaghan, PhD Thesis, Trinity College Dublin, 1996.

3 J. F. Nye, *The Physical Properties of Crystals*, (Clarendon Press, Oxford, 1985).

4 A. Yariv, *Quantum Electronics*, Holt, (Rinehart and Winston, New York, 1985).

5 N. N. David Oxtoby, *Modern Chemistry*, (Saunders College Publishing, Fort Worth, 1996).

6 E. N. Abrahart, *Dyes and their Intermediates*, (Edward Arnold Ltd., London, 1977).

7 R. L. M. Allen, *Colour Chemistry*, (Nelson, London, 1971).

8 C. Nitschke, MSc Thesis, Trinity College Dublin, 2003.

9 R. M. Eisberg and R. Resnick, *Quantum physics of atoms, molecules, solids, nuclei, and particles,* 2nd Edition, (John Wiley, New York, 1985).

Chapter 3

Materials and Optical Experimental Techniques

3.1 Introduction to the Phthalocyanine

3.1.1 The Initial Discoveries[1]

In 1907, working at the South Metropolitan Gas Company, London, Braun and Tcherniac observed a highly coloured, insoluble material as a by-product during the preparation of *ortho*-cyanobenzamide from phthalimide and acetic acid. This was the birth of the class of organic compounds that would later be termed phthalocyanines (Pc). In similar circumstances twenty years later in 1927 de Diesbach and von der Weid at Fribourg University obtained a 23% yield of an exceptionally stable, blue material, again as a by-product, during the reaction of *ortho*-dibromobenzene with copper cyanide in refluxing pyridine. With the benefit and privilege of 'hindsight' one can interpret these by-products as being the first synthetic experimental observations of metal-free and copper centred Pcs respectively.

The quest to determine the molecular structure of the Pc began in 1928 at Scottish Dyes Ltd. During the preparation of phthalimide from phthalic anhydride[2] the glass-lined reaction vessel cracked exposing the outer steel casing to the reaction and yielded a blue-green material. Given the business nature of the company, employees Dandrige and Dunsworth were tasked with investigating the novel material that had been produced. Their studies revealed that the iron-containing by-

product was exceptionally stable and exhibited clear potential for application as a pigment. The preparation process was patented and some time later samples of the material were sent to Professor J.F. Thorpe at Imperial College, London, for structural investigations by Imperial Chemical Industries, who had by that time acquired Scottish Dyes. From Thorpe's hand the samples found their way to R.P. Linstead and the collaboration culminated in six papers published in the *Journal of the Chemical Society* that described the structure and synthesis of the Pc and some of its metal derivatives.[3-8] It was Linstead who coined the name phthalocyanine, combining the prefixes *phthal* and *cyanine* from the Greek words *naphtha* (rock oil) and *cyanine* (blue).

Phthalocyanines became commercially available from Imperial Chemical Industries in the mid-1930s with the parent and its copper complex marketed as Monastral Fast Blue B and G, respectively (Figure 3.1).

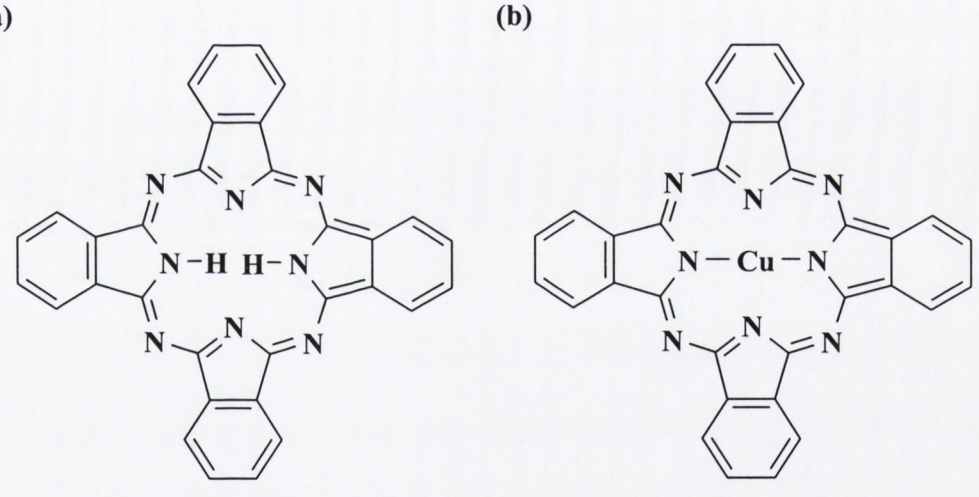

Figure 3.1 Chemical structure of (a) Monastral Fast Blue B and (b) Monastral Fast Blue G.

3.1.2 Physical Structure and Nomenclature for Phthalocyanines

The phthalocyanine molecule is a highly versatile entity that can be chemically modified in many ways. The substitutions that are possible to the main macrocycle generally fall into three categories. The peripheral of the macrocycle can have chemical substituents attached, the cavity can be substituted with about seventy different elemental ions and subsequent to the central cavity modification, and of course depending on the element in the cavity, chemical groups can be attached to the cavity ion to form axial groups that grow approximately perpendicular to the macrocycle. The choice of central metal cation and peripheral groups can strongly

influence the physical properties of the Pc and thus provide a method of tailoring the response of the Pc unit to react differently and predictably to different stimuli. Due to the many variations of the parent compound (Figure 3.1a) that are possible an unambiguous system for compound nomenclature is required to distinguish between the many Pc variations that will be discussed in this thesis.

The Pc structure depicted in Figure 3.2 is a schematic where the possible substitution sites have been labelled. Substitutions at locations 2, 3, 9, 10, 16, 17, 23 and 24 are generally termed peripheral benzo-substitutions and at locations1, 4, 8, 11, 15, 18, 22 and 25 are generally termed non-peripheral benzo-substitutions. The cavity substitution site M indicates the central cation, and subsequent possible modifications at A, bonded to M, are termed axial substitutions.

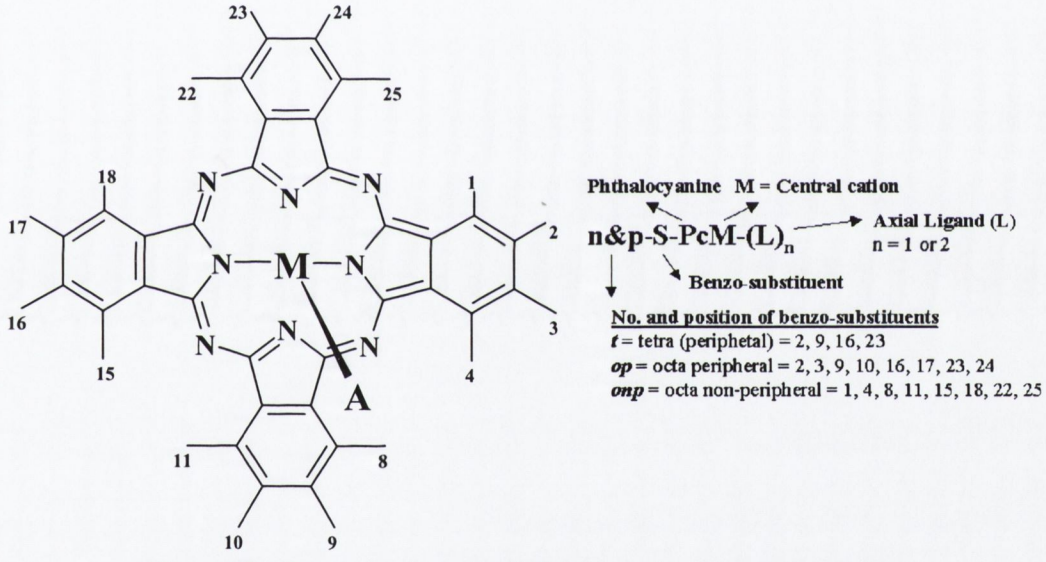

Figure 3.2 Chemical schematic of phthalocyanine where the possible substitution sites have been labelled. Substitutions at 2, 3, 9, 10, 16, 17, 23 and 24 are generally termed peripheral benzo-substitutions and at 1, 4, 8, 11, 15, 18, 22 and 25 are generally termed non-peripheral benzo-substitutions. M indicates the central cation, and modifications at A are termed axial substitutions.

The complete method of naming any given compound takes the following format: n&p-S-PcM-$(L)_n$, where n and p denote the number and position of the benzo-substituents, S denotes the substituent name, Pc denotes the phthalocyanine macrocycle, M as before indicates the central cation and L denotes the axial ligand attached to M where n = 1 or 2 if L represents a single atom. Thus in this notation the structures in Figure 3.1a and 3.1b are called PcH_2 and PcCu respectively, as neither compound has neither axial nor benzo substituents. However, clearly this

notation rapidly becomes longwinded and a reduced notation is generally utilised throughout this thesis. In this reduced notation the compound is represented by R_xPcML where R_x denotes x benzo-substituents of type R and the other symbols are as they were defined previously.

3.1.3 Electronic Structure of Phthalocyanines

The remarkable clear blue or green colours found in Pcs led to their adoption for use as industrial pigments and dyes soon after their discovery. The physical origin in the electronic structure of the colour exhibited by Pcs will be briefly described here. Phthalocyanines are closely related to the naturally occurring porphyrins having 18 π electrons. Every methin-group (-CH=) donates one π-electron and every aza-group (-N=) donates another. Additionally, the tertiary nitrogen atoms (-NH-) supply the ring with their free electron pairs. This cannot be done by the aza-groups, as their electrons are in the plane of the macrocycle. This electron constitution thus implies an aromatic system, independent of the external benzene rings obeying Hückel's rule, with (4n+2) π-electrons, n=4.[9]

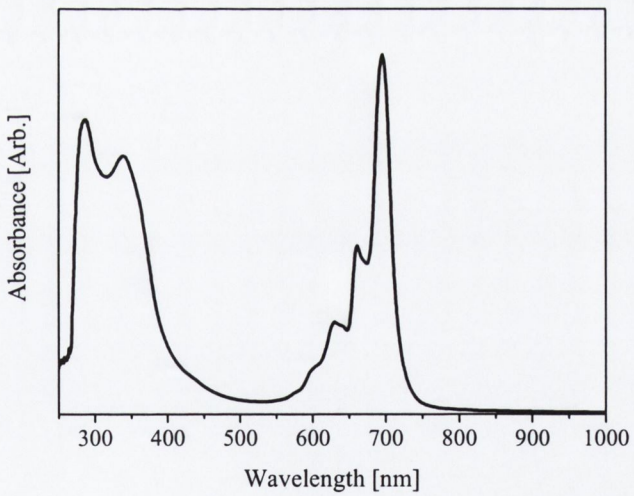

Figure 3.3 Typical linear absorption spectrum of visible light for a dilute metallo-phthalocyanine solution, where the B- (UV-Blue, ~350nm) and Q- (Red, ~700 nm) absorption bands are clearly evident.

Phthalocyanines exhibit a signature absorption spectrum across the visible wavelengths. There is always a strong absorption in the region of 650-700 nm termed the Q-band and another in the ultra-violet (UV) region between 320-400 nm termed the B-band (or Soret band). The former absorption is responsible for the

characteristic intense blue or blue-green colour exhibited by these compounds. A typical linear UV-visible absorption spectrum is depicted in Figure 3.3 where the Q- and B-bands can be seen. The weaker bands at approximately 650 nm and 620 nm are vibrational overtones of the Q-band.

The electronic molecular orbital structure of a typical metal substituted Pc was mapped using extended Hückel calculations by Schaffer *et al.* in 1973.[10] The Q-band absorption was assigned to a $\pi \rightarrow \pi^*$ transition from the highest occupied molecular orbital (HOMO) of a_{1u} symmetry to the lowest unoccupied molecular orbital (LUMO) of e_g symmetry.

3.1.4 Semi-Empirical Structure Modelling of Phthalocyanines

In this section the geometric effect of inserting a metal into the cavity of a phthalocyanine molecule will be investigated using semi empirical calculations, on titanium phthalocyanines as a case study. Although many variations of the Pc were modelled, with various peripheral and axial groups only the similar distortions seen in all cases are described here. The intention is not to predict any electronic properties; it is merely to observe the distortion of the Pc planar ring after metal insertion into the cavity. ZINDO methods were used, as these are capable of performing calculations on molecules containing transition row elements. The ZINDO method is a variation of the Intermediate Neglect of Differential Overlap (INDO) method extended to transition row elements. These are self-consistent field (SCF) techniques. The ZINDO/1 parameter set was used in calculations.[11,12] The parameter set was applied without alteration for geometry optimisation and the σ-σ and π-π overlap weighting factors were set equal to unity. The optimisation algorithm was halted once the magnitude of the energy gradient was reduced to less than 0.1 kcal $Å^{-1}$ mol^{-1}.

The starting geometries had the macrocyclic ring planar and the axial section normal to the 'plane'. Standard textbook bond lengths and angles were used in the starting conformation of the molecules. The results of the geometry optimisation show a consistent distortion of the 'planar' macrocyclic ring. The typical distortion is shown in Figure 3.4. This 'saddle' type distortion was seen for all variations of

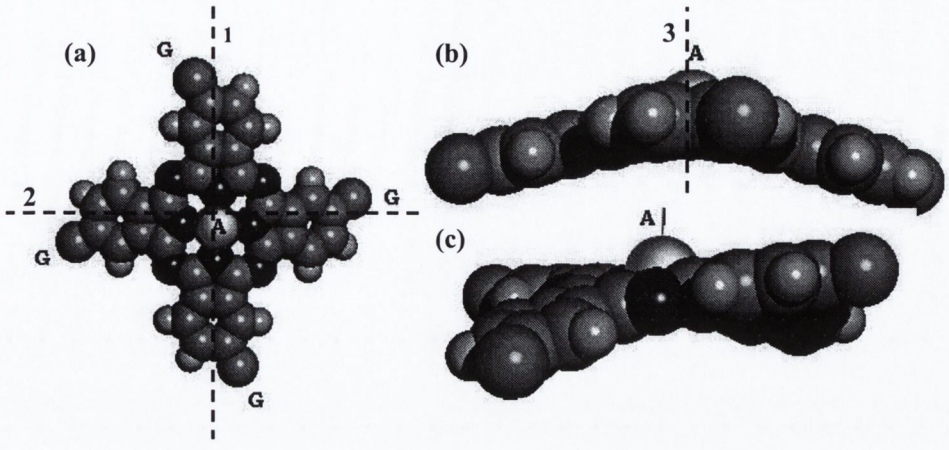

Figure 3.4 A close look at the typical distortion of the metallo-Pc ring after the geometry optimisation has been applied. The dashed lines 1, 2 and 3 are the inertial axes of the molecule. (a) is an overhead view in the direction if inertial axis 3, (b) is in the direction of inertial axis 2 and (c) is in a direction at an angle to inertial axis 2 but still normal to inertial axis 3. The axial (A) and the macrocyclic side groups have been removed from the diagrams for clarity. The 'saddle' type shape is typical and is seen for all PcTi molecules.

the PcTi that were tested.[13] In the diagram the macrocyclic peripheral groups and the axial substitution groups have been removed to show the distortion more clearly.

The Ti atom is bonded to two Nitrogen atoms in the macrocycle and is seen to sit above the 'plane' of the macrocycle. The average bond length for Ti-N bonds was found to be ≈ 2.1 Å with a standard deviation between all the molecules of ≈ 0.01 Å. This value compares well with that from X-ray crystallographic data of 2.07 Å[14], and from previous ZINDO/S calculations by Henari *et al.* who reported 2.13 Å[15]. The averaged value found here differs by ≈1% from the previous results. These calculations can be remade with other metals in the central cavity and a saddle type similar to here or a more spherical type distortion of planarity is generally seen.

3.2 Introduction to Carbon Nanotubes

3.2.1 The Initial Discoveries

The uniqueness of carbon amongst the other elements is partly due to its stability in sp^3, sp^2 and sp hybridised form and also partially due to it being the only group four element that can form stable double bonds allowing it to assume a wide range of different structures and forms. Before 1985 carbon was known to exist in two different ordered stable allotropes, they were graphite (sp^2 hybridisation, Figure 3.5a) and diamond (sp^3 hybridisation, Figure 3.5b). However in 1985 a new third allotrope

of carbon, the fullerene, composed of 60 carbon atoms in the form of a spherical cage was discovered by Kroto *et al.*[16] (Figure 3.5c). This C_{60} molecule, also known as the 'Buckminster Fullerene' in honour of Richard Buckminster Fuller the architect who had utilised this structure in the design of many buildings, was the parent compound of a whole new family of carbon nanostructures that were waiting to be uncovered.

One of the most significant subsequent discoveries in the fullerene family was made by S. Ijima who in 1991 reported the first observation of carbon nanotubes from the NEC Research Laboratory in Tsukuba, Japan.[17] In pristine condition, these macromolecules are hollow graphite cylinders without any distortion of the six-membered carbon rings, except for the distortion induced by the curvature of the tube, capped at each end with hexagonal and pentagonal membered hemi-spherical structures (Figure 3.5d). Due to their almost entirely one-dimensional geometry and high symmetry these molecules aroused the imagination of scientists and engineers who immediately predicted that unique mechanical and electronic properties would be exhibited by these nanotubes.

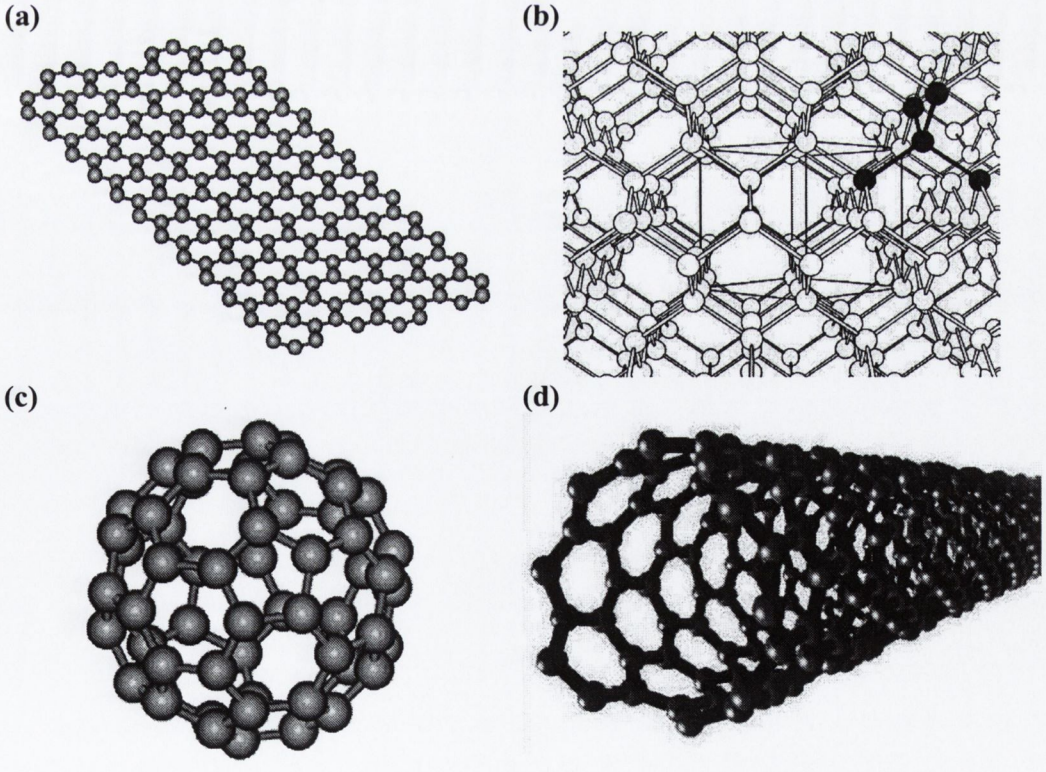

Figure 3.5 Allotropes of carbon (a) graphite, (b) diamond[18], (c) the C_{60} fullerene and (d) a carbon nanotube[19].

3.2.2 Physical Structure and Nomenclature for Carbon Nanotubes

Defect free carbon nanotubes consist of two-dimensional hexagonal lattices of carbon rolled into a cylindrical geometry. Nanotubes that consist of a single graphene cylinder are known as single-walled carbon nanotubes (SWNT), and those with more than one wall where the system is composed of concentric SWNTs with each successive layer wrapped about the previous layers are called multi-walled carbon nanotubes (MWNT). All cylindrical nanotubes are capped at both ends by endcaps where, as in the case of C_{60}, pentagonal structures are necessary to provide the required curvature to close the tube. Imperfections along the tube are commonly observed causing bending or kinks in the structure and are usually caused by pentagons, heptagons or sp^3 hybridised carbon in the lattice. MWNTs are generally of order tens of nanometres in diameter and SWNTs have diameters of order of nanometres. Both MWNTs and SWNTs can be hundreds of nanometres to microns in length.

The graphene sheet from which the nanotube originates can be rolled into many different geometries, and is generally characterised by the angle that the lattice makes with the cylinders axis. Mathematically this is described via the chiral vector where $C = na_1 + ma_2$, where n and m are integers and a_i represents the unit vectors in the graphene lattice. These vectors are depicted in Figure 3.6. For a perfect defect free SWNT the (n, m) pair of numbers from the chiral vector can be used to determine the diameter, chiral angle (angle between the lattice and the cylindrical lattice) and the electronic properties, such as the bandgap, of the nanotube. For example the chiral angle (θ_C) is given by $\theta_C = \tan^{-1}\left(\sqrt{3}n/(2m+n)\right)$, the diameter ($d$) is given by $d = \left(\sqrt{3}/\pi\right) r_{C\text{-}C}\sqrt{m^2+mm+n^2}$ where $r_{C\text{-}C}$ is the carbon-carbon bond length in nanometres and the bandgap energy (or the gap between the first two van Hove singularities for metallic tubes) is given by $E_G = 2r_{C\text{-}C}\gamma_0/d$ where γ_0 is the C-C tight binding overlap energy, and has been experimentally determined to be (2.7 ± 0.1) eV for nanotubes.[20]

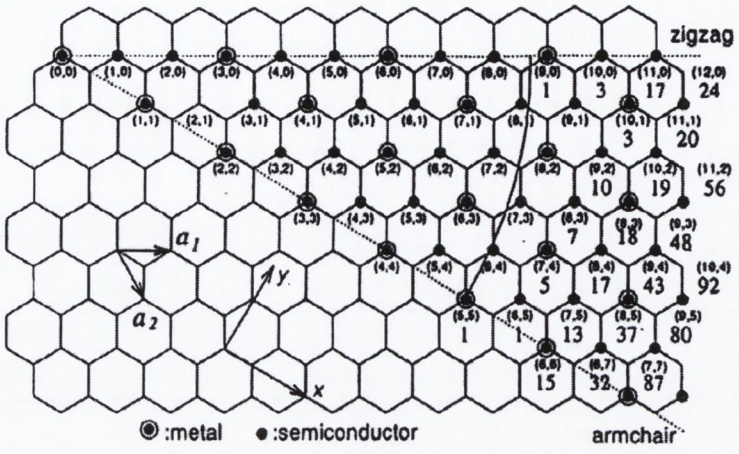

Figure 3.6 Sketch of the many possible chiral vectors for a carbon nanotube. For perfect closure the tube must be symmetrical under rotation by 2π.

The possible chiral vectors and their relationship to the lattice are depicted in Figure 3.6. Generally the chirality of a carbon nanotube falls into one of three categories. Zigzag nanotubes have chiral vectors of the form (n, 0) and therefore the rows of the lattice are perpendicular to the nanotube axis, armchair nanotubes have chiral vectors of the form (n, n) and thus they have C-C bonds lying perpendicular to the nanotube axis and all other chiral possibilities generally termed chiral nanotubes have chiral vectors of the form (n, m) with $n \neq m$ and $n,m \neq 0$. The three types of nanotube are depicted in Figure 3.7.

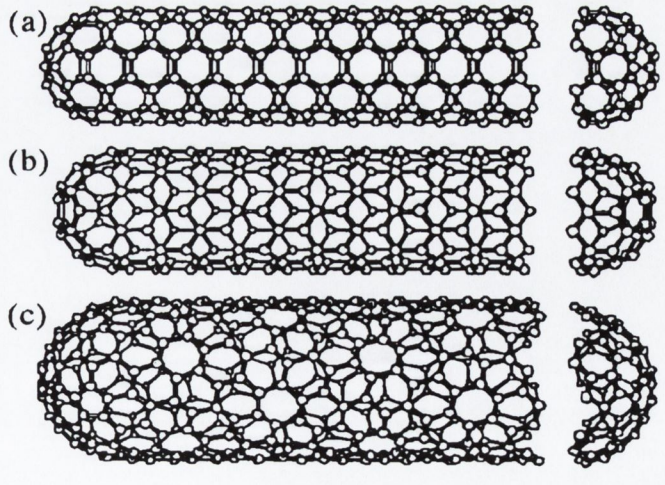

Figure 3.7 Categories of carbon nanotubes: (a) armchair, (b) zigzag and (c) chiral nanotubes.

3.2.3 Electronic Structure of Carbon Nanotubes

Carbon nanotubes are can be thought of as a cylindrically rolled graphene sheet. Thus the carbon atoms in these system are, as for graphite, in an sp^2 hybridised geometry. An idealised graphene sheet is a semiconductor with a 0 eV bandgap, and accordingly it usually exhibits metallic like conduction properties. However one has to combine this with the one-dimensional nature of nanotubes and it is this that has generated so much interest when considering their electronic properties. If one considers directions perpendicular to the tube axis it becomes clear that electrons are confined on the graphene sheet and thus are confined at the radius of the tube. Electrons are free to propagate along the entire length of the tube and thus all possible electronic wave-vectors are in the direction of the tubes' axis, implying that quantum confinement only exists in the radial directions. Moreover, as nanotubes of graphene exhibit perfect rotational symmetry (if the tube is considered defect free) there then exists periodic boundary conditions around the circumference of the nanotube. Thus, the electronic density of states (DOS) is forced also to have this periodicity. This boundary condition of periodicity is known as the Born-von Karmen boundary condition, and all allowable electronic states have to obey this condition. It can be expressed mathematically as:

$$\underline{k} \cdot \underline{C} = 2\pi q \qquad (3.1)$$

where q is an integer, $\underline{k}$ is the wave-vector and $\underline{C}$ is the chiral vector. If this model is applied to the electronic structure of the nanotube it can be seen that dependence on the circumference of the nanotube (and hence on (n, m) of the chiral vector) is critical. Depending on the length of the periodicity, allowed states can exist at the Fermi energy, and therefore the nanotube will be metallic, or a bandgap can exist at the Fermi level, and therefore the nanotube will be semiconducting. Sample band structure calculations for SWNTs taken from *Science of Fullerenes and Nanotubes* by M. S. Dresselhaus *et al.*[20] are depicted in Figure 3.8. These dispersion relations represent the three possible categories into which the electronic structure of all nanotubes must fall. The metallic tube (Figure 3.8a) has states at the Fermi level. The dispersion relation for the zero-bandgap pseudo-metallic nanotube (similar to graphene) is depicted in Figure 3.8b. In this case the nanotube will exhibit metallic behaviour at all temperatures above absolute zero, as thermal energy will ensure that

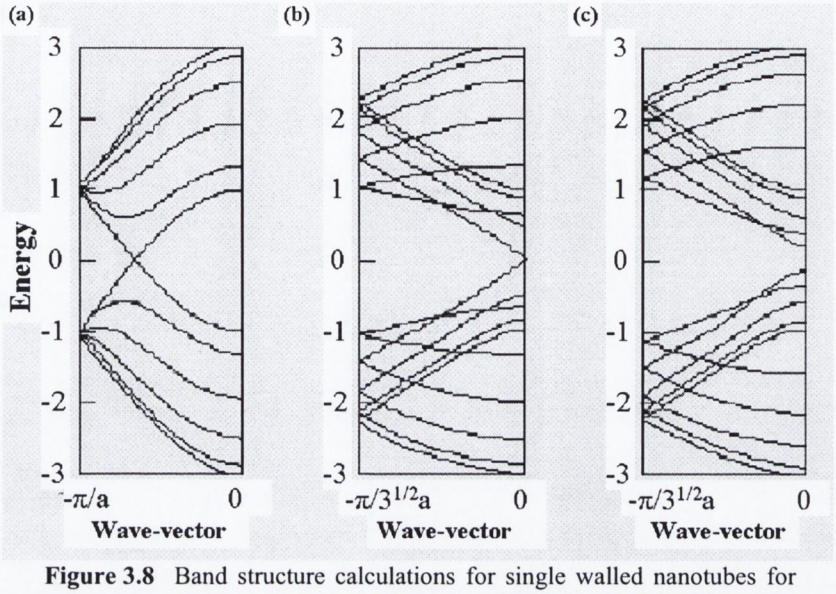

Figure 3.8 Band structure calculations for single walled nanotubes for (a) a truly metallic nanotube as there is a finite density of states at the Fermi energy, (b) a semiconducting nanotube with zero bandgap and (c) a semiconducting nanotube with a definite bandgap.

there is a large amount of occupied states in the conduction band. A semiconducting nanotube with finite bandgap is depicted in Figure 3.8c.

It turns out that the relationship that determines whether a nanotube will be metallic or semiconducting follows directly from n and m of the chiral vector and can be expressed as:

$$\frac{n-m}{3} = p \tag{3.2}$$

If $p = 0$ the nanotube is metallic, if p is an integer then it is pseudo-metallic or semiconducting. It is then immediately evident that one third of all possible chiral vectors (or possible nanotubes) are metallic, and that all armchair nanotubes ($n = m$) are metallic. It was stated in the previous section that the bandgap in SWNTs was inversely proportional to the tube diameter and given by $E_G = 2r_{C-C}\gamma_0/d$. This can be thought of and rationalised, if one considers that the curvature of the lattice induces a strain in the graphene sheet, which manifests itself in the electronic bandgap. As the curvature ever decreases with increasing diameter the bandgap reduces. If one extends this logic to the limit where the diameter tends to infinity, the result is a flat semiconducting graphene sheet with zero bandgap. This is simply what is experimentally observed for graphite.

It is also worth mentioning that one other electronic feature is generally

observed in SWNTs. These are singularities, known as van Hove singularities, in the density of states on the tube and are a direct consequence of the one-dimensional nature of the nanotube. More specifically they can be attributed to the confinement of the electronic wave vectors parallel to the nanotube axis. In the density of states they appear as sharp spikes arranged symmetrically about the Fermi level.[20]

The preceding general discussion on the electronic structure of SWNTs refers only to an idealised single defect free nanotube shell. This refers to perfectly hexagonal carbon units forming a lattice and rolled into a shell, and it is thus a simplification of what is generally experimentally observed. Usually nanotubes are not completely free from defects such as heptagonal units, pentagonal units or the presence of sp^3 hybridised carbon in the lattice leading to charge localisation, kinks or bends in the nanotube.[21]

Multi-walled carbon nanotubes (MWNT) consist of many concentric shells, which may interact with each other and add new levels of complexity to the electronic structure. The initial work on inter-shell interactions by Saito *et al.*[22] where they modelled a double-walled carbon nanotube suggested that interlayer coupling had little effect on the electronic structure of the individual shells. The shells were predicted to retain their semiconducting or metallic nature irrespective of the neighbouring shell. This leads to the fascinating concept of insulated conductors where a metallic nanotube may be encased in a semiconducting nanotube with a high-bandgap. However Charlier *et al.*[23] modelled a (5, 5) nanotube encased in a (10, 10) nanotube (both are metallic) and found for certain orientations of one nanotube inside the other interlayer interactions could force both nanotubes to exhibit semiconducting characteristics. They also reported on other combinations of double-walled nanotube systems and found cases where relative orientations did not effect the metallic or semiconducting nature of the respective layers of the multi-walled system. The density of states of a MWNT is far more complex than that of its SWNT counterparts, however it is generally thought that the outer shell dominates the electronic structure, as it is this that interacts with the ambient environment in which the tube resides.

3.2.4 The Polymer and Carbon Nanotube Composite System

Initially most work on nanotubes concentrated on characterising their unique properties. In recent years, as these properties have become better understood, the emphasis has shifted towards developing applications for these materials. Proposed applications have been diverse, ranging from biosensors[24] to molecular diodes[25,26] templates for assemblies of nanowires[27] to reinforcement for plastics and epoxy resins.[28] There has been many obstacles in the realisation of these devices such as the reliably of manipulating nanoscale objects and the economic production in large quantities of pure nanotube samples. Carbon nanotubes have been used as bulk mechanical reinforcement in commercial polymers, where in this case the application is not critically dependent upon the purity of nanotube samples. However problems with using nanotubes as mechanical reinforcement of non-interacting commercial polymers have been noted.[28] These problems include nanotube aggregation, and the lack of a strong polymer-nanotube interaction. The strong tendency for nanotubes to aggregate means that they tend not to be well dispersed throughout the sample, leaving weak points at which these composites can fracture, and also dramatically limits the surface area between the polymer and nanotubes.

Research in Trinity College Dublin (TCD) has focussed on composites of polymers and nanotubes. The polymer that has been principally used is poly(m-phenylenevinylene-co-2,5-dioctyloxy-p-phenylenevinylene), or PmPV[29,30], (Figure 3.9). The polymer is a poly(phenylene-vinylene), PPV, derivative, a conjugated electronically active polymer notable for its use in organic LEDs.[31] The formation of these composites is an integral step in the sample preparation for Chapter 4 and thus it will be briefly reviewed that this polymer has a strong interaction with nanotubes, so the lack of interfacial binding that is problematic with some other polymers is not an issue here. Furthermore, as will be described, it has been shown that during the composite formation, the nanotube aggregates are broken up, and the polymer coating hinders their re-aggregation. This interaction has several interesting properties. It binds to the lattice structure of the nanotubes, and as PmPV is soluble in many organic solvents, unlike the pure nanotubes themselves, temporally stable dispersions of these composites are readily attainable. This also allows the preferential selection of nanotubes from the raw nanotube soot, giving a previously unachieved method of both purifying and characterising raw nanotube soot.

(a) (b)

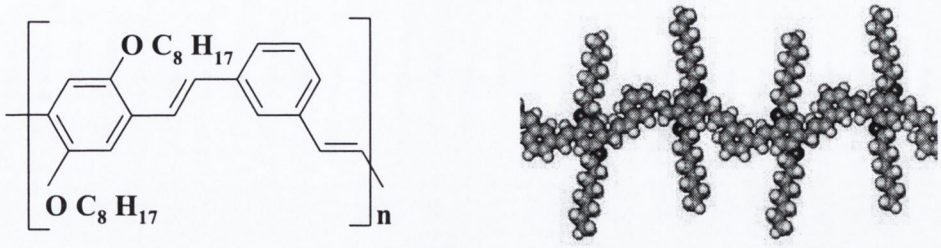

Figure 3.9 (a) and (b) Repeat unit chemical structure of poly(meta-phenylenevinylene-co-2,5-dioctyloxy-para-phenylenevinylene), (PmPV).

Initial work on the purification abilities of the composite concentrated on characterising the phase separation effects of the composite, the preferential selection and suspension of nanotubes. This was first suggested by a transmission electron microscope (TEM) image showing nanotubes coated in PmPV protruding from the edge of a composite film[32] (Figure 3.10).

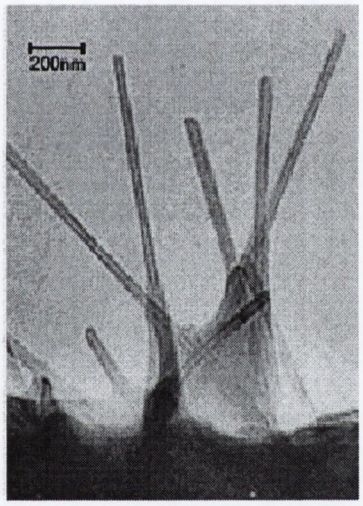

Figure 3.10 TEM image of PmPV and MWNT composite film.

The PmPV film can be clearly seen to wet all the nanotubes protruding from the composite film and there were no graphitic impurities visible. The absence of these particles usually seen attached to the walls of nanotubes, suggests that the PmPV coating the nanotube in some way displaces the graphitic particles from the nanotube. The PmPV thus acts as a filtering system, removing the nanotubes from the accompanying graphitic particles. Similarly Raman scattering studies of these composites verified this observation where peaks associated to MWNTs and impurities were observed in the raw soot and almost exclusive MWNT peaks were observed in the composite system.[33]

This preferential suspension of nanotubes was further investigated using electron paramagnetic resonance[34] (EPR). EPR is a very useful method for characterising nanotube samples. It measures the absorption of microwaves by a sample in the presence of a magnetic field. Transitions are induced for unpaired electrons between the $m_s=1/2$ and $m_s=-1/2$ states, which split due to the magnetic field. Unpaired electrons in different environments may be distinguished using this technique by differences in their resonance spectra. The local environment of unpaired electrons of a MWNT differs strongly from that of other graphitic impurity structures and this is reflected in both the position and the width of the absorption peak. For MWNT electrons, the Lorentzian linewidth is approximately 10G, and the g_0 value (a experiment independent parameter describing the position of absorption) is approximately 2.01. For an unpaired electron in to other graphitic non-nanotube structures, the values are 15G and 2.02 respectively. Thus, EPR makes it a simple matter to investigate relative changes in the raw nanotube samples due to the effects of the PmPV.

To characterise the effects of the PmPV, composite solutions with 10% mass fraction of nanotube soot in 20g PmPV/L in toluene were prepared. After allowing this to settle for a week, this was decanted, giving a solute, that which was kept in solution, and a precipitate, which had fallen out of solution. EPR was then used to investigate these samples. The results are shown in Figure 3.11a. It can be seen that the solute is highly symmetrical, indicating a one-phase system, i.e. one of the parts of the raw powder (MWNTs or graphitic impurities) had precipitated completely. The g-values and widths of the absorption lines for these two fractions agree well with expected values for MWNT, indicating that it is the MWNT that remain in solution, whereas the graphitic impurities had precipitated completely. The graphitic impurity absorption line was dominant in the precipitate, that taken from the bottom of the solution. Finally, to show that the polymer interaction was responsible for this suspension, and it was not due to other effects, such as viscosity or buoyancy, this was repeated with a non-interacting polymer, polystyrene. This showed that all soot had precipitated, with none left in the top fraction, and the bottom fraction's spectrum being similar to that of the raw soot.

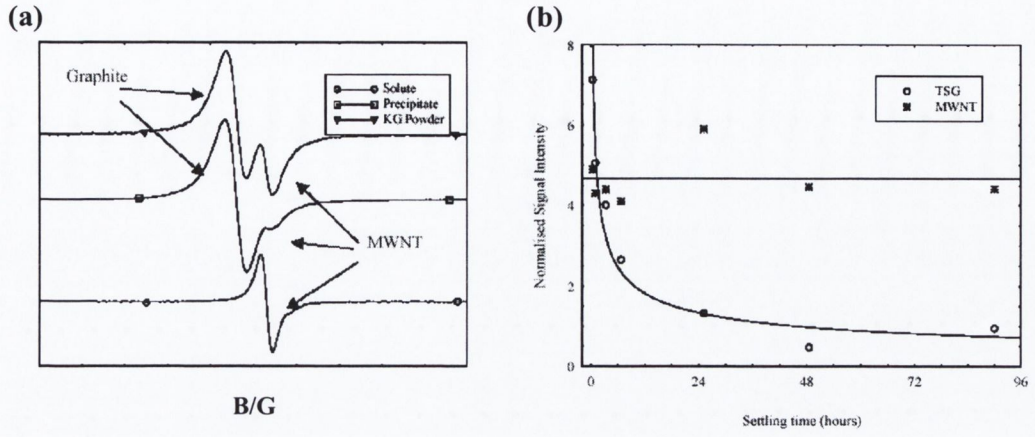

Figure 3.11 (a) EPR spectra of different composite fractions and raw nanotubes. From top to bottom the graphs show the raw soot, the precipitate, and the dispersion respectively. (b) Normalised Signal Intensities (NSI) for nanotube and impurity components for various settling times. These NSIs are proportional to the entire mass of each component for each dispersion. Note that while the nanotube component remains approximately constant the graphitic impurity component decreases as the impurities fall out of solution.

This was then further extended to determine the mass of each component that contributed to the signal.[34] The signal intensities of each line could be measured, and these were proportional to the mass of the component that gave rise to these lines. By assuming that the measured sample was representative of the total fraction, the measured intensities were normalised to be representative of the total sample. Multiplying the measured signal intensity by a factor of M_T/M_{EPR} where M_T is the total sediment mass, or solute mass and M_{EPR} is the mass of the sample measured yields a normalised signal intensity (NSI). These NSI are presented in Figure 3.11b for samples allowed to settle for different amounts of times. It can be seen that the graphitic impurities fall out rapidly once the solution is allowed to settle. The majority had fallen out within approximately 6 hours, and after 48 hours, there was practically none left. This is in sharp contrast to the MWNT, which exhibited no change over 96 hours.

Thus a method of forming stable MWNT dispersions where the MWNTs were coated in a polymer had been developed. As a launch pad for MWNT related work this process was repeated in Chapter 4 and optical experiments on these composites, as well as on another distinctly different composite system that was developed in the course of this work, are reported.

3.3 Optical Experimental Techniques

3.3.1 Linear UV-Visible Light Absorption Spectroscopy

A UV-Visible spectrum records linear absorption coefficient as a function of wavelength, corresponding to electronic excitations between the energy levels of the lowest molecular orbitals of the system. In particular, transitions involving π orbitals and lone pairs (n = non-bonding) are important and so UV-Visible spectroscopy is useful for identifying conjugated systems, which tend to have strong linear absorptions at certain wavelengths. The lowest energy transition, or peak in the spectrum, generally corresponds to a transition between the highest occupied molecular orbital (HOMO) and the lowest unoccupied molecular orbital (LUMO) in the ground state. The more conjugated a system is generally implies the smaller is the HOMO-LUMO gap (ΔE), and therefore the lower the frequency and higher the wavelength of the corresponding peak. A sample spectrum for a metal Pc was depicted in Figure 3.3.

All UV-Visible spectra presented in this work were collected from a double beam set-up. To achieve wavelength selection the lamp output is dispersed using a grating monochromator. If the sample is in solution, it is necessary to correct for the solvent, which generally exhibits ultra violet absorption features by splitting the beam and passing one side through the sample solution, and the other through the pure solvent as a reference. Thus recording the light intensities transmitted through both cells the absorption spectrum of the sample can be recorded.

3.3.2 The Z-scan Technique

3.3.2.1 Overview of the Z-scan Technique

Consider, as depicted in Figure 3.12, a Gaussian laser beam in a tight focus geometry, whose transmittance is monitored in the far field through an aperture as a function of the sample position z about the focus of the lens. This is a typical 'closed aperture' z-scan apparatus used for determining the nonlinear refraction of a sample under investigation.

If one assumes that the sample exhibits a negative nonlinear refractive index and that its thickness is smaller than the diffraction length of the focused beam (a thin sample) then this sample can be regarded as a thin lens itself of variable focal

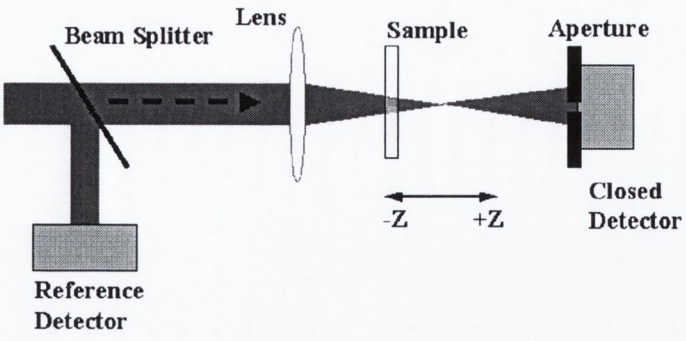

Figure 3.12 Schematic of typical 'closed aperture' Z-scan experiment.

length. The scan (traversing from –z to +z) can thus be qualitatively described. Initially, at maximum –z position, the beam irradiance is low and consequently negligible nonlinear refraction occurs; hence, the transmittance at the detector is approximately constant. As the sample approached the focus the beam irradiance obviously increases leading to self-lensing in the sample. A negative self-lensing prior to focus will tend to collimate the beam, causing a beam narrowing at the aperture, which results in an increase in the measured transmittance. After focus, as the scan continues, the same self-defocusing increases the beam divergence, leading to beam broadening at the aperture and consequently a decrease in transmittance is detected by the detector. Completion of the z-scan is realised as the sample is moved away from focus (travelling in +z direction) such that the transmittance becomes linear since the irradiance is again low. A pre-focal transmittance maximum (peak) followed by a post-focal transmittance minimum (valley) is thus typical of negative refractive nonlinearity. Positive refractive nonlinearity is analogous with a reversal in the order of occurrence of the peak and the valley of the transmittance. Thus from z-scan data the sign of the refractive nonlinearity is immediately evident. The above qualitative discourse neglects the effects arising from nonlinear absorption, such as multiphoton or saturation of the absorption. For example multiphoton absorption will suppress the peak while enhancing the valley. The sensitivity of the apparatus to nonlinear refraction is entirely due to the presence of the aperture and removal of this completely eliminates this effect. In this case the apparatus can be termed an 'open aperture' z-scan (Figure 3.13) and nonlinear absorption coefficients can be extracted such 'open aperture' experiments.

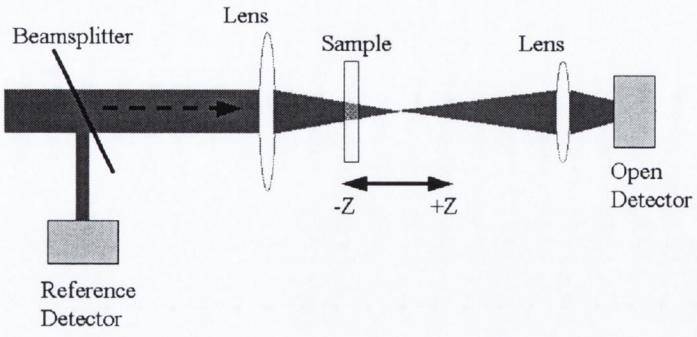

Figure 3.13 Schematic of typical 'open aperture' Z-scan experiment.

3.3.2.2 Mathematical Treatment of focused Gaussian beams

In practice nonlinear optical experiments are often realised by focusing laser beams into the nonlinear medium. Focusing of the incident radiation into nonlinearly active media obviously greatly increases the optical intensity and thus the efficiency of the nonlinear optical processes. In the Z-scan technique the beam is focused in order to produce a large intensity range over which the sample is traversed to measure the nonlinearity as a function of intensity. Before a mathematical exploration of the Z-scan technique can be broached an understanding of focused Gaussian beams has to be gained. This section explores the nature of nonlinear interactions that are excited by focused laser beams.

If one considers the part of the wave equation at frequency ω_n defined as:

$$\nabla^2 \underline{E}_n - \frac{1}{v^2}\frac{\partial^2 \underline{E}_n}{\partial t^2} = \frac{4\pi}{c^2}\frac{\partial^2 \underline{P}_n}{\partial t^2} \tag{3.3}$$

where v is the velocity of the wave in the medium, c is the speed of light in a vacuum then if the propagation is assumed to be a direction denoted z the electric field $\underline{E}_n$ and the polarization $\underline{P}_n$ can be represented as:

$$\underline{E}_n = \underline{A}_n(r)\exp\left(i\left(\underline{k}_n z - \omega_n t\right)\right) + \underline{A}_n^*(r)\exp\left(-i\left(\underline{k}_n z - \omega_n t\right)\right) \tag{3.4}$$

$$\underline{P}_n = \underline{p}_n(r)\exp\left(i\left(\underline{k}'_n z - \omega_n t\right)\right) + \underline{p}_n^*(r)\exp\left(-i\left(\underline{k}'_n z - \omega_n t\right)\right) \tag{3.5}$$

where $\underline{k}_n$ and $\underline{k}_n'$ are the wave vectors associated with $\underline{E}_n$ and $\underline{P}_n$ respectively. In these expressions $\underline{E}_n$ and $\underline{P}_n$ are allowed to represent nonplane waves by allowing the complex amplitudes $\underline{A}_n$ and $\underline{p}_n$ (and consequently the amplitudes of their complex conjugates $\underline{A}_n^*$ and $\underline{p}_n^*$ also) to be spatially varying quantities. Additionally, for generality, the possibility of a wave vector mismatch between $\underline{E}_n$ and $\underline{P}_n$ has been

implicitly included through the use of two different wave vectors. Since propagation has been assumed in the z direction it then becomes useful to transform the Laplacian operator as $\nabla^2 = \frac{\partial^2}{\partial x^2} + \frac{\partial^2}{\partial y^2} + \frac{\partial^2}{\partial z^2} = \nabla_T^2 + \frac{\partial^2}{\partial z^2}$ where transverse Laplacian ∇_T^2 has been introduced to isolate it from the propagation direction derivatives. The slowly varying amplitude approximation (SVAA), that is variations in A_n with z are assumed to occur over distances much larger than the optical wavelength, can then be applied to reduce the wave equation to

$$2i\underline{k}_n \frac{\partial \underline{A}_n}{\partial z} + \nabla_T^2 \underline{A}_n = \frac{4\pi\omega_n^2}{c^2} \underline{p}_n \exp\left(i\left(\underline{k}'_n - \underline{k}_n\right)z\right) \tag{3.6}$$

This is the paraxial wave equation, because the approximation of neglecting derivatives in z on the left-hand side is justifiable insofar as the wave $\underline{E}_n$ is primarily propagating in the z direction.

The solution to the preceding equation can be considered in the case of free propagation of the optical wave. In this approximation the terms of $\underline{p}_n$ are assumed

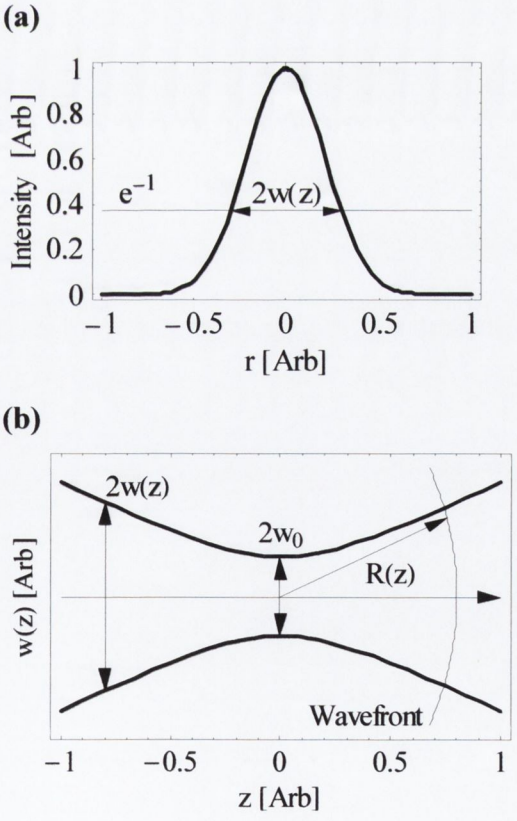

Figure 3.14 (a) Intensity distribution of a Gaussian laser beam and **(b)** the variation of the beam radius w(z) (calculated from Equation 3.8) and the curvature of the wavefront as with radius R(z) as a function of z.

to be negligible thus the paraxial wave equation can be solved with a beam having a transverse intensity distribution that is Gaussian and can thus be represented as:

$$\underline{A}(z,r) = \underline{A'}\frac{w_0}{w(z)}\exp\left(-\frac{r^2}{w^2(z)} - \frac{i\underline{k}r^2}{2R(z)} - i\phi(z,t)\right) \tag{3.7}$$

where

$$w(z) = w_0\sqrt{1+\frac{z^2}{z_0^2}} \tag{3.8}$$

and represents the e^{-1} radius of the field distribution and where $z_0 = kw_0^2/2$ is the diffraction length of the beam, $k = 2\pi/\lambda$ is the wave number, λ is the laser wavelength and w_0 represents the beam waist radius, that is the radius of the beam at focus. The parameter $R(z) = z\,(1 + z_0^2/z^2)$ is the radius of curvature of the wavefront at z and $\phi(z) = tan^{-1}(z/z_0)$ represents the spatial variations of the phase of the wave relative to that of an infinite plane wave. The nature of the solutions are displayed pictorially in Figure 3.14 where the intensity distribution of a Gaussian laser beam is depicted in Figure 3.14a and the variation of the beam radius $w(z)$ and the curvature of the wavefront with radius $R(z)$ as a function of z are depicted in Figure 3.14b.

3.3.2.3 Theory of Z-scan[35]

The geometries presented in Figure 3.12 and Figure 3.13 will be considered here and the theory formulated and discussed for analysing z-scan data. For simplicity cubic nonlinearities will be assumed where the intensity dependant refractive index, $n(I)$, is defined as:

$$n(I) = n_0 + n_2 I \tag{3.9}$$

n_0 is the linear refractive index, n_2 [m^{-2} W] is the nonlinear refractive index and I is the excitation intensity [W m^{-2}]. If one assumes that the exciting optical beam consists of a TEM_{00} Gaussian beam of waist radius ω_0 travelling in the +z direction then its electric field can be written as:

$$\underline{E}(z,r,t) = \underline{E}_0(t)\frac{\omega_0}{\omega(z)}\exp\left(-\frac{r^2}{\omega^2(z)} - \frac{i\underline{k}r^2}{2R(z)} - i\phi(z,t)\right) \tag{3.10}$$

where, as in the previous section, $w(z) = w_0\,(1+z^2/z_0^2)^{1/2}$ is the beam radius propagating as a function of z. ω_0 is the beam radius at focus. $R(z) = z\,(1 + z_0^2/z^2)$ is the radius of curvature of the wavefront at z, $z_0 = kw_0^2/2$ is the diffraction length of

the beam, $k = 2\pi/\lambda$ is the wane number, and λ is the laser wavelength, all in free space. $\underline{E}_0(t)$ denotes the radiation electric field at the focus and contains the temporal envelope of the laser pulse. The $exp(-i\phi(z, t))$ term contains all the radially uniform phase variations. As radial phase variation calculations are all that is of concern $\Delta\phi(r)$ the slow varying envelope approximation (SVEA) applies and all other phase changes that are uniform in r are ignored.

If the sample thickness is small such that changes in the beam diameter within the sample due to either diffraction or refraction can be neglected then the sample is said to be thin. Mathematically a medium is regarded as thin if for linear refraction $L << z_0$ while for nonlinear refraction this implies $L << z_0/\Delta\phi(0)$. In most experiments using the Z-scan technique, it has been found that this second criterion is automatically met since $\Delta\phi_0$ is small. It has also been empirically found that the first criterion for linear diffraction is more restrictive than it need be, and the condition $L < n_0 z_0$ is sufficient. Thus the problem can be considerably simplified and the and the amplitude $\sqrt{I}$ and phase ϕ of the electric field as a function of z are now governed in the SVEA by the following simultaneous equations

$$\frac{d\Delta\phi}{dz'} = \Delta n(I)\underline{k} \tag{3.11}$$

and

$$\frac{dI}{dz'} = -\alpha(I)\underline{I} \tag{3.12}$$

where in this case z' implies the propagation depth in the sample and the intensity dependent absorption coefficient $\alpha(I)$ in general contains both linear and nonlinear absorption terms.

If one assumes negligible nonlinear absorption and cubic nonlinearities then the previous two equations can be simultaneously solved to give the phase shift $\Delta\phi$ at the exit surface of the sample which simply follows the radial variation of the incident irradiation such that:

$$\Delta\phi(z,r,t) = \Delta\phi_0 \exp\left(-\frac{2r^2}{\omega^2(z)}\right) \tag{3.13}$$

with

$$\Delta\phi_0(z,t) = \frac{\Delta\Phi_0}{1+\left(z/z_0\right)^2} \tag{3.14}$$

$\Delta\Phi_0$ is the on axis phase shift at the focus defined as:

$$\Delta\Phi_0 = \underline{k}\Delta n_0(t)L_{eff} \tag{3.15}$$

where $L_{eff} = (1\text{-}exp(-\alpha_0 L))/\alpha_0$ is called the effective length of the sample defined in terms of the linear absorption coefficient α_0 and the true length of the sample L, and $\Delta n_0 = n_2\underline{I}_0(t)$ with $\underline{I}_0(t)$ being the on axis irradiance at focus (i.e. z = 0). The terms $(1 + (z/z_0)^2)$ are implicit to a propagating Gaussian beam and they account for the beam spreading, and thus the on axis irradiance increasing or reducing, for –z to 0 propagation and 0 to +z propagation respectively. Thus the electric field exiting the sample now contains a nonlinear phase distortion

$$\underline{E}_{exit} = \underline{E}(z,r,t)\exp\left(-\frac{\alpha_0 L}{2} + i\Delta\phi(z,r,t)\right) \tag{3.16}$$

Using the above expression one can, by virtue of Huygens principle, obtain the far field pattern of the beam at the aperture plane through a zeroth-order Hankel transformation of $\underline{E}_{exit}$.[36] Alternatively the Gaussian decomposition method presented by Wearie *et al.*[37] (applicable here due to the Gaussian nature of the input beam) can be used to decompose the complex electric field at the exit plane into a summation of of Gaussian beams through a Taylor series expansion of the nonlinear phase term $exp(-i\Delta\phi(z, r, t))$ such that:

$$\exp\left(i\Delta\phi(z,r,t)\right) = \sum_{m=0}^{\infty}\frac{\left[i\Delta\phi_0(z,t)\right]^m}{m!}\exp\left(-\frac{2mr^2}{\omega^2(z)}\right) \tag{3.17}$$

Each Gaussian beam can be propagated to the aperture plane where they will be re-summed to reconstruct the beam. When including the initial beam curvature for the focused beam the resultant electric field pattern at the aperture (E_a) has been derived

$$\underline{E}_a = \underline{E}(z,r=0,t)\exp\left(-\frac{\alpha_0 L}{2}\right)\sum_{m=0}^{\infty}\frac{\left[i\Delta\phi_0(z,t)\right]^m}{m!}\frac{\omega_{m0}}{\omega_m}\exp\left(-\frac{r^2}{\omega_m^2} - \frac{ikr^2}{2R_m} + i\theta_m\right) \tag{3.18}$$

If one then defines d as the propagation distance from the sample to the aperture plane and g = 1 + d/R(z) the remaining parameters in the preceding equation can be defined as:

$$\omega_{m0}^2 = \frac{\omega^2(z)}{2m+1},\ d_m = \frac{k\omega_{m0}^2}{2},\ \omega_m^2 = \omega_{m0}^2\left(g^2 + \frac{d^2}{d_m^2}\right),$$

$$R_m = d\left(1 - \frac{g}{g^2 + d^2/d_m^2}\right)^{-1} \text{ and } \theta_m = \tan^{-1}\left(\frac{d/d_m}{g}\right) \tag{3.19a-e}$$

Thus equation is the general case of that derived by Wearie *et al.*[37] where they considered a collimated beam (R = ∞) for which g = 1. It has been found that this method has been useful for the small phase distortions detected with the z-scan method, since only a few terms in the summation of Equation 3.18 are needed, and the method can be easily extended to higher nonlinearities.

The transmitted power P_T through the aperture then can be found by spatially integrating the $E_a(r, t)$ given by equation up to the radius of the aperture,

$$\underline{P}_T(\Delta\phi(t)) = c\varepsilon_0 n_0 \pi \int_0^{r_a} \left|\underline{E}_a(r,t)\right|^2 r dr \tag{3.20}$$

where ε_0 is the permittivity of free space. Thus the normalised transmission can be defined as:

$$T(z) = \frac{\int_{-\infty}^{\infty} \underline{P}_T(\Delta\phi_0(t))dt}{S\int_{-\infty}^{\infty} \underline{P}_i(t)dt} \tag{3.21}$$

where $\underline{P}_i(t) = \pi\omega_0^2 \underline{I}_0(t)/2$ and physically is the instantaneous input power within the sample and $S = 1 - exp(-2r_a^2/\omega_a^2)$ is the aperture linear transmission where ω_a denotes the beam radius at the aperture in the linear regime, and r_a is the aperture radius. Thus in the case of cubic nonlinearity and small phase change ($|\Delta\phi| << 1$) the on-axis z–scan transmittance can be obtained by letting r = 0 in equation and assuming the far field condition $d >> z_0$ in a geometry independent function as:

$$T(z,\Delta\Phi_0) = 1 - \frac{4\Delta\Phi_0 z/z_0}{\left(z^2/z_0^2+9\right)\left(z^2/z_0^2+1\right)} \tag{3.22}$$

The above discussion considered the case where negligible nonlinear absorption was assumed. However, nonlinear absorption arising from either direct multiphoton absorption, saturation of the single photon absorption or dynamic free-carrier absorption have to be considered in any general discussion of the z-scan technique. If one considers Figure 3.13, a z-scan with a fully open aperture (S = 1 in Equation (3.21) insensitive to refraction, a symmetric trace with respect to the focal plane (z = 0) would be expected with either a minimum or maximum at the focal point. A maximum here implies saturable absorption while a minimum implies multiphoton absorption, reverse saturable absorption or intensity dependent scattering. If nonlinear absorption is present then the third order susceptibility then becomes in

general complex:

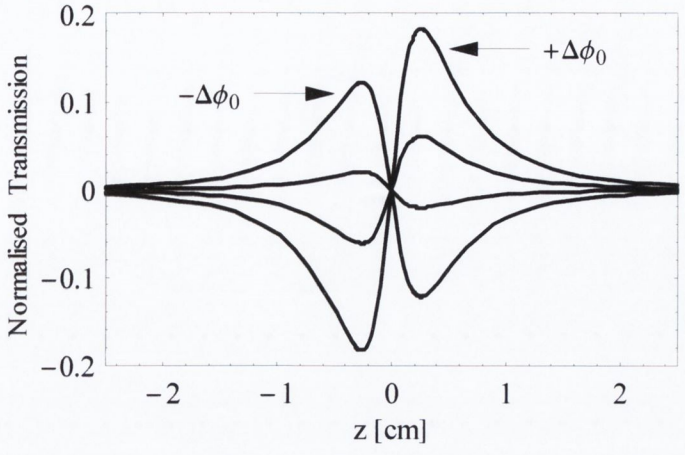

Figure 3.15 Theoretical plots of normalised transmission against position z for closed aperture Z-scan calculated using Equation (3.22). In these plots *z0 = 0.3 cm* and *Δφ = 0.9, -0.6, 0.3, -0.1* for the scans in order of decreasing magnitude nonlinear refraction.

$$\chi^{(3)} = \mathrm{Re}\left(\chi^{(3)}\right) + \mathrm{Im}\left(\chi^{(3)}\right) \tag{3.23}$$

where the imaginary part is directly related to the nonlinear absorption coefficient β

$$\mathrm{Im}\left(\chi^{(3)}\right) = \frac{n_0^2 \varepsilon_0 c^2}{\omega} \beta \tag{3.24}$$

and the real part is related to n_2 (Equation 3.9) through

$$\mathrm{Re}\left(\chi^{(3)}\right) = 2 n_0^2 \varepsilon_0 c n_2 \tag{3.25}$$

Assuming that the free-carrier effects can be neglected (low excitation regime) then the absorption coefficient can be expanded as:

$$\alpha(I) = \alpha_0 + \beta \underline{I} \tag{3.26}$$

This yields the irradiance distribution and phase shift of the beam at the exit surface of the sample as:

$$\underline{I}_{exit}(z,r,t) = \frac{\underline{I}(z,r,t)\exp(-\alpha_0 L)}{1+q(z,r,t)} \tag{3.27}$$

and

$$\Delta\phi(z,r,t) = \frac{k n_2}{\beta} Log_e\left(1+q(z,r,t)\right) \tag{3.28}$$

where $q(z, r, t) = \beta \underline{I}(z, r, t) L_{eff}$, and $L_{eff} = (1 - exp(-\alpha_0 L))/\alpha_0$ as before. The previous two equations (Equations (3.27) and (3.28)) can be combined to give the complex electric at the exit surface of the sample as:[38]

$$\underline{E}_{exit} = \underline{E}(z,r,t)\exp\left(-\frac{\alpha_0 L}{2}\right)(1+q)^{(i\underline{k}n_2/\beta - 1/2)} \tag{3.29}$$

This equation is the generalisation of Equation (3.16) to account for nonlinear absorption. In general a zeroth order Hankel transform of Equation (3.29) will give the field distribution at the aperture, which can be substituted back to Equations (3.20) and (3.21) to yield the transmittance. For $|q| < 1$ using a binomial expansion in powers of q Equation (3.29) can be expressed as a infinite sum of Gaussian beams as:

$$\underline{E}_{exit} = \underline{E}(z,r,t)\exp\left(-\frac{\alpha_0 L}{2}\right)\sum_{m=0}^{\infty}\frac{q(z,r,t)^m}{m!}\left[\prod_{n=0}\left(i\frac{\underline{k}\gamma}{\beta}-\frac{1}{2}-n+1\right)\right] \tag{3.30}$$

where the Gaussian profiles are implicit in $q(z, r, t)$ and $E(z, r, t)$. Thus, the complex field pattern at the aperture plane can be obtained as before and Equation (3.18) can be used again after replacing the $(i\Delta\phi_0(z, t))^m / m!$ terms with

$$f_m = \frac{(i\Delta\phi_0(z,t))}{m!}\prod_{m=0}^{m}\left(1+i(2n-1)\frac{\beta}{2\underline{k}\gamma}\right) \tag{3.31}$$

where $f_0 = 1$.

It is therefore clear that the absorptive and refractive contributions to the far field beam profile, and hence to the z-scan transmittance are coupled. However the z-scan transmittance variation at the open aperture (s = 1) is insensitive to the beam distortion and is solely a function of the nonlinear absorption. The total transmitted fluence can be calculated by spatially integrating Equation (3.27) without needing to account for the free space propagating process. This the total transmitted power $\underline{P}(z, t)$, integrating over z and r, returns $\underline{P}(z, t)$ as follows:

$$\underline{P}(z,t) = \underline{P}_i(t)\exp(-\alpha_0 L)\frac{Log_e(1+q_0(z,t))}{q_0(z,t)} \tag{3.32}$$

where $q_0(z, t) = \beta \underline{I}_0(z, t) L_{eff}$, $\underline{I}_0(z, t) = \underline{I}_0(t)/(1 + z^2/z_0^2)$ and $\underline{P}_i(t) = \pi\omega_0^2 \underline{I}_0(t)/2$ is, as before, the instantaneous input power within the sample. Kwak *et al.*[39] considered a spatial integral at z over the entire r yielding the transmission T as a function of z for all q_0 as:

$$T(z) = \exp(-\alpha_0 L)\frac{Log_e(1+q_0(z))}{q_0(z)} \tag{3.33}$$

Theoretical plots of normalised transmission, $T(z)/exp(-\alpha_0 L)$, as a function of z are presented in Figure 3.16.

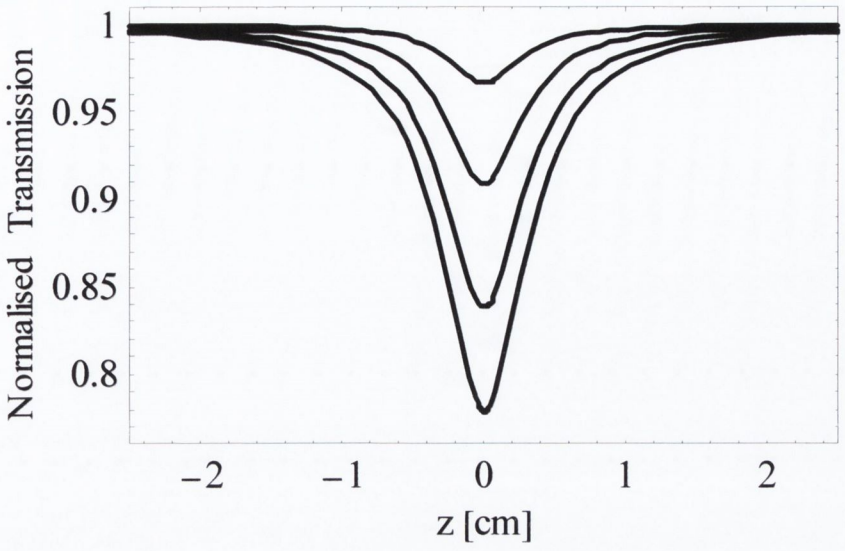

Figure 3.16 Theoretical plots of normalised transmission against position z for open aperture Z-scan calculated using Equation (3.33). In these plots $z0 = 0.3\ cm$ and $q_{oo} = 0.9, 0.6, 0.3, 0.1$ for the scans in order of decreasing magnitude nonlinear absorption.

3.3.2.4 Experimental Set-up

The Z-scan apparatus was built as depicted in Figure 3.17. The optical limiting experiments described in this study were performed using the open aperture of this

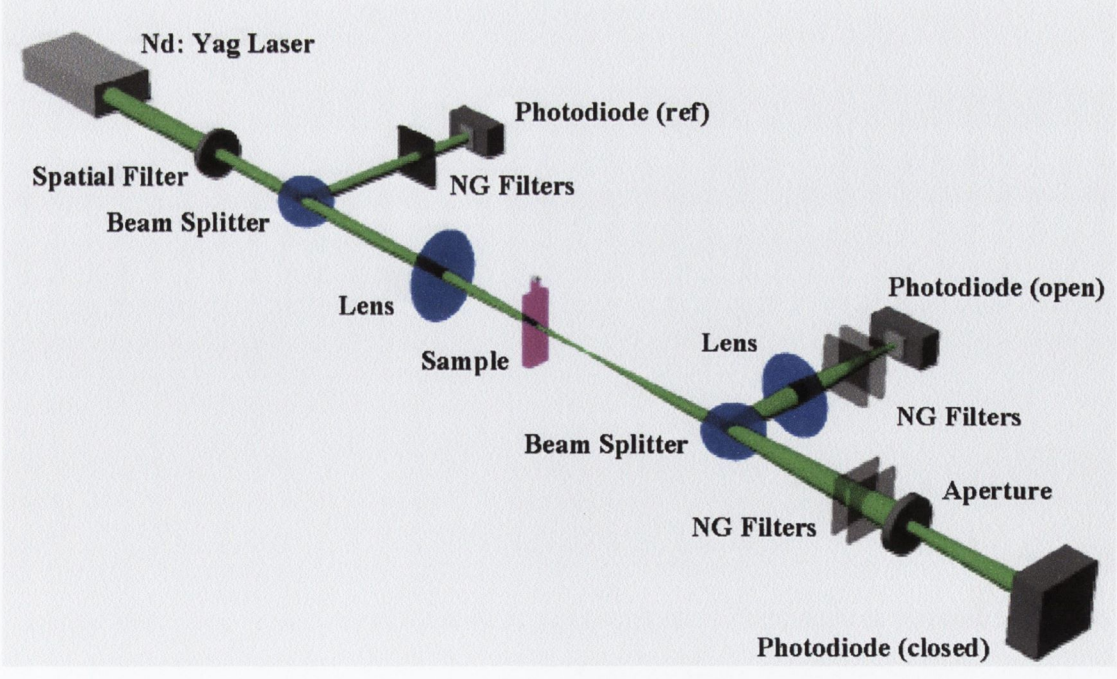

Figure 3.17 Experimental set-up for Z-scan measurements, where the optical filters (NG, supplied by Schott) are of neutral density.

set-up with 6 ns pulses from a Q switched Nd:YAG laser. The beam was spatially filtered to remove the higher order modes and tightly focused with a 9 cm focal length lens.

The laser was operated with its frequency doubled, during this process two 1064 nm photons (fundamental mode of the Nd:YAG laser) enter the doubling crystal collinear and with their polarisations in phase. The two photons are absorbed simultaneously in a two-photon absorption process and reemitted as a single photon with double the energy, double the frequency and half the wavelength. Thus the second harmonic photon is reemitted at 532 nm. The laser was operated with a pulse repetition rate of 10 Hz. All solution or suspension measurements were performed in quartz cells with a 1 mm or 1 cm through path length.

3.3.3 Scattering Techniques

Scattering measurements were made using two distinctly different methods in this thesis. These methods were intensity dependent scattering and angular dependent scattering. The sample was placed on the focus of a lens. The forward and backward scattered light (measured in arbitrary units) was simultaneously collected using additional lenses of diameter 6 cm with their axes at 45^0 to the z-axis of the focusing lens corresponding to a solid angle 1.05 steradian. The set-up for the intensity dependent measurements is depicted in Figure 3.18. Changing the energy per laser pulse was used to vary the intensity.

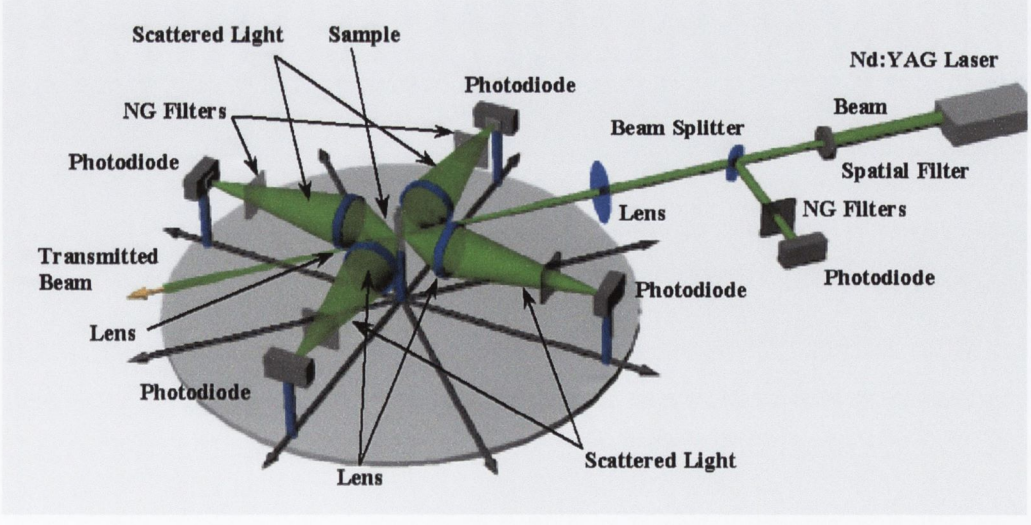

Figure 3.18 Experimental set-up for intensity dependent scattering measurements.

Angular dependent scattering measurements can be used to investigate the composition of materials at a nanoscale level. The apparatus was similar to that presented in Figure 3.18 for the intensity dependent measurements but only one photodiode was used and this was traversed about the sample along a circular arc where the sample is on the centre of the arc from approximately a 15^0 to a 170^0 angle to the z-axis of the focusing lens, with the signal being collected at regular intervals along the arc. The set-up is schematically sketched in Figure 3.19.

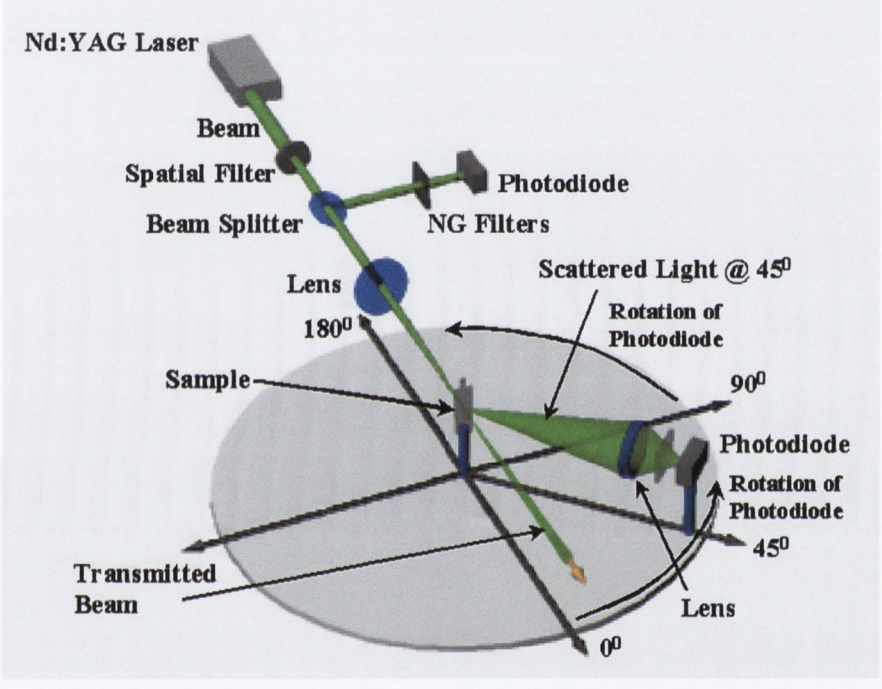

Figure 3.19 Experimental set-up for angular dependent scattering measurements.

References

[1] N. B. McKeown, *Phthalocyanine Materials: Synthesis, Structure and Function* (Cambridge University Press, Cambridge, 1998).

[2] C. J. T. Cronshaw, Endeavour **1,** 79-83 (1942).

[3] C. E. Dent and R. P. Linstead, Journal of the Chemical Society, 1033-1037 (1934).

[4] C. E. Dent and R. P. Linstead, Journal of the Chemical Society, 1027-1031 (1934).

[5] G. T. Byrne, R. P. Linstead, and A. R. Lowe, Journal of the Chemical Society, 1017-1022 (1934).

[6] R. P. Linstead, Journal of the Chemical Society, 1016-1017 (1934).

[7] R. P. Linstead and A. R. Lowe, Journal of the Chemical Society, 1022-1027 (1934).

[8] R. P. Linstead, E. G. Noble, and J. M. Wright, Journal of the Chemical Society, 1031-1033 (1934).

[9] B. D. Berzin, *Coordination Compounds of Porphyrins and Phthalocyanines* (John Wiley & Sons, Chichester, 1981).

[10] A. M. Schaffer, M. Gouterman, and E. R. Davidson, Theoretica Chimica Acta **30,** 9-30 (1973).

[11] W. P. Anderson, W. D. Edwards, and M. C. Zerner, Inorganic Chemistry **25,** 2728-2732 (1986).

[12] J. E. Ridley and M. C. Zerner, Theoretica Chimica Acta **42,** 223-226 (1976).

[13] M. E. Brennan, S. M. O'Flaherty, M. Barthel, T. Kobayashi, M. Hanack, and W. J. Blau, Chemical Physics Letters, Submitted.

[14] W. Hiller, J. Strähle, W. Kobel, and M. Hanack, Z. Krostallogr. **159,** 173 (1982).

[15] F. Z. Henari, A. Davey, W. Blau, P. Haisch, and M. Hanack, Journal of Porphyrins and Phthalocyanines **3,** 331-338 (1999).

[16] H. E. Kroto, J. R. Heath, D. F. O'Brien, R. F. Curl, and R. E. Smalley, Nature **318,** 162 (1985).

[17] S. Iijima, Nature **354,** 56-58 (1991).

[18] http://astrobiology.ucla.edu/ESS116/L09/0903%20diamond%20structure.jpg

[19] http://cms.mpi.univie.ac.at/spisak/gallery/nanotube.jpg

[20] M. S. Dresselhaus, G. Dresselhaus, and P. C. Eklund, *Science of Fullerenes and Carbon Nanotubes* (Academic Press, New York, 1996).

[21] P. Lambin, A. Fonseca, J. P. Vigneron, J. B. Nagy, and A. A. Lucas, Chemical Physics Letters **245,** 85-89 (1995).

[22] R. Saito, G. Dresselhaus, and M. S. Dresselhaus, Journal of Applied Physics **73,** 494-500 (1993).

[23] J. C. Charlier and J. P. Michenaud, Physical Review Letters **70,** 1858-1861 (1993).

[24] F. Balavoine, P. Schultz, C. Richard, V. Mallouh, T. W. Ebbesen, and C. Mioskowski, Angewandte Chemie-International Edition **38,** 1912-1915 (1999).

[25] L. Chico, V. H. Crespi, L. X. Benedict, S. G. Louie, and M. L. Cohen, Physical Review Letters **76,** 971-974 (1996).

[26] P. G. Collins, K. Bradley, M. Ishigami, and A. Zettl, Science **287,** 1801-1804 (2000).

[27] S. Fullam, D. Cottell, H. Rensmo, and D. Fitzmaurice, Advanced Materials **12,** 1430-1432 (2000).

[28] P. M. Ajayan, L. S. Schadler, C. Giannaris, and A. Rubio, Advanced Materials **12,** 750-+ (2000).
[29] A. P. Davey, A. Drury, S. Maier, H. J. Byrne, and W. J. Blau, Synthetic Metals **103,** 2478-2479 (1999).
[30] A. Drury, S. Maier, A. P. Davey, A. B. Dalton, J. N. Coleman, H. J. Byrne, and W. J. Blau, Synthetic Metals **119,** 151-152 (2001).
[31] J. H. Burroughes, D. D. C. Bradley, A. R. Brown, R. N. Marks, K. Mackay, R. H. Friend, P. L. Burns, and A. B. Holmes, Nature **347,** 539-541 (1990).
[32] S. A. Curran, P. M. Ajayan, W. J. Blau, D. L. Carroll, J. N. Coleman, A. B. Dalton, A. P. Davey, A. Drury, B. McCarthy, S. Maier, and A. Strevens, Advanced Materials **10,** 1091-+ (1998).
[33] J. N. Coleman, A. B. Dalton, S. Curran, A. Rubio, A. P. Davey, A. Drury, B. McCarthy, B. Lahr, P. M. Ajayan, S. Roth, R. C. Barklie, and W. J. Blau, Advanced Materials **12,** 213-216 (2000).
[34] J. N. Coleman, D. F. O'Brien, A. B. Dalton, B. McCarthy, B. Lahr, A. Drury, R. C. Barklie, and W. J. Blau, Chemical Commmunications, 2001-2002 (2000).
[35] M. Sheik-Bahae, A. A. Said, T.-H. Wei, D. J. Hagan, and E. W. Van Stryland, IEEE Journal of Quantum Electronics **26,** 760-769 (1990).
[36] J. D. Gaskill, *Linear Systems, Fourier Transforms and Optics* (Wiley, New York, 1978).
[37] D. Weaire, B. S. Wherrett, D. A. B. Miller, and S. D. Smith, Optics Letters **4,** 331-333 (1974).
[38] Y. Ando, X. Zhao, and H. Shimoyama, Carbon **39,** 569-574 (2001).
[39] C. H. Kwak, Y. L. Lee, and S. G. Kim, Journal of the Optical Society of America B **16,** 600-604 (1999).

Chapter 4

Axially and Peripherally Modified Metallo-Phthalocyanines for Nonlinear Optics

4.1 Introduction

4.1.1 Background Information

It was discussed in the previous chapter that among the large number of nonlinear optical absorbers that have been identified[1-4], phthalocyanines (Pcs) and their derivatives have recently emerged as promising materials due to their large optical nonlinearities, ultrafast response times and easy processability.[5-7] Chemical modifications of phthalocyanines through axial substitution at the central metal atom, or through peripheral substitution on the Pc macrocycle, offer opportunities to reduce the intermolecular interactions and to tailor the nonlinear response and thus control the optoelectronic properties of these molecules.[8] Consequently, Pcs and their derivatives have attracted considerable attention in the field of optical limiting.[5,6,8-10]

Optical limiting with Pcs was first reported for the chloroaluminum phthalocyanine (PcAlCl)[11] and subsequently many other Pc compounds, e.g. tBu$_4$PcInCl[12] and (β-CP)$_4$PcPb[13] have also been investigated as passive optical limiting materials. This chapter summarises a comprehensive study of experimentally measured optical limiting in novel axially and peripherally substituted Pcs. These materials have been introduced in the previous chapter. Processes that might be useful for passive optical limiting inevitably involve some

form of nonlinear response to light. Among these are nonlinear absorption, nonlinear refraction, nonlinear scattering and beam fanning. Phthalocyanines, like C_{60} fullerenes, are materials that optically limit via a nonlinear absorption process at 532 nm laser irradiation (i.e. Nd:YAG second harmonic). The absorption mechanism exhibited by phthalocyanine compounds at 532 nm laser irradiation is due to the population of excited states through multi-step nonlinear absorption, leading to Reverse Saturable Absorption (RSA).[12,14,15] It has been shown that certain phthalocyanine compounds exhibit RSA in the nanosecond regime because of an intersystem crossing approaching unity from the lowest excited singlet state (S_1) to the lowest triplet state (T_1), and the subsequent increase in the population of the T_1 state, during the lifetime of the laser pulse.[16] There has been a large body of works published which have demonstrated much the same phenomenon.[12,14,15,17-19] Perry *et al.*[14] prepared a practical optical limiting device using the theoretical structure detailed by Miles[20] using the tetrasubstituted chloroindium phthalocyanine (tBu$_4$PcInCl). Under nanosecond irradiation this device was able to attenuate laser pulses by up to a factor of 540. Henari *et al.* reported the nonlinear optical properties of a series of phthalocyaninatotitanium (IV) oxides with different peripheral groups (R_xPcTiO).[17] The optical limiting properties of an octasubstituted lead phthalocyanine ([$C_{12}H_{25}O$]$_8$PcPb) has also been studied by Qu *et al.*[19] Recently, the nanosecond optical limiting properties of nickel phthalocyanines[18], gallium and indium phthalocyanines[15,21], and gallium naphthalocyanines[22] have also been reported. Shirk *et al.*[12] studied the effects of axial substitution to the central metal atom on the optical limiting performance of indium phthalocyanines. They found that the optical limiting properties of these materials were robust to structural modifications in the axial position reporting that when the axial substituents were changed from chloro to *p*-trifluoromethylphenyl (*p*-TMP) the optical limiting response was enhanced. Tian *et al.*[23] reported the nonlinear properties of non-aggregated zinc and vanadium phthalocyanines, where they found that the zinc phthalocyanine had a larger macroscopic optical nonlinearity than the vanadium phthalocyanine. The optical nonlinearities of bisphthalocyanine solutions have also been reported, ($PcYb_2$) by Mendonca *et al*;[24] and lutetium ($PcLu_2$), neodymium ($PcNd_2$) and europium ($PcEu_2$) by Wen *et al.*[25] Furthermore the nonlinear optics of tin phthalocyanine thin films have been investigated by Yamashita *et al.*[26]

4.1.2 Optical limiting parameters

In order to have some independent 'yardstick' or gauge by which the efficacy of optical limiting materials under investigation might be 'weighed', quantified and compared, various parameters have been defined and quoted in the literature. Some authors have referred to threshold fluence, which is defined as that fluence at which the transmission drops to one half of its linear value. Justus *et al.*[27] reported a value of 0.33 J cm^{-2} for C_{60}, Qu *et al.*[19] reported a value of 27 mJ/cm^{-2} for $[C_{12}H_{25}O]_8PcPb$, Sun *et al.*[28] quoted 1 J cm^{-2} for multiwalled carbon nanotubes suspended in H_2O and 1.1 J cm^{-2} for C_{60} in toluene at 532 nm where these samples had linear transmissions $\approx$ 50%, Vivien *et al.*[29] also adopted this approach when discussing the wavelength dependence of optical limiting in single walled carbon nanotube suspensions, reporting threshold fluences at 532 nm excitation of 150 mJ cm^{-2} for H_2O suspensions and 40 mJ cm^{-2} for chloroform suspensions. Alternatively, the saturation fluence may also be used to quantify the optical limiting response. This is the fluence at which the output fluence reaches its saturated value. Tutt and Kost[30] reported the saturation fluence as 1 J cm^{-2} for an 80% transmitting C_{60} solution, and Perry *et al.*[14] reported 0.47 J cm^{-2} for tBu$_4$PcInCl. McLean *et al.*[31] further introduced another fluence parameter as a figure of merit for optical limiting in the nanosecond case. It was defined as $F_c = h\nu / (\sigma_{ex} - \sigma_0)$, where $h\nu$ is the photon energy and σ_{ex} and σ_0 are the excited triplet state and ground state absorption cross sections, quoting 60 mJ cm^{-2} for 55% transmitting solution of C_{60}. It should be clearly noted that reports on suspensions or solutions of materials quoting certain linear transmissions instead of the mass or molar concentration once again affords further ambiguity when attempting to estimate a molecular property from the macroscopic response.

Despite frequent use of the numerous fluence parameters cited above by various authors, the excited state to ground state absorption cross section ratio, σ_{ex}/σ_0, appears to have been widely accepted as being an excellent indicator of limiting action. However Shirk *et al.*[12] argue that the σ_{ex}/σ_0 ratio does not characterise the strength of the nonlinear absorption and suggested that the cross section difference (σ_{ex}-σ_0) is a more useful indicator of limiting action. Henari *et al.*[32] quote the σ_{ex}/σ_0 ratio as being 2.9 for C_{60} under 0.5 ns irradiation at 520 nm while Li *et al.*[33] using values measured by Ebbesen *et al.*[34] estimate σ_T/σ_0 to be $\approx$ 3.2 and σ_S/σ_0 to be $\approx$ 5.7 where σ_T and σ_S are the excited singlet and triplet state

absorption cross sections respectively. In phthalocyanines, the largest σ_{ex}/σ_0 ratio reported was 33 by Shirk *et al.*[12] for *t*Bu$_4$PcInCl under 532 nm irradiation but they did not estimate the uncertainty in that value. Perry *et al.*[14] reported (30 ± 6) for the same compound and (3.1 ± 0.3) for C_{60}. A σ_{ex}/σ_0 ratio of 30 at 532 nm has been reported by Wood *et al.*[35] for a tetrabenzoporphyrin with Zn as the central metal atom of the porphyrin structure.

Clearly, there exists some disagreement as to how to quantitatively define the magnitude of the limiting action of nonlinearly active materials. This is partly due to the different dissipating mechanisms that may be involved in the optical limiting action, partly due to differences in experimental techniques employed to measure the response and also partly due to differences in the opinions of the various authors. In this chapter a range of different parameters will be quoted for each Pc compound that is measured. The mass concentration, linear absorption coefficient (α_0), the σ_{ex}/σ_0 ratio, the energy density (J cm^{-2}) at which the material saturates (F_{Sat}), the effective imaginary third order susceptibility ($Im\{\chi^{(3)}_{eff}\}$), the effective imaginary second order molecular hyperpolarizability ($Im\{\gamma_{eff}\}$) and the intensity dependent nonlinear absorption coefficient (β_I) will be reported for a range of modified phthalocyanines. A RSA based model will be built, discussed, developed and fitted to the experimental data. This will allow the calculation of any of the various other parameters that other authors have used and will also allow a concise mathematical discussion and method of comparison of the optical limiting data obtained in the experimental section. Finally an attempt to link the monomeric molecular structure to the macroscopic nonlinear response of the Pc systems will be made.

4.2 Nonlinear Absorption

4.2.1 Linear Absorption

Under ambient light irradiation (low intensity) materials typically exhibit a constant linear absorption coefficient α_0 usually described by the Lambert-Beer law as:

$$\frac{dI}{z} = -\alpha_0 I \,, \tag{4.1}$$

This simple differential equation can be solved by integrating with limits on *dz* going from $z = 0 \rightarrow L$ and the limits on *dI* going from $I = I_{In} \rightarrow I_T$. If one defines the transmission as a function of the incident intensity as $T(I_{In}) = I_T/I_{In}$ then the solution

to Equation (4.1) is

$$T = \exp(-\alpha_0 L) = \exp(-\sigma_0 NL), \tag{4.2}$$

where L denotes the sample length, σ_0 represents the absorption cross section of the ground state to first excited singlet state transition ($S_0 \rightarrow S_1$ transitions) and N represents the total population under excitation. Thus, in this operating regime the transmission T is independent of the excitation intensity. In this regime the ground state population never gets significantly depopulated and consequently as the population has to be conserved the excited state never achieves a significant population either. Thus, the light irradiating the sample experiences an approximately homogeneous population distribution as it propagates through the medium. As the excitation intensity increases to levels where the photon density is comparable to the population density an induced regime transition may occur where the absorption coefficient is depleted or enhanced corresponding to increases or decreases in the transmission respectively. The resultant regime depends upon the absorption cross sections of the ground and excited state levels and the lifetimes of the various allowable transitions in the system.

4.2.2 Multi-Photon Absorption

Multi-photon dissipative nonlinearities associated with simultaneous absorptions of two or more photons (multi-photon absorption) are not observed in this chapter nor are they discussed in any detail in this thesis. However one cannot complete any discussion of nonlinear absorption without a brief introduction to this phenomenon. A short description of the simplest multi-photon absorption, namely two-photon absorption will be presented here.

Two-photon absorption is the simultaneous absorption of two photons of energy hv to span an energy bandgap of energy approximately equal but more likely slightly less $2hv$. One can consider an incident optical beam, with frequency v irradiating a material with, for example, an $S_0 \rightarrow S_1$ transition of energy $\approx 2hv$ with sufficient intensity such that two photons may be simultaneously absorbed through a virtual energy level lying between S_0 and S_1. This hypothetical system is sketched in Figure 4.1. After a small vibrational relaxation the excited population may then occupy the S_1 orbital from where it may subsequently re-radiate or vibratinally relax back to the ground state. This is the same principle by which second harmonic

generation (SHG) operates where two photons of frequency v are absorbed simultaneously in a crystal and re-radiated as a single photon of frequency $2v$ or with wavelength equal to half that of the initial excitation.

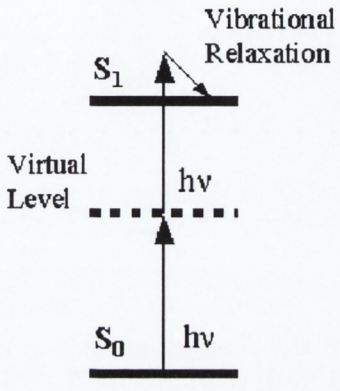

Figure 4.1 Sketch of two-photon absorption process. In the hypothetical system the $S_0 \rightarrow S_1$ transition is of energy $\approx 2hv$, where hv is the energy of a single incident photon.

4.2.3 Excited State Absorption

Saturable Absorption refers to the case of excited state absorption (ESA) where the transmission increases with incident intensity and indicates that the ground state absorption has bleached. Conversely, the opposite situation, where the transmission decreases with increasing incident intensity the process is termed Reverse Saturable Absorption (RSA). This occurs when the excited state absorption cross-section is greater than that of the ground state and was initially discussed by Guiliano and Hess in 1967.[36]

Hercher[37] (1967) conducted a general analysis of saturable absorbers using a three level scheme. Under the steady state approximation, where the populations remain constant for the duration of the pulse, he derived a general expression for the absorption coefficient in terms of a parameter called the saturation intensity, I_{Sat}.

$$\alpha = \frac{\alpha_0}{1 + \frac{I}{I_{Sat}}}, \tag{4.1}$$

where $I_S = h\nu/(\sigma_0 \tau_{10})$ and τ_{10} refers to the excited state relaxation time of the bleaching transition. In terms of the development discussed here this refers to the lifetime of the $S_1 \rightarrow S_0$ transition. I_{Sat} is the intensity at which the absorption coefficient drops to approximately half of its normal state value. He also

investigated the effect of excited state absorption on the transmission of a saturable absorber and noted that it precluded the possibility of the absorption bleaching totally and this was termed residual absorption.

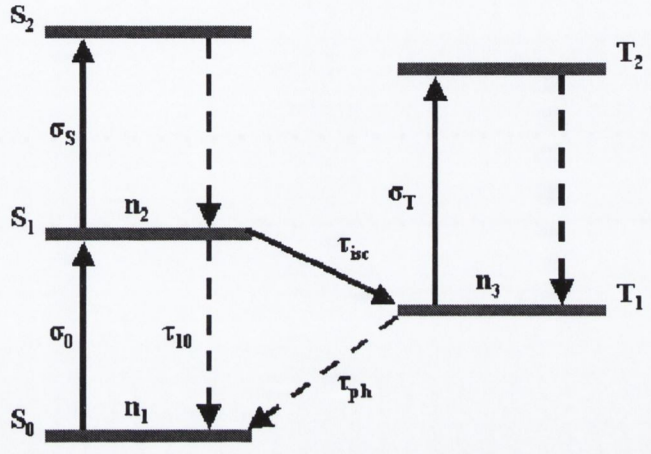

Figure 4.2 Generalized 5 level system used in deriving the excited state absorption model used to simulate RSA in the phthalocyanine system. S_i represents singlet levels and T_i represents triplet levels. Solid arrows imply an excitation resulting from photon absorption and dashed arrows represent relaxations.

To discuss the importance of the various parameters that influence RSA in the phthalocyanine system, a general 5-level molecular orbital model system such as that shown in Figure 4.2 has been investigated, and approximations suitable for the phthalocyanine system under nanosecond irradiation have been applied. Laser rate equations were used to stimulate the excitation and subsequent relaxation of the system. The vibrational levels of the electronic states were ignored and for the sake of simplicity the laser pulse width was assumed to be longer than any of the lifetimes associated with the levels. This is still a complicated system and in an effort to further simplify matters it was assumed that relaxation out of states S_2 and T_2 were very rapid so that the population of these two levels may be neglected.

Generally for this 5-level system after initial excitation, the first excited singlet state S_1 is populated, from here the electrons may be subsequently excited into S_2 within the duration of the pulse. Once in S_2, they rapidly relax to S_1 again. From S_1 the population may undergo an intersystem crossing to the first excited triplet T_1 with a time constant τ_{isc} and thereafter be excited into T_2. Similarly to S_2, this state relaxes rapidly and the population is exchanged between these two

cyclically as the lifetime of T_1 (τ_{ph}) is generally very long in comparison to τ_{isc}. Furthermore, stimulated emission from S_1 is excluded due to the small fluorescence quantum yield. The system now reduces to the following set of three differential rate equations,

$$\frac{\partial n_1}{\partial t} = -\frac{\sigma_0 I}{h\nu} n_1 + \frac{n_2}{\tau_{10}} + \frac{n_3}{\tau_{ph}} \tag{4.2}$$

$$\frac{\partial n_2}{\partial t} = \frac{\sigma_0 I}{h\nu} n_1 - \frac{n_2}{\tau_{isc}} - \frac{n_2}{\tau_{10}} \tag{4.3}$$

$$\frac{\partial n_3}{\partial t} = \frac{n_2}{\tau_{isc}} - \frac{n_3}{\tau_{ph}} \tag{4.4}$$

where n_1, n_2 and n_3 refer to the populations of S_0, S_1, and T_1 and the total population of the system $N = n_1+n_2+n_3$. Attenuation of the laser beam is governed by a propagation equation, the Lambert-Beer law, where the intensity dependent absorption coefficient $\alpha(I)$ now includes the excited state absorption from S_1 and T_1

$$\frac{\partial I}{\partial z} = -\alpha(I)I = -\left(\sigma_0 n_1 + \sigma_S n_2 + \sigma_T n_3\right) I \tag{4.5}$$

Under the steady state approximation, which is valid when the pulse width is much longer than any relaxation time, all the time derivatives may be set to zero. This is a valid assumption for nano-seconds pulses as the lifetimes in phthalocyanines are typically of order pico-seconds. This assumption can be discussed a little further using a numerical integration of Equations (4.2) to (4.4) and this will be presented in the next section, Section 4.2.4.

The total population, N, is now reintroduced and n_1 expressed in terms of it.

$$n_1 = N - n_2 - n_3 \tag{4.6}$$

This can then be substituted back into the rate equations above to give n_2,

$$n_2 = \frac{\sigma_0 I}{h\nu}\left(N - n_2 - n_2\frac{\tau_{ph}}{\tau_{isc}}\right)\tau_{isc} \tag{4.7}$$

where the following approximation has been applied

$$\frac{1}{\tau_{isc}} \approx \frac{1}{\tau_{isc}} + \frac{1}{\tau_{10}} \tag{4.8}$$

Noting that $\tau_{isc} << \tau_{ph}$ and using the expression for I_{Sat} quoted above, an expression for n_2 in terms of the total population N is found and is given by

$$n_2 = \frac{\tau_{isc}}{\tau_{ph}} \cdot \frac{I}{I_{Sat}} \cdot \frac{N}{1+\frac{I}{I_{Sat}}} \tag{4.9}$$

n_3 is then found to be given by

$$n_3 = \frac{I}{I_{Sat}} \cdot \frac{N}{1+\frac{I}{I_{Sat}}} \tag{4.10}$$

and n_1 is then expressed as

$$n_1 = \frac{N}{1+\frac{I}{I_{Sat}}} \tag{4.11}$$

Substituting these expressions for the populations of each level into Equation (4.5) for the nonlinear absorption coefficient then yields the following

$$\alpha(I) = \frac{\sigma_0 N}{1+\frac{I}{I_{Sat}}}\left(1+\frac{\sigma_S}{\sigma_T}\cdot\frac{\tau_{isc}}{\tau_{ph}}\cdot\frac{I}{I_{Sat}}+\frac{\sigma_T}{\sigma_0}\cdot\frac{I}{I_{Sat}}\right) \tag{4.12}$$

Noting that $\alpha_0 = \sigma_0 N$ (N is the total number density of dissolved molecules), and noting that σ_T and σ_S are probably approximately of the same order where $\tau_{isc} << \tau_{ph}$ and as the triplet yield is large for metallo-phthalocyanines under nanosecond irradiation one is then in a position to eliminate the term with σ_S in the numerator. This effectively reduces the 5 level model to a 3 level model. One can then define the intensity dependent absorption coefficient:

$$\alpha(I, I_{Sat}, \kappa) = \frac{\alpha_0}{1+\frac{I}{I_{Sat}}}\left(1+\kappa\frac{I}{I_{Sat}}\right) \tag{4.13}$$

where in this case the excited state absorption cross section (σ_{ex}) is due almost entirely to σ_T and thus $\kappa = \sigma_{ex}/\sigma_0$. It can be noted that the intensity (I) and the pulse energy density defined as $F = E_{Pulse}/(\pi w(z)^2)$, where E_{Pulse} is the energy per pulse and $\pi w(z)^2$ is the surface area through which the pulse is propagating at any position denoted by z, are directly related to each other and consequently the parameter I/I_{Sat} can be replaced with F/F_{Sat} in Equation (4.13), where in this case F_{Sat} is the saturation energy density. In general, the optical limiting results and plots in this thesis will be presented as normalised transmission as a function of incident energy

(a)

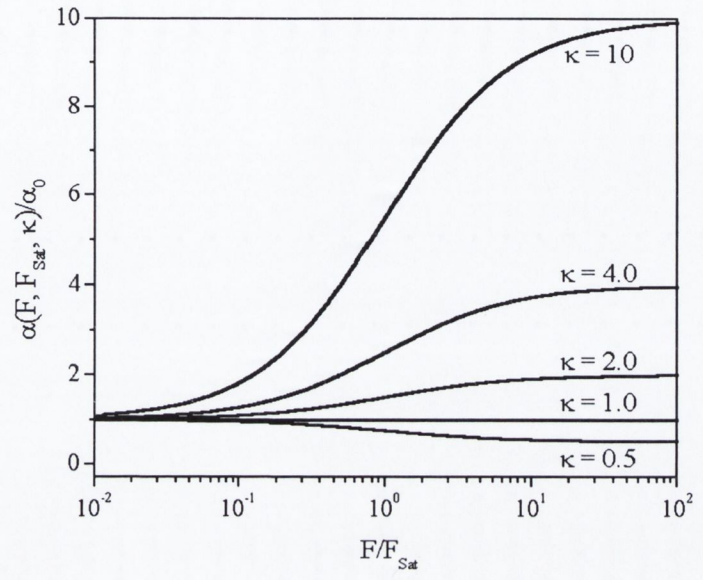

(b)

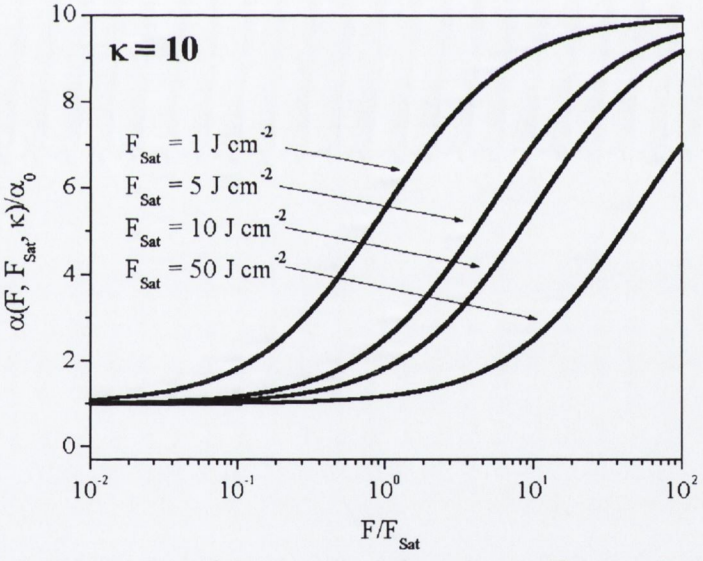

Figure 4.3 **(a)** Plot of the normalised absorption coefficient $\alpha(F, F_{Sat}, \kappa)/\alpha_0$ against normalised pulse energy density F/F_{Sat} (F_{Sat} = *1 J cm*$^{-2}$) for different values of κ, (σ_{ex}/σ_0). **(b)** Plot of $\alpha(F, F_{Sat}, \kappa)/\alpha_0$ against F/F_{Sat} (κ = *10*) for different values of F_{Sat}.

density and the saturations quoted will be energy saturation densities.

The changes in the normalised absorption coefficient ($\alpha(F, F_{Sat}, \kappa)/\alpha_0$) with F/F_{Sat} are displayed for different values of κ in Figure 4.3a where the saturation energy density has been fixed at 1 J cm^{-2}. Similarly, the changes in the normalised absorption coefficient ($\alpha(F, F_{Sat}, \kappa)/\alpha_0$) with F/F_{Sat} are displayed for different values

of F_{Sat} in Figure 4.3b where the κ coefficient has been fixed at 10. From these, it is apparent that whenever the excited state absorption cross-section is greater than that of the ground state i.e. $\kappa > 1$, RSA is observed as an increase in the normalised intensity (or energy density) dependent absorption coefficient ($\alpha(F, F_{Sat}, \kappa)/\alpha_0$) with respect to increasing normalised pulse energy density F/F_{Sat}. Whenever the converse is true, $\kappa < 1$, saturable absorption is observed as a reduction in $\alpha(F, F_{Sat}, \kappa)/\alpha_0$ with increasing F/F_{Sat}. This model, though simple, reproduces the gross effects of RSA and highlights the crucial role that the excited state absorption plays in the overall absorption coefficient. This steady state model approximates a dynamic model in the limit of temporally long pulse widths, ie. nanosecond irradiation when all other lifetimes in the material are of the order of picoseconds. A full dynamic model cannot be approached analytically as the rate equations involved then make up a set of coupled partial differential equations which must be numerically integrated over time and space, and in this study it was assumed that the dynamic response in the phthalocyanines was approximated well with the steady state model. Although this model may not be spectroscopically exact over the entire range of phthalocyanines that will be examined in this thesis it produces parameters F_{Sat} and κ that can be used to describe the magnitude of the nonlinear absorption.

4.2.4 Numerical Simulation of Population Dynamics and Rate Equations

4.2.4.1 Introduction

In this section numerical simulation of the laser rate equations (Equations (4.2) to (4.4)) will be presented to develop an understanding of the population dynamics in the phthalocyanine system subject to laser irradiation. A more general three level system, describing a three-state model of lasing, than the system described above will be developed first to introduce the numerical methods. After this the initial conditions that will be applied to the populations in the phthalocyanine system are discussed, followed by attempted solutions to the differential equations describing the phthalocyanine system in the different possible operating regimes.

4.2.4.2 General Three Level Model of a Laser

In general, the allowable transitions of a three level system can be in the form of photonic excitations and spontaneous or induced emissions and vibrational

relaxations. In this section a hypothetical three-state laser model will be constructed incorporating photonic absorption with spontaneous and induced emissions. The purpose of this section is to introduce the numerical methods that will be applied to the rate equations of Section 4.2.3. The energy levels in this system are sketched in Figure 4.4 where the rates for each transition are indicated in the figure, the superscript is either A, S or I to indicate absorption, spontaneous emission and induced emission respectively and the subscript indicates the initial and final energy level of the atom.

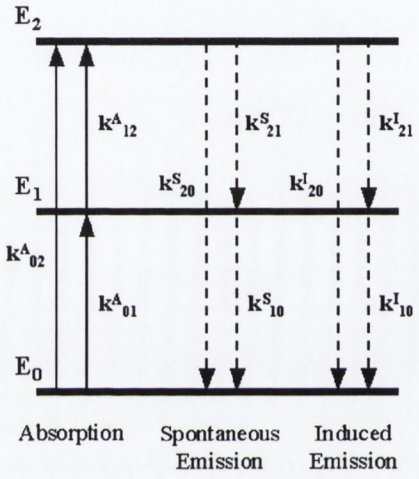

Figure 4.4 Sketch of the levels in a general three state system where solid arrows represent excitations and the dashed lines represent relaxations.

In an ensemble of N three-state atoms at equilibrium, the number of atoms in the j^{th} atomic state is governed by the Boltzmann distribution and expressed as

$$N_j = N \frac{\exp\left(-E_j/k_B T\right)}{\sum_{i=0}^{2} \exp\left(-E_i/k_B T\right)} \tag{4.13}$$

where j is the state label 0, 1, or 2, T is the temperature in Kelvin, N is the total number of atoms in all states and k_B is Boltzmann's constant. Thus at room temperature and with the energies that will be considered here, the populations of states 1 and 2 are negligible when the system is at equilibrium.

For lasing to occur in this material at a frequency of ω_{21} by stimulated emission, the collection of three-state atoms must be supplied with energy in the form of photons of frequency $\geq (E_2 - E_0)/(h/2\pi)$. This pumping of the system disrupts the equilibrium distribution of states and creates a population inversion, the number

of atoms in state 2 becomes greater than the number of atoms in state 1. When this condition exists, the presence of a photon of frequency ω_{21} catalyses the transition from 2 to 1 and produces another coherent photon. If the population inversion can be maintained, significant numbers of coherent photons can be produced resulting in an output of monochromatic or laser light.

The rate equations describing this system can easily be written as spontaneous emission reactions follow rate laws that depend only on the number of atoms in the reactant state. From these rules and the nine transitions seen in Figure 4.4, one can write six coupled rate equations; one for the population of each of the three states and one for the number of photons at each of the three different frequencies. Using $N_0(t)$, $N_1(t)$, and $N_2(t)$ as the populations of states 0, 1, and 2, respectively, and $N_{01}(t)$, $N_{12}(t)$, and $N_{02}(t)$ in place of $N_{xy}(t)$ as the number of photons (photon population) having frequency $(E_y-E_x)/(h/2\pi)$ respectively, the equations are:

$$\frac{dN_0}{dt} = -k_{02}^A N_{02}(t)N_0(t) - k_{01}^A N_{01}(t)N_0(t) + k_{20}^S N_2(t) + k_{10}^S N_1(t) + k_{20}^I N_{02}(t)N_2(t) + k_{10}^I N_{01}(t)N_1(t) \tag{4.14}$$

$$\frac{dN_1}{dt} = -k_{12}^A N_{12}(t)N_1(t) + k_{01}^A N_{01}(t)N_0(t) + k_{21}^S N_2(t) - k_{10}^S N_1(t) + k_{21}^I N_{12}(t)N_2(t) - k_{10}^I N_{01}(t)N_1(t) \tag{4.15}$$

$$\frac{dN_2}{dt} = -\frac{dN_0}{dt} - \frac{dN_1}{dt} \tag{4.16}$$

$$\frac{dN_{01}}{dt} = -k_{01}^A N_{01}(t)N_0(t) + k_{10}^S N_1(t) + k_{10}^I N_{01}(t)N_1(t) - k_{01}^D N_{01}(t) \tag{4.17}$$

$$\frac{dN_{01}}{dt} = Pump_{02}(t) - k_{02}^A N_{02}(t)N_0(t) + k_{20}^S N_2(t) + k_{20}^I N_{02}(t)N_2(t) - k_{02}^D N_{02}(t) \tag{4.18}$$

$$\frac{dN_{01}}{dt} = -k_{12}^A N_{12}(t)N_1(t) + k_{21}^S N_2(t) + k_{21}^I N_{12}(t)N_2(t) - k_{12}^D N_{12}(t) \tag{4.19}$$

where three further transitions have been added with rates k^D_{xy} which represent the number of ω_{xy} photons per second that escape from the chamber. The function $Pump_{02}(t)$ represents the optical pumping of the system and was modelled as an infinite train of Gaussian laser pulses separated in time by Δt, governed by the following equation.

$$Pump_{02}(t) = \sum_{i=0}^{\infty} N_P \exp\left(-\left[\frac{2(t-(i\times\Delta t))}{\tau_{FWHM}}\right]^2\right) \tag{4.20}$$

where N_P is the number of photons per second incident on the system The initial conditions for the system were assumed to be $N_i(t=0)$ as quantified by the Boltzmann distribution (Equation (4.13)) and $N_{xy}(t=0) = 0$. The constants that were substituted

Coefficient	Value	Coefficient	Value
k_B	1.381×10^{-16} erg K^{-1}	k^A_{02}	1.1×10^{7} s^{-1}
h	6.626×10^{-27} erg s	k^S_{20}	1.1×10^{7} s^{-1}
E_0	0.1×10^{-11} erg	k^S_{21}	1.1×10^{7} s^{-1}
E_1	1.05×10^{-11} erg	k^S_{10}	1.1×10^{7} s^{-1}
E_2	1.06×10^{-11} erg	k^J_{20}	0.1×10^{7} s^{-1}
N	1000	k^J_{21}	0.2×10^{7} s^{-1}
Np	2×10^{11}	k^J_{10}	0.3×10^{7} s^{-1}
T	293 K	k^D_{01}	1×10^{9} s^{-1}
k^A_{01}	1.1×10^{7} s^{-1}	k^D_{12}	1×10^{7} s^{-1}
k^A_{12}	1.1×10^{7} s^{-1}	k^D_{02}	1×10^{9} s^{-1}

Table 4.1. Numerical values for the coefficients used in Equations (4.14) to (4.20)

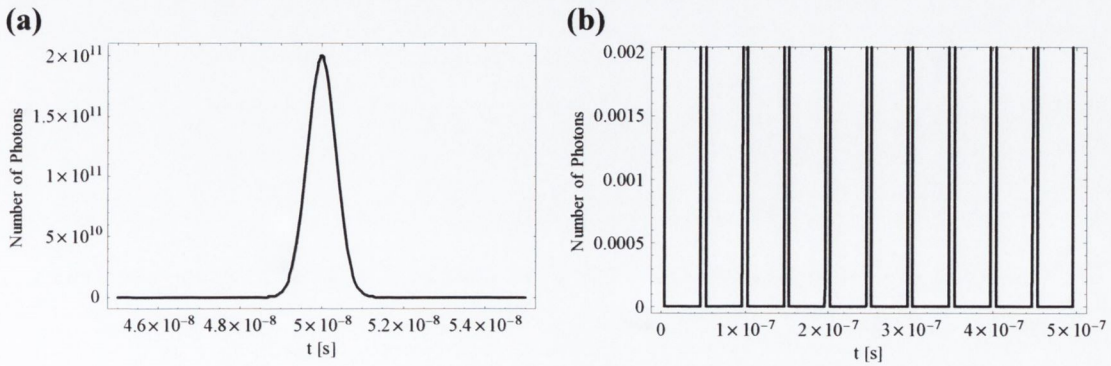

Figure 4.4 Temporal evolution of the pump beam with the number of photons plotted as a function of time. **(a)** Temporal profile single pulse from the beam and **(b)** a pulse train.

into the rate equations are quoted in Table 4.1. The equations were incorporated into a computer code and numerically solved.

The laser pumping function quoted in Equation (4.20) was constructed with the parameters Δt and τ_{FWHM} set to 50 ns and 1ns respectively and snapshots of the temporal evolution of the pump beam can be seen in Figure 4.4.

Thus, the pump beam was constructed of nanosecond pulses with a repetition rate of 20 MHz. The incident photonic temporal profile of a single pulse in the pump beam can be seen in Figure 4.4a and a pulse train in Figure 4.4b. The pulse width and frequency were chosen to ensure that a population inversion would be observed.

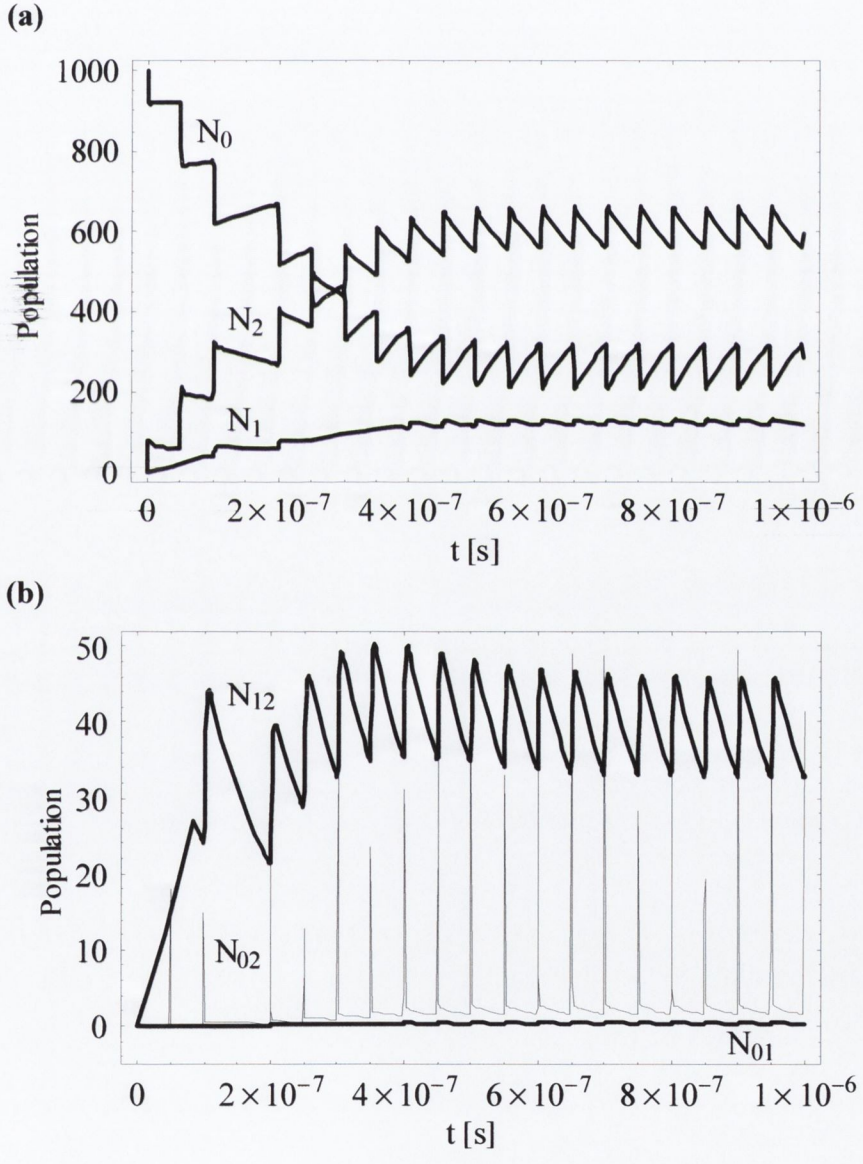

Figure 4.5 Simulation of Equations (4.14) to (4.19) subject to pumping with a train of Gaussian pulses described with Equation (4.20), depicted in Figure 4.4. In **(a)** the populations $N_0(t)$, $N_1(t)$ and $N_2(t)$ are plotted in time and in **(b)** the photon populations $N_{01}(t)$, $N_{12}(t)$ and $N_{02}(t)$ over time.

The numerical simulations of Equations (4.14) to (4.19) subject to pumping with a train of Gaussian pulses described with Equation (4.20), depicted in Figure 4.4, are presented in Figure 4.5. It can be noted from Figure 4.5a that the populations reach a quasi steady state type regime after approximately 0.4 μs. The steady state populations are greater for state 2 than state 1, which is the expected condition for population inversion required in a laser to create stimulated emission for lasing. In this figure, the populations are seen to be modulated at the repetition rate of the pump pulses, and hence this regime was referred to as quasi steady state. In Figure 4.5b it can be seen that, modulated at the repetition rate of the pumping, the photon population N_{12} is greater that than other photon frequencies again indicative of lasing action. The 'spikes' in the N_{02} photonic population coincide with the peaks of pumping pulses, as one would expect.

4.2.4.3 The Phthalocyanine System

The tools that were developed and tested in the previous section will be used here and applied to the phthalocyanine population model that was explored in Section 4.3.3. In this section, the population changes during a single pulse were simulated. The transitions that were considered were, as outlined in the derivation, absorptive excitations from the lowest and the first singlet energy levels and in the lowest triplet energy levels. Thus, the populations $n_1(t)$, $n_2(t)$ and $n_3(t)$ corresponding to the populations in energy levels S_0, S_1 and T_1 respectively are simulated here. All vibrational relaxations were treated as instantaneous, and fluorescence and phosphorescence emission were included in the simulation. Initially the populations at $t = 0\ s$ were set as $n_1(0)=N$, and $n_2(0) = n_3(0) = 0$. The pumping pulse that was used, similar but simplified from Equation (4.20), is given in Equation (4.21) and was set with τ_{FWHM} = 6ns and λ = 532 nm in all the following simulations to match the laser that will be used in the experiments.

$$Pump(t) = I_0' \exp\left(-\left[\frac{2(t-\Delta t)}{\tau_{FWHM}} \right]^2 \right) \tag{4.21}$$

The pulse peak was set to occur 10 ns (Δt = 10 ns) after the start of the simulation in all cases. If one considers that typically a 1 g L^{-1} solution of Pcs could have a linear absorption coefficient of order $\alpha_0 \approx 1\ cm^{-1}$ and a Pc molecule has

Parameter	Simulation 1	Simulation 2	Simulation 3	Simulation 4
τ_{FWHM} [ns]	6	6	6	6
λ [nm]	532	532	532	532
N	1×10^{18}	1×10^{18}	1×10^{18}	1×10^{18}
I'_0 [GW cm^{-2}]	0.1	0.1	0.1	0.1
σ_0 [cm^2]	1×10^{-18}	1.8×10^{-18}	1×10^{-18}	1×10^{-18}
τ_{10} [ns]	10	0.5	5	0.5
τ_{isc} [ns]	10	0.3	300	10
τ_{ph} [μs]	1	1	1	1

Table 4.2 Numerical values used in the simulations for the Pc system

molecular weight of order 1000. This would give a ground state absorption cross-section coefficient of order $\sigma_0 \approx 10^{-18}$ cm^2 and a total population of order 10^{18}. Thus, in all simulations 10^{18} entities in the ensemble were assumed. Miles[20], in his first paper dealing with the optimal design and fabrication of practical optical limiters constructed from excited state absorbers, quoted typical life times for the various allowable transitions in organic dyes. The first simulation was carried out using these values, which are quoted in Table 4.2 under Simulation 1.

The results from the first simulation of the temporal evolution of the populations $n_1(t)$, $n_2(t)$ and $n_3(t)$ (Simulation 1 of the Pc system) are depicted in Figure 4.6. The dynamic behaviour of the populations is presented in Figure 4.6a and the temporal profile of the laser pulse is depicted in Figure 4.6b. Initially the ground state population (n_1) is completely depleted and the population in S_1 denoted n_2 rises sharply. As time evolves the population of S_1 reaches a maximum approximately 4 ns before the peak of the laser pulse. After this, the inter system crossing facilitates the transfer of the population into the first triplet state T_1 and as the pulse ends the population of the ground state is seen to grow again as the fluorescent and phosphorescent decays return the populations to their starting locations in S_0.

In the second simulation (Simulation 2) the population dynamical behaviour for the chloroindium phthalocyanine studied by Shirk *et al.*[12], Perry *et al.*[14,16] and

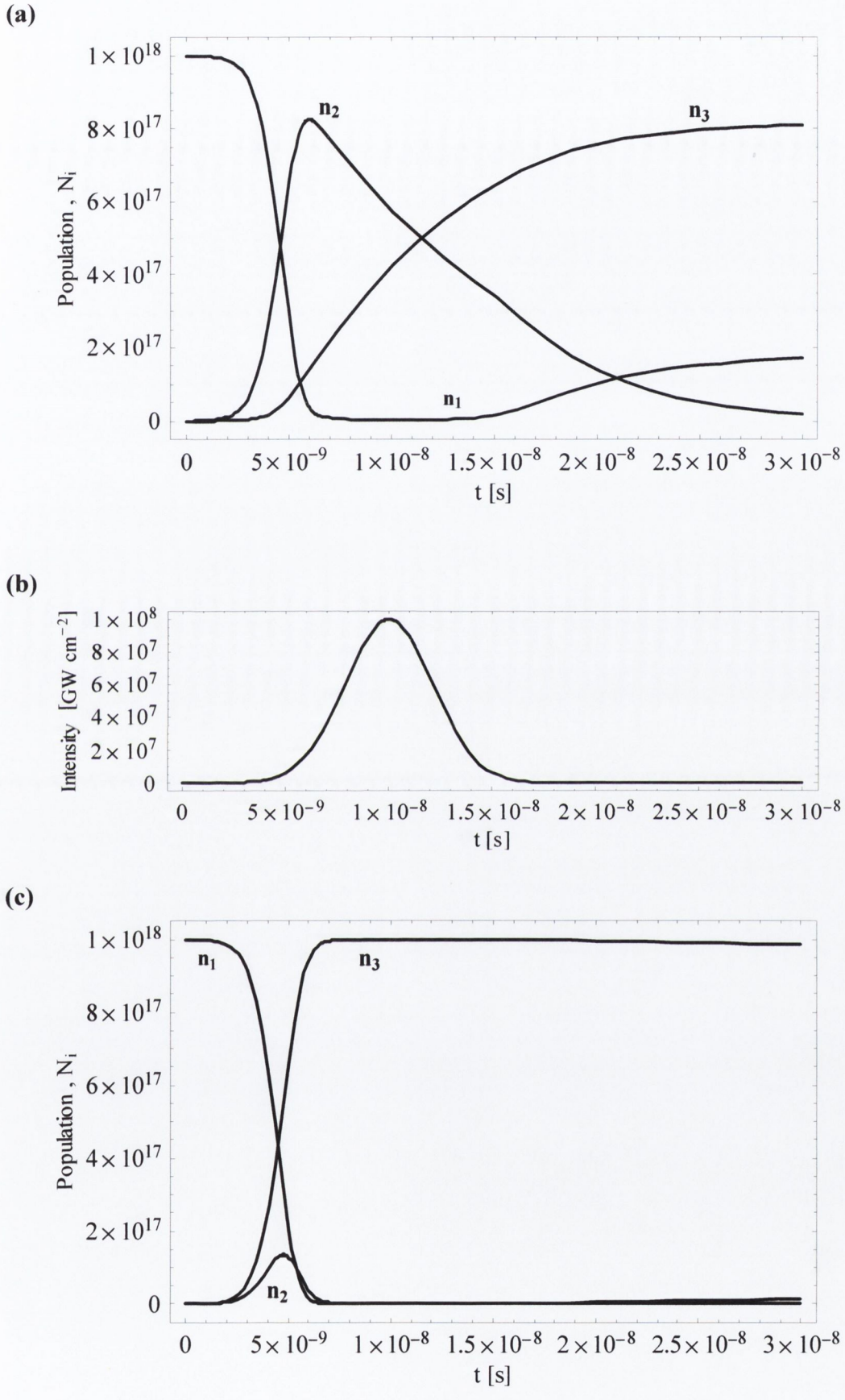

Figure 4.6 Temporal evolution **(a)** of the populations for Simulation 1 of the Pc system, **(b)** of the laser pulse and **(c)** of the populations for the chloroindium phthalocyanine system, Simulation 2.

Chen *et al.*[21] has been modelled. Shirk *et al.*[12] reported that the intersystem crossing in this system was of 0.3 ns and Perry *et al.*[14] reported that the ground state absorption cross-section was of the order of 1.8×10^{-18} cm^2 while recently we, Chen *et al.*[21], have reported that the fluorescence lifetime is of the order of 0.5 ns for this compound. These parameters were inserted into the rate equations and the behaviour simulated over 30 ns with the laser pulse peaking after 10 ns, as before. It can be seen in Figure 4.6c that the population in S_1 represented by n_2 peaks just before 5ns. From this point on, the short intersystem crossing facilitates the rapid transfer of the population into the T_1 level, measured by n_3. The n_1 population in S_0 is rapidly depleted tending toward zero after about 6 ns. Comparison with the laser pulse shows that the pulse is still relatively weak at this time and therefore, for the majority of the event, the population in T_1 undergoes excitations and subsequent rapid relaxations to and from higher triplet states. This is in excellent agreement with the assumptions made in Section 4.2.3 when deriving the static case nonlinear absorption coefficient where three level or state behaviour was assumed to occur. In this regime with the short intersystem crossing time the nonlinear absorption coefficient described by Equation 4.12 is spectroscopically accurate, where the nonlinear absorption coefficient cross-section, σ_{ex}, is due almost entirely to the triplet state transitions described above.

The opposite situation to the entire transfer of population to the T_1 level as described for the chloroindium Pc, as discussed above in Simulation 2, is where the intersystem crossing relative to the pulse is extremely long. In the third simulation (Simulation 3 in Table 4.2) the characteristic intersystem crossing was set to 300 ns to simulate this behaviour. The resulting simulation is depicted in Figure 4.7a, and the incident pulse is presented in Figure 4.7b. In this case it can be seen that the population in T_1, denoted n_3, grows only slightly and slowly and that the vast majority of the population resides in S_1 undergoing higher singlet excitations and subsequent vibrational relaxations back to S_1 during the pulse. In this regime with the relatively long intersystem crossing time the nonlinear absorption coefficient described by Equation 4.12 is again spectroscopically accurate. In this case the nonlinear absorption coefficient cross-section σ_{ex} is due almost entirely to the singlet state transitions described above.

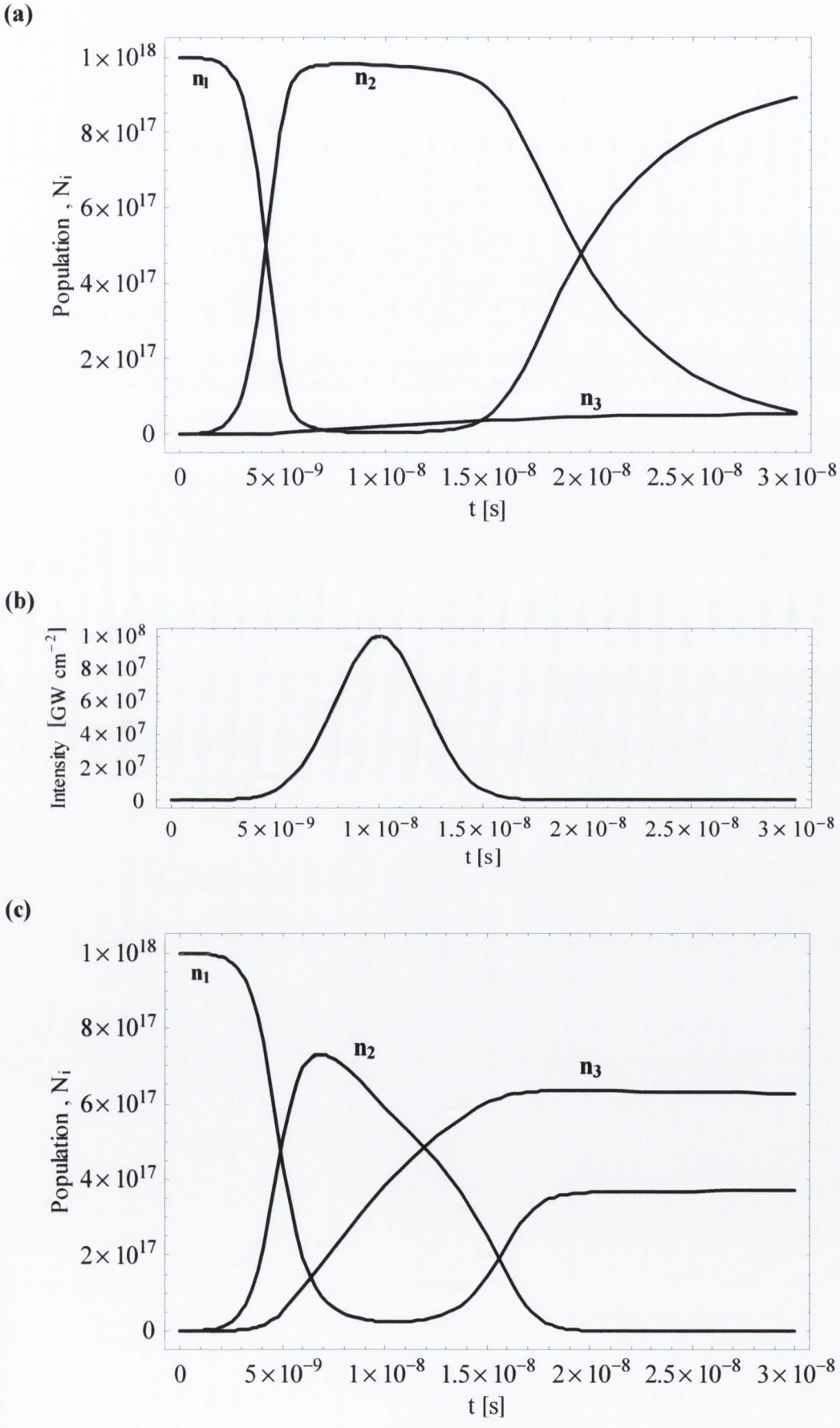

Figure 4.7 Temporal evolution **(a)** of the populations for Simulation 3 of the Pc system, **(b)** of the laser pulse and **(c)** of the populations for Simulation 4.

The previous two simulations (Simulations 2 and 3) describe the phthalocyanine system in two extreme regimes relative to the experimental laser pulse. Each case exhibits high intensity optical excitations in either the triplet levels or the singlet levels exclusively, that can be described by an effective three level absorption coefficient. Intersystem crossing with a lifetime of the order of the pulse width describes the transitional regime between these two extremes. This has been modelled in Simulation 4 where the intersystem crossing, τ_{isc}, has been set to 10 ns which is comparable to the 6 ns laser pulse. The population dynamics are depicted in Figure 4.7c. It can be seen in the figure that during the high intensity region of the laser pulse centred about 10 ns after the commencement of the simulation that the S_1 and T_1 populations, n_2 and n_3 respectively, are both of similar magnitude. As a result, high intensity optically pumped perturbations in such a system involves singlet state and triplet state excitations and relaxations. Consequently the energy dissipation of the laser pulse involves both the singlet and triplet manifolds. The nonlinear absorption cross-section in this system is a combination of the S_1 to higher singlet levels and the T_1 to higher triplet levels absorption cross-sections. If this system is treated with a simplified three level model the nonlinear absorption cross-section results from a combination of both the singlet and triplet absorptions. In this case the model is not spectroscopically accurate, but can be used to calculate effective excited to ground state absorption cross-section ratios that can be used to describe the magnitude of the nonlinear absorption regardless of the source of the dissipation.

As population transfer lifetimes are generally not measured in this work, and the three state model is used in all cases to fit the nonlinear absorption, it is recognised that in some cases the model may not be spectroscopically correct. The intention of this study is therefore to attempt to link the magnitude of the nonlinear response with the molecular constitution, regardless of the singlet or triplet origin of the excited state behaviour.

4.2.5 Application of the nonlinear absorption model

Before application of the RSA model to experimental data the nonlinear absorption coefficient $\alpha(I, I_{Sat}, \kappa)$ given by Equation (4.13) had to be substituted back into the Lambert-Beer law and a function describing the transmission as a function of the other parameters had to be obtained.

$$\frac{dI}{dz} = -\frac{\alpha_0}{1+I/I_{Sat}}\left(1+\kappa\frac{I}{I_{Sat}}\right)I \tag{4.22}$$

One can then consider an integral over a homogeneous sample of thickness L where I_{In} gives the incident intensity and the transmitted intensity is represented by I_T. The integration was performed with limits on dz going from $z = 0 \rightarrow L$ and the limits on dI going from $I = I_{In} \rightarrow I_T$, as in the linear case in Section 4.2.1.

$$\int_{I_{In}}^{I_T}\left(\frac{1}{1+I/I_{Sat}}+\frac{\kappa\, I/I_{Sat}}{1+I/I_{Sat}}\right)^{-1}\frac{dI}{I} = -\alpha_0\int_0^L dz \tag{4.23}$$

This can then be trivially rearranged as:

$$\int_{I_{In}}^{I_T}\left(\frac{1}{I+\kappa I^2/I_{Sat}}+\frac{1}{I_{Sat}+\kappa I}\right)dI = -\alpha_0\int_0^L dz \tag{4.24}$$

This expression can then be sequentially integrated which results in:

$$\left[Log(I)-Log(I_{Sat}+\kappa I)+\frac{Log(I_{Sat}+\kappa I)}{\kappa}\right]\Bigg|_{I_{In}}^{I_T} = -\alpha_0 z\Big|_0^L \tag{4.25}$$

where the following two standard integrals have been exploited,

$$\int\frac{dx}{x+(a/b)x^2} = Log(x)-Log(b+ax) \tag{4.26}$$

$$\int\frac{dx}{a+bx} = \frac{Log(a+bx)}{b} \tag{4.27}$$

Equation (4.25) can then be rewritten as:

$$\left[Log(I)+\left(\frac{1-\kappa}{\kappa}\right)Log(I_{Sat}+\kappa I)\right]\Bigg|_{I_{In}}^{I_T} = -\alpha_0 z\Big|_0^L \tag{4.28}$$

which can be reduced to the following equation when the integration limits are substituted into the expression

$$\frac{1}{\kappa}\left[\kappa\, Log\left(T\frac{I_{Sat}/I+\kappa}{I_{Sat}/I+\kappa T}\right)+Log\left(\frac{I_{Sat}/I+\kappa T}{I_{Sat}/I+\kappa}\right)\right] = -\alpha_0 L \tag{4.29}$$

where, as before, the transmission T has been defined as $T = I_T/I_{In}$. This is a

transcendental equation of T, where T is essentially a function of I, κ and I_{Sat}, and can be rewritten as follows after raising both sides of the expression as powers of exponentials.

$$T(I,\kappa,I_{Sat}) = \exp(-\alpha_0 L)\left(\frac{I_{Sat}+\kappa T(I,\kappa,I_{Sat})I}{I_{Sat}+\kappa I}\right)^{1-\frac{1}{\kappa}} \qquad (4.30)$$

This requires a numerical solution and is fitted to the experimental data with $T(I, \kappa, I_{Sat})$ treated as the dependent variable, I is the independent variable and κ (realistically σ_{ex} as α_0 was measured) and I_{Sat} are both free parameters where as in Section 4.2.3, $T(I, \kappa, I_{Sat}) = T(F, \kappa, F_{Sat})$ by replacing I with F and I_{Sat} with F_{Sat} in the expression denoted by Equation (4.30).

4.3 Materials Studied

The phthalocyanines studied in this thesis are all variations of the basic phthalocyanine unit depicted in Figure 3.1 and Figure 3.2. The compounds can generally be separated into eight main groups or categories depending on the type or locations of the peripheral and non-peripheral substituents and these categories will be labelled (a) to (h). The chemical structure of a selection of these phthalocyanine compounds (from each category) has been sketched in Figure 4.8, and the molecular formula for each phthalocyanine is given in Table 4.3. The chemical structure of each of the axial or peripheral groups is presented opposite its molecular label in Table 4.4.

The first compound on Table 4.3 (compound **1**) is the Buckminster Fullerene (C_{60}) and after this the phthalocyanine categories are presented where category (a) represents those compounds with four *t*Bu groups on the monomer phthalocyanine periphery (compounds **2-9**) including three different central metal oxo-bridged dimers (compounds **7-9**). Category (b) represents those compounds with eight [C_6H_{13}], eight [$C_{10}H_{21}$] or eight [$Ciso_5H_{11}$] groups attached to the periphery at the locations shown in the Figure 4.8b (compounds **10-23**). Category (c) represents those compounds with eight [$OSO_2C_3H_7$] or [$OSO_2C_8H_{17}$] groups attached to the periphery (compounds 24-27). Category (d) represents the Ga naphthalocyanine compounds including one Ga-O-Ga bridged dimer (compounds **28-30**). Category (e)

(a)

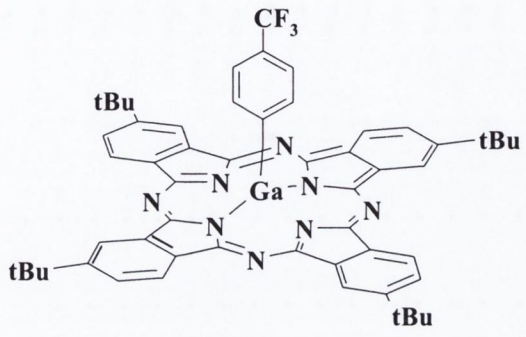
CF3
tBu
tBu
Ga
tBu
tBu

(b)

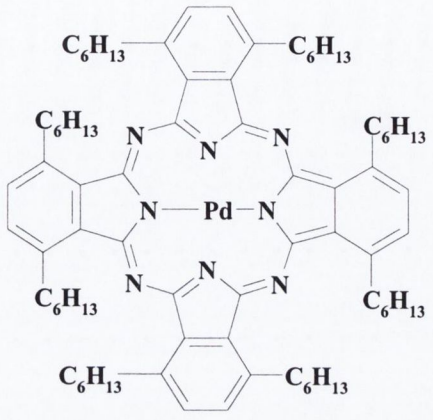
C6H13
C6H13
C6H13
C6H13
Pd
C6H13
C6H13
C6H13
C6H13

(c)

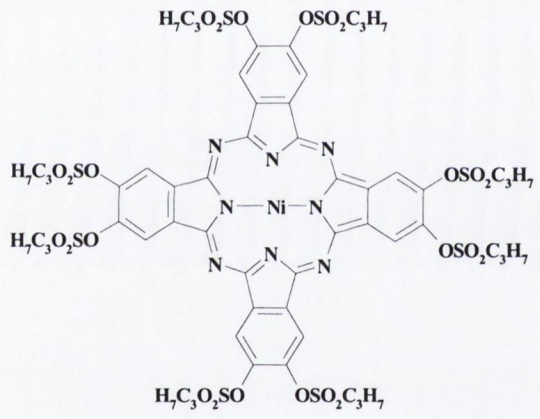
H7C3O2SO
OSO2C3H7
H7C3O2SO
H7C3O2SO
Ni
OSO2C3H7
OSO2C3H7
H7C3O2SO
OSO2C3H7

(d)

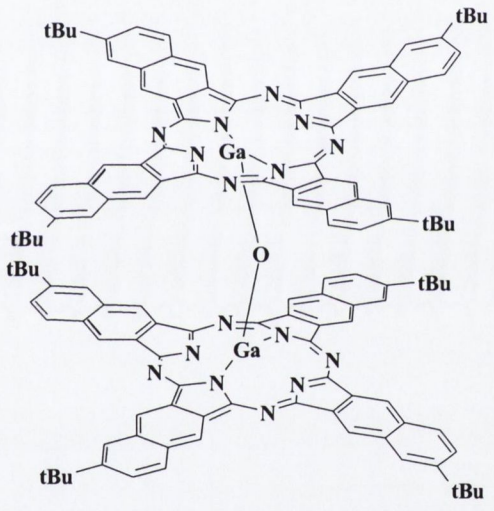
tBu
tBu
Ga
tBu
tBu
O
tBu
tBu
Ga
tBu
tBu

(e)

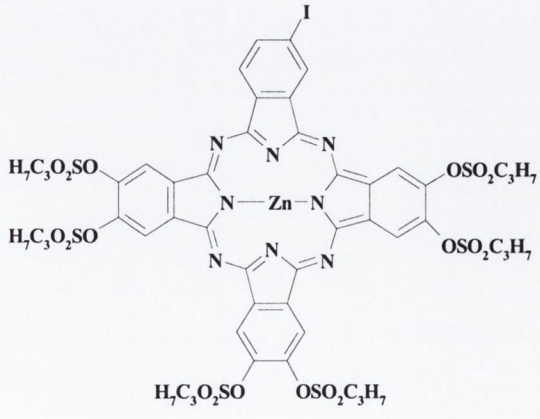
I
H7C3O2SO
OSO2C3H7
H7C3O2SO
Zn
OSO2C3H7
H7C3O2SO
OSO2C3H7

(f)

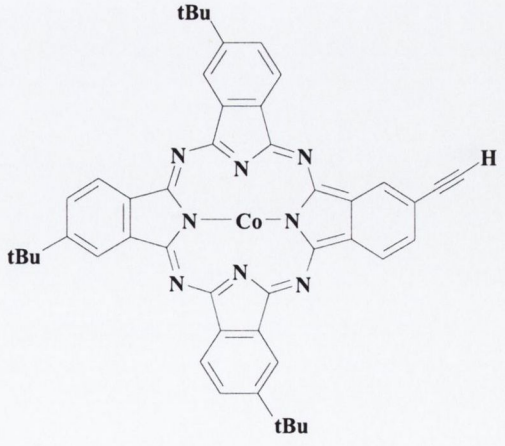
tBu
H
Co
tBu
tBu

(g)

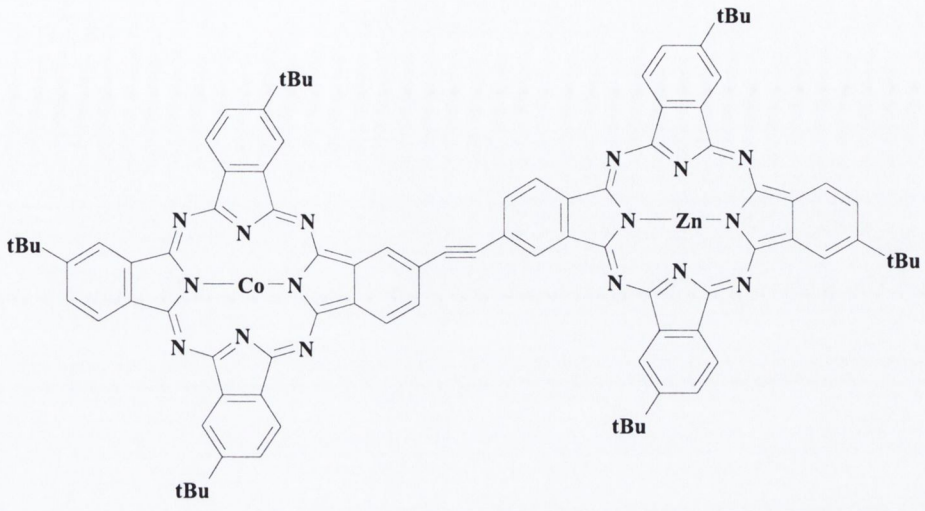

(h)

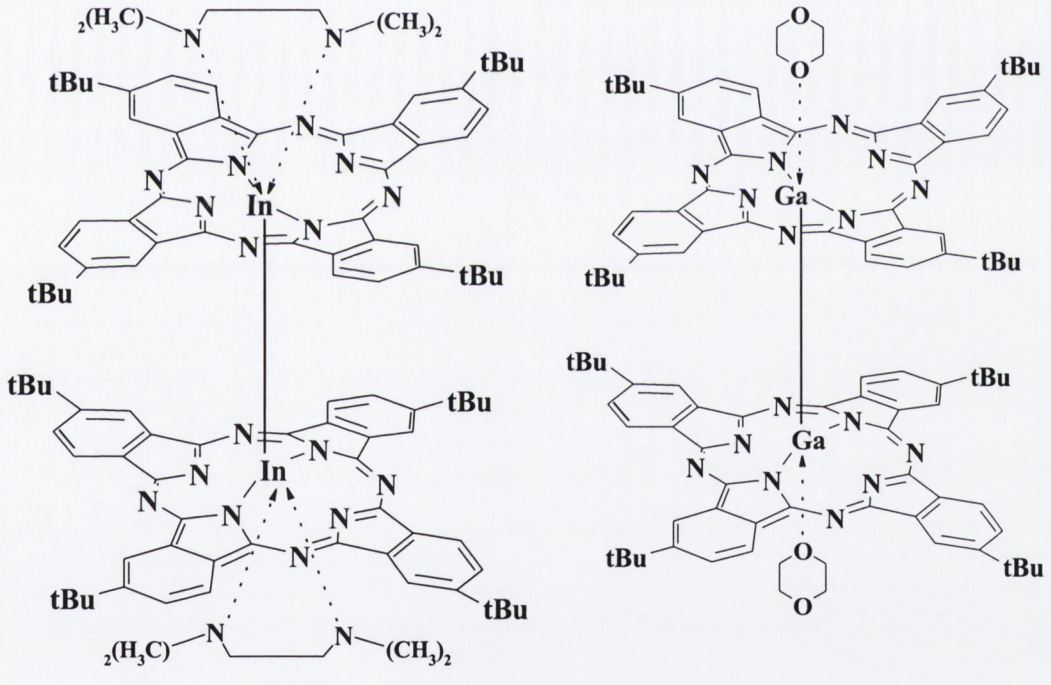

Figure 4.8 The phthalocyanine compounds in this study are separated into seven main groups depending on their peripheral substituents and a sample of one compound from each group is displayed: **(a)** four *t*Bu peripheral groups (compounds **2-9**), **(b)** eight C_6H_{13}, $C_{10}H_{21}$ or $Ciso_5H_{11}$ non-peripheral groups (compounds **10-23**), **(c)** eight $OSO_2C_3H_7$ or $OSO_2C_8H_{17}$ peripheral groups (compounds **24-27**), **(d)** four *t*Bu-peripherally peripherally substituted naphthalocyanines (compounds **28-30**), **(e)** six $OSO_2C_3H_7$ or $OSO_2C_8H_{17}$ peripheral groups and one peripheral I atom (compounds **31-33**), **(f)** three *t*Bu groups and one C≡CH (compounds **34-36**), **(g)** peripherally bridged dimers with three peripheral *t*Bu groups (compounds **36-40**) and **(h)** two direct M-M bonded dimers with four *t*Bu groups on each macrocycle at peripheral locations (compounds **41** and **42**).

represents those asymmetric compounds with six [$OSO_2C_3H_7$] or [$OSO_2C_8H_{17}$] groups and one I atom attached to the periphery (compounds **31-33**). Category (f) represents those compounds with three *t*Bu and one C≡CH groups attached to the periphery (compounds **34-36**) and category (g) represents the peripherally bridged phthalocyanine dimers where each monomer unit has three *t*Bu groups with the dimer

#	C	Structure	#	C	Structure
1	—	C_{60}	**22**	b	$(Ciso_5H_{11})_8PcCu$
2	a	tBu_4PcZn	**23**	b	$(Ciso_5H_{11})_8PcCo$
3	a	tBu_4 PcCo	**24**	c	$(C_3H_7OSO_2)_8PcNi$
4	a	$tBu_4PcGaCl$	**25**	c	$(C_3H_7$ $OSO_2)_8PcZn$
5	a	$tBu_4PcGa(p\text{-TMP})$	**26**	c	$(C_3H_7$ $OSO_2)_8PcCo$
6	a	$tBu_4PcInCl$	**27**	c	$(C_8H_{17}$ $OSO_2)_8PcCo$
7	a	$[tBu_4PcGa]_2O$	**28**	d	$tBu_4NcGaCl$
8	a	$[tBu_4PcIn]_2O$	**29**	d	$tBu_4NcGa(p\text{-TMP})$
9	a	$tBu_4PcIn\text{-}O\text{-}GaPctBu_4$	**30**	d	$[tBu_4NcGa]_2O$
10	b	$(C_6H_{13})_8PcPd$	**31**	e	$[(C_3H_7OSO_2)_6I]PcZn$
11	b	$(C_6H_{13})_8PcInCl$	**32**	e	$[(C_3H_7OSO_2)_6I]PcCo$
12	b	$(C_6H_{13})_8PcZn$	**33**	e	$[(C_8H_{17}OSO_2)_6I]PcCo$
13	b	$(C_6H_{13})_8PcPb$	**34**	f	$[(OC_4H_9)_6(C{\equiv}CH)]PcCo$
14	b	$(C_6H_{13})_8PcNi$	**35**	f	$[tBu_3(-C{\equiv}CH)]PcZn$
15	b	$(C_6H_{13})_8PcH_2$	**36**	f	$[tBu_3(-C{\equiv}CH)]PcCo$
16	b	$(C_{10}H_{21})_8PcCo$	**37**	g	$PcCo[tBu_3(-C{\equiv}C-C{\equiv}C-)tBu_3]PcCo$
17	b	$(C_{10}H_{21})_8PcH_2$	**38**	g	$PcCo[tBu_3(-C{\equiv}C-)tBu_3]PcZn$
18	b	$(C_{10}H_{21})_8PcNi$	**39**	g	$PcZn[tBu_3(-C{\equiv}C-)tBu_3]PcZn$
19	b	$(C_{10}H_{21})_8PcZn$	**40**	g	$PcZn[tBu_3(-C{\equiv}C-C{\equiv}C-)tBu_3]PcZn$
20	b	$(Ciso_5H_{11})_8PcZn$	**41**	h	$[tBu_4PcIn]_2.2tmed$
21	b	$(Ciso_5H_{11})_8PcH_2$	**42**	h	$[tBu_4PcGa]_2.2dioxane$

Table 4.3 The molecular formula for each phthalocyanine.

bridge at the fourth location (compounds 36-40). The final category, (h) represents a PcGa and a PcIn dimer bridged at the axial position with direct Ga-Ga or In-In bonds, (compounds 41 and 42).

The complete molecular formula for each of the phthalocyanines that was measured in this work is presented in Table 4.3. In each case, to avoid the longwinded notation that was described in Chapter 3, the locations of the peripheral

Notation	Molecular Structure
*t*Bu	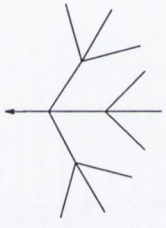
p-TMP	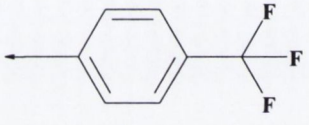
C_3H_7	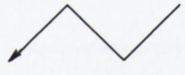
C_6H_{13}	
$C_{10}H_{21}$	
$Ciso_5H_{11}$	
$C_3H_7OSO_2$	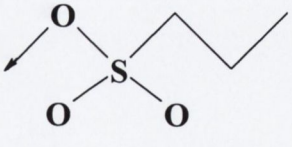
$C_8H_{17}OSO_2$	
OC_4H_9	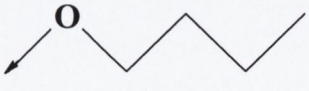

Table 4.4 Molecular structure for the poly-atomic ligands, in all cases the arrowhead marks the location where the ligand joins the Pc.

or non-peripheral ligands can be found by comparing the molecule with the sketch of the representative molecule from its category in Figure 4.8. Ligands that are composed of more than single atoms are detailed in Table 4.4. In the molecular sketches featured in this table the arrowhead in all cases marks the point where the ligand in question joins either the peripheral or non-peripheral bonding location or the central metal at the axial position.

4.4 Sample Preparation and Linear Optical Properties

All samples for optical experiments were prepared by dissolving the compound in a suitable common organic solvent (toluene or chloroform) at either 0.5 or 1 g L^{-1} followed by gentle agitation for ≈ 1 hour in a low-power (60 W) sonic bath to ensure complete and uniform dispersal. The solvents used and concentrations of all forty two compounds are detailed in Table 4.5. All measurements were performed in quartz cells with a 1 mm path length.

The linear absorption spectra, as was mentioned in Chapter 3, of phthalocyanine compounds have two main features: a Q-band in the region of 700 nm and a B-band in the region of 350 nm. These materials exhibit a transmission window between these two absorption bands with high linear transmittance making them attractive as limiters of visible light (window region ≈ 420-650 nm). Similarly, naphthalocyanines compounds have their B-band in the region of 350 nm but conversely they have their Q-bands shifted about 100 nm to red in the region of 800 nm. As a result, in contrast to phthalocyanines, naphthalocyanines are almost transparent in the red light region (≈ 600 to 670 nm) where phthalocyanines exhibit a considerable linear absorption coefficient due to their Q-bands. Sample UV-Visible spectra, collected using a standard spectrophotometer at room temperature, are shown in Figure 4.9a where as an example of a naphthalocyanine compound **29**, tBu$_4$NcGa(p-TMP), has been presented and as an example of a phthalocyanine compound **34,** [$(OC_4H_9)_6$(C≡CH)]PcCo, has been presented. In this figure the absorbance has been normalised to the λ_{max} absorbance value (the peak of the Q-band) for both compounds, this is the lowest energy peak.

In Figure 4.9b the linear optical features of the butadyinyl-bridged binuclear zinc phthalocyanine compound **40** are seen to differ from that of its corresponding

(a)

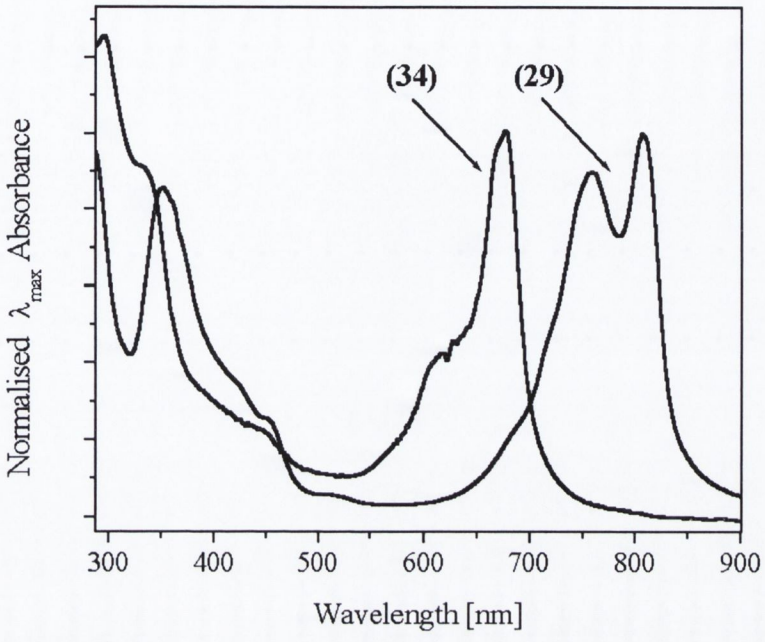

(b)

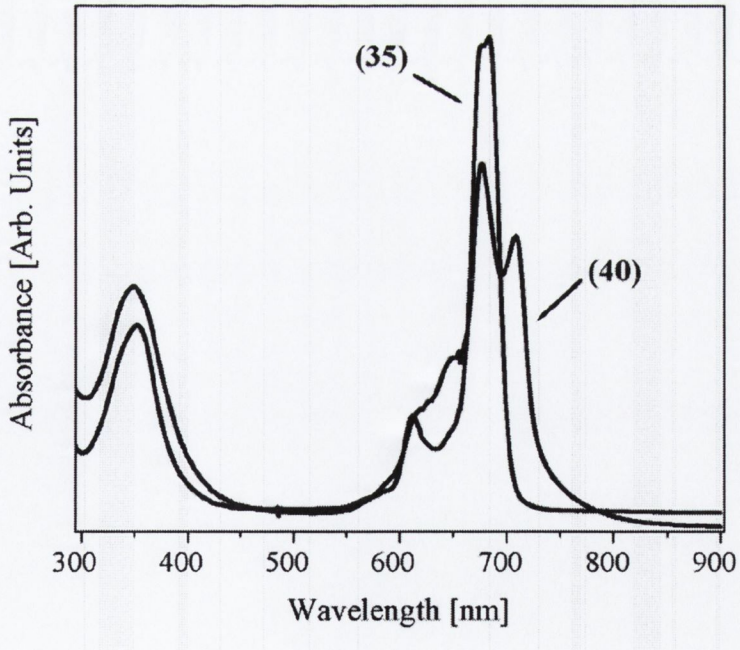

Figure 4.9 **(a)** UV-Visible spectra for compounds **29** [tBu$_4$NcGa(p-TMP)] in chloroform and **34** [$(OC_4H_9)_6(C{\equiv}CH)$]PcCo] in toluene where the absorbance has been normalised to the λ_{max} value. **(b)** UV-Visible spectra in toluene of compounds **35** [tBu$_3$($-C{\equiv}CH$)]PcZn and dimerised compound **40** PcZn[tBu$_3$($-C{\equiv}C-C{\equiv}C-$)tBu$_3$]PcZn.

unsymmetrically substituted parent **35**. In general, both the ethynyl-bridged (**39**) and the butadyinyl-bridged (**40**) binuclear phthalocyanines show broad Q bands that are red-shifted with regard to their mononuclear counterparts. This was also true for the cobalt phthalocyanines **36**, **37** and **38**. This shift to the red could be attributed to the enlargement of the π-conjugated system. The broadening and splitting of the Q band as a consequence of the splitting of the energetic levels must be due to electronic coupling between the two halves of the molecule more than to an intermolecular effect, since the spectra remain invariant when the concentration is changed. The λ_{max} vales for the entire series of compounds are given in Table 4.5.

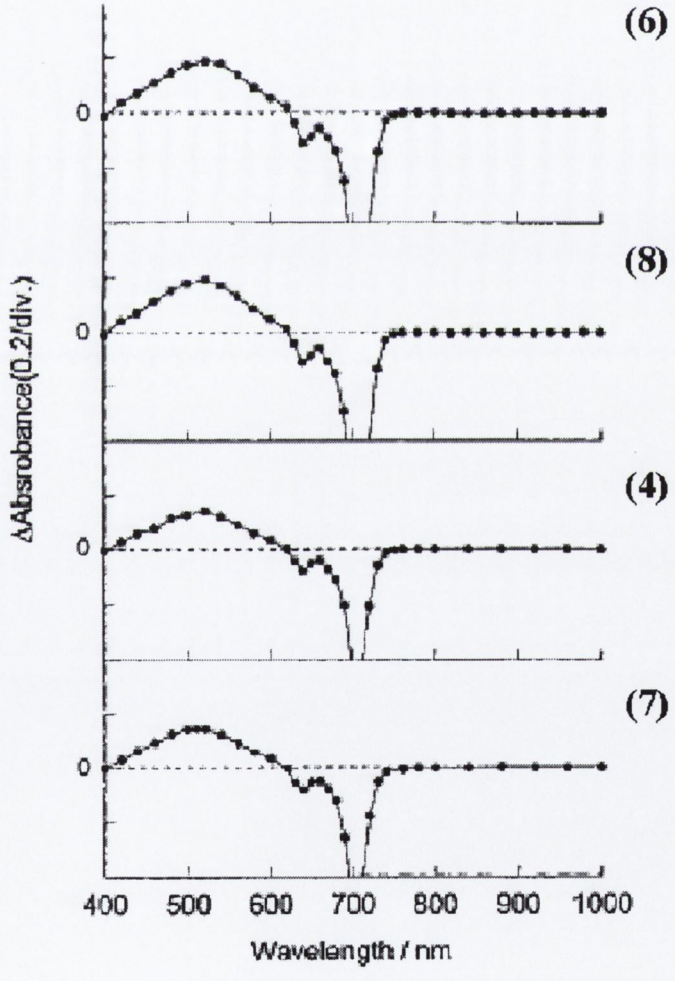

Figure 4.11 Transient absorption spectra of the chlorogallium and chloroindium monomers *t*Bu$_4$PcGaCl **4** and *t*Bu$_4$PcInCl **6**, and their oxo-bridged dimers [*t*Bu$_4$PcGa]$_2$O **7** and [*t*Bu$_4$PcIn]$_2$O **8** in toluene. The spectra were collected 250 ns after the excitation pulse. The excitation consisted of nanosecond irradiation at 355 nm.

Previously we have performed nanosecond laser flash-photolysis on the indium and gallium monomers as well as their oxo-bridged dimers, compounds **4**, **6**, **7** and **8**.[21] The samples were excited at 355 nm and similar transient absorption spectra for all compounds were observed, (see Figure 4.10). The transient absorption peaked in the region of 520 nm and was easily quenched in the presence of a triplet energy quencher such as oxygen. Consequently the transient absorption was assigned to transitions from the lowest triplet excited state to the upper triplet excited states. The gallium phthalocyanine compounds **4** and **7** had triplet state lifetimes of order hundreds of microseconds and the indium compounds **6** and **8** exhibited lifetimes approximately one order of magnitude less. It is worth noting that for all samples the triplet-state peak maximum was found between the Q and B bands in the UV-Visible spectra, implying that the cross section of the excited-state was at a maximum at approximately 520 nm, thus implying that 532 nm irradiation was a near resonant excitation of these phthalocyanine systems.

#	C	Structure	c g L^{-1}	α_0 cm^{-1}	λ_{max} nm	I_0 GWcm^{-2}	β_I cm W^{-1}	Im{$\chi^{(3)}_{eff}$} esu	Im{γ_{eff}} esu	F_{Sat} J cm^{-2}	κ σ_{ex}/σ_0
1		C_{60}	1.8 (T)	2.81	n/a	0.5	$(6.6 \pm 0.9)\times10^{-8}$	$(2.1 \pm 0.4)\times10^{-11}$	$(3.5 \pm 0.7)\times10^{-33}$	5.0 ± 0.5	5.2 ± 0.6
2	a	*t*Bu_4PcZn	0.5 (T)	1.13	678	0.3	$(2.9 \pm 0.5)\times10^{-8}$	$(1.1 \pm 0.2)\times10^{-11}$	$(7.3 \pm 1.4)\times10^{-33}$	8.8 ± 0.5	11.3 ± 0.5
3	a	*t*Bu_4 PcCo	0.5 (T)	1.28	669	0.5	$(9.3 \pm 1.6)\times10^{-10}$	$(3.5 \pm 0.7)\times10^{-13}$	$(2.3 \pm 0.4)\times10^{-34}$	45.0 ± 5.0	6.5 ± 0.4
4	a	*t*Bu_4PcGaCl	0.5 (T)	1.10	695	0.5	$(3.2 \pm 0.6)\times10^{-8}$	$(1.2 \pm 0.2)\times10^{-11}$	$(8.4 \pm 1.6)\times10^{-33}$	27.0 ± 1.0	13.5 ± 0.4
5	a	*t*Bu_4PcGa(*p*-TMP)	0.5 (T)	0.91	696	0.5	$(2.9 \pm 0.5)\times10^{-8}$	$(1.1 \pm 0.2)\times10^{-11}$	$(8.7 \pm 1.7)\times10^{-33}$	8.4 ± 0.4	13.6 ± 0.4
6	a	*t*Bu_4PcInCl	0.5 (T)	0.53	697	0.5	$(4.4 \pm 0.9)\times10^{-8}$	$(1.6 \pm 0.3)\times10^{-11}$	$(1.3 \pm 0.2)\times10^{-32}$	24.2 ± 0.8	27.4 ± 0.6
7	a	[*t*Bu_4PcGa]$_2$O	0.5 (T)	1.60	693	0.5	$(3.5 \pm 0.7)\times10^{-8}$	$(1.3 \pm 0.2)\times10^{-11}$	$(1.8 \pm 0.3)\times10^{-32}$	13.5 ± 1.0	11.3 ± 0.1
8	a	[*t*Bu_4PcIn]$_2$O	0.5 (T)	1.13	696	0.5	$(4.6 \pm 0.9)\times10^{-8}$	$(1.7 \pm 0.3)\times10^{-11}$	$(2.4 \pm 0.4)\times10^{-32}$	7.6 ± 0.3	12.4 ± 0.3
9	a	*t*Bu_4PcIn-O-GaPc*t*Bu_4	0.5 (T)	1.02	697	0.5	$(2.9 \pm 0.5)\times10^{-8}$	$(1.1 \pm 0.2)\times10^{-11}$	$(1.5 \pm 0.3)\times10^{-32}$	14.6 ± 0.6	10.0 ± 0.2
10	b	$(C_6H_{13})_8$PcPd	1.0 (T)	2.60	687	0.5	$(9.6 \pm 1.9)\times10^{-8}$	$(3.6 \pm 0.7)\times10^{-11}$	$(2.1 \pm 0.4)\times10^{-32}$	2.1 ± 0.1	5.9 ± 0.1
11	b	$(C_6H_{13})_8$PcInCl	1.0 (T)	0.93	730	0.5	$(3.2 \pm 0.6)\times10^{-8}$	$(1.2 \pm 0.2)\times10^{-11}$	$(7.3 \pm 1.4)\times10^{-33}$	10.1 ± 0.5	16.1 ± 0.3
12	b	$(C_6H_{13})_8$PcZn	1.0 (T)	1.17	705	0.5	$(4.0 \pm 0.8)\times10^{-8}$	$(1.5 \pm 0.3)\times10^{-11}$	$(8.6 \pm 1.7)\times10^{-33}$	7.1 ± 0.3	11.4 ± 0.3
13	b	$(C_6H_{13})_8$PcPb	1.0 (T)	0.83	741	0.5	$(2.9 \pm 0.6)\times10^{-8}$	$(1.1 \pm 0.2)\times10^{-11}$	$(7.0 \pm 1.4)\times10^{-33}$	9.8 ± 0.3	16.1 ± 0.3
14	b	$(C_6H_{13})_8$PcNi	1.0 (T)	1.05	702	0.5	$(1.6 \pm 0.3)\times10^{-9}$	$(5.9 \pm 1.1)\times10^{-13}$	$(3.4 \pm 0.6)\times10^{-34}$	18 ± 3	2.4 ± 0.2
15	b	$(C_6H_{13})_8$PcH$_2$	1.0 (T)	0.94	733	0.5	$(1.8 \pm 0.3)\times10^{-8}$	$(6.6 \pm 1.3)\times10^{-12}$	$(3.6 \pm 0.7)\times10^{-33}$	16.8 ± 0.6	14.5 ± 0.3
16	b	$(C_{10}H_{21})_8$PcCo	1.0 (T)	0.83	700	4.5	$(1.6 \pm 0.3)\times10^{-10}$	$(5.9 \pm 1.1)\times10^{-14}$	$(4.5 \pm 0.9)\times10^{-35}$	95 ± 70	2.2 ± 0.7
17	b	$(C_{10}H_{21})_8$PcH$_2$	1.0 (T)	0.83	730	0.5	$(1.5 \pm 0.3)\times10^{-8}$	$(5.8 \pm 1.1)\times10^{-12}$	$(4.3 \pm 0.8)\times10^{-33}$	20.2 ± 1.0	14.4 ± 0.5
18	b	$(C_{10}H_{21})_8$PcNi	1.0 (T)	0.94	702	0.5	$(1.5 \pm 0.3)\times10^{-9}$	$(5.5 \pm 1.1)\times10^{-13}$	$(4.2 \pm 0.8)\times10^{-34}$	13.3 ± 2.0	2.1 ± 0.1

#	C	Structure	c g L^{-1}	α_0 cm^{-1}	λ_{max} nm	I_0 GWcm^{-2}	β_1 cm W^{-1}	Im{$\chi^{(3)}_{eff}$} esu	Im{γ_{eff}} esu	F_{Sat} J cm^{-2}	κ σ_{ex}/σ_0
19	b	$(C_{10}H_{21})_8$PcZn	1.0 (T)	1.17	705	0.5	$(2.4 \pm 0.4)\times10^{-8}$	$(9.1 \pm 1.8)\times10^{-12}$	$(6.9 \pm 1.3)\times10^{-33}$	13.6 ± 0.5	11.7 ± 0.3
20	b	$(Ciso_5H_{11})_8$PcZn	1.0 (T)	1.05	703	0.5	$(4.0 \pm 0.8)\times10^{-8}$	$(1.5 \pm 0.3)\times10^{-11}$	$(7.9 \pm 1.5)\times10^{-33}$	6.6 ± 0.2	12.2 ± 0.3
21	b	$(Ciso_5H_{11})_8PcH_2$	1.0 (T)	0.94	731	0.5	$(1.6 \pm 0.3)\times10^{-8}$	$(5.9 \pm 1.1)\times10^{-12}$	$(3.0 \pm 0.6)\times10^{-33}$	14.4 ± 0.5	11.3 ± 0.3
22	b	$(Ciso_5H_{11})_8$PcCu	1.0 (T)	1.63	705	0.5	$(6.4 \pm 1.0)\times10^{-8}$	$(2.4 \pm 0.4)\times10^{-11}$	$(1.3 \pm 0.2)\times10^{-32}$	4.6 ± 0.1	8.8 ± 0.1
23	b	$(Ciso_5H_{11})_8$PcCo	1.0 (T)	2.74	696	3.2	$(8.5 \pm 1.7)\times10^{-10}$	$(3.2 \pm 0.6)\times10^{-13}$	$(1.7 \pm 0.3)\times10^{-34}$	170 ± 190	3.4 ± 2.0
24	c	$(C_3H_7OSO_2)_8$PcNi	1.0 (T)	1.39	675	1.0	$(7.4 \pm 1.4)\times10^{-9}$	$(2.8 \pm 0.5)\times10^{-12}$	$(1.6 \pm 0.3)\times10^{-33}$	16.5 ± 0.8	8.7 ± 0.2
25	c	$(C_3H_7\ OSO_2)_8$PcZn	1.0 (T)	2.11	685	0.5	$(1.4 \pm 0.3)\times10^{-8}$	$(5.4 \pm 1.0)\times10^{-12}$	$(3.2 \pm 0.6)\times10^{-33}$	17.6 ± 0.7	5.4 ± 0.1
26	c	$(C_3H_7\ OSO_2)_8$PcCo	1.0 (C)	1.86	676	1.0	$(1.3 \pm 0.3)\times10^{-8}$	$(4.5 \pm 0.9)\times10^{-12}$	$(3.0 \pm 0.6)\times10^{-33}$	27.0 ± 1.0	8.1 ± 0.2
27	c	$(C_8H_{17}\ OSO_2)_8$PcCo	1.0 (T)	2.20	676	3.4	$(7.3 \pm 1.4)\times10^{-11}$	$(2.8 \pm 0.5)\times10^{-14}$	$(2.3 \pm 0.4)\times10^{-35}$	40.0 ± 70	1.1 ± 0.2
28	d	tBu$_4$NcGaCl	1.0 (C)	4.40	807	0.5	$(5.8 \pm 1.1)\times10^{-8}$	$(2.2 \pm 0.4)\times10^{-11}$	$(9.6 \pm 1.9)\times10^{-33}$	5.6 ± 0.2	4.8 ± 0.2
29	d	tBu$_4$NcGa (p-TMP)	1.0 (C)	2.30	807	0.3	$(2.6 \pm 0.5)\times10^{-8}$	$(9.7 \pm 1.9)\times10^{-12}$	$(4.7 \pm 0.9)\times10^{-33}$	8.5 ± 0.9	9.2 ± 0.8
30	d	[tBu$_4$NcGa]$_2$O	1.0 (C)	5.00	807	0.5	$(4.8 \pm 0.9)\times10^{-8}$	$(1.8 \pm 0.3)\times10^{-11}$	$(1.5 \pm 0.3)\times10^{-32}$	3.9 ± 0.2	4.1 ± 0.1
31	e	$[(C_3H_7OSO_2)_6I]$PcZn	1.0 (T)	1.28	704	0.5	$(1.5 \pm 0.3)\times10^{-8}$	$(5.7 \pm 1.1)\times10^{-12}$	$(3.2 \pm 0.6)\times10^{-33}$	18.1 ± 0.6	13.4 ± 0.3
32	e	$[(C_3H_7OSO_2)_6I]$PcCo	1.0 (T)	1.17	694	2.0	$(5.8 \pm 1.1)\times10^{-10}$	$(2.2 \pm 0.4)\times10^{-13}$	$(1.2 \pm 0.2)\times10^{-34}$	35 ± 19	2.0 ± 0.4
33	e	$[(C_8H_{17}OSO_2)_6I]$PcCo	1.0 (T)	2.21	694	1.0	$(2.3 \pm 0.4)\times10^{-10}$	$(8.5 \pm 1.7)\times10^{-14}$	$(6.2 \pm 1.2)\times10^{-35}$	160 ± 100	1.7 ± 1.2
34	f	$[(OC_4H_9)_6(C\equiv CH)]$PcCo	0.5 (T)	1.80	677	1.0	$(7.2 \pm 1.4)\times10^{-9}$	$(2.7 \pm 0.5)\times10^{-12}$	$(2.3 \pm 0.4)\times10^{-33}$	32 ± 3	4.9 ± 0.3
35	f	[tBu$_3$(−C≡CH)]PcZn	0.5 (T)	1.95	684	0.5	$(3.5 \pm 0.7)\times10^{-8}$	$(1.3 \pm 0.2)\times10^{-11}$	$(8.3 \pm 1.6)\times10^{-33}$	13.9 ± 0.7	8.9 ± 0.3
36	f	[tBu$_3$(−C≡CH)]PcCo	0.5 (T)	1.76	673	2.0	$(1.4 \pm 0.3)\times10^{-9}$	$(5.1 \pm 1.0)\times10^{-13}$	$(3.2 \pm 0.6)\times10^{-34}$	76 ± 30	3.3 ± 0.8

#	C	Structure	c $g\ L^{-1}$	α_0 cm^{-1}	λ_{max} nm	I_0 $GWcm^{-2}$	β_I $cm\ W^{-1}$	$Im\{\chi^{(3)}_{eff}\}$ esu	$Im\{\gamma_{eff}\}$ esu	F_{Sat} $J\ cm^{-2}$	κ σ_{ex}/σ_0
37	g	PcCo[tBu$_3$(-C≡C−C≡C-)tBu$_3$]PcCo	0.5 (T)	1.60	691	0.5	$(3.5 \pm 0.7)\times10^{-8}$	$(1.3 \pm 0.2)\times10^{-11}$	$(1.7 \pm 0.3)\times10^{-32}$	9.5 ± 0.2	11.0 ± 0.1
38	g	PcCo[tBu$_3$(−C≡C−)tBu$_3$]PcZn	0.5 (T)	1.22	677	0.5	$(5.6 \pm 1.1)\times10^{-9}$	$(2.1 \pm 0.4)\times10^{-12}$	$(2.6 \pm 0.5)\times10^{-33}$	1.3 ± 0.1	1.8 ± 0.1
39	g	PcZn[tBu$_3$(−C≡C−)tBu$_3$]PcZn	0.5 (T)	1.06	678	0.2	$(1.2 \pm 0.2)\times10^{-8}$	$(4.6 \pm 0.8)\times10^{-12}$	$(5.8 \pm 1.1)\times10^{-33}$	1.9 ± 0.1	3.0 ± 0.1
40	g	PcZn[tBu$_3$(-C≡C−C≡C-)tBu$_3$]PcZn	0.5 (T)	1.19	709	0.5	$(2.3 \pm 0.5)\times10^{-8}$	$(8.7 \pm 1.6)\times10^{-12}$	$(1.1 \pm 0.2)\times10^{-32}$	3.9 ± 0.3	5.4 ± 0.2
41	h	[tBu$_4$PcIn]$_2$.2tmed	0.5 (T)	0.93	694	0.5	$(2.4 \pm 0.4)\times10^{-8}$	$(9.3 \pm 1.6)\times10^{-12}$	$(1.3 \pm 0.3)\times10^{-32}$	10.0 ± 0.5	12.5 ± 0.4
42	h	[tBu$_4$PcGa]$_2$.2dioxane	0.5 (T)	1.30	693	0.5	$(3.5 \pm 0.7)\times10^{-8}$	$(1.3 \pm 0.3)\times10^{-11}$	$(1.8 \pm 0.4)\times10^{-32}$	8.9 ± 0.4	10.4 ± 0.3

Table 4.5 The molecular formula for each of the compounds (1-42) used in this study, including the category (a)-(h) into which each phthalocyanine falls, linear optical properties, calculated nonlinear optical coefficients and optical limiting parameters. In the concentration section T implies toluene and C implies chloroform. The $Im\{\chi^{(3)}_{eff}\}$ and $Im\{\gamma_{eff}\}$ are quoted in esu units from the gaussian formalism, and conversion between this and the SI formalism is detailed in Appendix I.

4.5 Results and Discussion of Nonlinear Absorption Experiments

4.5.1 Comments on Open Aperture Z-scan Studies

The open aperture z-scans performed in this study in all cases exhibited a reduction in the transmission about the focus of the lens. This was typical of an induced positive nonlinear absorption of the incident light, in this case assumed to be due to reverse saturable excited state absorption. All open aperture z-scan datasets were fitted using the method of least squares regression with Equation (3.33). The beam waist radius w_0 and the nonlinear absorption coefficient β_I were treated as free

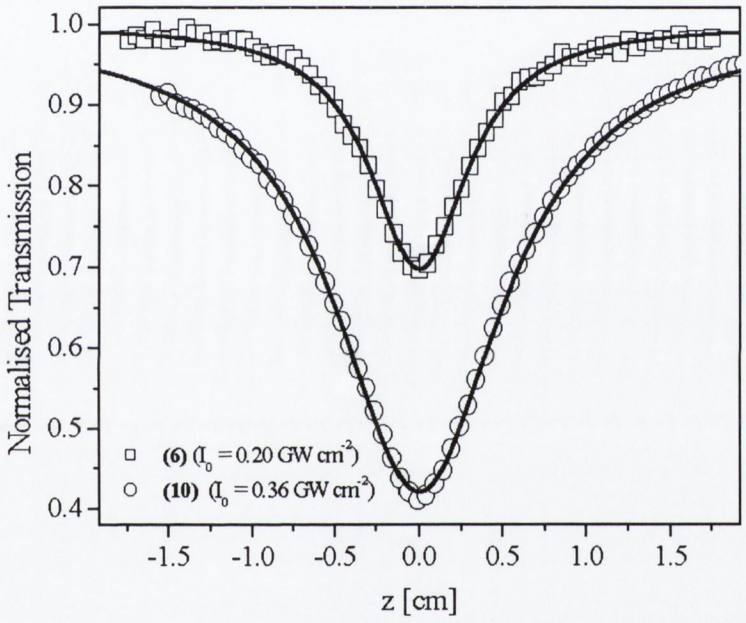

Figure 4.12 Typical open aperture z-scan spectra with normalised transmission plotted as a function of sample position z. Sample curves for compounds **6** [tBu$_4$PcInCl] and **10** [(C$_6$H$_{13}$)$_8$PcPd] are depicted for incident intensities of 0.2 GW cm^{-2} and 0.36 GW cm^{-2} respectively.

parameters in the fit, and all fits converged typically with R^2 values in excess of 0.99. The waist radius w_0 was found to be stable as a function of I_0 deviating in successive scans by no more than ±10%. A sample of typical open aperture z-scan spectra with normalized transmission plotted as a function of sample position z are depicted in Figure 4.12 for compounds **6** [tBu$_4$PcInCl] and **10** [(C$_6$H$_{13}$)$_8$PcPd] under incident intensities of 0.2 GW cm^{-2} and 0.36 GW cm^{-2} respectively.

It was noticed, however, that the nonlinear absorption coefficient β_I in all cases was not stationary with respect to the on focus intensity. In Figure 4.13

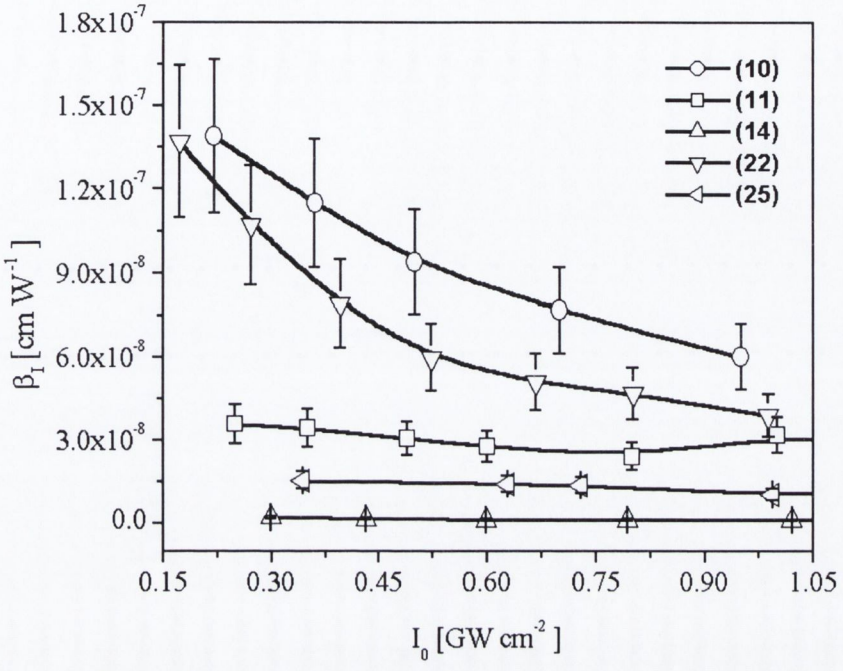

Figure 4.13 Plot of effective nonlinear absorption coefficient β_I against the on focus beam intensity I_0 for compounds **10** [$(C_6H_{13})_8PcPd$], **11** [$(C_6H_{13})_8PcInCl$], **14** [$(C_6H_{13})_8PcNi$], **22** [$(Ciso_5H_{11})_8PcCu$] and **25** [$(OSO_2C_3H_7)_8PcZn$]. Each data point represents an independent open aperture z-scan and the solid lines are intended as guides to the eye.

sample plots of the effective nonlinear absorption coefficient β_I against the on focus beam intensity I_0 are presented. These results are for compounds **10** [$(C_6H_{13})_8PcPd$], **11** [$(C_6H_{13})_8PcInCl$], **14** [$(C_6H_{13})_8PcNi$], **22** [$(Ciso_5H_{11})_8PcCu$] and **25** [$(OSO_2C_3H_7)_8PcZn$]. Each data point on the plot represents an independent open aperture z-scan of the compound in question and the solid lines are sketched merely as guides to the eye. It can clearly be seen that the nonlinear absorption coefficient β_I reduces in magnitude with increasing focal intensity I_0 in the figure. If the nonlinear absorption under investigation was operating in an unsaturated regime at very low intensities where $I << I_{Sat}$ Equation (4.13) can be modified by expanding the $(1 + I/I_{Sat})^{-1}$ terms in the denominator using a binomial expansion. This, assuming that all terms of orders I^2 and higher are negligible, yields the intensity dependent absorption coefficient as:

$$\alpha\left(I, I_{Sat}, \kappa\right) \approx \alpha_0\left(1+(\kappa-1) I/I_{Sat}\right) \tag{4.31}$$

which is simply the equation of a straight line of slope (κ - 1). However for a reverse saturable absorber, defined by exhibiting $\kappa > 1$ excited to ground state absorption

cross section ratios, it can be clearly seen that in this unsaturated regime where $I << I_{Sat}$ one would expect the nonlinear absorption coefficient to increase as a function of I_0. This is in contrast to β_I as a function of I_0, which was measured here and, so these materials are not behaving as effective third order nonlinear absorbers. The reduction in the nonlinear absorption coefficient could be due to some sort of saturation of the accessible energy levels under high intensity pumping. Despite this, effective third order nonlinear absorption coefficients β_I were estimated by suitably interpolating data similar to that in Figure 4.13 for all forty two compounds at on focus intensities of 0.5 GW cm^{-2} (arbitrarily chosen) where possible. This β_I value for each compound interpolated for irradiation of 0.5 GW cm^{-2} is presented in Table 4.5. Subsequently using Equation (3.24) the effective third order susceptibilities $Im\{\chi^{(3)}_{eff}\}$ and the effective molecular second hyperpolarisabilities $Im\{\gamma_{eff}\}$ were calculated for this sample I_0 value using Equation (4.32), where the experimentally interpolated β_I was inserted into the equation. All calculated coefficients are presented in Table 4.5.

$$\mathrm{Im}\left\{\gamma_{eff}\right\} = \frac{\mathrm{Im}\left\{\chi^{(3)}_{eff}\right\}}{f^4 c_m N_A} \tag{4.32}$$

In this expression $f = (n_0^2+2)/3$ and is termed the Lorentz local field enhancement factor, n_0 is the linear refractive index of the sample, c_{mol} is the molar concentration and N_A is Avogadro's number.

The open aperture spectra were manipulated, and the normalised transmission (T_{Norm}) was plotted against the incident energy density per pulse (F), to further investigate the optical limiting. The nonlinear transmission governed by Equation (4.30) was used to fit the normalised transmission as a function of this energy density to a superposition of all open aperture datasets for each compound. The parameters κ (realistically σ_{ex} as α_0 was measured) and F_{Sat} were treated as free constants in the fitting algorithm. The α_0, κ and F_{Sat} values for each compound are also presented in Table 4.5.

It can be seen that the effective third order nonlinear absorption coefficient β_I ranges from values of order 10^{-10} to 10^{-8} cm W^{-1}, which corresponds to effective second order molecular hyperpolarisabilities ranging from orders of 10^{-34} to 10^{-32} esu. The ratio of the excited to ground state absorption cross sections for C_{60} was

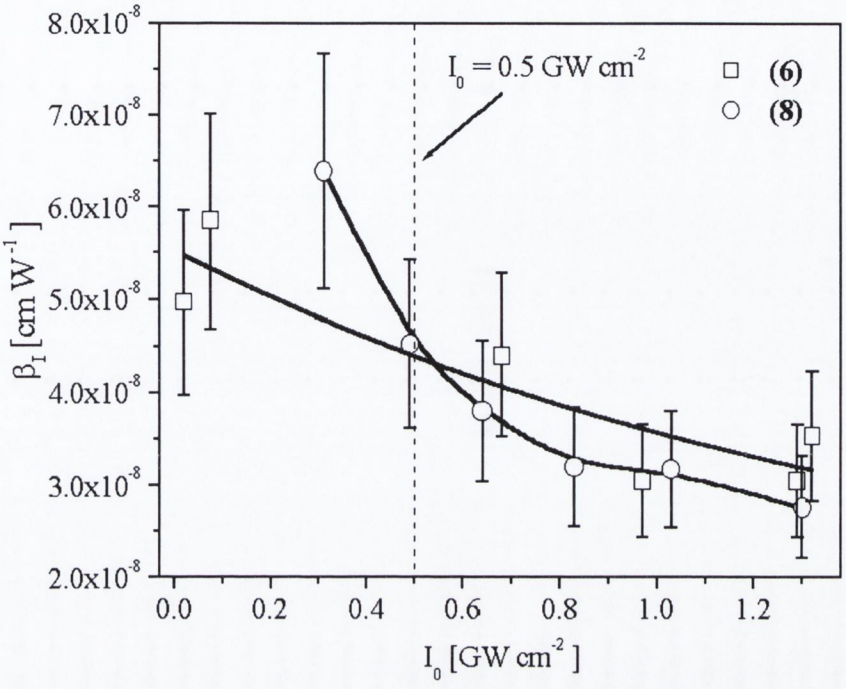

Figure 4.14 Plot of effective nonlinear absorption coefficient β_I against the on focus beam intensity I_0 for compounds **6** [tBu$_4$PcInCl] and **8** [[tBu$_4$PcIn]$_2$O]. Each data point represents an independent open aperture z-scan and the solid lines are intended as guides to the eye.

calculated as $\kappa \approx (5.2 \pm 0.6)$. This is acceptable given that the S_1 to T_1 transition is of order 1.2 ns[33] and thus the static case model applied here does not approach the dynamic solution for this compound. The pumped excited states accessed here probably have both excited singlet and triplet state contributions as described in the modelling section of this chapter.

4.5.2 Case Study I: The Chloroindium Phthalocyanine

The chloroindium phthalocyanine (**6**) is worth discussing as it is probably the best understood nonlinearly active phthalocyanine that has been produced to date having been extensively studied by both Perry *et al.*[14] and Shirk *et al.*[12]. Perry *et al.* reported the absorption cross section ratio κ as being (30 ± 6) while Shirk *et al.* found it to be equal to 33 (uncertainty not quoted). In this study κ for **6** was found to be $\approx (27.4 \pm 0.6)$, in conservative agreement with the previous findings. β_I values for **6** and its associated axially μ-oxo bridged dimer **8,** [tBu$_4$PcIn]$_2$O, are plotted as a

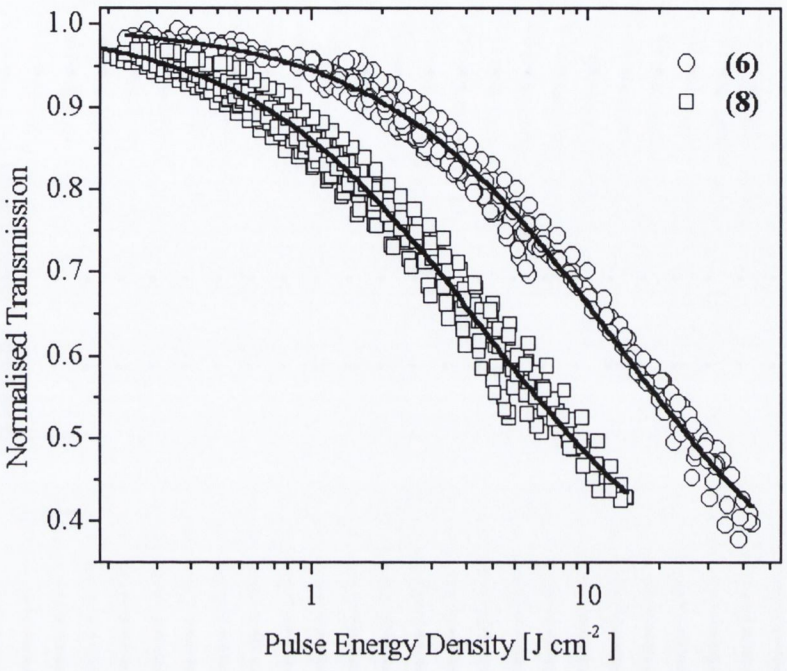

Figure 4.15 Plots of normalised transmission against incident pulse energy density for compounds **6** [*t*Bu$_4$PcInCl] and **8** [[*t*Bu$_4$PcIn]$_2$O]. The solid lines are the theoretical curve fits.

function of I_0 in Figure 4.14. They were measured under identical conditions and interpolated and found to be approximately equal at (4.4 ± 0.9) cm W^{-1} and (4.6 ± 0.9) cm W^{-1} for the monomer and dimer respectively under 0.5 GW cm^{-2} laser irradiation. This shows that dimerisation of the monomer unit does not significantly increase the magnitude of the nonlinear response at this intensity. The trends in the nonlinear absorption coefficients in Figure 4.14 show that the β_I value for the dimer is larger than the β_I value for the monomer at intensities less than 0.55 GW cm^{-2} and lower at higher intensities. The corresponding effective imaginary second order molecular hyperpolarisabilities $Im\{\gamma_{eff}\}$ at 0.5 GW cm^{-2} differ principally due only to the differences in their molecular weights.

The optical limiting plotted as the normalised transmission against incident pulse energy density for compounds **6** and **8** are presented in Figure 4.15. The significant differences in the response of these compounds are in their α_0, F_{Sat}, and κ values. The chloroindium phthalocyanine monomer (**6**) exhibited the largest κ value in the entire study at $\kappa \approx (27.4 \pm 0.6)$, despite its nonlinear absorption coefficient not being the largest in the study. The κ coefficient for the dimer is less than 50% of the

value for the monomer unit. It is worth mentioning that its linear absorption coefficient α_0 is just over double that for the monomer unit though, which explains the much lower κ value despite the approximate equivalence of the magnitude of the nonlinear response indicated by the measurements of the nonlinear absorption coefficients. The other glaring difference apparent from Figure 4.15 in the nonlinear response of the In monomer and axially bridged dimer is the saturation energy density F_{Sat}. The dimer saturates at (7.6 ± 0.3) J cm^{-2} while the monomer exhibits its saturation at an energy density ≈ 3.2 times greater. This implies that although the magnitude of the nonlinear response is equivalent the dimer extinguishes laser pulses of much lower energies more efficiently than the monomer unit does.

The other indium monomeric phthalocyanine (**11**) used in this study has eight C_6H_{13} groups attached to the periphery of the macrocycle. The addition of these groups reduced the saturation energy density F_{Sat} by a factor of about 2.1 and the κ value by a factor of about 1.7 relative to **6**. However, as these compounds (**6** and **11**) were measured at different concentrations it may be more sensible to compare them in terms of their effective second order molecular hyperpolarisabilities $Im\{\gamma_{eff}\}$. Compound **11** has a lower $Im\{\gamma_{eff}\}$ value than compound **6** by a factor of approximately 1.8, similar to the differences in their κ coefficients.

4.5.3 Case Study II: The Chlorogallium Naphthalocyanines

The effects of extending the conjugated plane of the phthalocyanine macrocycle are investigated in Figure 4.16. Differences in the optical response of the gallium phthalocyanines **4**, **5** and **7** relative to their naphthalocyanine counterparts **28-30** are studied. The F_{Sat} values of **28** and **30** follow the same trend as their phthalocyanine analogues **4** and **7**, with the dimer having a lower value than that of the monomer for both species of compound. In the case of gallium naphthalocyanines **28-30**, the difference between the F_{Sat} values is considerably reduced compared to the gallium phthalocyanine case. Considerinng the magnitude of F_{Sat} for the gallium phthalocyanine case, compounds **4** and **7** have F_{Sat} values ≈ (27 ± 1.0) J cm^{-2} and (13.5 ± 1.0) J cm^{-2}, respectively, while the corresponding naphthalocyanine analogues exhibit F_{Sat} in the region of (5.6 ± 0.2) J cm^{-2} and (3.9 ± 0.2) J cm^{-2} respectively. However, these compounds were measured at different concentrations

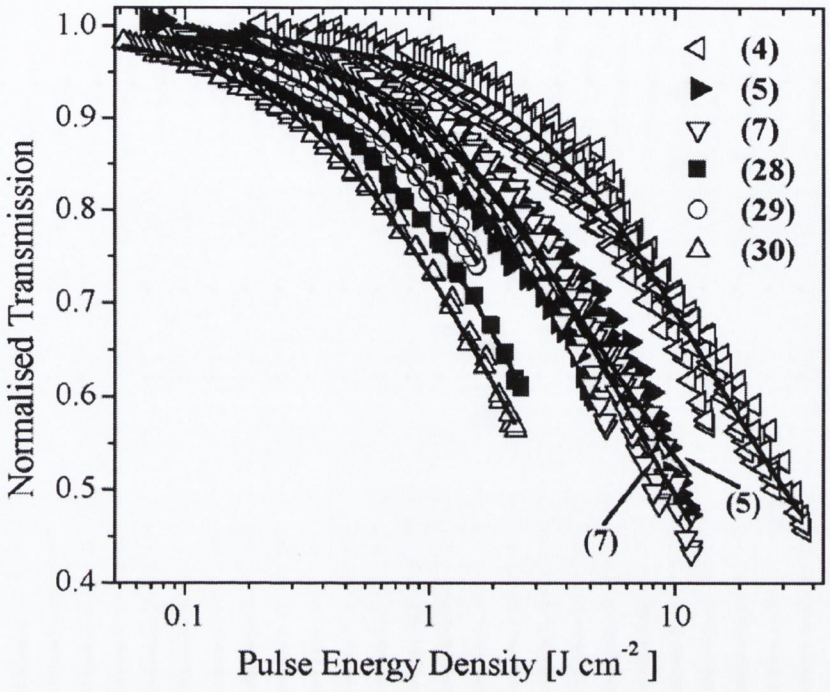

Figure 4.16 Plots of normalised transmission against incident pulse energy density for gallium phthalocyanine compounds: **4** [*t*Bu$_4$PcGaCl], **5** [*t*Bu$_4$PcGa(*p*-TMP)], **7** [[*t*Bu$_4$PcGa]$_2$O)] and gallium naphthalocyanines : **28** [*t*Bu$_4$NcGaCl], **29** [*t*Bu$_4$NcGa(*p*-TMP)], **30** [[*t*Bu$_4$NcGa]$_2$O]. The solid lines are the theoretical curve fits.

in different solvents so the comparison of magnitudes is perhaps not an entirely infallible approach. This may require more study and analysis.

In contrast to the gallium phthalocyanine case **5**, the saturation density F_{Sat} for the axially *p*-TMP substituted gallium naphthalocyanine **29** does not follow the same trend. The saturation density of **29** is larger than that of both compounds **28** and **30**, while in the case of the gallium phthalocyanines the saturation density of **5** is smaller than that of **4** and **7**. The ratio of the absorption cross-sections κ for compounds **28** and **30** also follow the same trend as their phthalocyanine analogues, with the monomer being larger than the dimer. Compound **29** and its phthalocyanine analogue **5** (both *p*-TMP axially substituted) exhibit a different trend in their response again, with the naphthalocyanines κ value being larger than the κ value of other naphthalocyanine compounds by a factor of ≈ 2. This is in contrast to the *p*-TMP axially substituted gallium phthalocyanine compound **5**, where its κ value was smaller than the unsubstituted monomer and axially bridged dimer. It is clear from Figure 4.16 that the magnitude of the nonlinear absorption is not hugely different for

the three different compounds **28-30**. The differences in the magnitude of the absorption cross-section ratios κ for these compounds are therefore dominated by the differences in their linear absorption coefficients α_0. This explains why compound **29** has a κ value larger than the other two compounds **28** and **30** by a factor of ≈ 2, despite exhibiting a weaker nonlinear response in terms of transmission as a function of pulse energy density, where maximum transmission attenuation for minimum incident energy density is considered desirable. Its linear absorption coefficient is significantly smaller than that for the other compounds, approximately by a factor of 2 giving it a significantly lower linear absorption cross section σ_0.

4.5.4 Case Study III: The C_6H_{13} Non-peripherally Substituted Phthalocyanines

The palladium phthalocyanine **10** [$(C_6H_{13})_8$PcPd] exhibited the largest β_I, $\beta_I \approx (9.6 \pm 1.9)\times10^{-8}$ cm W of the forty two compounds presented here and its optical limiting is plotted as normalised transmission against energy density in Figure 4.17. In this figure data from three other phthalocyanines with the same peripheral substituents at the same locations (category (b)) are included; they are compounds **13** [$(C_6H_{13})_8$PcPb], **14** [$(C_6H_{13})_8$PcNi] and **15** [$(C_6H_{13})_8PcH_2$]. In terms of the magnitude of the reduction in normalised transmission relative to the incident energy density the palladium compound clearly outperforms the others. It also has a much lower saturation energy density F_{Sat} than the other phthalocyanines on the plot. Interestingly, the ratio of the absorption cross sections κ is smallest for the nickel phthalocyanine **14**, largest for the lead phthalocyanine **13** and the κ coefficient for the palladium phthalocyanine is approximately 2.7 times smaller than that for the lead compound and approximately 2.5 times larger than that for the nickel compound. The κ coefficient of the palladium compound is smaller despite having a larger nonlinear absorption coefficient than compounds **13** and **15** because of its relatively large linear absorption coefficient $\alpha_0 \approx 2.6$ cm^{-1}. It is clear that substituting nickel into the central cavity has nothing but undesirable effects in terms of optical limiting as the unsubstituted phthalocyanine **15** clearly has a much larger nonlinear response than the nickel compound. They have comparable F_{Sat} values (18 ± 3) J cm^{-2} for nickel and (16.8 ± 0.6) J cm^{-2} for the unsubstituted case but the κ coefficient for the nickel compound is approximately 6 times smaller than that for

the unsubstituted phthalocyanine.

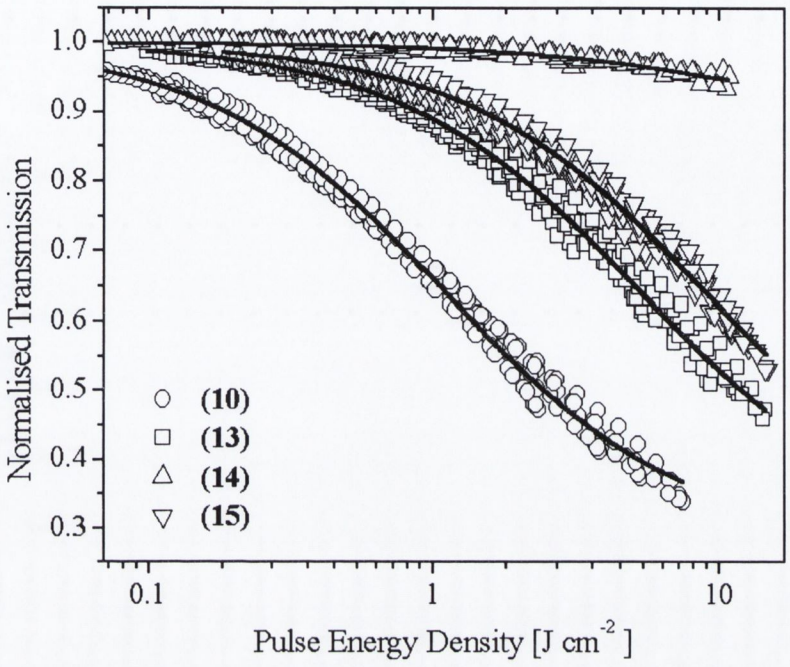

Figure 4.17 Plots of normalised transmission against incident pulse energy density for a series of phthalocyanine compounds from category (b). The compounds are **10** [$(C_6H_{13})_8$PcPd], **13** [$(C_6H_{13})_8$PcPb], **14** [$(C_6H_{13})_8$PcNi] and **15** [$(C_6H_{13})_8$PcH$_2$] and the solid lines are theoretical curve fits.

4.5.5 Case Study IV: Effects of Varied Non-peripheral Substituents

In order to assess the differences due to the addition of different peripheral groups to the macrocycle one can look at, for example, the zinc phthalocyanine monomers with varying macrocycle substituents. Compounds **12** [$(C_6H_{13})_8$PcZn], **19** [$(C_{10}H_{21})_8$PcZn], **20** [$(Ciso_5H_{11})_8$PcZn], **25** [$(OSO_2C_3H_7)_8$PcZn] and **31** [[$(OSO_2C_3H_7)_6$I]PcZn] were all measured at mass concentrations of 1 g L^{-1} in toluene and are a series that can be used for relative comparison. These compounds all exhibit nonlinear absorption of order 10^{-8} cm W^{-1} the largest exhibited equally by compounds **12** and **20** at $(4.0 \pm 0.8)\times10^{-8}$ cm W^{-1} though neither of these possess the largest κ coefficient. The lowest β_I was exhibited by compounds **25** and **31** at $(1.4 \pm 0.3)\times10^{-8}$ cm W^{-1} and $(1.5 \pm 0.3)\times10^{-8}$ cm W^{-1} respectively though compound **25** exhibits the smallest κ coefficient and compound **31** the largest, with compound **19** exhibiting a relative midrange values with $\beta_I \approx (2.4 \pm 0.4)\times10^{-8}$ cm W^{-1} and $\kappa \approx (11.7 \pm 0.3)$. The carbon chain side groups on the macrocycle then clearly appear to be

more beneficial, from the point of view of the magnitude of the nonlinear absorption, to the optical limiting than the other types of side groups. Compounds **25** and **31** also exhibit the highest saturation energy densities of the five compounds.

4.5.6 Case Study V: Peripherally Bridged Dimers

The compounds labelled **37** to **40** represent the peripherally bridged dimers of the mononuclear compounds **35** and **36** and all were measured at 0.5 g L^{-1} in toluene. These dimers are bridged with ethyne (−C≡C−) and butadiyne (−C≡C−C≡C−) linkages and are expected to be suitable for enabling electronic interactions between chromophores. Consequently, this series of ethynyl-substituted mononuclear Pcs and ethynyl- and butadiynyl-bridged binuclear phthalocyanines **35-40** is a useful case study to attempt to ascertain the effect of the electronic communication between phthalocyanine macrocycles and its manifestation on the nonlinear absorption properties. Compounds **35** and **36** are the initial mononuclear entities with molecular formulae [*t*Bu$_3$(−C≡CH)]PcZn and [*t*Bu$_3$(−C≡CH)]PcCo respectively. Compound **39** is an ethyne bridged zinc phthalocyanine binuclear molecule (PcZn[*t*Bu$_3$(−C≡C−)*t*Bu$_3$]PcZn) and compound **38** is an ethyne linked zinc to cobalt phthalocyanine (PcCo[*t*Bu$_3$(−C≡C−)*t*Bu$_3$]PcZn). The butadiynyl linked zinc (**40**) and cobalt (**37**) dimers have molecular formulae PcZn[*t*Bu$_3$(−C≡C−C≡C−)*t*Bu$_3$]PcZn and PcCo[*t*Bu$_3$(−C≡C−C≡C−)*t*Bu$_3$]PcCo respectively.

In Figure 4.18a the normalised transmission against incident pulse energy density is plotted for the mononuclear phthalocyanines **35** and **36**. The solid lines are the theoretical curve fits. The zinc centred phthalocyanine **35** is the strongest nonlinear absorber of the mononuclear compounds. It also exhibits the largest excited to singlet state absorption cross-section ratio κ and the lowest saturation energy density F_{Sat}. The optical limiting response of the ethynyl-bridged bisphthalocyanines **39** and **38** is presented in Figure 4.18b. The zinc dimer **39** exhibits a larger optical limiting response than that of the cobalt-zinc compound **38**. The κ coefficient exhibited by **4** is the lowest in the study at $\kappa \approx 1.8 \pm 0.1$ and it also exhibits the lowest saturation energy density at $F_{Sat} \approx (1.3 \pm 0.1)$ J cm^{-2}. Compound

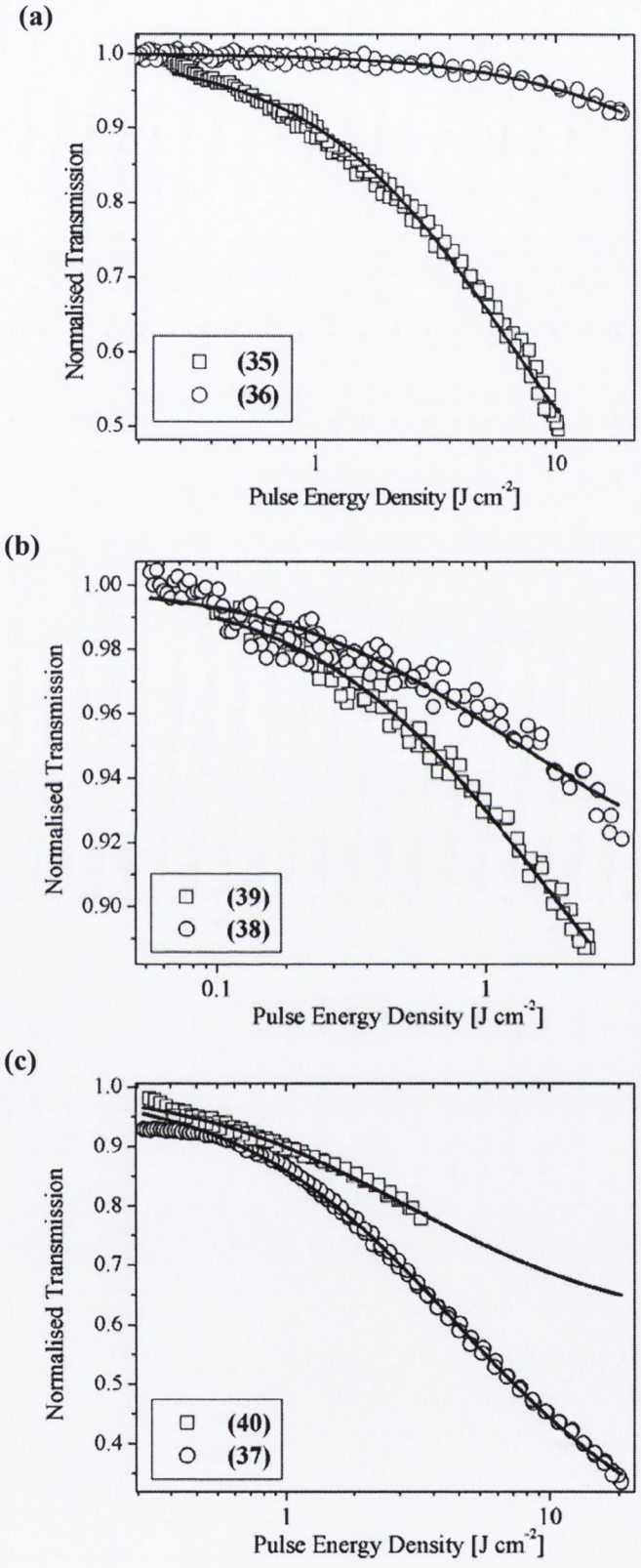

Figure 4.18 Plots of normalised transmission against incident pulse energy density for **(a)** mononuclear phthalocyanines **35** and **36**, **(b)** ethynyl-bridged bisphthalocyanines **39** and **38** and **(c)** butadiynyl-bridged bisphthalocyanines **40** and **37**. The solid lines are theoretical curve fits

39 saturated at 1.9 J cm^{-2} and exhibited a κ coefficient approximately 1.8 times that of **38** ($\kappa \approx 3.0 \pm 0.1$). Plots of normalised transmission against incident pulse energy density for the butadiynyl-bridged bisphthalocyanines compounds **40** and **37** are presented in Figure 4.18c where again the solid lines are the theoretical curve fits. In this case the cobalt dimer **6** exhibits a much larger nonlinear absorption than the zinc dimer **5**. This contradicts the trend in the associated mononuclear analogues **35** and **36**. The cobalt dimer **37** exhibited the largest κ coefficient in this case study where $\kappa \approx 11.0 \pm 0.1$, approximately two times that of **40**. It can also be noted that compound **37** exhibited a much higher saturation energy density, by a factor ≈ 2.4, than that of **40**.

In summary, the mononuclear cobalt derivative is a weaker nonlinear absorber than its zinc counterpart. In contrast, the butadiyne bridged cobalt dimer **40** exhibits the largest β_I response of all the binuclear derivatives. It can be noted that for the zinc series, the nonlinear absorption, the saturation energy density F_{Sat} and also the κ coefficients decrease in the following order **39** < **40** < **35**. One would expect that the electronic interaction between the two macrocycles would be a maximum for **39** as the spatial separation of the macrocycles is less than that for **40**. Therefore, the trends in the data imply that the derivative with the highest degree of electronic interaction between the two chromophores (**39**) is the weakest nonlinear absorber. On the other hand, intermolecular interactions seem to positively affect the nonlinear response in the cobalt series since the butadiyne cobalt dimer **37** exhibits the largest β_I of all six compounds in this case study. These results seem to indicate that there is an inseparable link between the peripheral structure and the central metal in these types of systems. Thus, one cannot separately tune the nonlinear optical response by changing either the main structure or the central metal of the chromophore because both factors are inextricably intertwined. All dimers exhibit lower F_{sat} than their mononuclear parent compounds, however the cobalt dimer **37** has the highest of the four bridged dimers. Notably this compound also exhibits the largest κ coefficient of the seven compounds studied with $\kappa \approx (11.0 \pm 0.1)$.

4.5.7 Case Study VI: Direct M-M binuclear complexes

The mononuclear chlorogallium and chloroindium compounds **4** and **6** were dimerised with a direct M-M linkage to create compounds **42** [*t*Bu$_4$PcGa]$_2$.2dioxane and **41** [*t*Bu$_4$PcIn]$_2$.2tmed respectively. The nonlinear absorption coefficients β_I plotted as a function of incident focal intensity I_0 are depicted in Figure 4.19 for all four compounds of this subset where each data point on the plot represents an independent open aperture z-scan of the compound in question and the solid lines again are sketched merely as guides to the eye.

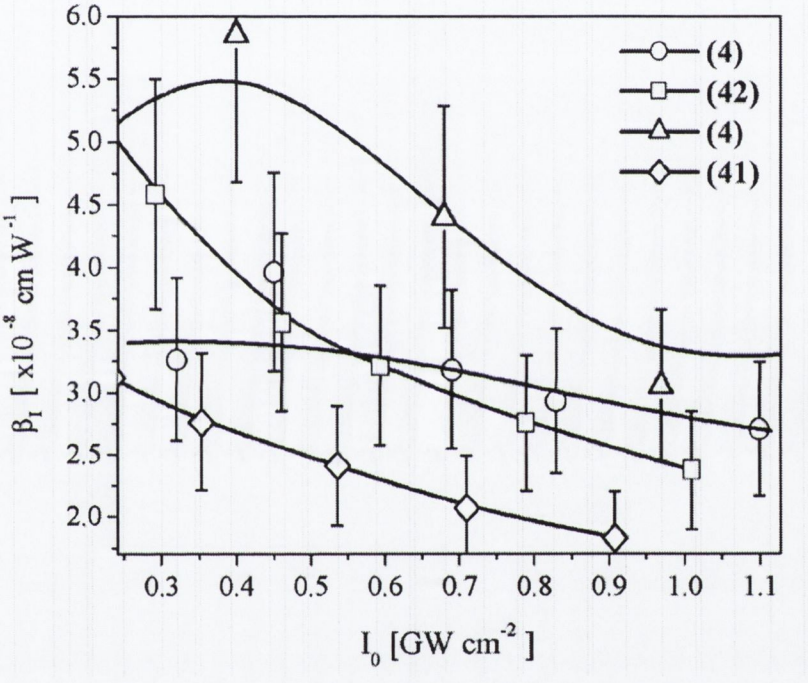

Figure 4.19 . Plot of effective nonlinear absorption coefficient β_I against the on focus beam intensity I_0 for both Ga and In mononuclear (compounds **4** [*t*Bu$_4$PcGaCl]and **6** [*t*Bu$_4$PcInCl] respectively) and direct M-M linked binuclear compounds (compounds **42** [[*t*Bu$_4$PcGa]$_2$.2dioxane] and **41** [[*t*Bu$_4$PcIn]$_2$.2tmed] respectively). Each data point represents an independent open aperture z-scan and the solid lines are intended as guides to the eye.

It can be seen that β_I reduces in magnitude with increasing focal intensity I_0 in the figure, as has been observed for other compounds. It can be seen that the Ga compounds exhibit similar nonlinear absorption coefficients with the dimer **42** tending to exhibit a larger β_I than the chlorogallium mononuclear derivative **4** at lower I_0 values. The indium mononuclear phthalocyanine **6** exhibited a larger β_I than its dimer **41** over the entire intensity range.

(a)

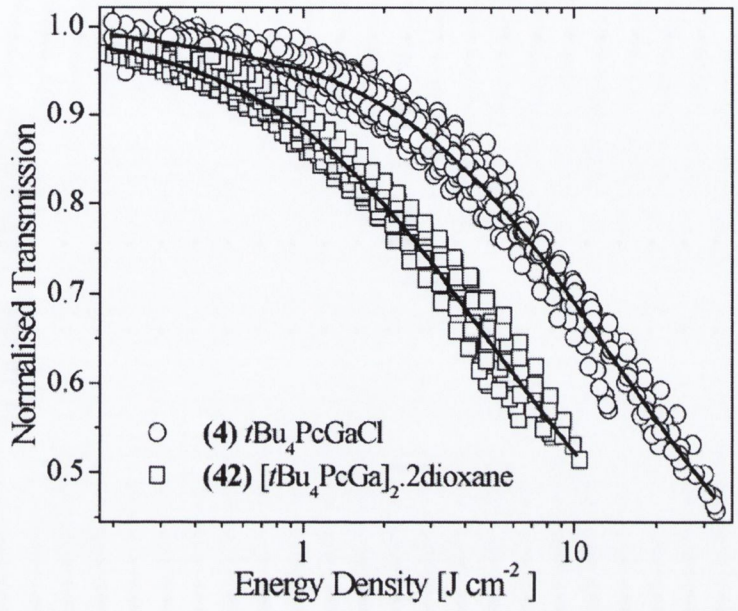

(b)

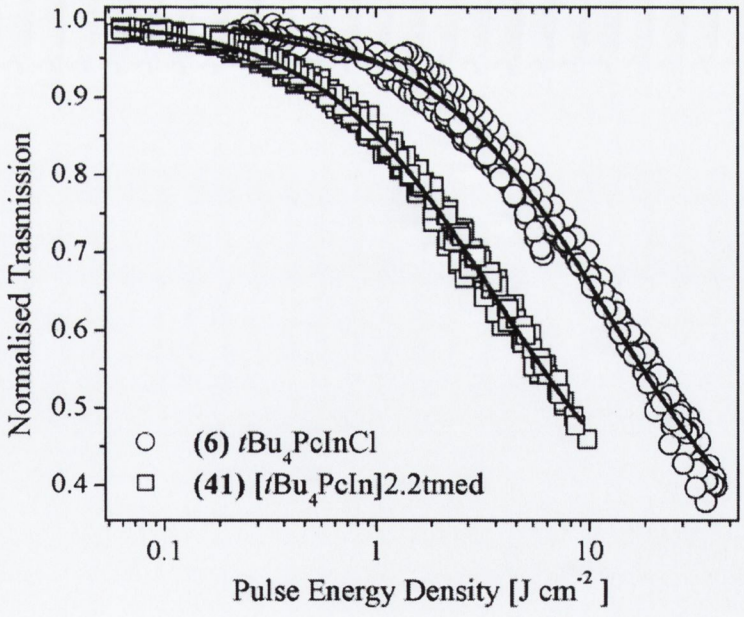

Figure 4.20 Plot of normalised transmission against incident energy density for **(a)** the Ga monomer (compounds **4** [tBu$_4$PcGaCl]) and its associated direct M-M linked binuclear dimmer (compounds **42** [[tBu$_4$PcGa]$_2$.2dioxane]) and **(b)** the In monomer (**6** [tBu$_4$PcInCl]) and its direct M-M linked binuclear analogue (**41** [[tBu$_4$PcIn]$_2$.2tmed]). The solid lines are theoretical curve fits to the data.

The normalised transmission against incident energy density optical limiting plots are presented in Figure 4.20, where the Ga compounds are presented in Figure 4.20a and the In compounds in Figure 4.20b. It was found that the dimerised Ga compound **42** exhibits a significantly lower F_{Sat} than that of its mononuclear parent **4**, by approximately a factor of 3. The ratio of their excited and ground state absorption cross sections is similar with **4** exhibiting a κ coefficient approximately 1.35 times that of **42**. Hence, dimerisation of **4** in this manner to yield **42** is clearly a viable method for tuning the saturation energy density (F_{Sat}) of the material, reducing F_{Sat} by a factor of 3. This reduction in F_{Sat} is coupled with a slight increase of β_I at low incident intensity and with approximately equivalent β_I*'s* at higher intensities. Dimerisation of **4** to **42** results in the κ coefficient is reduced by approximately 22%. This can probably be mostly attributed to the increase linear absorption coefficient by approximately 18% over the same molecular modification.

The optical limiting of the chloroindium phthalocyanine dimer **41** ([*t*Bu$_4$PcIn]$_2$.2tmed) with a direct In-In bond compared to the starting *t*Bu$_4$PcInCl, **6**, will be considered here. Similar to the results for the Ga-Ga phthalocyanine dimer it was found that dimerisation of the starting single chloroindium unit reduced the F_{Sat} value by a factor of approximately 2.5 (comparable to a factor of approximately 3 for the Ga-Ga dimer discussed above). The binuclear indium compound also exhibited a slightly lower F_{Sat}, $F_{Sat} \approx (24.2 \pm 0.8)$ J cm^{-2}, than that of compound **42** presented above. The reduction of κ for the mononuclear to binuclear transition for the indium phthalocyanines by a factor of about 2.2 after dimerisation is far more significant than the reduction by a factor of 1.3 for the Ga compounds. However, this difference can at least be partially attributed to the particularly low linear absorption coefficient of the *t*Bu$_4$PcInCl (**6**) molecule, which allows it to exhibit a large κ coefficient compared to other phthalocyanines.

4.5.8 Trends in the Optical Response Related to the Molecular Structure

As has just been seen, in this work and in the studies by Shirk *et al.*[12] κ has various limitations and potential for misconception as an indicator of limiting action. Despite this it has widespread acceptance as an excellent indicator of optical limiting action and so it will be studied in a little more detail here. In Figure 4.21 κ is plotted against the atomic weight of the central metal in the monomer phthalocyanine cavity. In this plot only data calculated from optical limiting fits of high quality are included and the dimer data are also omitted for obvious reasons. High quality fitting implies that the values predicted by the model were almost equal to that mapped by the real data and thus, it was not unreasonable to discard the poor fits at this point. The datasets that were omitted due to poor quality fitting of the nonlinear absorption coefficient were for compounds **16**, **23**, **27**, **32**, **33**, and **36**, which were all phthalocyanines with cobalt in the central cavity. These compounds exhibited the lowest magnitude nonlinear absorption, and the poor quality of the fit was indicated in the uncertainty in F_{Sat} that ranges from ± 40% to greater than ± 100% of the calculated value.

In Figure 4.21a the κ coefficient for all the metal centered phthalocyanines was plotted opposite the atomic mass of their central metal. It can be seen that there does not appear to be any definite trend in this data although κ does appear to approximately increase with the central metals atomic mass. Note that the data from compounds **15**, **17** and **21** was omitted here, as these compounds do not have a central metal. In Figure 4.21b the region of atomic mass from 58 to 70 has been expanded in the interest of clarity although it shows nothing more conclusive than the preceding figure.

The relationship between the saturation energy density F_{Sat} and the atomic mass of the central metal has been explored for the same compounds in Figure 4.22a and the region of atomic mass ranging from 58 to 70 has been expanded in Figure 4.22b as before. The data does not appear to follow a definite trend although F_{Sat} does appear to approximately decrease with increasing in the central metal atomic mass. It is interesting to note that the highest F_{Sat} magnitudes are for cobalt, gallium and indium centred compounds, which represents those compounds with the lowest κ coefficients (cobalt) and the highest κ coefficients (indium).

(a)

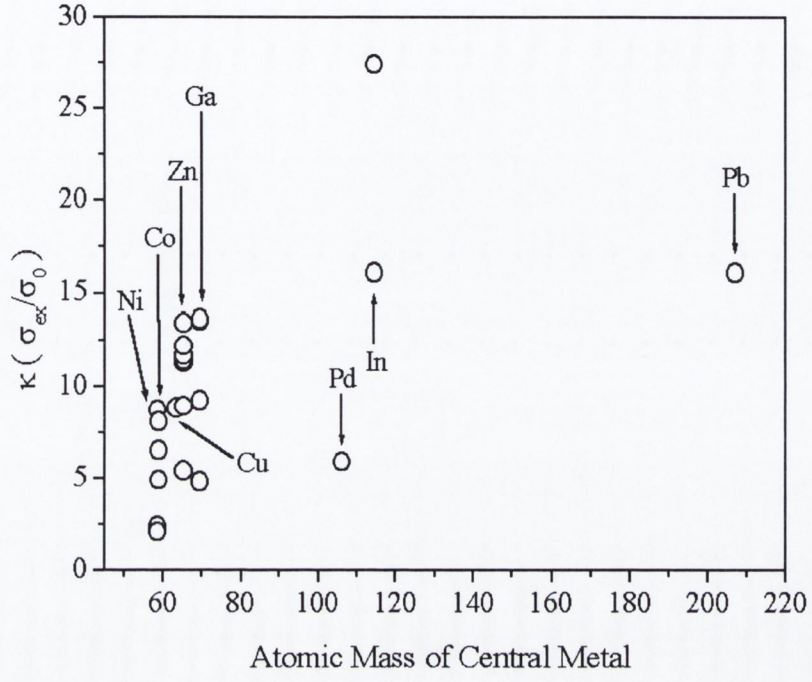

(b)

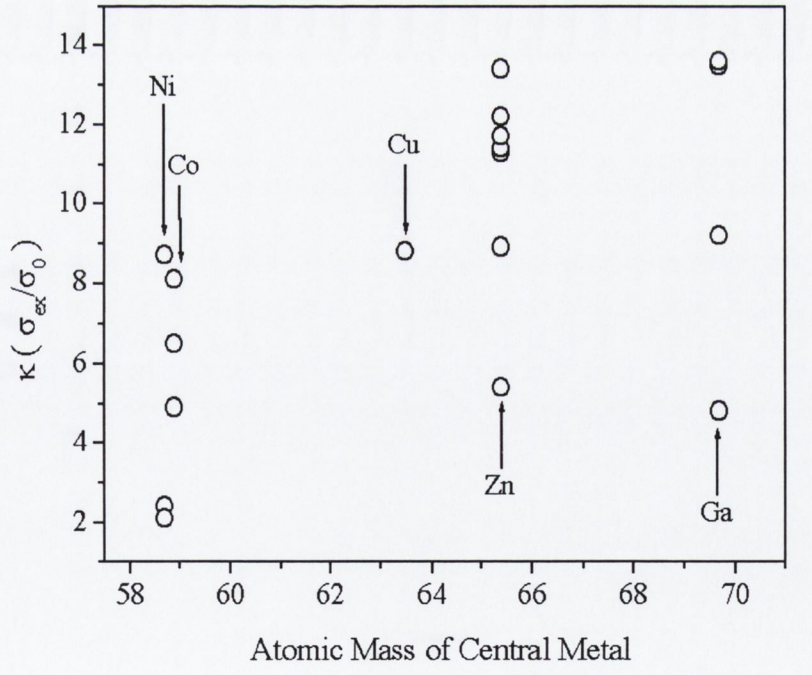

Figure 4.21 **(a)** Plot of the ratio of excited to ground state absorption cross-sections (κ) against the atomic mass of the central metal for the monomer phthalocyanines. **(b)** Expanded view of the atomic mass region spanning 58-70.

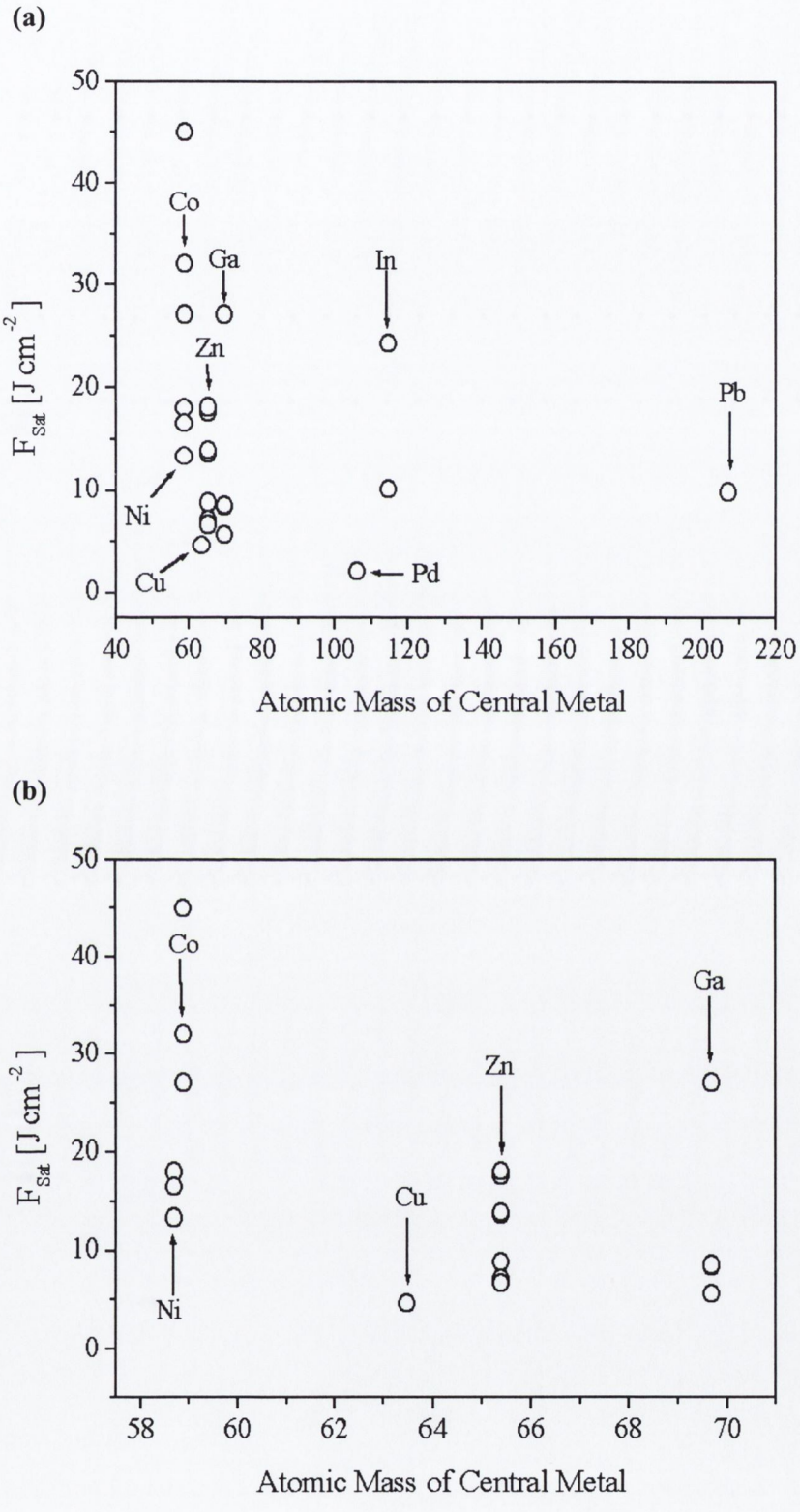

Figure 4.22 **(a)** Plot of the saturation energy density F_{Sat} against the atomic mass the central metal for the monomer phthalocyanines. **(b)** Expanded view of the atomic mass region spanning 58-70.

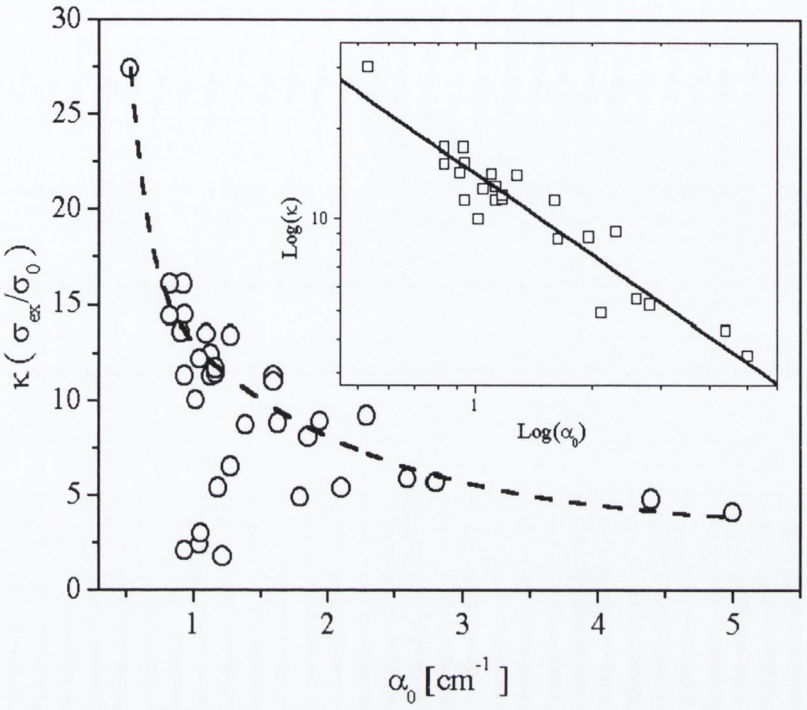

Figure 4.23 Plot of the ratio of excited to ground state absorption coefficients (κ) against the linear absorption coefficient α_0, where the dashed line is intended as a guide to the eye. In the inset the plot has been reproduced with logarithmic scales without contributions from cobalt, nickel or peripherally bridged dimer phthalocyanines.

The ratio of excited to ground state absorption coefficients (κ) is plotted against the linear absorption coefficient α_0 in Figure 4.23 with data from all compounds included, except the aforementioned data that were omitted. The relationship between κ and α_0 appears to exhibit a clearer trend than that between κ and the atomic mass of the central metal. The dashed line, intended as a guide to view the data, appears to span the data points in an approximate way with the exception of a few data points with relatively low κ coefficients in the region of $\alpha_0 \approx 1$ cm^{-1}. It is interesting that these data points all correspond to compounds that are either peripherally bridged dimers or phthalocyanine monomers with nickel as their central metal. The nickel centred phthalocyanines were poor optical limiters, as they did not exhibit large nonlinear absorption. In the inset, the plot has been reproduced on logarithmic scales without contributions from cobalt, nickel or peripherally bridged dimer phthalocyanines. Phenomenologically, the data (including the results for the C_{60} fullerene, compound **1**) appears to approximately follow a straight line of

negative slope on the logarithmic scale with Log(κ) decreasing for increasing Log(α_0). This seems to suggest that the ratio of the excited to ground state absorption coefficients has a far closer link to the linear absorption coefficient than to the type of substituents in the central cavity or on the periphery of the phthalocyanine macrocycle.

4.6 Further and Future Work

Due to the remarkable amount of modifications that are possible with the phthalocyanine structure it is inevitable that future work on new synthesis of novel compounds for the field of optical limiting will be undertaken. These compounds will certainly be tested for their nonlinear optical response in solution and in thin films fabricated from these compounds embedded in polymer guest-host systems. However, there exist many different methods for using phthalocyanines in the optical limiting field. In this section a short overview of three different possible areas with some preliminary results will be presented. Initially optical limiting from commercially available phthalocyanines embedded in polymer films will be discussed, this will be followed by an example of a polymerised phthalocyanine system and finally optical limiting from dispersed nanoparticles fabricated from phthalocyanines will be presented.

4.6.1 Solid State Optical Limiting

The use of guest-host systems, where phthalocyanines assume the role of guest inclusions in an otherwise homogeneous host polymer film is the first step, after solution experimentation, towards applying the phthalocyanine in real world optical limiting applications. A demonstration of the methods required to undertake such a study is presented here. The phthalocyanines used in this section were purchased from Aldrich (Product Code: $(PhS)_4PcZn$ 41,823-4; $t Bu_4PcZn$ 43,099-4) and used without further purification. Their chemical structures are sketched in Figure 4.24.

The polymer that was used was poly(methyl methacrylate) (PMMA), a clear plastic commonly used as a shatterproof replacement for glass. The chemical company Rohm and Haas, for example, uses PMMA to fabricate windows and calls it Plexiglas. The materials were prepared as follows. Initially the polymer was

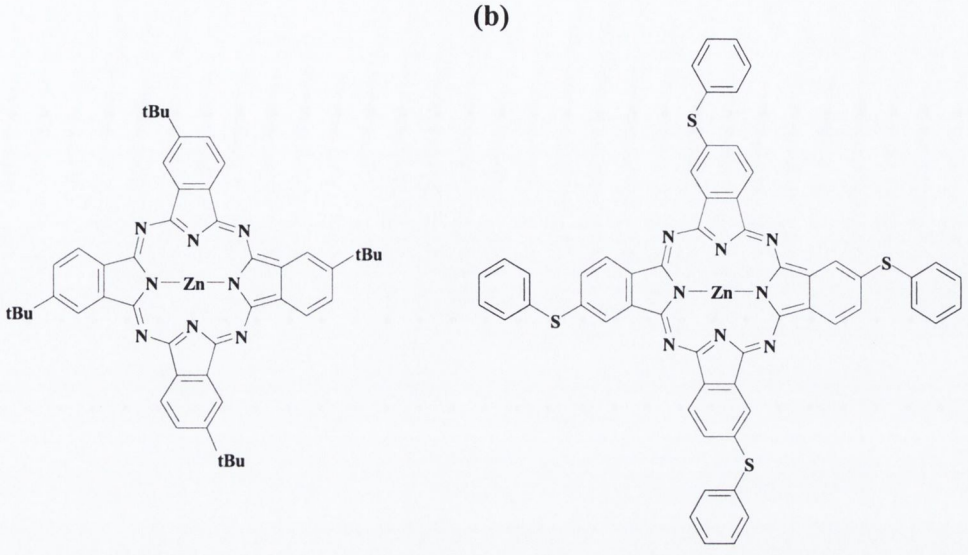

Figure 4.24 Chemical structure for commercially available phthalocyanines from Aldrich **(a)** tBu$_4$PcZn and **(b)** (PhS)$_4$PcZn.

dissolved in the solvent cyclohexanone at a concentration of 100 g L^{-1}. This required approximately 40 hours of low power (60 W) agitation in a sonic bath to form a clear viscous solution. The phthalocyanines were added to this solution at a mass ratio of 1:5 (Pc:PMMA), thus implying a 20 g L^{-1} partial concentration of the phthalocyanine in the solution. Multi-layer films (5 layers) were then cast using a conventional spin coating system where the quartz substrate was spun at 1000 RPM without ramping. The film was baked at 55 ^{0}C for 90 minutes between successive layers. The film was seen to grow in thickness by about 1μm for each layer and the finished optically homogeneous films had a deep glassy blue or green appearance for the PMMA(tBu$_4$PcZn) and PMMA((PhS)$_4$PcZn) films respectively. Solutions of both phthalocyanines at 0.5 g L^{-1} in spectroscopic grade toluene were also prepared for comparison reasons.

The linear UV-Visible absorption spectra for the solutions and films are presented in Figure 4.25. In Figure 4.25a solutions of tBu$_4$PcZn and (PhS)$_4$PcZn at 0.5 g L^{-1} in spectroscopic grade toluene are presented and in Figure 4.25b the spectra of the PMMA(tBu$_4$PcZn) and PMMA((PhS)$_4$PcZn) thin films are presented. In Figure 4.25b a spectrum of a pure PMMA film, without any other inclusions has been added and it can be seen that the PMMA has a flat profile of low absorbance over the visible region as evidenced by its clear appearance. The Q-band for both films containing phthalocyanines is broadened for the films compared to the

(a)

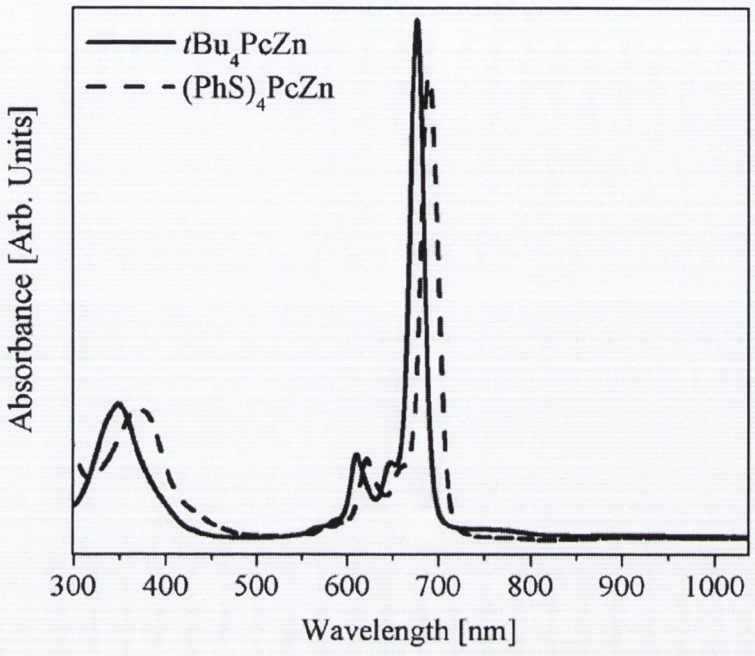

(b)

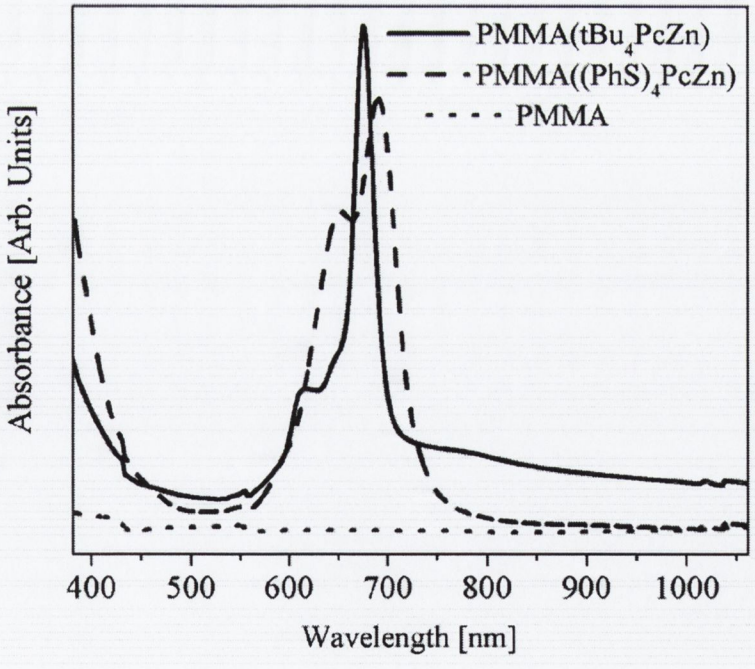

Figure 4.25 Linear UV-Visible absorption spectra for **(a)** solutions of tBu$_4$PcZn and (PhS)$_4$PcZn at 0.5 g L^{-1} in spectroscopic grade toluene and **(b)** of PMMA(tBu$_4$PcZn), PMMA((PhS)$_4$PcZn) and PMMA thin films. It can be seen that the PMMA has a flat profile of low absorbance over the visible region leading to its clear appearance.

solutions indicative of aggregated behaviour, not unexpected owing to the large partial concentration of 20 g L^{-1} that was used in the film construction and the fact that the solid state is naturally more condensed. The spectral position of the Q-band is not significantly shifted for the solution to solid state transition (only by about 2 nm to red for the $(PhS)_4PcZn$ case and by about 1 nm to the blue for the $t Bu_4PcZn$ case). It can be seen that the 'window region' between the Q- and B-bands is preserved, although slightly narrowed, in the films indicating that the films are also suitable for optical limiting of 532 nm light. The absorbance curve for the PMMA($t Bu_4PcZn$) film exhibited a larger magnitude in the region of 532 nm than the PMMA($(PhS)_4PcZn$) film.

Optical limiting measurements were performed on these solutions and films using the same experimental approach as was used in the phthalocyanine studies earlier. The optical limiting plots, where normalised transmission is plotted against incident energy density are presented in Figure 4.26. In Figure 4.26a the optical limiting from solutions of $t Bu_4PcZn$ and $(PhS)_4PcZn$ at 0.5 g L^{-1} in spectroscopic grade toluene in 1mm quartz cells is presented and in Figure 4.26b the plots for the PMMA($t Bu_4PcZn$) and PMMA($(PhS)_4PcZn$) thin films are depicted. The pure PMMA film exhibited no response of its own and was omitted from the plot. The model that was developed earlier in this chapter for the phthalocyanine system was fitted to both classes of sample to calculate effective excited to ground state absorption cross-sections, κ, and the saturation energy density F_{Sat} as before. The results are presented in Table 4.6.

Sample	α_0 [cm^{-1}]	κ (σ_{ex}/σ_0)	F_{Sat} [J cm^{-2}]
$t Bu_4PcZn$	1.64	8.0 ± 0.4	9.9 ± 0.7
$(PhS)_4PcZn$	1.49	9.9 ± 0.3	7.5 ± 0.3
PMMA($t Bu_4PcZn$)	937	4.1 ± 0.3	4.4 ± 0.7
PMMA($(PhS)_4PcZn$)	528	6.3 ± 0.4	7.5 ± 0.6

Table 4.6 Numerical results for the optical limiting experiments of solutions of $t Bu_4PcZn$ and $(PhS)_4PcZn$ at 0.5 g L^{-1} in spectroscopic grade toluene and of PMMA($t Bu_4PcZn$) and PMMA($(PhS)_4PcZn$) thin films.

(a)

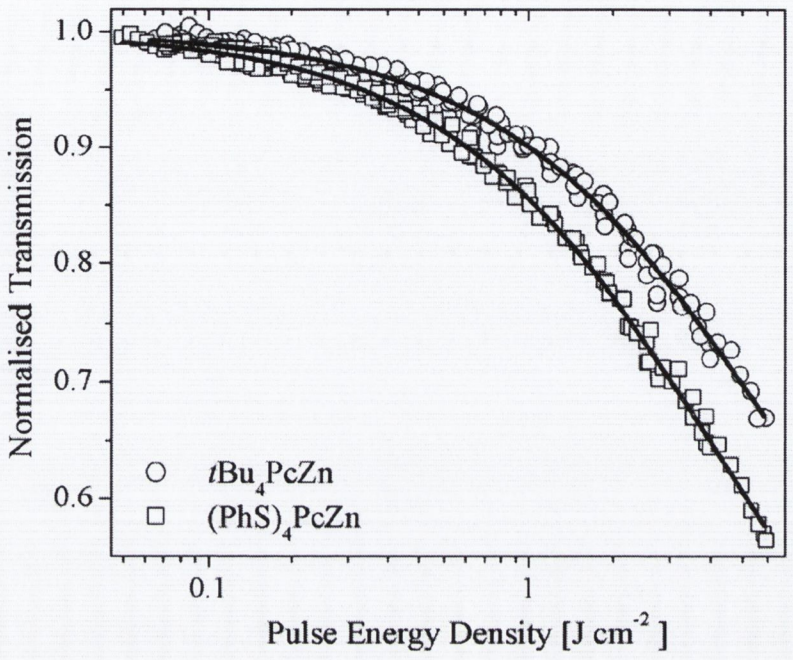

(b)

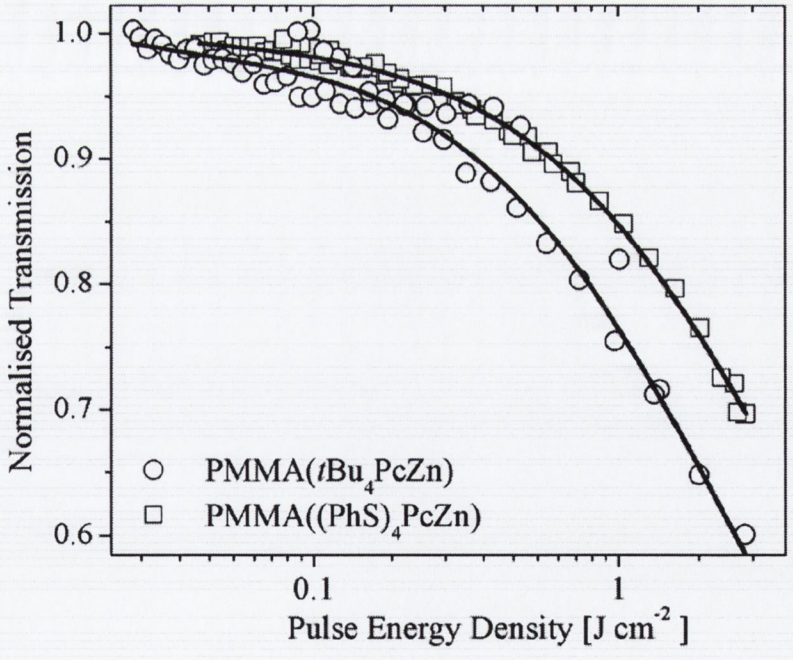

Figure 4.26 Plot of normalised transmission against incident energy density for **(a)** solutions of tBu$_4$PcZn and (PhS)$_4$PcZn at 0.5 g L^{-1} in spectroscopic grade toluene in 1mm quartz cells and **(b)** of PMMA(tBu$_4$PcZn) and PMMA((PhS)$_4$PcZn) thin films on quartz substrates. The PMMA film exhibited no response of its own and was omitted from the plot.

It can be seen from Figure 4.26a for the solutions that the tBu$_4$PcZn exhibits a higher saturation energy density F_{Sat} than the (PhS)$_4$PcZn solution. For the films it can be seen from Figure 4.26b that this effect is reversed where the PMMA((PhS)$_4$PcZn) film exhibited a higher F_{Sat} than the PMMA(tBu$_4$PcZn) film. The origin of this may be related either to the increased aggregation in the solid state or to the differences in phthalocyanine-polymer intermolecular interactions and deserves further study. The κ coefficient for the solutions and films are in the same relative magnitudes with the (PhS)$_4$PcZn based sample exhibiting a larger κ coefficient than the tBu$_4$PcZn analogues in both cases.

It can be seen that transferring the results of solution studies to solid state systems may not be straight forward. A future study repeated with all promising phthalocyanine molecules for optical limiting, identified in this thesis, embedded in multi-layer polymer films would be extremely beneficial, yielding important information for the fabrication of solid state practical optical limiters.

4.6.2 Polymerised Phthalocyanines

Over the past twenty years, the phthalocyanine has been incorporated covalently into polymers[38] by a variety of reactions. It has been incorporated as part of the main chain,[39] at the end of side chains,[40] as end groups,[41,42] as branch points of a star,[43] and as junctions of networks.[44,45] Generally in most polymerised phthalocyanine systems cofacial association predominates the aggregation in the system and only axial substitution of the central ion in the polymerised system is successful for its prevention.[38] To date much less work has been done on the axial polymeric modification of metallophthalocyanines compared to other methods of polymerisation. Recently we have reported the synthesis of an indium phthalocyanine axially grafted polystyrene (PS) polymer (PS-[tBu$_4$PcIn]). The chemical structure of the polymerised phthalocyanine is depicted in Figure 4.27. The polymer PS-[tBu$_4$PcIn] was obtained by the reaction of tBu$_4$PcInCl, compound **6** of this chapter, with freshly prepared PS(MgBr)$_n$ at room temperature.[46] The nonlinear optical response of the polymerised tBu$_4$PcInCl will be reviewed briefly here.

The transient absorption spectra of tBu$_4$PcInCl and PS-[tBu$_4$PcIn] showed that both these two materials are suitable for optical limiting in the spectra range of

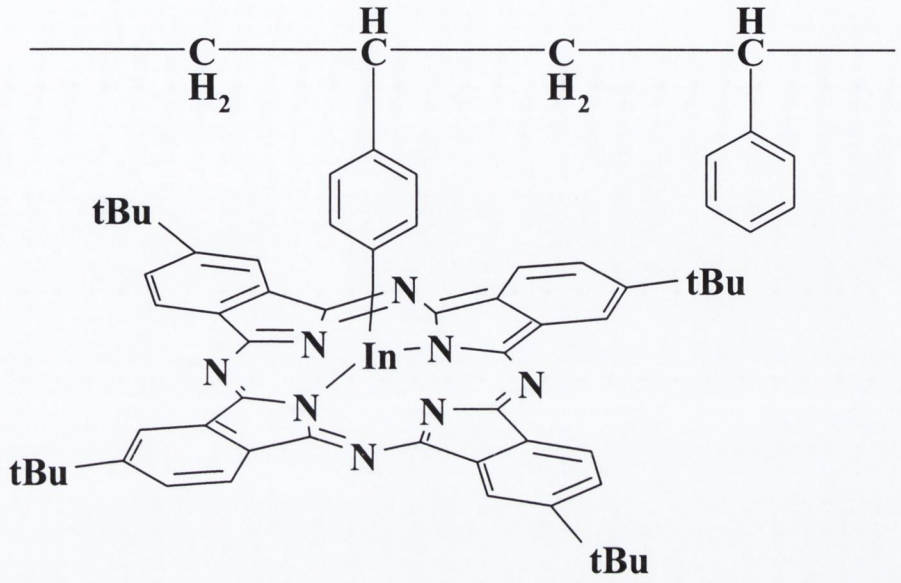

Figure 4.27 Chemical structure of the indium phthalocyanine axially grafted polystyrene (PS) polymer (PS-[*t*Bu$_4$PcIn]).

450 to 550 nm for nanosecond laser pulses, with triplet state absorption cross-section spectra peaking at approximately 520 nm for both materials. Open aperture Z-scan spectra in toluene were collected for each sample and all scans performed exhibit a decrease of transmittance about the focus typical of an induced positive nonlinear absorption of incident light. The values of $Im\{\chi^{(3)}_{eff}\}$ at 532 nm for *t*Bu$_4$PcInCl and PS-[*t*Bu$_4$PcIn] were determined to be about 1.56×10^{-11} and 0.62×10^{-11} esu, respectively. The corresponding effective second-order hyperpolarisability (γ_{eff}) values for these compounds were approximately 1.15×10^{-32} and 0.26×10^{-32} esu, respectively. Polystyrene and poly(*p*-bromostyrene) exhibited no nonlinear optical response of its own under the same experimental conditions.

Typical optical limiting plots are presented in Figure 4.28, where the normalised transmission is plotted as a function of excitation pulse energy density. The samples were measured at concentrations of about 10^{-4} M in spectroscopic grade toluene. The F_{Sat} and κ values for the mononuclear and polymerised indium phthalocyanine exhibit significant differences. The F_{Sat} values for the mononuclear tBu$_4$PcInCl **6** and PS-[*t*Bu$_4$PcIn] in toluene are (24.2 ± 0.8) and (10.8 ± 0.7) J cm^{-2}, respectively. The F_{Sat} value for the polymerised phthalocyanine is thus approximately smaller by 55% than that of the mononuclear **6**.

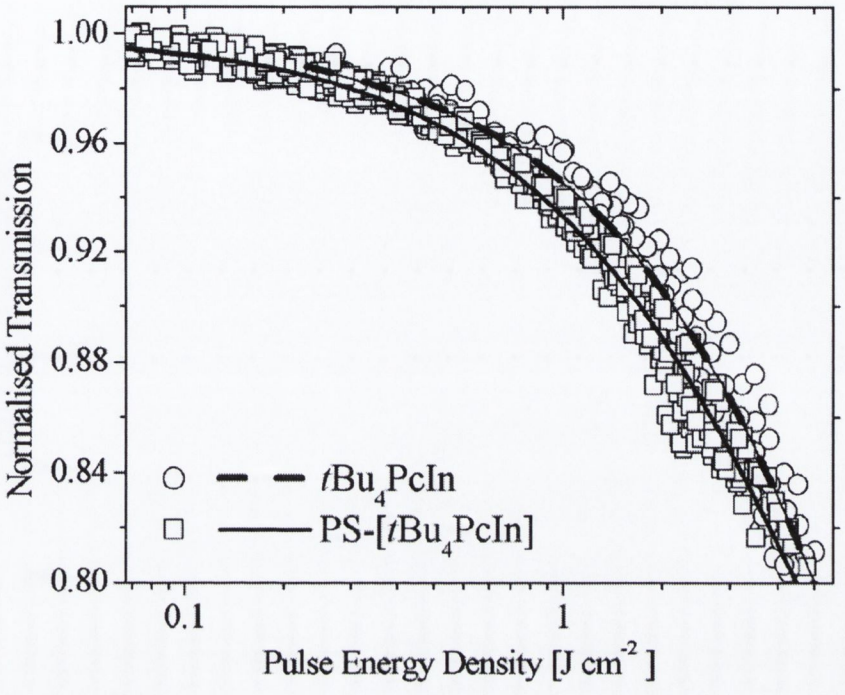

Figure 4.28 Plots of normalised transmission against incident pulse energy density for tBu$_4$PcInCl and the PS-[tBu$_4$PcIn] copolymer. The solid line and dashed line are the theoretical curve fits. All samples were measured at concentrations of about 10^{-4} M in spectroscopic grade toluene.

The ratio of the excited to ground state absorption cross sections also differ significantly with the mononuclear unit exhibiting a κ coefficient ($\kappa \approx 27.4 \pm 0.6$) just in excess of two times that of the polymerised sample which exhibited $\kappa \approx 13.2 \pm 0.7$.

The incorporation of other phthalocyanines into other polymers in this manner would be of interest. Future work in this direction would also involve the fabrication of solid state samples and subsequent testing of these films for optical limiting applications.

4.6.3 Phthalocyanine Nanoparticles

The use of chemical synthesis to modify the phthalocyanine mononuclear unit to improve its optical responses has been addressed in this thesis. There exists however other methods to modify the phthalocyanine system at the nanoscale by creating novel aggregated systems without the need for chemical or structural alterations, expected to exhibit interesting responses to external stimuli such as optical excitation. To this end, we have recently reported the first study of nanoparticles fabricated from phthalocyanines. Furthermore, it was demonstrated that a significant improvement in the nonlinear response of the nanoparticles over solutions of the same phthalocyanines was obtainable.[47] The nonlinear optical response of the nanoparticles fabricated from the zinc centred phthalocyanine $(PhS)_4PcZn$ (Figure 4.24b) compared to solutions of the same phthalocyanine will be presented here.

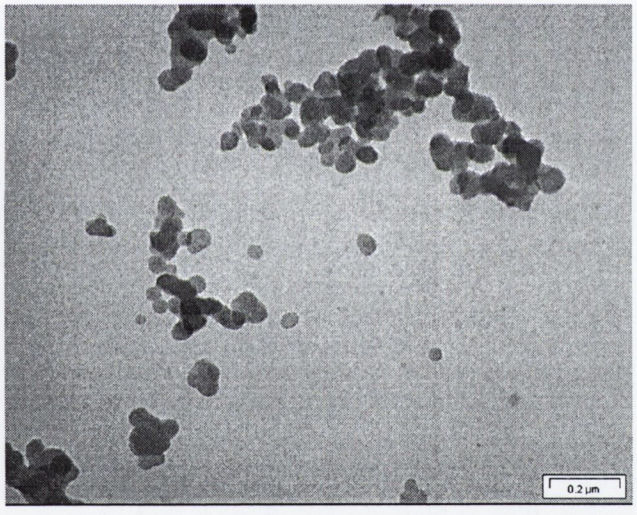

Figure 4.29 Transmission electron microscopy (TEM) image of the $(PhS)_4PcZn$ nanoparticles. The average diameter of the spherical particles was of order 65 nm.

Nanoparticles from $(PhS)_4PcZn$ were fabricated using the microwave method as detailed by Nitschke *et al.*[47] A typical transmission electron microscopy (TEM) image of the nanoparticles is depicted in Figure 4.29, where the spherical geometry of the particles can clearly be observed. The particle size was confirmed by tapping mode atomic force microscopy imaging and the average particle size was found to be of order 65nm for the $(PhS)_4PcZn$ nanoparticles.

For solutions of the molecule and nanoparticles, prepared with the same mass concentration, the nanoparticle B-band absorption in the linear absorption spectrum

was found to be increased by a factor of about 3.5 for the $(PhS)_4PcZn$ nanoparticles compared to their molecular analogues. This increase in the B-band was probably due to acetone, which was the solvent used for the mononuclear solution, that seemed to be trapped within the particle. In addition, the areas under the Q-bands exhibited a reduction by a factor of about 1.5 after the molecule to nanoparticle transition. Furthermore, a broadening of the Q-band was observed as well as peak shifts to the red and to the blue probably due to a mixture of cofacial and edge-to-edge stacked molecules inside the particle.

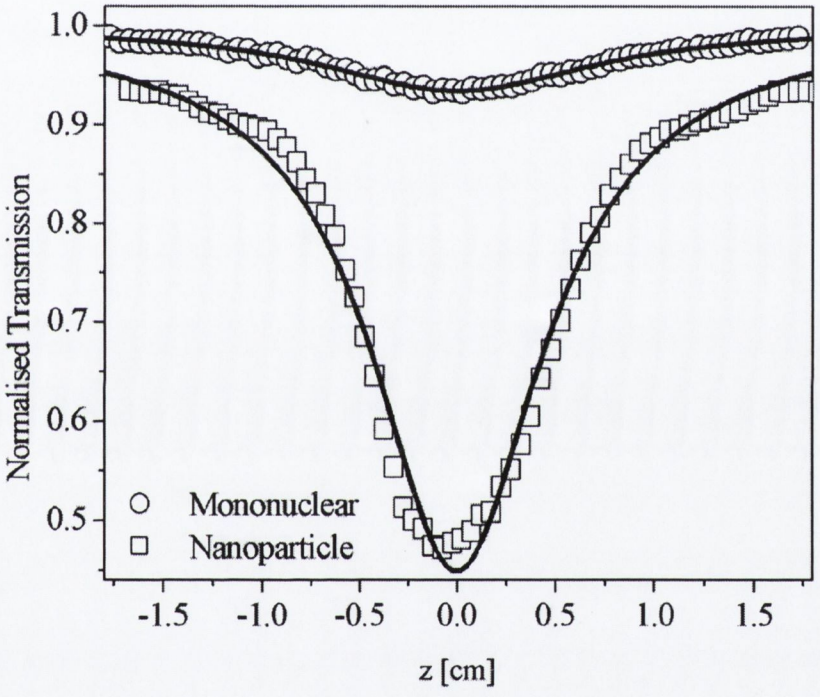

Figure 4.30 Typical open aperture z-scans for $(PhS)_4PcZn$ molecular solutions and nanoparticle dispersed samples

A sample of typical open aperture Z-scan results with normalised transmission plotted as a function of sample position z is depicted in Figure 4.30 for the molecular and nanoparticle $(PhS)_4PcZn$ sample for incident pulse energies of ≈ 0.16 and 0.3 mJ respectively.

It was noted that for the $(PhS)_4PcZn$ nanoparticles, the effective nonlinear absorption coefficient β_I was found to be significantly larger than that of its associated molecular solution. The $(PhS)_4PcZn$ molecular solution exhibited $\beta_I \approx (4.0 \pm 0.8)\times10^{-10}$ cm W^{-1} while its associated nanoparticle exhibited a β_I coefficient

approximately 5.3 times larger at $(2.1 \pm 0.4)\times10^{-9}$ cm W^{-1}.

It can be noted that this represents a significant enhancement of the nonlinear absorption. This indicates that this method of phthalocyanine nanoparticle preparation has significant impact and potential for exploitation in the field of optical limiting. Further work in this area should involve the fabrication of nanoparticles from other phthalocyanines to investigate if the nonlinear absorption enhancement is general for phthalocyanine molecules, or limited to certain classes of the compound. Subsequently, attempts to embed these nanoparticles in polymer films would be of significant interest to the optical limiting field.

4.7 Conclusions

The nonlinear response of 41 structurally different phthalocyanine compounds has been experimentally measured. The results have been fitted using a five level model that was effectively reduced to a three level system due to the lengthy pulse duration relative to all other lifetimes in the system. The model, although not generally spectroscopically correct, fitted the data well and produced reasonable results verified by other authors using similar compounds. It was found that putting nickel or cobalt into the central phthalocyanine cavity produced nothing but undesirable effects from the point of view of optical limiting. This was because the introduction of Ni or Co was found to reduce the magnitude of the nonlinear absorption compared to that of similar phthalocyanines without a metal in the central cavity. It has become increasingly clear that no single lone parameter can be used to describe the efficacy of optical limiters. This is clear from many cases such as the chloroindium monomer (compound **6**) exhibiting the largest ratio of excited to ground state absorption cross sections κ, meanwhile the palladium phthalocyanine (compound **10**) was found to exhibit the largest nonlinear absorption coefficient β_I. As a result the gauging of the optical limiting response requires a comprehensive set of values besides κ and β_I, such as the linear absorption coefficient α_0, the saturation intensity or energy density (F_{Sat}), which in turn is inversely proportional to σ_0 and τ_{10} (first excited singlet to ground state characteristic lifetime). The effective molecular imaginary hyperpolarisability ($Im\{\gamma_{eff}\}$ was employed here) can be useful as a comparable value of the molecular response as opposed to the macroscopic response.

The κ coefficient did not exhibit a clear dependence on the atomic mass of

the central metal. However, it did appear to show a more stable dependence on the linear absorption coefficient, especially after removing the contributions from cobalt, nickel and peripherally bridged dimer phthalocyanines. As cobalt and nickel were found not to be useful as optical limiters, it is interesting that the 'good' materials follow such a trend. However, it is a little disappointing that the peripherally bridged dimers broke this trend as they do show promise when one would require low F_{Sat}. They exhibit some of the lowest F_{Sat} values in this study. The apparent linearity in the relationship between Log(κ) and Log(α_0) is a phenomenological result that appears to represent an experimental molecular engineering design rule.

The future of research in phthalocyanines will certainly involve further developments in novel synthesis to reduce the linear absorption while increasing the nonlinear absorption. However, techniques such as polymerised phthalocyanines and phthalocyanine nanoparticles may also provide useful advances in the development of phthalocyanines for optical limiting applications. Initially, a study of the compounds presented here, where the measurements are carried out in the solid state with the phthalocyanines embedded in host polymers would be of immediate interest. A practical limiter built from phthalocyanines will inevitably involve incorporating the phthalocyanine units into some form of a multi layered solid-state entity. Polymerising the phthalocyanines, or embedding the phthalocyanines as inclusions in a polymer host to form a composite material would allow traditional methods such as spin casting to be employed to produce suitable films for these solid state applications. An incident offending light pulse would then have to pass through the various layers before final transmission to the target under protection. These layers would be chosen depending on the properties of the phthalocyanine and the attenuation that would be necessary for the limiter to fulfil its purpose. As a trivial example one can consider a two layer device comprising of the indium monomer (tBu$_4$PcInCl) and dimer ([tBu$_4$PcIn]$_2$O) phthalocyanine whose optical limiting curves are shown in Figure 4.15 under non-focused irradiation with green laser light. The two layered device would have the compound with the higher saturation energy density as the first layer followed by the second layer fabricated from the phthalocyanine with the lower saturation, and assuming that the response is as shown in the figure in this case a layer of indium monomers followed by a layer of indium dimers. One can consider 20 J cm^{-2} 532 nm irradiation, and including the

linear absorption, the first layer will transmit approximately 9.6 J cm^{-2}, followed by a sequential linear and nonlinear absorption by the second layer reducing the transmittance to approximately 4.1 J cm^{-2}. This despite the triviality of the situation represents a reduction on transmission of approximately 80%. One can easily envisage the expansion of this into a real application consisting of multiple layers specifically chosen to perform specific responses under specific laser energy densities or intensities. In addition one can consider the many theoretical device structures that have been proposed by others for the use of excited state absorbers as limiters of focused Gaussian pulses.[20,48,49] Phthalocyanines therefore offer a tremendous degree of design flexibility that they may be employed to fabricate practical organic passive optical limiters.

References

[1] H. S. Nalwa and S. Miyata, *Nonlinear Optics of Organic Molecules and Polymers* (CRC Press, Boca Raton, 1997).

[2] D. S. Chemla and J. Zyss, *Nonlinear Optical Properties of Organic Molecules and Crystals* (Academic Press, Orlando, 1987).

[3] J. L. Bredas, C. Adant, P. Tackx, A. Persoons, and B. A. Pierce, Chemical Reviews **94,** 243 (1994).

[4] J. Zyss, *Nonlinear Optics: Materials, Physics and Devices* (Academic Press, Boston, 1993).

[5] C. G. Classens, W. J. Blau, M. Cook, M. Hanack, R. J. M. Nolte, T. Torres, and D. Woehrle, Monatshefte fur Chemie **132,** 3-11 (2001).

[6] N. B. McKeown, *Phthalocyanine Materials: Synthesis, Structure and Function* (Cambridge University Press, Cambridge, 1998).

[7] H. S. Nalwa and J. S. Shirk, *Phthalocyanines: Properties and Applications*, Vol. 4 (John WIley and Sons, New York, 1996).

[8] Y. Chen and M. Hanack, Journal of Materials Chemistry **sub** (2002).

[9] D. Dini, M. Barthel, and M. Hanack, European Journal of Organic Chemistry, 3759-3769 (2001).

[10] M. Hanack, T. Schneider, M. Barthel, J. S. Shirk, S. F. Flom, and R. G. S. Pong, Coordination Chamistry Reviews **219-221,** 235-258 (2001).

[11] D. R. Coulter, V. M. Miskowski, J. W. Perry, T. H. Wei, E. W. V. Stryland, and D. J. Hagan, Proceedings of SPIE **1105,** 42 (1989).

[12] J. S. Shirk, R. G. S. Pong, S. R. Flom, H. Heckmann, and M. Hanack, Journal of Physical Chemistry A **104,** 1438-1449 (2000).

[13] J. S. Shirk, R. G. S. Pong, F. J. Bartoli, and A. W. Snow, Applied Physics Letters **63,** 1880 (1993).

[14] J. W. Perry, K. Mansour, I. Y. S. Lee, X. L. Wu, P. V. Bedworth, C. T. Chen, D. Ng, S. R. Marder, P. Miles, T. Wada, M. Tian, and H. Sasabe, Science **273,** 1533-1536 (1996).

[15] Y. Chen, S. O'Flaherty, M. Fujitsuka, L. R. Subramanian, O. Ito, W. J. Blau, and M. Hanack, Advanced Materials, in press (2002).

[16] J. W. Perry, K. Mansour, S. R. Marder, K. J. Perry, D. Alvarez, and I. Choong, Optics Letters **19,** 625-627 (1994).

[17] F. Z. Henari, A. Davey, W. Blau, P. Haisch, and M. Hanack, Journal of Porphyrins and Phthalocyanines **3,** 331-338 (1999).

[18] Y. Chen, Y. L. Song, S. L. Qu, and D. Y. Wang, Optical Materials **18,** 219-223 (2001).

[19] S. L. Qu, Y. Chen, Y. X. Wang, Y. L. Song, S. T. Liu, X. L. Zhao, and D. Y. Wang, Materials Letters **51,** 534-538 (2001).

[20] P. A. Miles, Applied Optics **33,** 6965-6979 (1994).

[21] Y. Chen, L. R. Subramanian, M. Fujitsuka, O. Ito, S. O'Flaherty, W. J. Blau, T. Schneider, D. Dini, and M. Hanack, European Journal of Organic Chemistry **8,** 4248-4254 (2002).

[22] Y. Chen, S. O'Flaherty, L. R. Subramanian, W. J. Blau, and M. Hanack, Chemistry of Materials **14,** 5163-5168 (2002).

[23] M. Q. Tian, S. Yanagi, K. Sasaki, T. Wada, and H. Sasabe, Journal of the Optical Society of America B-Optical Physics **15,** 846-853 (1998).

[24] C. R. Mendonca, L. Gaffo, L. Misoguti, W. C. Moreira, O. N. O. Jr., and S. C. Zilio, Chemical Physics Letters **323,** 300-304 (2000).

[25] T. C. Wen and I. D. Lian, Synthetic Metals **83,** 111-116 (1996).
[26] M. Yamashita, F. Inui, K. Irokawa, A. Morinaga, T. Tako, A. Mito, and H. Morawaki, Applied Surface Science **130-132,** 883-888 (1998).
[27] B. L. Justus, Z. H. Kafafi, and A. L. Huston, Optics Letters **19,** 1603-1605 (1993).
[28] X. Sun, R. Q. Yu, G. Q. Xu, T. S. A. Hor, and W. Ji, Applied Physics Letters **73,** 3632-3634 (1998).
[29] L. Vivien, D. Riehl, P. Lancon, F. Hache, and E. Anglaret, Optics Letters **26,** 223-225 (2001).
[30] L. W. Tutt and A. Kost, Nature **356,** 225-226 (1992).
[31] D. G. McLean, R. L. Sutherland, M. C. Brant, D. M. Brandelik, P. A. Fleitz, and T. Pottenger, Optics Letters **18,** 858 (1993).
[32] J. Callaghan and W. J. Blau, Journal of Nonlinear Optical Physics & Materials **9,** 505-521 (2000).
[33] C. F. Li, L. Zhang, R. B. Wang, Y. L. Song, and Y. X. Wang, Journal of the Optical Society of America B **11,** 1356-1360 (1994).
[34] T. W. Ebbesen, K. Tanigaki, and S. Kuroshima, Chemical Physics Letters **181,** 501-504 (1991).
[35] G. L. Wood, M. J. Miller, and A. G. Mott, Optics Letters **20,** 973-975 (1995).
[36] C. R. Guiliano and L. D. Hess, IEEE Journal of Quantum Electronics **QE-3,** 338 (1967).
[37] M. Hercher, Applied Optics **6,** 947 (1967).
[38] N. B. Mckeow, Journal of Materials Chemistry **10,** 1979-1995 (2000).
[39] M. Kimura, K. Wada, K. Ohta, K. Hanabusa, H. Shirai, and N. Kobayashi, Macromolecules **34,** 4706-4711 (2001).
[40] F. Zamora and C. Gonzalez, Journal of Macromolecular Science-Physics **B35,** 709-729 (1996).
[41] H. Mandel and A. S. Hay, Journal of Macromolecular Science: Pure Applied Chemistry **A35,** 1797-1808 (1998).
[42] G. J. Clarkson, B. M. Hassan, D. R. Maloney, and N. B. Mckeown, Macromolecules **29,** 1854-1856 (1996).
[43] M. Ozdemir and E. Agar, Spectroscopy Letters **24,** 741-748 (1991).
[44] M. Hanack and H. Heckmann, European Journal of Organic Chemistry, 367-373 (1998).
[45] J. S. Shirk, R. G. S. Pong, S. R. Flom, H. Heckmann, and M. Hanack, Journal of Physical Chemistry A **104,** 1438-1449 (2002).
[46] Y. Chen, M. Hanack, S. O'Flaherty, G. Bernd, A. Zeug, B. Roeder, and W. J. Blau, Macromolecules, in press (2003).
[47] C. Nitschke, S. M. O'Flaherty, M. Kröll, and W. J. Blau, Advanced Materials, submitted (2003).
[48] P. Miles, Applied Optics **38,** 566-570 (1999).
[49] T. J. Xia, D. J. Hagan, A. Dogariu, A. A. Said, and E. W. VanStryland, Applied Optics **36,** 4110-4122 (1997).

Chapter 5

Optical Limiting Studies of Polymer and Multiwalled Carbon Nanotube Dispersions

5.1 Introduction

In recent years carbon nanotubes[1] have been investigated for many potential applications[2,3]. As described in Chapter 3, their unique one dimensional π-electron conjugation, mechanical strength and high thermal and chemical stability, whether they are single walled (SWNT) or multi-walled (MWNT) nanotubes, makes them very attractive for use in many applications. From the point of view of carbon nanostructures as optical limiters; originally carbon black and the C_{60} fullerene have been investigated as nonlinear limiters of high intensity laser pulses. Mansour *et al.*[4] performed an extensive study on the optical limiting of carbon black suspensions. They concluded that the dominant nonlinearity leading to optical limiting in carbon black suspensions and carbon black deposited on glass was thermally induced scattering. They also performed angular dependent scattering measurements on their samples where their results indicated that there was an increase in the scattered light in the forward direction, for energy densities (J cm^{-2}) for which limiting was observed. They attributed the scattering to Mie regime scattering and theoretical fits to the data revealed that the induced scattering centres were approximately three times larger than the initial particles for both 532 nm and 1064 nm irradiation. They attributed the production of the induced scattering centres to the formation and rapid expansion within the pulse width of microplasmas initiated by rapid heating and

subsequent thermo-ionisation of the carbon particles. It has been shown that C_{60} in solution[5-8] excited with high intensity at 532 nm[6] and 1064 nm[8] optically limits through an excited state absorption mechanism termed reverse saturable absorption, similar to the phthalocyanine system that has been discussed in the previous chapter.

Optical limiting studies of SWNTs[9-13] and MWNTs[14-16] in suspension have also been reported. Vivien *et al.*[12] conducted pulse duration and wavelength effects on the optical limiting behaviour of carbon nanotube (SWNT) suspensions. They performed these experiments in water and chloroform over a range of wavelengths from 430-1064 nm with samples that had 75% linear transmittance that was adjusted at each wavelength prior to the nonlinear optical characterisation. Essentially they concluded that nonlinear scattering due to thermally induced solvent-bubble formation and sublimation of carbon nanotubes was the principal mechanism leading to optical limiting in SWNT suspensions. Their conclusions concerning the solvent effects was that they obtained better performance with the chloroform dispersions at all wavelengths and pulse lengths. This they attributed to the fact that the very low heat of vaporisation, surface tension and viscosity of chloroform compared to water allowed for the more rapid formation and growth of solvent-bubbles. Similar results for MWNT and carbon black suspensions from optical limiting and pump-probe experiments led Sun *et al.*[14,15] to conclude that the limiting mechanism in MWNT suspensions was also nonlinear scattering. They conducted their experiments under 532 nm, 700 nm and 1064 nm pumping in the nanosecond regime. They also conducted experiments with MWNTs embedded in polymethyl methacrylate (PMMA) films and suggested that MWNT may be particularly suitable for optical limiting applications in the infrared spectral region. Riggs *et al.*[16] performed optical limiting experiments on suspended and solubilised full length and shortened SWNTs and MWNTs. For their suspended samples, the nanotubes were dispersed in water in the presence of a surfactant to stabilise the system. For their solubilised nanotube systems studies they solubilised shortened carbon nanotubes by attaching them to poly(propionylethylenimine-co-ethylenimine) or by functionalising the nanotubes with octadecylamine. These soluble carbon nanotubes then formed homogeneous solutions in chloroform at room temperature. This was the first reported attempt to temporally stabilise the dispersed nanotubes for optical limiting applications, as all other studies simply dispersed their SWNTs or MWNTs in a common organic

solvent or water, which does not form a temporally stable dispersion. In these latter systems the nanotubes will rapidly fall out of suspension. For their solubilised and stably dispersed nanotube studies Riggs *et al.*[16] performed their experiments under 532 nm pumping with 5 ns pulses. They reported that the dominant optical limiting mechanism was nonlinear scattering for the suspended systems and nonlinear absorption for the solubilised systems. Jin *et al.*[17] also reported two methods to obtain stable MWNT dispersions through functionalisation in dimethylformamide (DMF) for optical limiting. Their results yielded nothing new or different from the results previously discussed by the other authors.

In each of these studies that have been briefly overviewed above a detailed investigation of material composition was not undertaken from the point of view of MWNT or SWNT concentration or purity. Also there remains some debate as to whether the observed nonlinear effects are due to scattering or absorption mechanisms dependent upon the system, or a combination of both. To allow for this uncertainty, in this chapter the nonlinear optical dissipation of the incident light will be called a 'nonlinear optical extinction'. This is to signify that the dissipation of the incident light here may be caused by a combination of both absorption and scattering effects, or contributions from any other dissipative mechanisms for that matter.

Despite the previously discussed studies being of significant fundamental importance the use of nanotubes in a real optical limiting application would almost certainly require some form of matrix to disperse the nanotubes to allow for the fabrication of films, coatings, suspensions or solutions of the matrix and nanotube composite material. It was discussed in Chapter 3 that previously it has been shown that nanotubes can be held in suspension using the polymer poly(meta-phenylenevinylene-co-2,5-dioctyloxy-para-phenylenevinylene)[18] (PmPV), see Figure 5.1a. This procedure doubles as a purification technique[19] to remove the impurities (ie. non-nanotube material) via sedimentation to form temporally stable, high purity, polymer-MWNT dispersions. Essentially one is left with a suspended composite material solution consisting almost solely of solvent, PmPV and MWNTs. Of the studies that have been reported where the authors have prepared polymer-nanotube composite systems for optical limiting[14,16,17] another piece of invaluable information has never been provided. The mass content or concentration of nanotubes in the composite has not been discussed and as such it is impossible to quantitatively

examine and understand the effects of systematically varying the ratio of polymer to nanotube by mass. In addition to the absence of this crucial information the purity of the MWNT or SWNT samples under investigation has never been quoted.

In this chapter, a comprehensive material and optical limiting investigation of a new temporally stable, dispersed polymer and carbon nanostructure composite system is presented. This is compared with optical limiting studies performed on the aforementioned system (PmPV and MWNT from Chapter 3) discussed in the preceding paragraph. In this work the second polymer used was the commercially available poly(9,9-di-n-octylfluorenyl-2,7'-diyl) (PFO), depicted in Figure 5.1b. The fabrication technique and characterisation steps are described where it was found that in composites with PFO as the host polymer, MWNTs and other clearly defined carbon nanostructures were stably dispersed in the polymer. Thus, two distinctly different systems are under investigation and the properties of the materials are investigated to characterise the carbon phases present in each case. Furthermore the optical limiting is examined in relation to the ratio of the polymer to carbon nanostructure mass content. In all cases the carbon nanostructure mass content in the dispersions is measured in an attempt to overcome some of the weaknesses identified in earlier works by other authors. The possible mechanistic implications and the possible origins of the optical limiting are also investigated and examined using laser scattering studies.

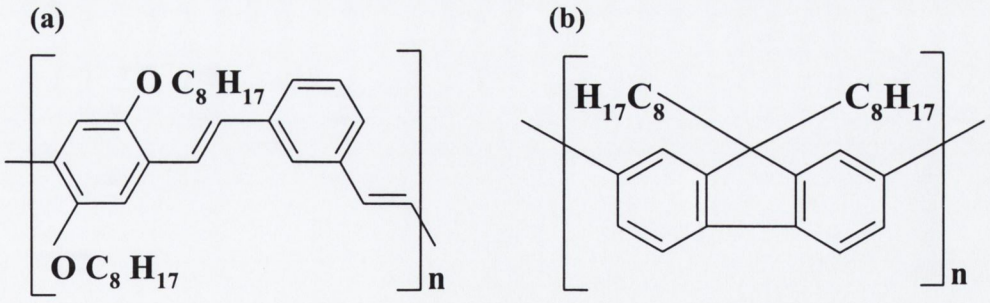

Figure 5.1 Repeat unit chemical structure of **(a)** poly(meta-phenylenevinylene-co-2,5-dioctyloxy-para-phenylenevinylene), (PmPV) and **(b)** poly(9,9-di-n-octylfluorenyl-2,7'-diyl), (PFO).

5.2 Material Preparation and Characterisation

5.2.1 Sample Preparation for Material Composition Investigations

The MWNT soot used here was a multiphase system consisting of carbon nanotubes, carbon onions and turbostratic graphite and was produced in our laboratory using a Krätschmer arc discharge generator[20]. As discussed in Chapter 3 it has previously been reported that the polymer poly(meta-phenylenevinylene-co-2,5-dioctyloxy-para-phenylenevinylene) (PmPV) was found to successfully disperse carbon nanotubes in solution, allowing the other graphitic particles to form a sediment below the almost pure PmPV-MWNT suspension (Figure 3.11).[21,22] Thus, as this is well known and has been extensively applied in the past the material composition properties of this composite system were not investigated further in this work. The PmPV (Figure 5.1a) used in this study was synthesized using a Horner-Eammons condensation co-polymerisation between isothalaldehyde and 2,5-di-n-octlyoxy-1,4-xylene-bis(diethylphosphonate) in dimethylformamide.[23]

In this chapter composite formation will also be investigated using the commercially available polymer, poly(9,9-di-n-octylfluorenyl-2,7'-diyl) (PFO) (Figure 5.1b), which was obtained from the American Dye Source, Inc. (product code ADS129BE). In order to examine the dispersion properties of PFO six identical samples were prepared, each with 60 mg of PFO added to 3 ml of toluene. These were then each heated at 50 °C for 30 minutes to dissolve the polymer. To each sample, 20 mg of nanotube soot were added and these composite mixtures were agitated for 1 min with a high-power sonic tip at 120 W. They were then agitated for an additional 2 hrs in a low-power (60 W) sonic bath to ensure complete and uniform dispersal. The composites were left to stand for different times varying from 0.5 to 96 hrs (in order to allow any impurities to fall out of solution). After this, each composite dispersion was decanted leaving two phases: a black sediment and a suspension with a blue-black appearance. The sediments were then dried and weighed.

As previously reported, the nanotube content of a sample can be measured using electron paramagnetic resonance (EPR).[18,19,24] This is a resonance technique, which measures the microwave-induced transitions between electron spin energy levels ($m_s = + ½$ and $m_s = - ½$ for spin ½ systems), in the presence of a varying magnetic field for a fixed microwave frequency. Information about the local

environment of the unpaired electrons in a sample is contained in the g value, a characteristic number that differs according to the species present. For nanotubes, g = 2.012[25,26] whereas for graphitic impurities g = 2.020 and the resonance in both cases is attributed to conduction electrons.[26] The difference in g values corresponds to a difference in central magnetic field of about 15 G which allows the deconvolution of the signal into a nanotube and a non-nanotube component as shown in Figure 5.2.

EPR* was performed on the decanted suspension and sediment for each settling time.[27,28] For each suspension, approximately 0.7 ml of the decanted solution were drop cast onto a spin-free quartz plate, after being briefly sonicated in the low power sonic bath to ensure homogeneity. This produced solutes weighing about 15 mg each. In the case of the sediments, 2 EPR samples were prepared for each powder due to the fact that they were not fully homogeneous. Approximately 4.5 mg of sediment powder were placed in spin-free quartz tubes. By correct normalisation[24], the EPR signals for the solute and sediment could be directly compared, allowing the percentage of MWNTs and graphitic particles held in solution to be calculated for each sample.

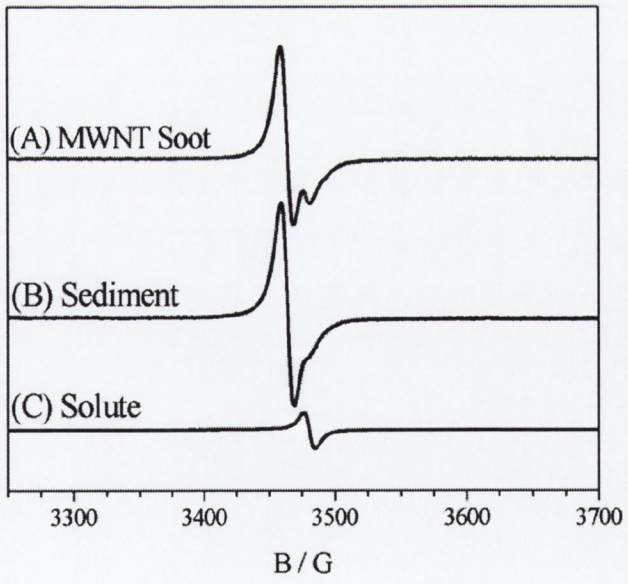

Figure 5.2 EPR derivative spectra of (A) original MWNT Krätschmer generated soot, (B) the sediment from a typical PFO composite formed after 96 hours settling time, (C) a drop cast film made from the solute of a typical PFO composite formed after 96 hours settling time.

* All Electron Paramagnetic Resonance (EPR) measurements were made by R. Murphy.[27,28]

5.2.2 Material Characterisation Studies

The percentage of available nanotubes that remained suspended in the PFO solution after a particular settling time can be measured using EPR as described by Coleman *et al.*[24] By direct comparison of the signal intensities for the nanotube component in both the sediment and the solute, the percentage of nanotubes that were held in the PFO solution could be calculated for each settling time. Similarly, the percentage of non-nanotube material held in the PFO solution was calculated in each case. These results are shown in Figure 5.3 as a function of settling time. It is quite apparent that the amount of non-nanotube material held in solution falls dramatically over time, from 27% after 0.5 hrs to approximately 5% after 96 hrs. The nanotube dispersion however appears to be more stable, with the percentage of MWNTs in solution falling from 55% after 0.5 hrs to 35% after 96 hrs. Additionally, after decantation the 96 hr solution remained stable over a period of months with only minimal additional sediment forming. Thus PFO can be considered a suitable material for the stable dispersion of nanotubes.

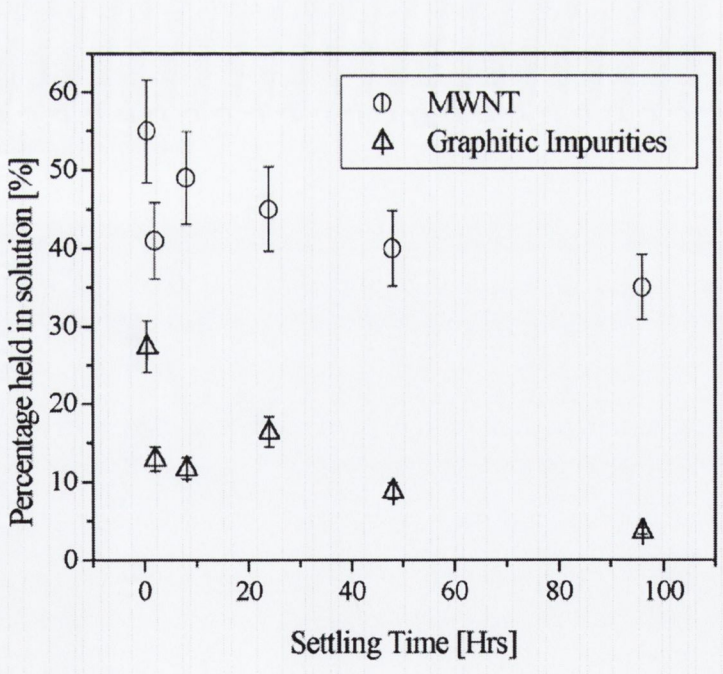

Figure 5.3. Percentage of MWNTs and graphitic particles held in PFO solution (calculated using EPR) as a function of settling time.

However this MWNT-PFO composite formation technique cannot be considered an efficient purification method for two reasons. Firstly, after 96 hours settling, over two thirds of the nanotubes present had sedimented out of solution

resulting in a rather low purification yield. In addition, combination of the EPR results with thermal analysis (Thermo gravemetric analysis (TGA) detailed in Section 5.2.3.2) of the decanted solutes show that at least 10% by mass of the non-polymer material in these purified samples consists of non-nanotube carbon impurities. This compares with a maximum of 8% impurities observed for the PmPV based composite purification method.[19]

Transmission electron microscopy (TEM) studies show that these carbon impurities in PFO composites are mainly in the form of nanoparticles. In Figure 5.4 TEM images of typical carbon nanostructures held in composites fabricated from

(a)

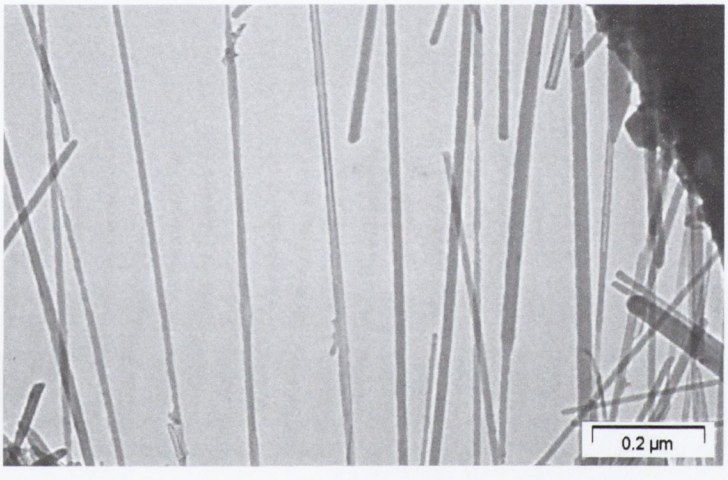

(b)

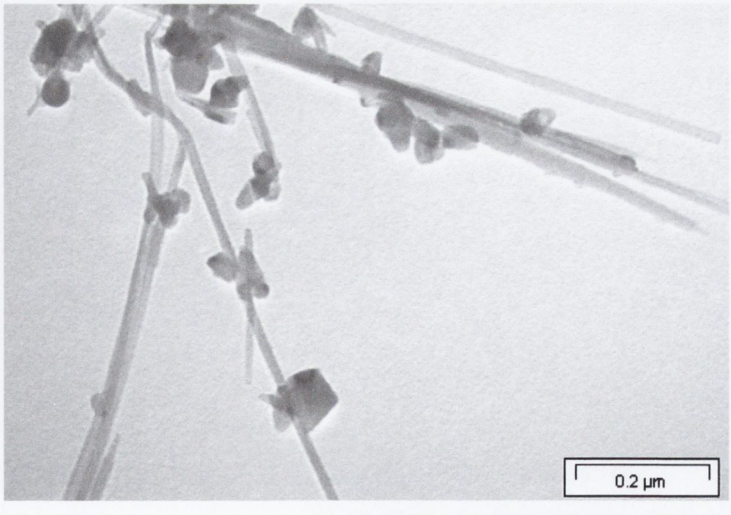

Figure 5.4 TEM images of typical carbon nanostructures held in composites fabricated from **(a)** PmPV[29] and MWNTs and **(b)** from PFO, MWNTs and other graphitic nanoparticles. In these images the polymer has been removed using Buchner filtration as described in reference [19]. The nanotubes and graphitic particles can clearly be seen in the images.

PmPV and MWNTs and from PFO, MWNTs and other graphitic nanoparticles are presented. In these images the polymer has been removed using Buchner filtration as described by Murphy *et al.*[19]. The nanotubes and graphitic particles present in the PFO composites can clearly be seen in the images compared to the almost exclusive MWNTs in the PmPV composites. TEM investigations show the non-nanotube material in purified PmPV composites to be in the form of a small number of large-scale graphitic impurities. Conversely, the non-nanotube material present in the PFO based composite consists of a large number of well-defined nanoparticles. Thus the nanostructure component of the PFO composite consists of ≈ 90% by mass of MWNTs and ≈ 10% by mass nanoparticles. If we assume that the average length and diameter of the MWNT used in this study are approximately 2 microns and 17 nm respectively and that the average diameter of the nanoparticles is similar to that of the nanotubes (as estimated from TEM) then it can be calculated that there are approximately 13 nanoparticles per nanotube in our stably dispersed composite materials. Thus while the nanostructured material is mainly nanotubes, the number density of nanoparticles far exceeds that of the tubes.[27,28]

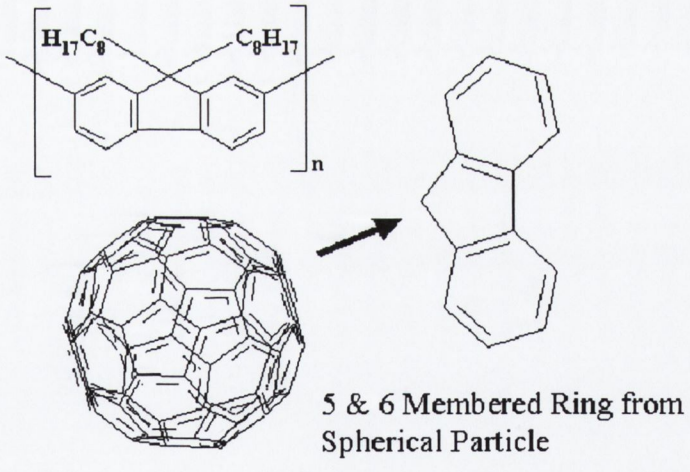

Figure 5.5 Sketch highlighting how the backbone of PFO monomers consist of two six membered rings connected by a pentagon which corresponds to the type of structure needed to provide curvature necessary for closure of graphitic nanoparticles.

The presence of large quantities of nanoparticles in the PFO based composites can possibly be explained by the structure of PFO itself. The backbone of the PFO monomer consists of two six membered rings connected by a pentagon. This is exactly the type of structure expected to provide the curvature needed for

closure of graphitic nanoparticles (see Figure 5.5). It has been shown previously that conjugated polymers tend to map onto the molecular structure of nanotubes.[30] It is therefore likely that the PFO backbone can bind efficiently to the graphitic nanoparticles present in the crude soot, resulting in their dispersion in PFO based composite solutions. Thus, these materials cannot be considered as polymer-nanotube composites in the strictest sense. However we can consider them as nanostructured carbon-polymer composites, which are interesting in their own right for optical applications.

5.2.3 Sample Preparation for Optical Experiments

5.2.3.1 Initial Preparation

The composites for the optical experiments were prepared as follows. Two 20 g L^{-1} solutions of the polymers PmPV and PFO in spectroscopic grade toluene were dissolved. To each solution a mass of Krätschmer arc discharge generated soot equal to half the total mass of the polymer in that solution was added. This was ultrasonically agitated using a high power sonic tip (120 W) over 60 s. As overexposure to ultrasound can damage the nanotubes the samples were then transferred to a low power sonic bath (60 W) where they were gently agitated for a number of hours. The solutions were then left to stand undisturbed for a number of days allowing the sedimentation of the non-nanotube graphitic particles. The suspension was then separated from the sediment by decantation. To vary the mass fraction of nanotubes or nanostructures the composites were blended with a pure polymer solution. These were then diluted down to 1 g L^{-1} for optical measurements.

5.2.3.2 Thermo-Gravimetric Analysis

The MWNT or carbon nanostructure mass fraction in each composite was measured using thermo-gravimetric analysis, (TGA). In this technique the sample is heated in air and the sample mass is monitored as it is oxidised. This involves measuring the mass of the sample as a function of temperature (from 25 to 1000 °C, at a constant heating rate of 10 °C min^{-1}). The gas used in all cases was air, with a flow rate of 20 L min^{-1}. This was performed on pure polymer samples, all the composites and a Krätschmer arc discharge generated soot sample. These oxidation curves are plotted in Figure 5.6, with the PmPV based composite materials depicted in Figure 5.6a and

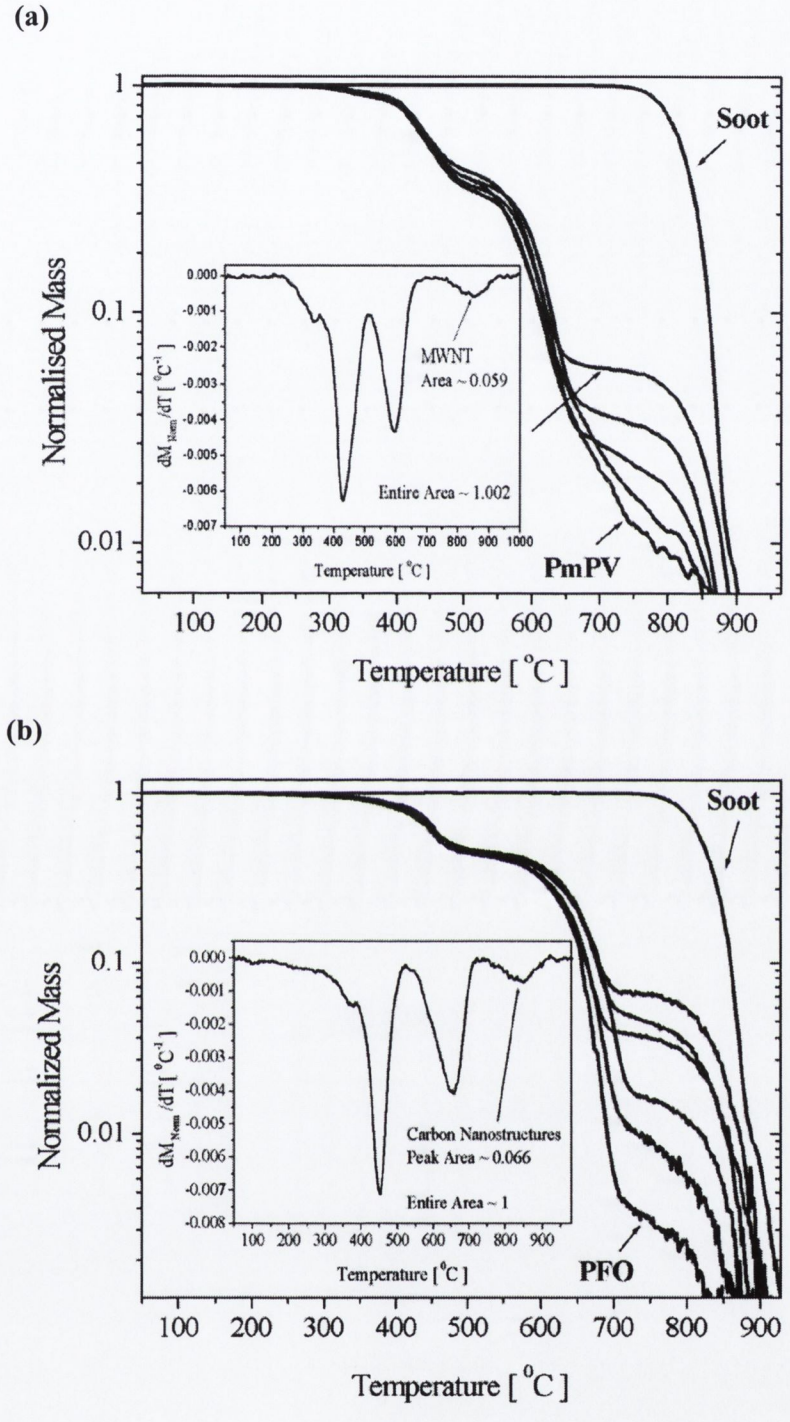

Figure 5.6 Thermo-Gravimetric Analysis (TGA) curves of the materials prepared for optical experiments, **(a)** Pure PmPV, PmPV-MWNT composites and arc discharge generated soot and **(b)** Pure PFO, PFO-carbon nanostructures (MWNTs and other nanostructures) composites and arc discharge generated soot. In both plots the normalised mass is plotted against the temperature of the sample. The insets in **(a)** and **(b)** are the first temperature derivative of the normalised mass for the composites with maximum MWNT or carbon nanostructure mass content.

the PFO based composite materials in Figure 5.6b. In Figure 5.6a for the PmPV-MWNT composite materials it can be seen that by 650 ^{0}C the PmPV sample is almost completely oxidized while the MWNT soot only begins to burn at ≈ 770 ^{0}C. For the composite samples almost no oxidation occurs between those temperatures. The stable mass in this region represents MWNTs, some traces of graphitic impurities and possibly some polymer impurities. In Figure 5.6b for the PFO and dispersed carbon nanostructures composite systems (these are referred as carbon nanostructures rather than MWNTs here as the nanostructure content is both MWNTs and spherical particles as discussed in the previous section) similar results can be observed. Again, it can be seen that by ≈ 650 ^{0}C the pure PFO polymer sample is almost completely oxidised while the MWNT soot only begins to burn at ≈ 770 ^{0}C. For the composite samples almost no oxidation occurs between those temperatures. The stable mass in this region represents certainly MWNTs, other carbon nanostructures, some traces of graphitic impurities and again possibly some polymer impurities.

In Figure 5.6 the normalised mass was plotted against the temperature of the sample. This has the advantage that a numerical integration of the first derivative with respect to temperature over the MWNT section (or at least the carbon nanostructures section) of the curve gives the fractional mass of MWNTs (or carbon nanostructures) in the sample. The numerical integration over the entire curve trivially gives a value of 1, the entire normalised mass. The insets in both Figure 5.6a and Figure 5.6b are the first temperature derivative of the normalised mass for the composite with maximum MWNT or carbon nanostructure mass fraction. These were found to be ≈ 0.059 calculated from the numerical integration of the MWNT peak for the PmPV based composites and ≈ 0.066 fraction by mass for the PFO case. Numerical integration of the other curves for the PmPV based composites gave MWNT mass fractions of 0.013, 0.025 and 0.036. Similar numerical integrations for the other curves relating to the PFO based composites gave carbon nanostructure mass fractions of 0.011, 0.019, 0.038 and 0.050 for the range of composite samples.

5.3 Linear Absorption Coefficients

The linear absorption spectra, recorded using a standard spectrophotometer at room temperature in the 200-1100 nm region, exhibited similar spectra for carbon nanostructure concentration variations for both series of materials. A representative spectrum from the composite dispersion with highest carbon nanostructure mass content for PmPV dispersed composites and PFO dispersed composites are shown in Figure 5.7a and Figure 5.7b respectively. The spectra for all samples were reasonably flat in the region of 532 nm with a relatively low linear absorption. The linear absorption coefficients (α_0) at 532 nm for each of the composite dispersions are plotted as a function of their carbon nanostructure mass fraction in the inset of both figures. As can be seen from this plot the linear absorption coefficients increase smoothly with the carbon nanostructure content for both the PmPV and the PFO composite materials. This was not unexpected, as successively increasing the relative volume of 'black' particles to partially transparent solutions would obviously result in increasing the linear absorption coefficient of the starting solution. The linear absorption coefficients as a function of carbon nanostructure content are presented in Table 5.1.

PmPV Composites		**PFO Composites**	
MWNT Fraction	**α_0 [cm^{-1}]**	**Nanostructure Fraction**	**α_0 [cm^{-1}]**
0.000	0.68	0.000	0.62
0.013	0.99	0.011	0.94
0.025	1.05	0.019	1.17
0.036	1.73	0.038	2.36
0.059	3.75	0.050	3.15
		0.066	4.30

Table 5.1 Linear absorption coefficients α_0 for PmPV and PFO composite samples opposite their corresponding MWNT or carbon nanostructure mass content.

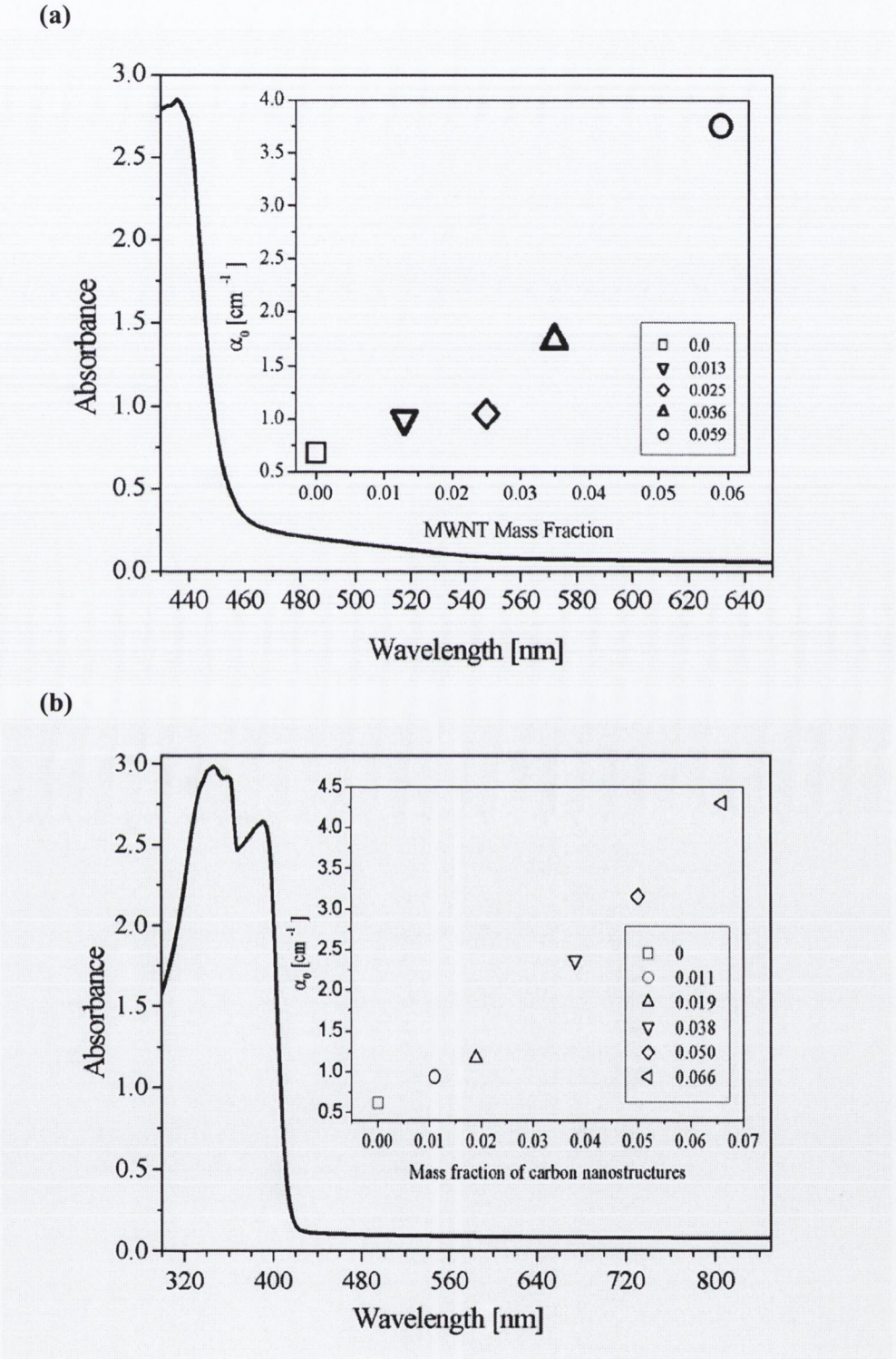

Figure 5.7 Typical UV-visible spectrum for **(a)** the PmPV-MWNT composites and **(b)** the PFO-carbon nanostructure materials. The inset in **(a)** and **(b)** plots the linear absorption coefficient as a function of the carbon nanostructure mass fraction in the sample at 532 nm.

5.4 Nonlinear Extinction Coefficients

An intensity dependent open aperture z-scan investigation (using the apparatus as described in Section 3.3.2 in 1mm quartz cells) was performed on all samples of PmPV-MWNT and PFO-carbon nanostructures composites described above. The results from theory outlined in Chapter 3, equation (3.33), were applied to the open aperture data using least squares regression. The magnitude of the dissipation quantified by the effective nonlinear absorption coefficient β_I, determined from the fitting of equation (3.33) to the open aperture scans was determined as a function of the focal intensity for all samples. The third order nonlinear absorption coefficient β utilised in Section 3.32 has been replaced with β_I here to signify an effective absorption coefficient. The word effective in itself signifies scattering or possible higher order absorption contributions to the nonlinear optical response. All of the performed open aperture z-scans, with the exception of the pure PFO sample (carbon nanostructures = 0.0), performed exhibited a decrease of transmittance about the focus typical of an induced positive nonlinear extinction of incident light over the intensity range that was explored. Typical open aperture z-scan fits using least squares regression of equation (3.33) with β_I and z_0 treated as free parameters for each PmPV-MWNT sample are shown in Figure 5.8. These typical examples all

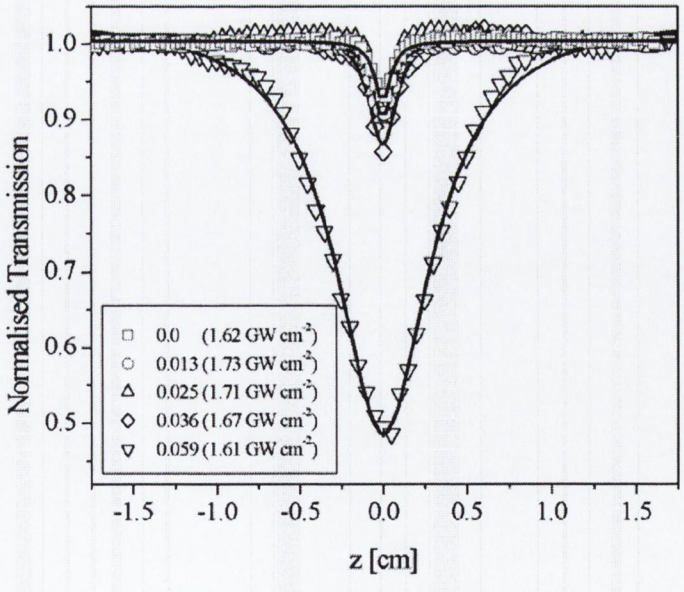

Figure 5.8 Typical open aperture data for each PmPV-MWNT sample, normalised transmission is plotted as a function of z position. Data is shown for $I_0 \sim 1.62$-1.73 GW cm^{-2}, precise values of I_0 are in the legend.

(a)

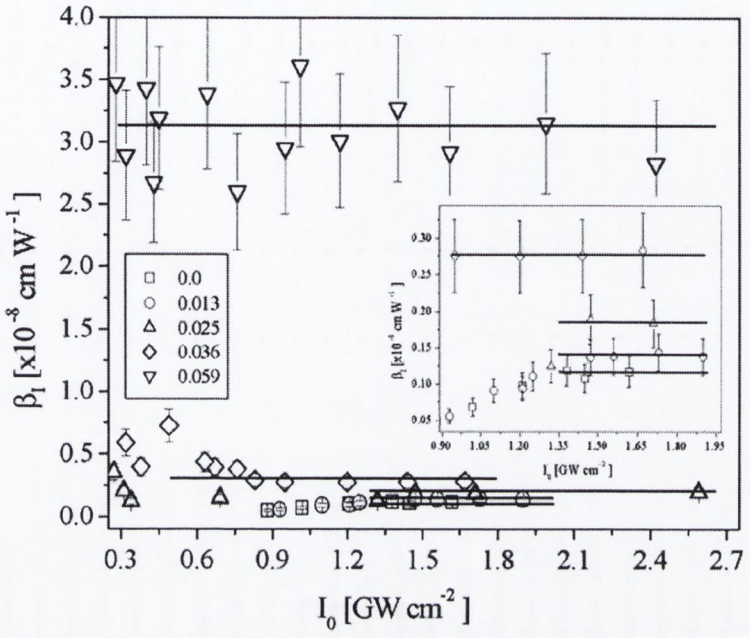

(b)

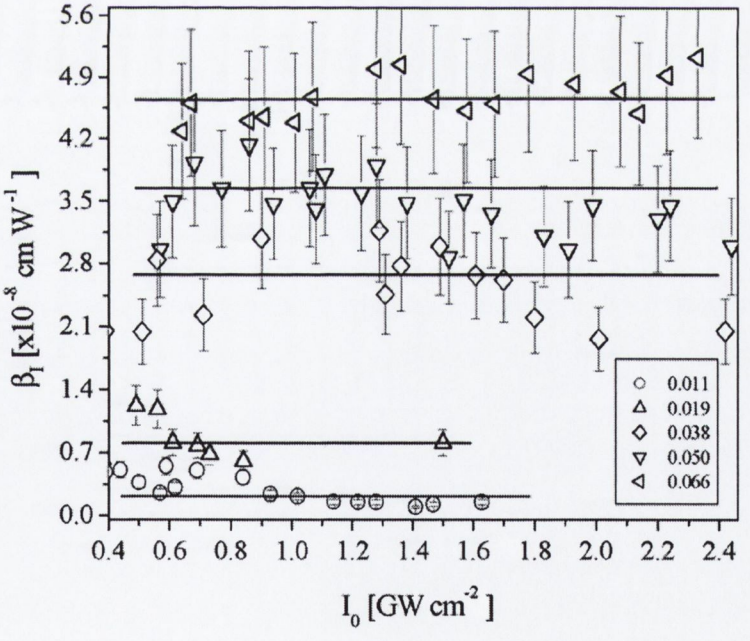

Figure 5.9 Plots of effective nonlinear absorption coefficient β_I as a function of incident focal intensity I_0 for **(a)** PmPV-MWNT composite samples and **(b)** PFO-carbon nanostructures samples. The inset in **(a)** is an expansion of the 0.9-1.9 GW cm^{-2} section of the data to show a clearer representation of the four samples with lower MWNT content. In both figures the solid lines are intended to approximately guide the eye to the average $\beta_I(I_0)$ exhibited by each sample.

have I_0 values in the region of 1.61 - 1.73 GW cm^{-2}. It can be seen that the curve fits to the data are mathematically good, typically with R^2 values in the region of 0.99.

It can be noted that while the 0.0 and 0.013 MWNT mass content curves almost overlap each other the reduction in transmission of the 0.025, 0.036 and 0.059 MWNT mass content curves can be clearly seen. The intensity dependence of β_I is displayed in Figure 5.9. In Figure 5.9a PmPV-MWNT composite samples are shown and in Figure 5.9b the PFO-carbon nanostructures samples are depicted. The inset in Figure 5.9a is an expansion of the 0.9-1.9 GW cm-2 section of the data to show a clearer representation of the four samples with lower MWNT content. In both figures the solid lines are intended to approximately guide the eye to the average $\beta_I(I_0)$ exhibited by each sample. In both of these figures an approximately constant β_I over I_0 is seen. The physical implication of this is that the effective absorption (or extinction) coefficient exhibited by these systems is behaving in a manner where only third order nonlinearities are required to describe the nonlinear response. The PmPV composites with 0.0 and the 0.011 MWNT mass fractions exhibit different lower intensity type behaviour from the other materials in the PmPV series (see inset of Figure 5.9a). The β_I coefficient increases with I_0 as opposed to the other materials that appear to be approximately constant over the region, and seems to suggest some type of unsaturated nonlinearity for lower intensities.

5.5 Case Study: Mixed Dielectric Investigation of PmPV Composites

5.5.1 Background Theory

The PmPV-MWNT system is reasonably well defined where the impurities are generally observed as large-scale infrequent graphitic particles. Thus if one assumes that the system is purely a host medium (dissolved PmPV) in which nanotube inclusions are randomly dispersed the average dielectric function for the polymer-MWNT system can be described using Maxwell-Garnett theory. This model describes an inhomogeneous two-component medium composed of 'inclusions' embedded in an otherwise homogeneous 'host' matrix. The PmPV composite system can be viewed as a polymer host dielectric with dielectric constant ε_h, doped with nanotube inclusions of dielectric constant ε_i. The generalized Maxwell-Garnett dielectric function for an inclusion-host system can be written as[31]

$$\varepsilon_{av} = \frac{(1-p)\varepsilon_h + pf_i\varepsilon_i}{1-p+pf_i} \tag{5.1}$$

where ε_{av} is the average dielectric constant, p is the volume fraction of the inclusions, f_i is the local field enhancement factor of the inclusions, ε_h and ε_i are the dielectric constants of the host and inclusions respectively.

As MWNTs are long rod-like cylindrical structures, considering the nanotube as a highly extended prolate spheroid structure reasonably approximates the nanotube geometrically. This spheroid would have an eccentricity approximately equal to unity, where the eccentricity, e, is defined as e = 1-((|*minor axis*|)^2 /(|*major axis*|)^2). This analytically defines an ellipsoidal needle-like structure. The local field factor of the inclusions is defined as[31]

$$f_i = \iint P(L_1, L_2)\frac{\sum_{j=1}^{3}\lambda_j}{3}dL_1 dL_2 \tag{5.2}$$

where $P(L_1,L_2)$ is the shape probability distribution function of the inclusions, L_1 and L_2 are geometrical factors, called demagnetisation factors, relating to the major and minor axes of the ellipsoidal inclusions respectively and λ_j are the principal components of the tensor relating the average electric field components in the host and the inclusions defined by:

$$\lambda_j = \frac{\varepsilon_h}{\varepsilon_h + L_j(\varepsilon_i - \varepsilon_h)} \tag{5.3}$$

For a prolate spheroid the demagnetisation factors are governed by the two following expressions.[31]

$$L_1 + L_2 + L_3 = L_1 + 2L_2 = -ab^2\int_0^{\infty}\frac{d}{dq}\frac{1}{f(q)}dq = 1 \tag{5.4}$$

$$L_1 = \frac{1-e^2}{e^2}\left(-1+\frac{1}{2e}\log_e\left[\frac{1+e}{1-e}\right]\right) \tag{5.5}$$

In these expressions a and b are the semi-major and semi-minor axes of the ellipsoid respectively and $f(q) = (2(q + a^2)(q + b^2))^{1/2}$. If it is assumed that e $\rightarrow$ 1 and this is inserted into Equation (5.5) this yields $L_1 = 0$. L_1 can then be inserted into Equation (5.4) and as the cross-section of the ellipsoid discussed here is circular this implies $L_2 = L_3 = 0.5$. These demagnetisation factors can then be substituted into Equation (5.3) to determine λ_j. These in turn can be substituted back into Equation (5.2) and

the local field factor of the cylindrical needle-like inclusions can be calculated as

$$f_i = \frac{5\varepsilon_h + \varepsilon_i}{3(\varepsilon_h + \varepsilon_i)} \tag{5.6}$$

under the following approximation. In order to simplify the derivation the integral over the shape probability distribution function was set to unity. This is a reasonable approximation as MWNTs are tens of nanometers in diameter and microns long with aspect ratios generally in excess of 1000. This assumption is further strengthened by the fact that during the composite preparation process almost solely nanotubes are held while other non-cylindrical graphitic particles fall out of the polymer host.[18] Thus, the eccentricity of the inclusions is typically in the region of $0.999 < e < 1$, as the inclusions are almost exclusively nanotubes.[19]

In the presence of an intense electric field the polarization induced in a material may be written as

$$\Delta P = P^{(1)} + P^{(2)} + P^{(3)} + \cdots \tag{5.7}$$

where $P^{(n)}$ with $n > 1$ is a nonlinear polarization term. As previously discussed in Chapter 3 for the case of an isotropic composite with a random distribution of inclusions $P^{(2n)} = 0$, for all n and

$$P^{(1)} = \varepsilon_0 \chi^{(1)} E \tag{5.8}$$

$$P^{(3)} = \varepsilon_0 \chi^{(3)} E^3 \tag{5.9}$$

where $\chi^{(1)}$ and $\chi^{(3)}$ are the linear and third order susceptibilities of the composite medium. The change in the polarization can be described as an optically induced change in the optical dielectric constant as

$$\delta\varepsilon \propto \chi^{(3)} \left| E(\omega) \right|^2 \tag{5.10}$$

If the third order susceptibility relevant to the internal field within the inclusions, E_i, is designated with $\chi_i^{(3)}$ then by analogy this can be expressed as

$$\delta\varepsilon_i \propto \chi_i^{(3)} \left| E_i \right|^2 \tag{5.11}$$

where in this case the subscript i relates to the inclusion. If E_i is given by $|E_i| = f_i|E|$ and f_i is taken as derived in Equation (5.6) then combining Equations (5.1), (5.10) and (5.11) yields

$$\chi^{(3)} = p \left| f_i^{-1} \right|^4 \chi_i^{(3)} \tag{5.12}$$

where p is the volume fraction of the MWNT inclusions.

5.5.2 Results and Discussion

Effective values for $Im\{\chi^{(3)}\}$, ($Im\{\chi_{eff}^{(3)}\}$), were calculated for each PmPV based sample by inserting the effective nonlinear absorption coefficients β_I, presented in Figure 5.9a into Equation (3.24). The calculated values of $Im\{\chi_{eff}^{(3)}\}$ are plotted against their corresponding focal intensities I_0 in Figure 5.10. It can be seen from this plot that the value of $Im\{\chi_{eff}^{(3)}\}$ is approximately constant within experimental error for the 0.036 and 0.059 mass content samples over the entire range of I_0. The lower MWNT mass fraction samples exhibit a sort of unsaturated type behaviour for values of I_0 less than $\approx$ 1.3 GW cm^{-2} and then the $Im\{\chi_{eff}^{(3)}\}$ value levels out to a constant value indicating a saturated constant value. Lines with slope = 0 were fitted to the higher intensity data to determine the average value of $Im\{\chi_{eff}^{(3)}\}$. These numerical values are presented in Table 5.2.

MWNT Fraction	α_0 [cm^{-1}]	$Im\{\chi_{eff}^{(3)}\}$ [esu]	$Im\{\chi_{i\,eff}^{(3)}\}$ [esu]
0.000	0.683	4.34×10^{-13}	0
0.013	0.998	5.26×10^{-13}	8.03×10^{-12}
0.025	1.053	7.16×10^{-13}	1.14×10^{-11}
0.036	1.732	1.06×10^{-12}	1.24×10^{-11}
0.059	3.754	1.16×10^{-11}	1.10×10^{-10}

Table 5.2 Numerical values for $Im\{\chi_{eff}^{(3)}\}$ and $Im\{\chi_{i\,eff}^{(3)}\}$ for PmPV composites.

Subsequently this $Im\{\chi_{eff}^{(3)}\}$ was inserted into Equation (5.12) to calculate an effective value of the susceptibility of the inclusions, $Im\{(\chi_{i\,eff}^{(3)})\}$. These values are presented in Table 5.2. It can be seen that at low level MWNT content (0.0, 0.013, 0.025 and 0.036) the magnitude of $Im\{(\chi_{i\,eff}^{(3)})\}$ shows a slight increase with mass fraction and that the magnitude of $Im\{(\chi_{i\,eff}^{(3)})\}$ is one order higher for the sample with highest MWNT mass content (0.059). This is interesting as $Im\{(\chi_{i\,eff}^{(3)})\}$ is an $Im\{(\chi_{eff}^{(3)})\}$ per unit volume, ignoring the local field correction, which seems to

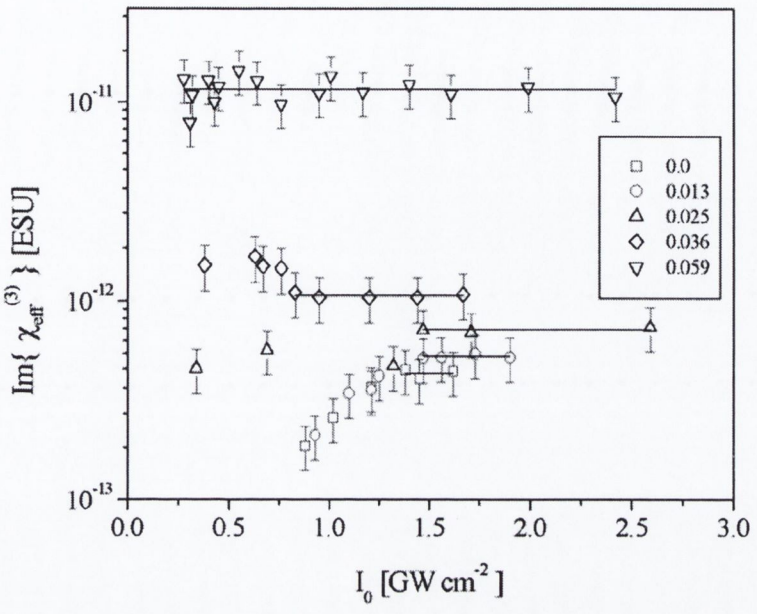

Figure 5.10 Plots of effective $Im\{\chi^{(3)}\}$, $Im\{\chi_{eff}^{(3)}\}$, as a function of incident focal intensity for each PmPV composite.

indicate that at high concentrations tube-tube interactions, or some other concentration induced source of nonlinear attenuation, may have to be accounted for to describe the observed effects. These interactions appear to significantly enhance the nonlinearity.

5.6 Optical Limiting and Nonlinear Transmission Studies

5.6.1 Introduction

In this section the nonlinear transmission in the PmPV and PFO based composite samples will be investigated. Initially the normalised nonlinear transmission will be plotted against incident pulse energy density for each of the samples measured using the open aperture z-scan technique outlined above. As several open aperture scans were taken for each sample, increasing the energy per pulse in successive scans all scans for each sample are overlaid on these plots where the normalised transmission is plotted against the energy density in a single pulse. The pulse energy density can be defined as $F_{Pulse} = E_{Pulse}/(\pi w(z)^2)$ in this case where E_{Pulse} is the energy in a single pulse and $w(z)$ is the radius of the propagating Gaussian pulse as a function of position z.

5.6.2 Optical Limiting exhibited by PmPV-MWNT composite materials

The PmPV-MWNT samples are presented in Figure 5.11a where normalised transmission has been plotted against energy density. In Figure 5.11b, for clarity, the data for the 0.0, 0.013 and 0.025 MWNT mass content samples has been re-plotted where the normalised transmission of the 0.0 MWNT mass content plot has been shifted by +15% and the normalised transmission of the 0.025 MWNT mass content plot has been shifted by –15%. All samples show positive nonlinear extinction, or 'optical limiting', corresponding to reductions in the normalised transmission at suitably high incident energy densities. The optical limiting performance is similar for the 0.0, 0.013 and the 0.025 MWNT mass content samples. It can be seen from analysis of Figure 5.11b that the maximum change in transmittance, in the energy density range studied, increases from ≈ 7% maximum extinction for the PmPV without any MWNT's (0.0 MWNT mass content) to ≈ 10% maximum extinction for the 0.013 MWNT mass content sample to ≈ 12% maximum extinction for the 0.025 MWNT mass content sample. These transmission changes occur at pulse energy densities ≈ 17-18 J cm^{-2}. The onset of the nonlinear transmission regime is similar for each of these three materials ≈ 11-12 J cm^{-2}. The samples with MWNT mass content ≈ 0.036 and 0.059 both begin to respond nonlinearly about one order of magnitude in energy density lower at a value slightly below 1 J cm^{-2}. At 10 J cm^{-2} the sample with ≈ 0.036 MWNT mass content has a normalised nonlinear extinction of about 12%, while the sample with ≈ 0.059 MWNT mass content has a normalised extinction of ≈ 41%. The other three samples (0.0, 0.013 and 0.025 MWNT content by mass) have ≈ 0% nonlinear extinction at this energy density. Thus the PmPV-MWNT materials exhibit a dramatic improvement in the optical limiting performance when the MWNT mass content is increased from 0.013 to 0.036 by mass. The point, at which nonlinear responses begin to occur, is reduced by an order of magnitude from approximately 10 J cm^{-2} to less than 1 J cm^{-2}. There is an even more pronounced and dramatic improvement in the optical limiting performance when the MWNT mass content is increased from 0.036 to 0.059. The onset (energy density at which nonlinearities become evident) of optical limiting is not significantly changed but the nonlinear extinction is greatly enhanced in magnitude. Quantitatively, the magnitude of the nonlinear extinction at 10 J cm^{-2} is enhanced by a factor ≈ 4 while the mass of MWNTs in the sample is only increased by a factor ≈

(a)

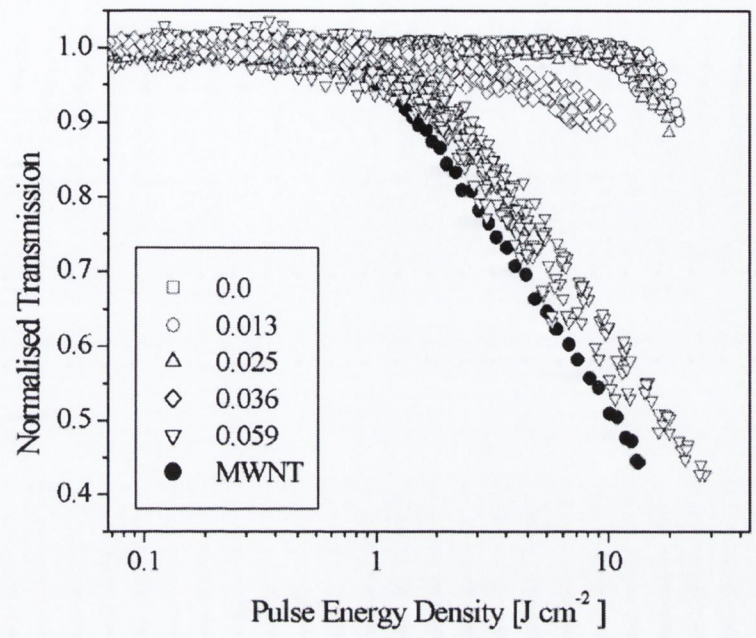

(b)

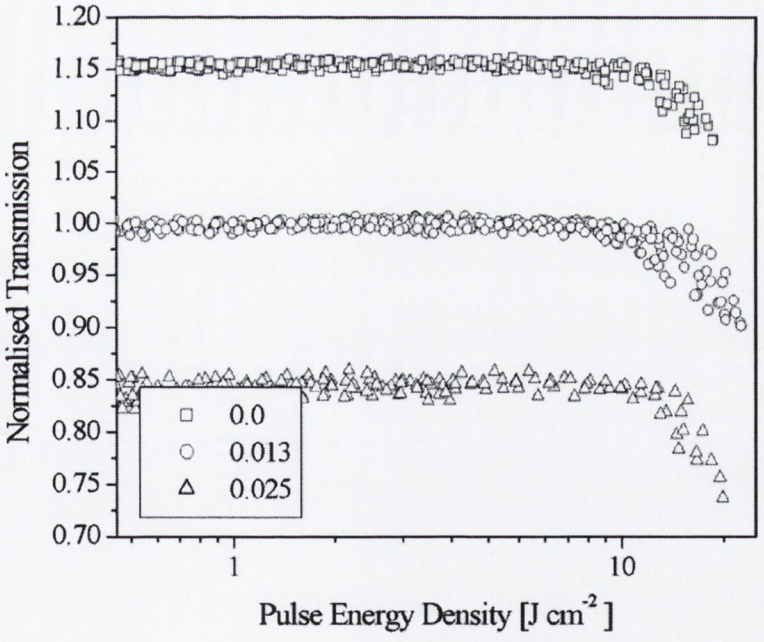

Figure 5.11 **(a)** Plots of normalised transmission against incident pulse energy density for the PmPV MWNT composites. The data labelled MWNT is the optical limiting exhibited by a purified dispersion of multi-walled carbon nanotubes in toluene with linear transmission ≈ 67%.
(b) The samples with MWNT mass content 0.0, 0.013 and 0.025 are re-plotted where the transmission of the 0.0 MWNT mass fraction plot was shifted by +15% and the transmission on the 0.025 MWNT mass fraction plot was shifted by –15% for clarity.

2. At pulse energy densities of ≈ 17-18 J cm^{-2} the change in transmittance is ≈ 55% for the 0.059 MWNT mass content sample. This is a factor of five times bigger than the changes in transmittance of the other samples at these energy densities.

Thus, as discussed in the previous paragraph, the nonlinear dissipation of the incident laser pulses shown in Figure 5.11a clearly shows two different operating regimes. The nonlinear responses of the lower MWNT mass content samples 0.0, 0.013 and 0.025 are dominated by the polymer response while the higher MWNT mass content samples, 0.036 and 0.059 exhibit MWNT dominant behaviour. This can clearly be seen in the figure, where the higher MWNT mass content samples (0.036 and 0.059 MWNT content by mass) are nonlinearly active below ≈ 1 J cm^{-2} and the lower MWNT mass content samples (0.013 and 0.025 MWNT by mass) are only nonlinearly active above ≈ 10 J cm^{-2}. A purified MWNT suspension in toluene with linear transmission of ≈ 67% at 532 nm, also tested under exactly the same experimental parameters as the composite materials, was also included in Figure 5.11a. This linear transmission percentage is approximately equal to the transmission of the composite with 0.059 MWNT mass content, which had a linear transmission ≈ 69%. The Buchner filtration purification method that was used to remove the polymer from the purified nanotubes has been described recently.[19]

There was thus only a slightly higher mass of nanotubes in this pure MWNT suspended sample than in the 0.059 MWNT mass content composite as the linear transmissions at 532 nm were similar, and the PmPV in the composite only contributes slightly to the absorption coefficient. Thus, one would expect that the onset of nonlinear behaviour, and the rate of the extinction relative to the incident energy density, to be similar if this were in fact truly a MWNT dominant regime. This can clearly be seen to be the case in the figure. The MWNT dominant regime becomes nonlinearly active at energy densities about one order of magnitude lower that the polymer matrix dominating regime. It is also interesting that the lower MWNT mass fraction samples show unsaturated behaviour at lower intensities as can be seen in Figure 5.10. It seems to suggest that at 1 g L^{-1} the PmPV-MWNT composite requires a critical MWNT inclusion percentage by mass ≈ (3.1 ± 0.6)% above which MWNT behaviour dominates and below which the polymer matrix dominates the response. The mechanism of the nonlinear behaviour of the PmPV is probably two-photon or multi-photon absorption of the incident radiation.

5.6.3 Optical Limiting by PFO-Carbon Nanostructure composite materials

The normalised nonlinear transmission plotted against incident pulse energy density for each of the PFO-carbon nanostructures samples measured are presented in Figure 5.12a. For clarity, the nonlinear transmission of the 0.038, 0.050 and 0.066 carbon nanostructure mass content samples were reproduced in Figure 5.12b where in this case the data was not normalised for clarity and contains both its linear and nonlinear components. As in the previous section data collected from a sample dispersion of purified multi-walled carbon nanotubes in toluene measured under exactly the same conditions as the composites, labelled MWNT in the figure, with linear transmission of approximately 67% at 532 nm was also included in the figure. This again was added to allow a comparison of the magnitude of the nonlinear response observed here with that of the response exhibited by other carbon nanostructure systems, such as the PmPV-MWNT composites presented above or other systems investigated by other authors. This linear transmission percentage of the purified MWNT sample is approximately equal to the transmission of the composite with 0.066 carbon nanostructure mass content, which had a linear transmission ≈ 68%.

All PFO samples, depicted in Figure 5.12a, containing carbon nanostructures exhibited positive optical limiting about the focal point of the lens, while the pure polymer (carbon nanostructure mass fraction = 0.0) exhibited no dissipation of the incident light, regardless of the incident intensities. The pure PFO data has thus been omitted from the Figure 5.12a in the interest of clarity. The onset of optical limiting for the other PFO samples is similar in all cases, and occurs at approximately 0.3 J cm^{-2}, indicating that the limiting is directly caused by the carbon nanostructures present in the composite dispersions. The limiting of the samples is dependent on the mass fraction of carbon nanostructures. The magnitude of the nonlinear effect increases systematically when the mass fraction of the nanostructures is increased from 0.011 to 0.038. The nonlinear effects however clearly become saturated at carbon nanostructure mass fractions in excess of 0.038. For example, at a pulse energy density of ≈ 8 J cm^{-2} the normalized transmission for the 0.011 nanostructure mass fraction sample is ≈ 94%, ≈ 80% for the 0.019 mass fraction sample and ≈ 56%, 55% and 53% for the remaining samples in order of increasing carbon nanostructure content. This corresponds to nonlinear extinction percentages of ≈ 6%, 20%, 44%,

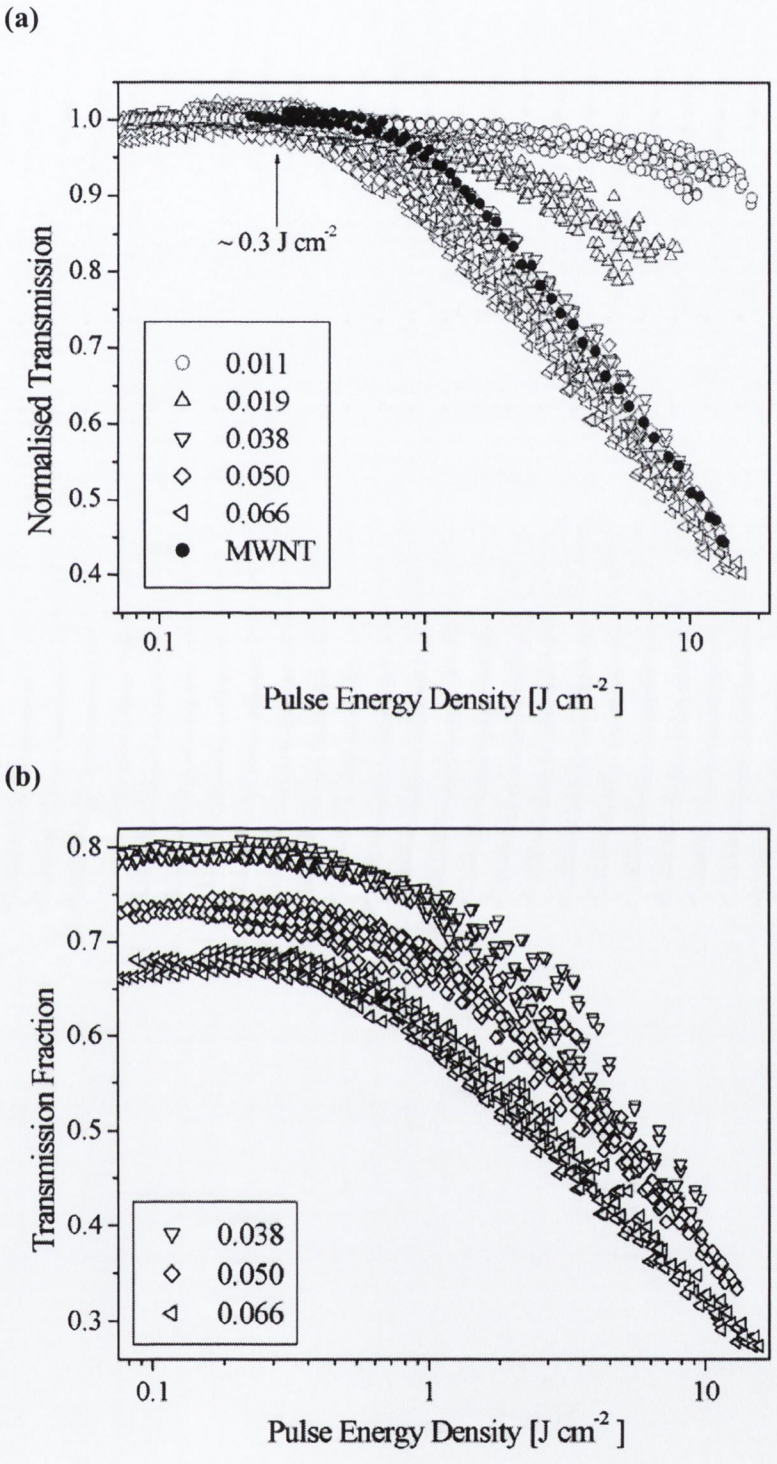

Figure 5.12 **(a)** Plots of normalised transmission against incident pulse energy density for the PFO-carbon nanostructure composites. The data labelled MWNT is the optical limiting exhibited by a purified dispersion of multi-walled carbon nanotubes in toluene with linear transmission ≈ 67%. **(b)** The samples with 0.038, 0.050 and 0.066 carbon nanostructure content are re-plotted as transmission against pulse energy density. The linear absorption is not normalised from the data in this case for clarity.

45% and 47% at 8 J cm^{-1} irradiation for the PFO-carbon nanostructure composites in order of increasing carbon nanostructure mass content. In all cases data was collected for each sample up to the point at which the sample exhibited burning effects, which occurred at ≈ 9.1 J cm^{-2}, ≈ 12.5 J cm^2 and ≈ 15.0 J cm^{-2} for the 0.038, 0.050 and 0.066 mass fraction of carbon nanostructures samples respectively. It can be seen from Figure 5.12b that the significant differences in the optical performance of the samples with nanostructure mass content 0.038, 0.050 and 0.066 are in the linear absorption regime (low energy density) and in the energy density above which the sample was damaged.

Thus in contrast to the pure PmPV and PmPV-MWNT composite samples a polymer response in PFO was not observed and thus, accordingly, only one regime where the nonlinearity was attributed to the carbon nanostructures was observed. It can also be noted that compared to the purified MWNT dispersion that the highest carbon nanostructure mass content sample appears to perform slightly better. The PFO-carbon nanostructure content ≈ 0.066 sample begins to respond nonlinearly at slightly lower energy densities and attenuates ≈ 5-7% more effectively that the purified MWNT dispersion for comparable energy densities incident on the samples.

5.6.4 An Alternative Optical Limiting Representation

An alternative approach to representing the optical limiting of a sample is to plot the input against the output (transmitted) intensity. In the case of the z-scan experiment this is most readily done by using the product of the transmission minimum on focus of the open aperture scan and the input focal intensity as the output intensity, plotted against the input focal intensity. The optical limiting performance of each of the PmPV-MWNT composite materials is presented using this approach in Figure 5.13. In this plot the straight lines indicate the linear transmittance in the absence of nonlinear contributions.

It can be clearly seen that each sample has enhanced optical extinction with increasing intensity as the data for each sample can be seen to dip further below its linear transmittance line as the incident intensity increases. In general for the PmPV-MWNT composites it was found that the samples with higher MWNT content, and

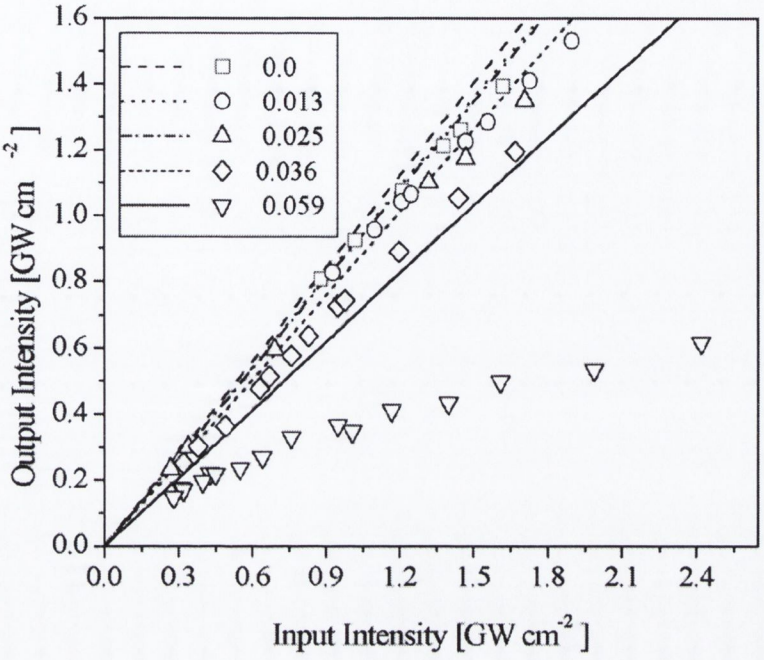

Figure 5.13 Plots of output against input on focus intensity for each PmPV-MWNT sample. The straight lines, defined in the legend, represent the linear optical transmission curve for the respective samples.

thus lower linear transmittance of low intensity light, see Figure 5.7a, block the incident light more effectively at higher incident energy densities or intensities than the lower MWNT content samples.

To allow for comparison between the maximum attenuations measured in the PmPV-MWNT and the PFO-carbon nanostructure composite dispersions the output against input intensity has been plotted for both the PmPV and PFO based materials with highest carbon nanostructure content in Figure 5.14. In the figure the straight lines, both the solid and the dashed line, represent the linear optical transmission curve for the PmPV-MWNT and PFO-carbon nanostructure composite samples respectively.

It can be seen from the curve that the PFO-carbon nanostructures dispersion optically limits more effectively that the PmPV-MWNT sample, as for comparable input intensities the PFO based sample has lower output intensities once the samples are in the nonlinear regime. This is very clear at input intensities in excess of approximately 0.6 GW cm^{-2}. This result was also evident from comparison of Figure 5.9a and Figure 5.9b where the PFO based sample was seen to exhibit a larger

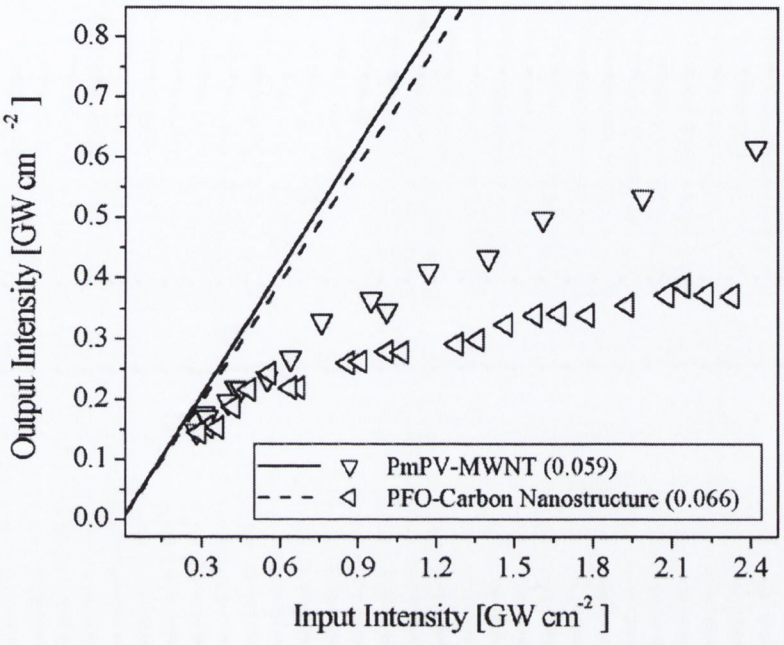

Figure 5.14 Plots of output against input on focus intensity for the PmPV-MWNT and PFO-Carbon Nanostructures samples with highest carbon nanostructure content. The straight lines, solid and dashed, represent the linear optical transmission curve for the PmPV-MWNT and PFO-carbon nanostructure composite samples respectively.

effective nonlinear absorption coefficient, β_I. The PFO sample also has a higher fraction of carbon nanostructures in its composition and accordingly a higher linear absorption coefficient, corresponding to its linear transmission curve having a lower slope than that of the PmPV based sample.

5.7 Intensity Dependent Scattering Studies

The mechanism causing the nonlinear optical extinction of high intensity laser pulses by MWNTs, as discussed in the literature, has been briefly summarised in the introduction to this chapter. In general other authors have concluded that thermally induced scattering was a major contribution to the optical limiting exhibited by these systems. In order to investigate the effects of polymer bound MWNTs and MWNTs combined with graphitic nanoparticles in the PmPV and PFO based composites respectively the intensity dependent scattering from the samples was qualitatively probed here. The approach adopted involved measuring the scattered light from the samples, using a similar approach adopted by Mansour *et al.*[4]

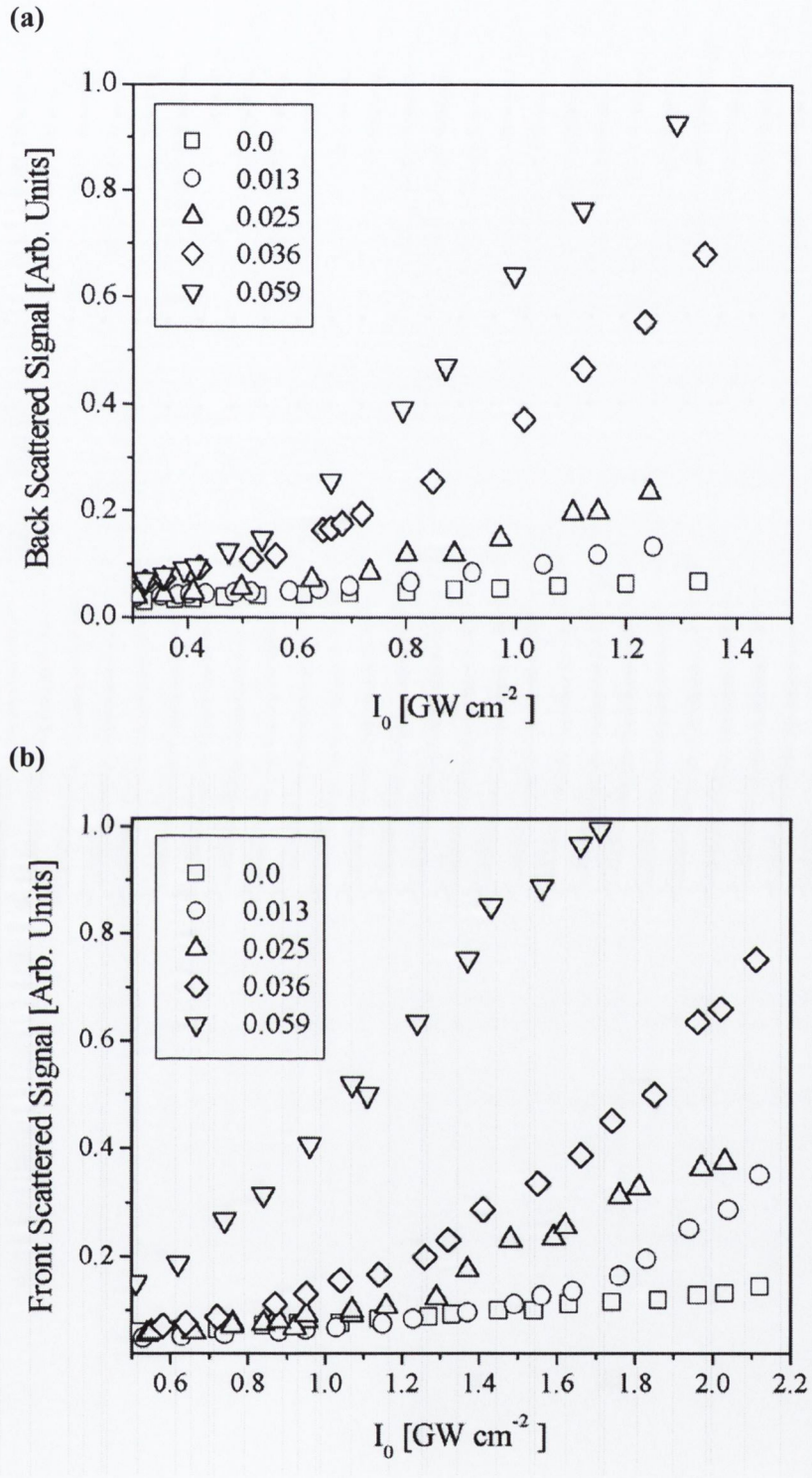

Figure 5.15 Plots of **(a)** normalised back scattered light signal and **(b)** normalised front scattered light signal as a function of incident intensity for the PmPV based composites. The scattered light was collected at 45^0 to the z-axis in a solid angle ≈ 1.05 steradian. Additional filters with ≈ 20% transmission were added to the front scattering detector.

where they made simultaneous measurements of transmittance, absorbance and scattering, and the apparatus has been described in Chapter 3, Section 3.3.3. The sample was placed on the focus of the z-scan focusing lens. The forward and backward scattered light (measured in arbitrary units) was simultaneously collected using additional lenses of diameter 6 cm with their axes at 45^0 to the z-axis of the experiment, positioned approximately 2 cm from the sample corresponding to a solid angle $\approx$ 1.05 steradian.

The normalised intensity dependent scattering data for the PmPV-MWNT composites are presented in Figure 5.15. The back scattering data is depicted in Figure 5.15a and the front scattering data is shown in Figure 5.15b. Additional filters with $\approx$ 20% transmission were added to the front scattering detector, as this was the dominant scattering region. There is clearly intensity and MWNT mass fraction dependence on the magnitude of the scattered signal in both the front and back scattering data displayed in these figures. However, it can be seen that the nonlinear dissipative behaviour, or optical limiting response, for these PmPV-MWNT samples, depicted in Figure 5.11 and Figure 5.13 does not correlate exactly with the measured scattered signals. The most obvious discrepancy is between the optical extinction of the samples with MWNT mass content $\approx$ 0.036 and 0.059. For example, the back scattered signals at 1 GW cm^{-2} are different from each other by a factor $\approx$ 1.8 and the front scattered signals differ by a factor $\approx$ 3.3 with the 0.036 MWNT content sample exhibiting a response less than the response of the 0.059 MWNT content sample in both cases. The corresponding magnitude of the nonlinear extinction differs at this incident intensity by about a factor $\approx$ 2, as shown in Figure 5.13. Thus, the back scattering signal is in approximate agreement with the nonlinear dissipation while the front scattering signal is at odds with the nonlinear extinction. The difference in the back scattered signal between the pure polymer (MWNT content = 0.0) and the 0.025 MWNT content sample is by a factor $\approx$ 3, and the difference in the front scattered signal is by a factor $\approx$ 1.2, again under 1 GW cm^{-2} incident irradiation. This does not compare favourably for the back scattering case but does compare favourably for the front scattering case with the differences in the magnitude of the respective nonlinear extinctions, which differ by a factor $\approx$ 1.2.

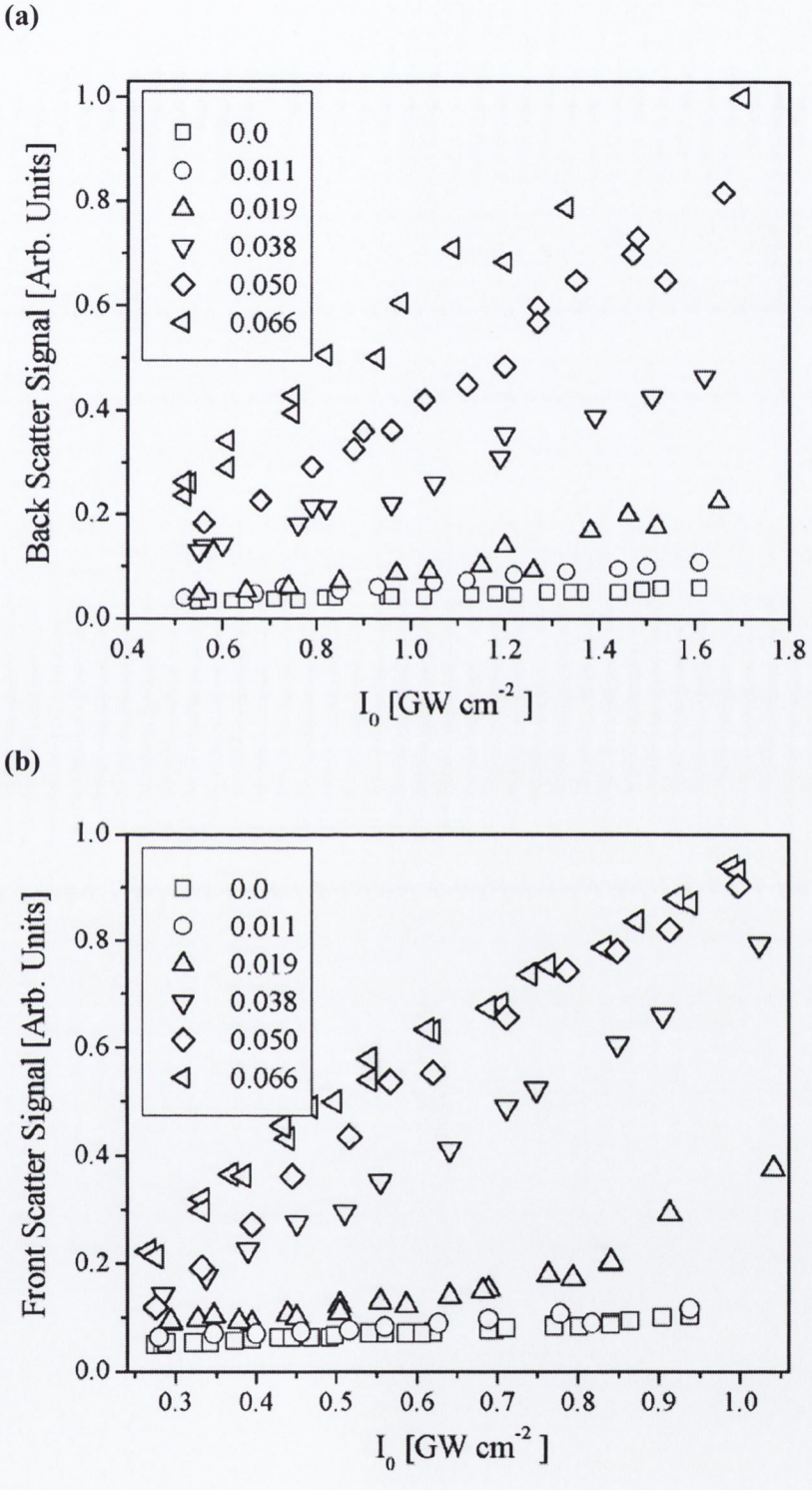

Figure 5.16 Plots of **(a)** normalised back scattered light signal and **(b)** normalised front scattered light signal as a function of incident intensity for the PFO based composites. The scattered was collected at 45^0 to the z-axis in a solid angle ≈ 1.05 steradian. Additional filters with ≈ 31% transmission were added to the front scattering detector.

Qualitatively, the MWNT content dependence on the scattered signal presented in Figure 5.15 appears to agree with the nonlinear extinction. Increasing the MWNT content increases the scattered signal giving good qualitative agreement with the nonlinear extinction. The increase in the scattering from the lower MWNT content samples (0.0, 0.013 and 0.025 MWNT mass content) is smallrelative to the increase in the signal from the other two samples (0.036 and 0.059 MWNT mass content), similar to the nonlinear extinction exhibited by these samples. However, there is no clear evidence observed in the scattering data of the two different operating regimes discussed above. Thus there exist both contradictions and correlations between the scattered signals and the nonlinear optical extinction.

The corresponding normalised intensity dependent scattering plots for the PFO-carbon nanostructure composites are displayed in Figure 5.16, where the back scattering data is depicted in Figure 5.16a and the front scattering data is shown in Figure 5.15b. Additional filters with $\approx$ 31% transmission were added to the front scattering detector, as this again was the dominant scattering region. The scattering data, as for the PmPV-MWNT composites presented above, exhibits both a definite mass of carbon nanostructure in the polymer and irradiation intensity dependence. The backscattering signal exhibits a clear mass fraction of carbon nanostructure dependence. This contrasts somewhat with the front scattering (dominant scattering regime) data. The front scattering signal has saturated for the samples with the highest mass of carbon nanostructures in the polymer. This is interesting when compared with the optical limiting data in Figure 5.12, which also appears to saturate at these carbon nanostructure mass fractions. The magnitude of the scattering signal for the 0.038 mass fraction sample in Figure 5.16b is fractionally smaller, but approximately parallel, to the 0.050 and 0.066 mass fraction samples indicating that its scattering potential has also almost saturated.

In conclusion it was found that these polymer-carbon nanostructure composite systems definitely exhibit an intensity and nanostructure content dependence on the scattering of high intensity incident light. In some cases the relative magnitudes of the scattered signal were seen to collaborate with the relative magnitudes of the optical limiting response. Thus it is clear that extinction by scattering is certainly present in the nonlinear response of these systems, and accordingly, all nonlinear absorption coefficients that were calculated earlier have to

be treated with care as effective absorption coefficients, as was assumed from the beginning of this study.

5.8 Angular Dependent Scattering Studies

In addition to the intensity dependent scattering studies presented in the previous section a study of the angular dependence of the scattered light was also undertaken in an effort to elucidate the nature of, or investigate the potential of exploiting, the scattering response. The experimental apparatus that was built and utilised for these experiments was described in Chapter 3, Section 3.3.3.

The angular profile of the scattered signal, measured from 20^0 to 160^0 where 0^0 is the direction of the optical beam, for the PmPV-MWNT composite with 0.059 MWNT mass fraction is plotted in Figure 17a. It can be seen that the scattering lobe to the front direction (20^0 to 90^0) is much larger than the scattering lobe observed in the backward direction (90^0 - 160^0). Front and back scattering lobes in these approximate proportions are characteristic of Mie regime scattering. Much the same results with scattering lobes in these proportions has previously been reported for dispersed carbon black[4] and multi-walled carbon nanotubes.[15] In Figure 5.17b the front scattered signal as a function of angular position from 20^0 to 90^0 for each of the different PmPV-MWNT composite samples is plotted. The data from 90^0 to 160^0 has been omitted from the plot, as it provides no additional information to the front scattering lobe. In these experiments for both Figure 5.17a and Figure 5.17b the samples were irradiated at $\approx$ 1.7 GW cm^{-2} and the scattered signal was plotted in arbitrary units.

Again there is good qualitative agreement in the MWNT content dependence of the scattered signal of the front scattering lobe presented in Figure 5.17b compared with the nonlinear extinction. Increasing the MWNT content increases the scattered signal at every angle, giving good agreement with the measured nonlinear extinction. The increase in the scattering from the lower MWNT content samples (0.0, 0.013 and 0.025 MWNT by mass) is small relative to the signal from the other two samples (0.036 and 0.059 by mass), again similar to the nonlinear extinction exhibited by these samples. It should be noted once again however that there is no evidence found in the scattering data of the two different operating regimes discussed above. Thus, once

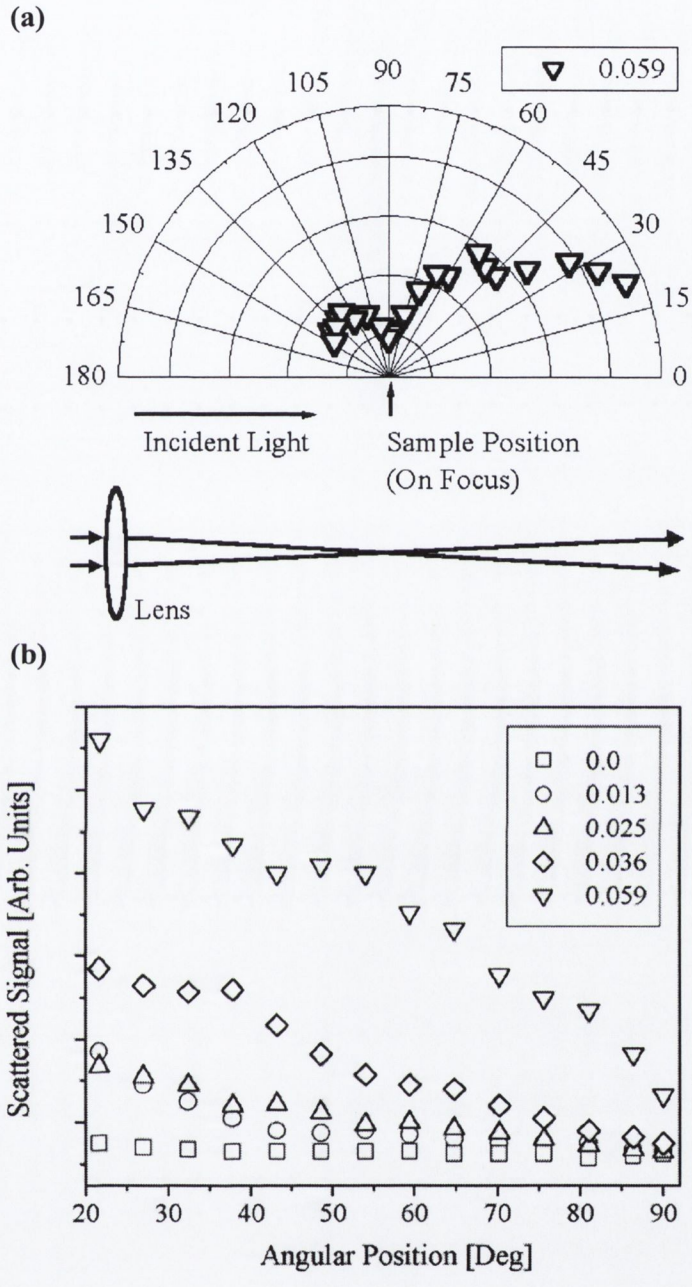

Figure 5.17 (a) Polar plot displaying the angular profile of scattered light from the PmPV-MWNT composite with 0.059 MWNT mass fraction. **(b)** Plot of the front scattered signal as a function of angular position from 20^0 to 90^0 for each PmPV-MWNT sample. The samples were irradiated at ≈ 1.7 GW cm^{-2} and the scattered signal is in arbitrary units in all cases.again, there exist both contradictions and correlations between the scattered signals and the nonlinear optical extinction.

again, there exist both contradictions and correlations between the scattered signals and the nonlinear optical extinction.

The angular dependence of the scattered light from the PFO-carbon

nanostructure composites was also measured. The angular scattering profile from the PFO based sample with maximum carbon nanostructure content (0.066 carbon nanostructures by mass) has been plotted in Figure 5.18, where as in Figure 5.17 the scattered signal in arbitrary units has been plotted as a function of angular position of the detecting diode. In this figure, the previously discussed scattering data from the PmPV-MWNT composite, with MWNT mass content ≈ 0.059, has been superimposed.

As was mentioned above in the discussion of Figure 5.17 for the PmPV-MWNT composite, the relative size of the front and back scattering lobes in Figure 5.18 for the PFO based composite dispersions are also in qualitative agreement with the results quoted for carbon black[4] and MWNTs[15]. In these studies the cause of the scattering was reported to be due to thermally induced Mie scattering. It can be seen in the figure that there is a difference in the angular scattering profile between the PmPV-MWNT and the PFO-carbon nanostructure composite dispersions. In the PmPV-MWNT composite the carbon nanostructure inclusions are almost exclusively

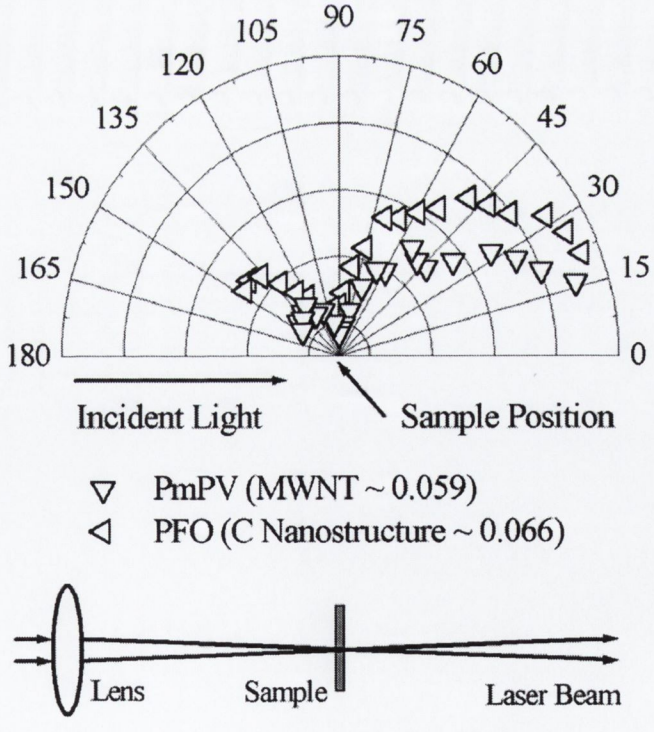

Figure 5.18 Polar plots of the scattered signal (arbitrary units) as a function of angular position of the detecting diode for the PFO-carbon nanostructure and PmPV-MWNT composite samples with maximum nanostructure content. The samples were irradiated at $I_0 \approx 1.7$ GW cm^{-2}.

MWNTs and accordingly it can be assumed that exclusive Mie regime scattering with the front scattering lobe much larger than the back scattering lobe is observed.

However, in PFO based composite dispersions there are many spherical nanoparticles that are held apart by the polymer binding. Spherical particles with dimensions smaller than the wavelength of the incident light in all directions would be expected to exhibit Rayleigh regime scattering.[31] Theoretically the angular profile of Rayleigh scattered light has front and back scattering lobes in equal proportions. An illustration depicting the theoretically different angular scattering profiles of Mie and Rayleigh regime scattering is presented in Figure 5.19.

It can thus be noted that in Figure 5.18 the PFO-carbon nanostructure composite dispersions' angular scattering profile is most likely a linear sum of Mie regime scattering from the MWNTs in the dispersion and Rayleigh regime scattering from the spherical graphitic particles in the dispersion. This provides a logical explanation as to why the back scattering lobe is larger relative to the front scattering lobe for the PFO composite dispersion than for the PmPV composite dispersion.

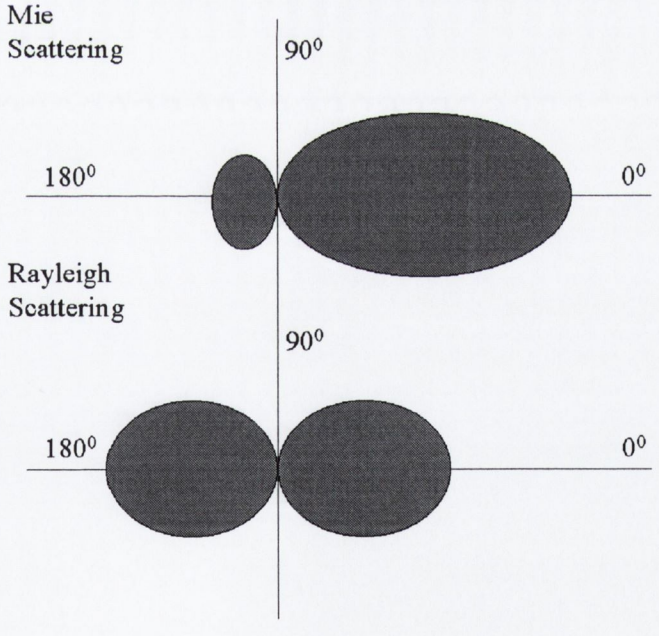

Figure 5.19 Illustration depicting the theoretically expected scattering profiles for the Mie and Rayleigh scattering regimes.

5.9 Spectral Profile of Scattered Light

In order to investigate the nature of the scattering further and also to provide some verification to the assumptions drawn in the preceding section it was necessary to

(a)

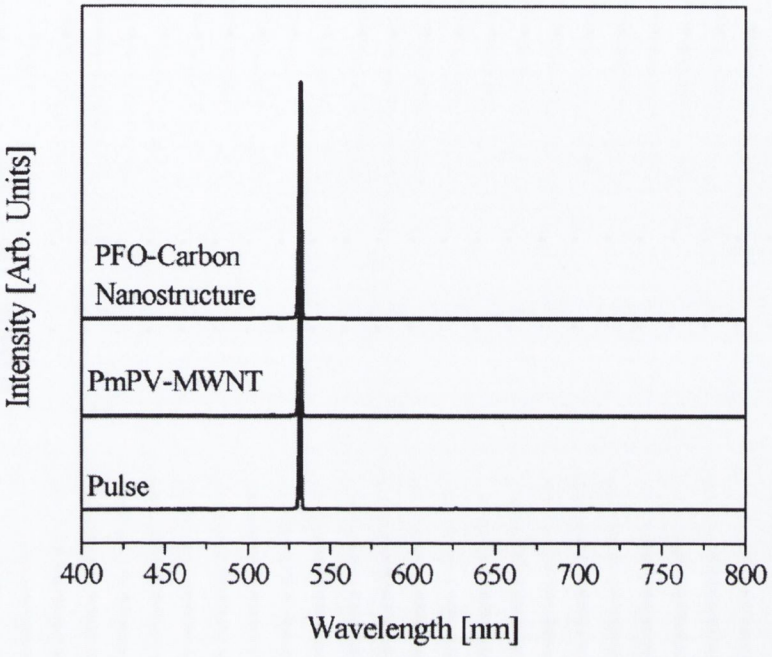

(b)

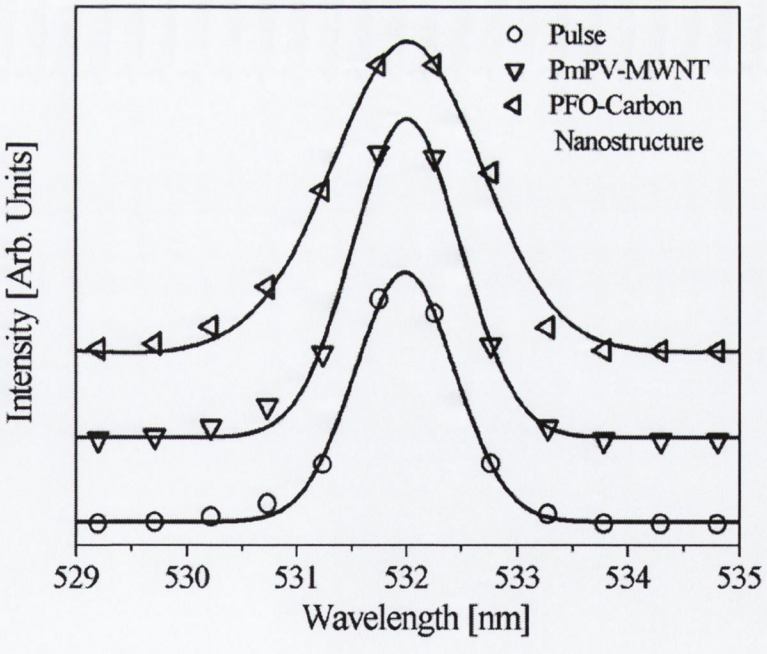

Figure 5.20 **(a)** Spectral profile of the scattered light from the 0.059 MWNT content PmPV-MWNT composite dispersion and the 0.066 nanostructure content PFO-carbon nanostructure composite dispersion compared with that of the laser pulse before incidence on the respective samples. **(b)** Expanded view of the incident and scattering peaks about 532 nm fitted with Gaussian functions.

remove the possibility that the scattered signal was due to, or had contributions from, an excitation and subsequent relaxation via photonic emission in the MWNTs. This was necessary as both Rayleigh and Mie regime scattering are completely elastic processes, and therefore, no shifts in the spectra of the incident compared to the scattered light should be observed if in fact scattering in either of these regimes was being observed. The apparatus used was similar to that used for the angular dependent scattering (see Figure 3.21) where the reference and detecting photodiodes were replaced with the probes of a standard CCD camera and spectrophotometer. The input signal (laser pulse) was probed at the reference detector and the scattered signal was collected using a 6 cm lens at 45^0 to the z-axis (similar to what was used for the intensity dependent scattering measurements) corresponding to a solid angle ≈ 1.05 steradian that was focused into the probe. A spectrum of the laser pulse and spectra of the scattered light from both the PmPV-MWNT and the PFO-carbon nanostructure composites were collected over wavelengths 320-850 nm, and the resulting spectra are plotted in Figure 5.20.

It can be seen from the spectral profile in Figure 5.20a, and in the expanded view of the peaks in Figure 5.20b, that the scattered photons in both systems are spectrally almost identical to that of the incident laser pulse indicating that the scattering in these systems are completely due to elastic photon scattering. It can be seen that the peaks are centred on 532 nm, and that the peaks are approximately Gaussian in profile with FWHM values of order 1 nm. When this is compared with the angular profile of the scattered light one is left with the conclusion that this is in fact Mie or Rayleigh scattering due to the needle like MWNT inclusions and the spherical graphitic nanoparticles respectively embedded in the polymer hosts.

5.10 Discussion

In this chapter the formation of a new temporally stable composite material where MWNTs were dispersed using the commercially availably polymer PFO was described. This is the second polymer after PmPV that has been identified as a suitable candidate for the stable dispersion of MWNTs. However it was found that the stable dispersal of large quantities of nanoparticles was also present in the new composite material. This was attributed to the five and six membered conjugation present in the backbone of the PFO polymer. As has been shown previously for

carbon nanotubes conjugated polymers tend to map to the molecular structure of carbon nanotubes.[30] Thus with this reasoning one would expect that a five and six membered conjugation entity would map to the structure of a spherical particle as this is exactly the type of structure that the particle would posses to allow for closure of the molecule. It should be noted that typically in Krätschmer arc discharge generated soot that the non-nanotube impurities, such as multi-shelled fullerenes or turbostratic graphite, occur on dimensions of nanometres up to microns. The selection made by the PFO polymer with diameters of spheres of order 20 nm is very clear in the TEM image depicted in Figure 5.4b. This is not simply impurities that have not sedimented out during the composite formation process as if this were the case a much broader spread of particle dimensions would be expected to be observed.

The nonlinear dissipation of high intensity laser pulses by MWNTs bound by conjugated polymers (PmPV and PFO) has been thoroughly investigated in this chapter. For the PmPV-MWNT composites the nonlinear dissipation of the incident laser pulses (Figure 5.11) appeared to exhibit two different operating regimes. The data seemed to suggest that at 1 g L^{-1} the PmPV-MWNT composite requires a critical MWNT inclusion percentage by mass $\approx (3.1 \pm 0.6)\%$ above which MWNT behavior dominates and below which the response is dominated by the polymer matrix. The higher MWNT mass content samples are nonlinearly active below 1 J cm^{-2} and the lower MWNT mass content samples are only nonlinearly active above 10 J cm^{-2}. A purified sample of MWNTs was seen to exhibit a similar onset of nonlinear behaviour and rate of the extinction relative to the incident energy density as the PmPV-MWNT composites in the MWNT dominant regime. For the PFO based composite materials one of the principal differences was that the pure PFO sample did not exhibit any response of its own over the intensity range that was explored. The onset of optical limiting for the other PFO based samples containing carbon nanostructures is similar in all cases, and occurs approximately at $\approx$ 0.3 J cm^{-2}, indicating that the limiting action was directly caused by the carbon nanostructures present in the composite dispersions. The magnitude of the nonlinear effect increased systematically when the mass fraction of the nanostructures was increased from 0.011 to 0.038. The nonlinear effects however clearly became saturated at carbon nanostructure mass fractions in excess of $\approx$ 0.038.

The polymer bound MWNTs and other carbon nanostructures that were investigated here form homogeneous solutions. Tang *et al.*[32] performed standard optical limiting measurements at 532nm using MWNT-polymer homogeneous solutions where they polymerised phenylacetylene in the presence of MWNTs. The linear transmittance of their samples spanned from 19% to 57% and the major difference between their samples was the nanotube content, although they did not quantify this. Their results are not directly comparable with those presented here as their polymer had a significant absorption coefficient of its own at 532nm. They concluded that the nanotubes were responsible for the optical limiting in their samples, and the onset of nonlinear behaviour was of the order of 1 J cm^{-2}, which is comparable to the optical limiting attributed to MWNT or MWNT and graphitic nanoparticles that has been presented here. It was generally demonstrated for both systems that the higher MWNT content samples, which correspondingly had lower linear transmittance, see Figure 5.7, block the incident light more effectively at higher incident energy densities or intensities, Figure 5.11 and Figure 5.12. This 'trade-off' between the magnitude of the linear transmittance and the magnitude of the nonlinear absorption, coupled with the critical MWNT mass fraction in PmPV-MWNT systems, and the observed saturation fraction in the PFO systems is important and would have to be considered from the point of view of designing potential optical limiting applications from these systems.

The model fitted to the open aperture z-scan data, Equation (3.33), was in all cases mathematically good (see Figure 5.8 for examples), typically with R^2 values in the region of 0.99. The results of the effective nonlinear absorption coefficient from each fitted open aperture scan were plotted in Figure 5.9. The physical implication of calculating β_I over I_0 using this theory was to assume that a third order nonlinear absorption mechanism was the dominating extinction mechanism. It can be seen in the figure that β_I was approximately constant over I_0, after an unsaturated regime for the lower MWNT mass fraction PmPV-MWNT composites at low intensity. This implies that the materials are behaving similar to a nonlinear absorber where the third order nonlinearity is all that is necessary to describe the system. However, this is only true over the intensity range presented on the plot and this intensity region is the total range over which the sample is not damaged. Non-zero slopes in these lines would imply higher order terms are necessary to describe the results. All nonlinear

coefficients calculated in this chapter have to be treated with care though as they are not simply absorption coefficients. They are simply effective coefficients that quantify the nonlinear response.

The magnitude of the nonlinear extinction compares well with other materials currently being developed for optical extinction applications such as the phthalocyanines or the naphthalocyanines that were discussed in the previous chapter. These chromophores begin to become nonlinearly active at similar pulse energy densities as the MWNT dominant samples and the magnitude of the nonlinearity exhibited by the both composites materials with higher MWNT or carbon nanostructure content is comparable with the most effective phthalocyanine or naphthalocyanine compounds. A subset of the optical limiting PmPV-MWNT data for the 0.059 MWNT content sample is plotted in Figure 5.21 where the optical limiting data for the chloroindium phthalocyanine *t*Bu$_4$PcInCl (compound **6** from Chapter 4) has been superimposed on the plot. It has already been noted in the previous chapter, and by other authors[33-35], that this particular phthalocyanine is

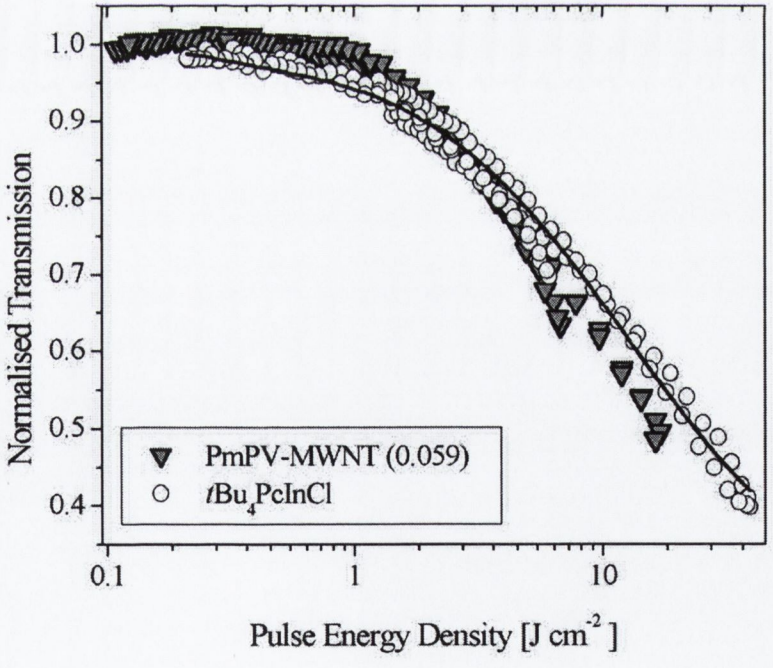

Figure 5.21 Plots of normalised transmission against incident energy density for the PmPV-MWNT composite with MWNT mass fraction ≈ 0.059, and the chloroindium phthalocyanine *t*Bu$_4$PcInCl (**6**) from Chapter 4. The solid line is the theoretical reverse saturable absorption fit to the optical limiting of the phthalocyanine.

promising for optical limiting studies due to its remarkably low linear absorption coefficient and thus, its corresponding large ratio of excited to ground absorption cross-sections (κ coefficient). In Figure 5.21 it should be noted that the phthalocyanine solution is prepared at 0.5 g L^{-1} and that the PmPV-MWNT composite is at 1 g L^{-1}. In the dispersed composite material the MWNT mass content is approximately 5.9% and this corresponds to the MWNTs being dispersed at approximately 0.06 g L^{-1} in the homogeneous composite dispersion. It can be seen in the figure that the optical limiting response of both of these materials is fairly comparable over the energy density range that was explored. Thus, irrespective of the mechanisms of the nonlinear attenuation, if one compares the magnitude of the nonlinear response with the mass concentration of the nonlinearly active entities in the optical limiting cell the MWNTs respond similar to the chloroindium phthalocyanines with one order of magnitude of material per litre less by mass than the phthalocyanines. Despite this being a rather naive comparison the results are impressive. It should also be noted however that the linear absorption coefficient of the PmPV-MWNT composite sample is approximately 7 times larger than that of the phthalocyanine solution.

The carbon nanostructures dispersed by polymer composite exhibited clear mass of nanostructure and intensity dependent scattering as was discussed in sections 5.7-5.9. It was most impressive that the differences in the carbon nanostructure components imaged in TEM (Figure 5.4) could be distinguished in the scattering data. In the PmPV composite the carbon nanostructure inclusions being almost exclusively MWNTs exhibited Mie regime scattering, while in the PFO based composite dispersions the many spherical nanoparticles added Rayleigh scattering contributions to the scattering angular profile. It can be concluded that the PFO composite dispersion angular scattering profile is probably a linear sum of Mie scattering from the MWNTs and Rayleigh scattering from the spherical graphitic particles. This has many potential applications. Particularly if one were using polymers to purify soot containing carbon nanostructures, using sedimentation and subsequent decantation as the separation of MWNT from other non-nanotube material process. High intensity light scattering could potentially be used to measure the composite purity.

There is undoubtedly an important scattering component in the optical

limiting exhibited by polymer-carbon nanostructure dispersions. However, it is also possible that the polymer bound nanotubes absorb nonlinearly at 532nm in the presence of high intensity adding electronic absorption contributions to the intensity dependant scattering in the overall optical limiting response. Riggs *et al.*[16] reported on mechanistic differences in the origin of nonlinear dissipation of laser pulses at 532 nm in suspended and solubilised MWNTs and SWNTs. They solubilised shortened carbon nanotubes by attaching them to poly(propionylethylenimine-co-ethylenimine) or by functionalising the nanotubes with octadecylamine. The soluble carbon nanotubes then formed homogeneous solutions in chloroform and water at room temperature. Essentially they concluded that the nonlinear extinction mechanism was principally nonlinear scattering in the aqueous suspensions of MWNTs while a reverse saturable absorption mechanism was principally responsible for the extinction in the solubilised systems. A reverse saturable process requires the existence of a photo-excited state with an absorption cross section exceeding that of the ground state absorption cross-section. They relied on their previous finding of luminescence from their homogeneous solutions of SWNTs and MWNTs[36] as proof of the existence of this excited state. They believed that the luminescence that they observed was caused by excited state energy trapping by structural defects in the carbon nanotube. Photoluminescence has also been reported in MWNTs purified using PmPV in our lab.[37,38] The purification process requires that the composite system be prepared as outlined in section 5.2, and then the PmPV removed from the MWNTs[28]. The MWNTs showed a cubic photoluminescence dependence on excitation intensity at 1064 nm pumping. Integrating the photoluminescence spectrum and plotting the log of magnitude of this integral against the log of the input intensity exhibited a linear trend. A linear fit resulted in a slope of 3, corresponding to a power law dependence of exponent 3 characteristic of a multiphoton excitation. Van Hove singularities in the density of states were found to coincide spectrally with the photoluminescence and thus optical transitions between these van Hove singularities were attributed to the observed photoluminescence. If excitation through multiphoton absorption is possible from 1064 nm light then it is possible that excited state absorption could take place in the presence of pumping with 532 nm photons. In principle then the observed optical extinction could have contributions due to an excited state absorption from states such as those responsible

for the luminescence. If this state had a larger absorption cross-section than the ground state then a reverse saturable absorption mechanism could contribute to the optical extinction.

In order to investigate the existence of this excited state we have recently reported picosecond degenerate four wave mixing results at 1064 nm pumping on a PmPV purified MWNT sample.[39] A typical temporal evolution of the phase conjugate signal from the MWNT sample exhibited two principal features. Initially an effectively instantaneous response was found about the zero delay position. This was fitted with a Gaussian function giving a FWHM value of (38 +/- 3) ps. Therefore, MWNTs exhibit a considerable ultra-fast component characteristic of an electronic contribution to the nonlinear response. At longer time delays (≈ 1 ns) the signal was seen to increase again and this was attributed to a thermally induced response. It was found that the time delay at which the thermal response arises was dependent upon the angle at which the probe beam enters the sample. The temporal properties of the thermal response were not investigated any further than this. It is worth noting that no phase conjugate signal was observed for graphitic particles (carbon black). The phase conjugate signal obtained for the pure PmPV (0.0 MWNT content) sample was not different from that determined for toluene alone.

Secondary evidence of electronic contributions to the nonlinear response of materials is found from closed aperture nonlinear refraction. This has been previously reported by Jin *et al.*[17] for polymer-nanotube composite materials irradiated with nanosecond pulses. Nonlinear refraction in PmPV-MWNT composite materials induced by nanosecond and picosecond laser pumping has also been reported in dispersions and solid state films.[40] The real third order susceptibility ($Re\{\chi^{(3)}\}$) was found to be negative with a magnitude ≈ 10^{-12} esu in dispersions and ≈ 10^{-10} esu in films for both nanosecond and picosecond pumping.

It is significant that the purified MWNTs suspended in toluene with the same linear transmittance as the 0.059 MWNT mass fraction PmPV-MWNT composite behaves almost exactly as the composite, Figure 5.11, indicating that the response is dominated by the MWNT response. During the preparation of PmPV-MWNT composites some MWNTs are held by the polymer while some are rejected. Possibly the nanotubes selected by the PmPV are more likely to exhibit electronic interactions at the incident wavelengths that have been used than the MWNTs that

are rejected. This could be attributed to electronic or geometric considerations. It should also be noted that in previous works by other authors when a MWNT sample without purification, with PmPV or any other means, was tested for optical limiting the nonlinear response was almost certainly measured in the presence of graphitic impurities, which makes comparison with other works difficult as these impurities would also be sources of intensity dependant scattering or absorption. Thermally induced scattering depends on bubble formation in the suspending solvent.[4,12,13] Future work in this area could involve identifying other suitable polymers to hold the MWNTs and form stable homogeneous polymer-MWNT composites. A different polymer-MWNT composite would have different characteristics, such as viscosity or heat capacity, and thus have different bubble forming properties, and correspondingly different optical limiting properties.

5.11 Conclusion

A systematically varied series of PmPV-MWNT and PFO-carbon nanostructure composites by nanostructure content have been fabricated, materially investigated and characterised with regards to optical limiting, or nonlinear extinction. Scattering measurements exhibited a clear nanostructure content dependence of perfectly elastically scattered light. The nanostructured composition of the materials was clearly distinguishable in the scattering data, suggesting that this method has potential for application in measuring polymer-MWNT composite purity.

These types of materials have the advantage that they are easily fabricated, the raw material is readily available and there is much potential for further optimisation. The polymer-MWNT composite is attractive compared to some of the other alternatives for optical limiting applications as the optically active entities (the nanotubes) are already embedded in a polymer host that can be used for solid-state casting. It is possible that using single walled nanotubes (SWNT) in place of MWNT could substantially reduce the mass fraction of nanotubes required for effective optical limiting, if one assumes that the outer shell electrons are those responsible for the response. In addition many potential host polymers remain to be tested. Future work in this are would inevitably involve variation of both nanostructured guest and polymer host to improve dispersion properties and increase optical limiting efficiency towards real world applications.

References

[1] S. Iijima, Nature **354,** 56-58 (1991).

[2] C. N. R. Rao, B. C. Satishkumar, A. Govindaraj, and M. Nath, Chem Phys Chem **2,** 78-105 (2001).

[3] P. Fournet, J. N. Coleman, B. Lahr, A. Drury, W. J. Blau, D. F. O'Brien, and H. H. Horhold, Journal of Applied Physics **90,** 969-975 (2001).

[4] K. Mansour, M. J. Soileau, and E. W. Van Stryland, Journal of the Optical Society of America B **9,** 1100-1109 (1992).

[5] J. Barroso, A. Costela, I. Garcia-Moreno, and J. L. Saiz, Journal of Physical Chemistry A **102,** 2527-2532 (1998).

[6] D. G. McLean, R. L. Sutherland, M. C. Brant, D. M. Brandelik, P. A. Fleitz, and T. Pottenger, Optics Letters **18,** 858 (1993).

[7] F. Henari, J. Callaghan, H. Stiel, W. Blau, and D. J. Cardin, Chemical Physics Letters **199,** 144-148 (1992).

[8] R. A. Ganeev, A. I. Ryasnyansky, M. K. Kodirov, and T. Usmanov, Optics Communications **185,** 473-478 (2000).

[9] L. Vivien, E. Anglaret, D. Riehl, F. Hache, F. Bacou, M. Andrieux, F. Lafonta, C. Journet, C. Goze, M. Brunet, and P. Bernier, Optics Communications **174,** 271-275 (2000).

[10] S. R. Mishra, H. S. Rawat, S. C. Mehendale, K. C. Rustagi, A. K. Sood, R. Bandyopadhyay, A. Govindaraj, and C. N. R. Rao, Chemical Physics Letters **317,** 510-514 (2000).

[11] L. Vivien, D. Riehl, F. Hache, and E. Anglaret, Journal of Nonlinear Optical Physics & Materials **9,** 297-307 (2000).

[12] L. Vivien, D. Riehl, P. Lancon, F. Hache, and E. Anglaret, Optics Letters **26,** 223-225 (2001).

[13] L. Vivien, D. Riehl, J. F. Delouis, J. A. Delaire, F. Hache, and E. Anglaret, Journal of the Optical Society of America B-Optical Physics **19,** 208-214 (2002).

[14] X. Sun, R. Q. Yu, G. Q. Xu, T. S. A. Hor, and W. Ji, Applied Physics Letters **73,** 3632-3634 (1998).

[15] X. Sun, Y. N. Xiong, P. Chen, J. Y. Lin, W. Ji, J. H. Lim, S. S. Yang, D. J. Hagan, and E. W. Van Stryland, Applied Optics **39,** 1998-2001 (2000).

[16] J. E. Riggs, D. B. Walker, D. L. Carroll, and Y. P. Sun, Journal of Physical Chemistry B **104,** 7071-7076 (2000).

[17] Z. X. Jin, X. Sun, G. Q. Xu, S. H. Goh, and W. Ji, Chemical Physics Letters **318,** 505-510 (2000).

[18] J. N. Coleman, D. F. O'Brien, A. B. Dalton, B. McCarthy, B. Lahr, A. Drury, R. C. Barklie, and W. J. Blau, Chemical Commmunications, 2001-2002 (2000).

[19] R. Murphy, J. N. Coleman, M. Cadek, B. McCarthy, M. Bent, A. Drury, R. C. Barklie, and W. J. Blau, Journal of Physical Chemistry B **106,** 3087-3091 (2002).

[20] W. Kratschmer, L. D. Lamb, K. Fostiropoulos, and D. R. Huffman, Nature **347,** 354-358 (1990).

[21] J. N. Coleman, A. B. Dalton, S. Curran, A. Rubio, A. P. Davey, A. Drury, B. McCarthy, B. Lahr, P. M. Ajayan, S. Roth, R. C. Barklie, and W. J. Blau, Advanced Materials **12,** 213-216 (2000).

[22] S. A. Curran, P. M. Ajayan, W. J. Blau, D. L. Carroll, J. N. Coleman, A. B. Dalton, A. P. Davey, A. Drury, B. McCarthy, S. Maier, and A. Strevens,

Advanced Materials **10,** 1091-+ (1998).
[23] A. Drury, S. Maier, A. P. Davey, A. B. Dalton, J. N. Coleman, H. J. Byrne, and W. J. Blau, Synthetic Metals **119,** 151-152 (2001).
[24] J. N. Coleman, D. F. O'Brien, A. B. Dalton, B. McCarthy, B. Lahr, R. C. Barklie, and W. J. Blau, Journal of Chemical Physics **113,** 9788-9793 (2000).
[25] S. Bandow, Journal of Applied Physics **80,** 1020-1027 (1996).
[26] O. Chauvet, L. Forro, W. Bacsa, D. Ugarte, B. Doudin, and W. A. Deheer, Physical Review B **52,** R6963-R6966 (1995).
[27] S. M. O'Flaherty, R. Murphy, S. V. Hold, M. Cadek, J. N. Coleman, and W. J. Blau, Journal of Physical Chemistry B **107,** 958-964 (2003).
[28] R. Murphy, J. N. Coleman, S. M. O'Flaherty, M. Cadek, B. McCarthy, A. Drury, R. C. Barklie, and W. J. Blau, Proceedings of SPIE 'Opto-Ireland 2002' **4876,** 659-667 (2002).
[29] TEM Image of purified MWNTs taken by B. McCarthy.
[30] B. McCarthy, J. N. Coleman, R. Czerw, A. B. Dalton, M. in het Panhuis, A. Maiti, A. Drury, P. Bernier, J. Nagy, B. Lahr, H. J. Byrne, D. L. Carroll, and W. J. Blau, Journal of Physical Chemistry B **106,** 3087-3091 (2002).
[31] C. F. Bohren and D. R. Huffman, *Absorption and scattering of light by small particles* (John Wiley & Sons, 1983).
[32] B. Z. Tang and H. Y. Xu, Macromolecules **32,** 2569-2576 (1999).
[33] J. W. Perry, K. Mansour, I. Y. S. Lee, X. L. Wu, P. V. Bedworth, C. T. Chen, D. Ng, S. R. Marder, P. Miles, T. Wada, M. Tian, and H. Sasabe, Science **273,** 1533-1536 (1996).
[34] J. S. Shirk, R. G. S. Pong, S. R. Flom, H. Heckmann, and M. Hanack, Journal of Physical Chemistry A **104,** 1438-1449 (2000).
[35] Y. Chen, L. R. Subramanian, M. Fujitsuka, O. Ito, S. O'Flaherty, W. J. Blau, T. Schneider, D. Dini, and M. Hanack, European Journal of Organic Chemistry **8,** 4248-4254 (2002).
[36] J. E. Riggs, Z. X. Guo, D. L. Carroll, and Y. P. Sun, Journal of the American Chemical Society **122,** 5879-5880 (2000).
[37] M. E. Brennan, J. N. Coleman, M. in het Panhuis, L. Marty, H. J. Byrne, and W. J. Blau, Elsevier. Synthetic Metals **119,** 641-2 (2001).
[38] M. E. Brennan, J. N. Coleman, M. in het Panhuis, T. Kobayashi, and W. J. Blau, Proceedings of SPIE, Linear and Nonlinear Optics of Organic Materials **4461,** 56-64 (2001).
[39] S. M. O'Flaherty, S. V. Hold, M. E. Brennan, M. Cadek, A. Drury, J. N. Coleman, and W. J. Blau, Journal of the Optical Society of America B **20,** 49-58 (2003).
[40] M. Brennan, Ph.D. Thesis, (Trinity College Dublin, Ireland, 2001).

Chapter 6

Probing the Concentration Dependent Kinetics of Single Walled Carbon Nanotube Bundles

6.1 Introduction and Motivation

There have been many potential applications mooted for the electronic and magnetic application of pure, defect-free single-walled carbon nanotubes (SWNTs) and Baughman *et al.*[1] have recently reviewed the current state of the art. These applications almost exclusively rely on the manipulation of a single isolated SWNT of known electronic properties located at a specific location (ie. between the two electrodes of an electrical device). However, SWNTs in the preparation phase form bundles with close-packed two-dimensional triangular lattices, first reported by Thess *et al.*[2] in 1996. They produced SWNTs by laser vaporisation of a graphite rod in an oven at 1200 ^{0}C with SWNT purities in excess of 70 %. They found that the SWNTs were remarkably uniform in diameter and that they self-organised into rope-like crystallites 5-10 nm in diameter and tens to hundreds of microns in length, where the lattice constant in the crystallite was approximately 1.7 nm. The two-dimensional lattice structure through the cross-section of a SWNT rope is evident from the image in Figure 6.1, which depicts a transmission electron microscope (TEM) image of SWNT rope composed of about 100 SWNTs as it bends through the image plane of the microscope. The conclusions of their study revealed that the formation of these crystalline ropes of SWNTs was a result of the collisions between

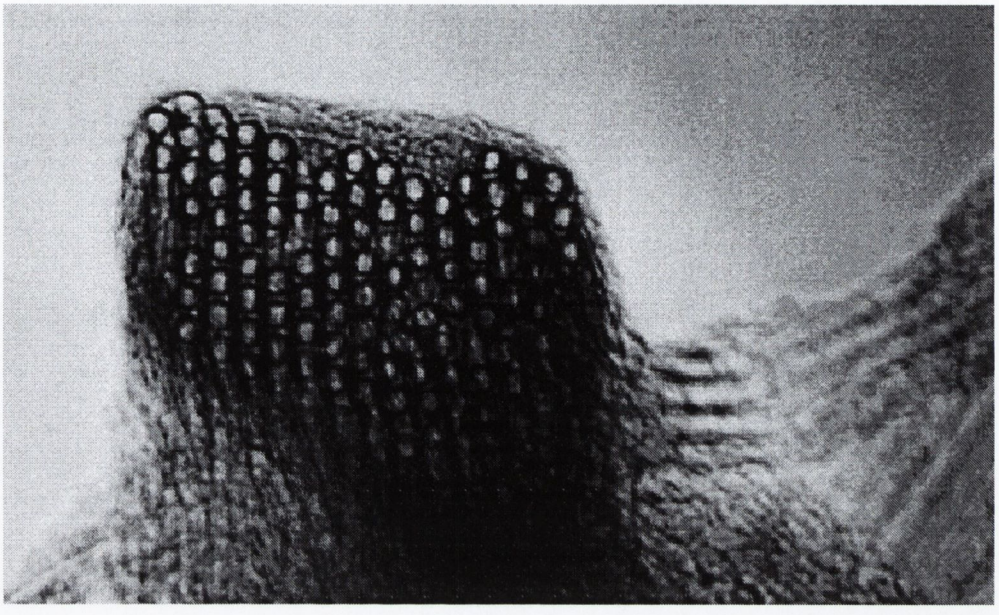

Figure 6.1 A single single-walled nanotube (SWNT) rope composed of about 100 SWNTs as it bends through the image plane of the microscope. The relatively uniform diameter and triangular packing of the tubes within the ropes can clearly be seen.[3]

growing tublets in the gas phase while they were still short enough to align by van der Waals forces without becoming tangled. These ropes of SWNTs have received much attention in their own right. Experimental evidence has indicated that these ropes exhibit an unusual temperature dependence of conductivity[4,5], magnetoresistance[6] and thermoelectric power[7,8] and investigations as to the nature or causing phenomena of these effects have been reported.[9,10]

The polymer-nanotube composite dispersion system that has been investigated in the preceding chapter of this thesis has provided from optical attenuation experiments a range of useful and interesting results as to the nanoscale geometries of the system. In this chapter the principle goal is to construct a concentration dependent range of polymer-nanotube composite dispersions to try to observe the break-up of single walled carbon nanotube bundles at low concentration. The principle aim is to use standard open-aperture z-scan nonlinear optical attenuation as the detecting experiment.

6.2 Materials and Sample Preparation

The nanotubes used in this study were high purity single walled carbon nanotubes produced by the high pressure carbon monoxide (HiPCo) method, and are simply denoted SWNT as usual. The polymer used in this study was poly(*m*-phenylene-co-(1,5-dioctyloxy-2,6-naphthylene vinylene)) (*m*-PNV) and its chemical structure is sketched in Figure 6.2a. The geometric properties of the polymer molecule were investigated using semi empirical calculations with the AM1 Hamiltonian. As when the metallo-phthalocyanine was investigated in Chapter 3 the intention was not to predict any electronic properties; it was merely to observe the spatial geometry of the polymer chain. The optimisation algorithm was halted once the magnitude of the energy gradient was reduced to less than 0.1 kcal $Å^{-1}$ mol^{-1}. The resulting optimised

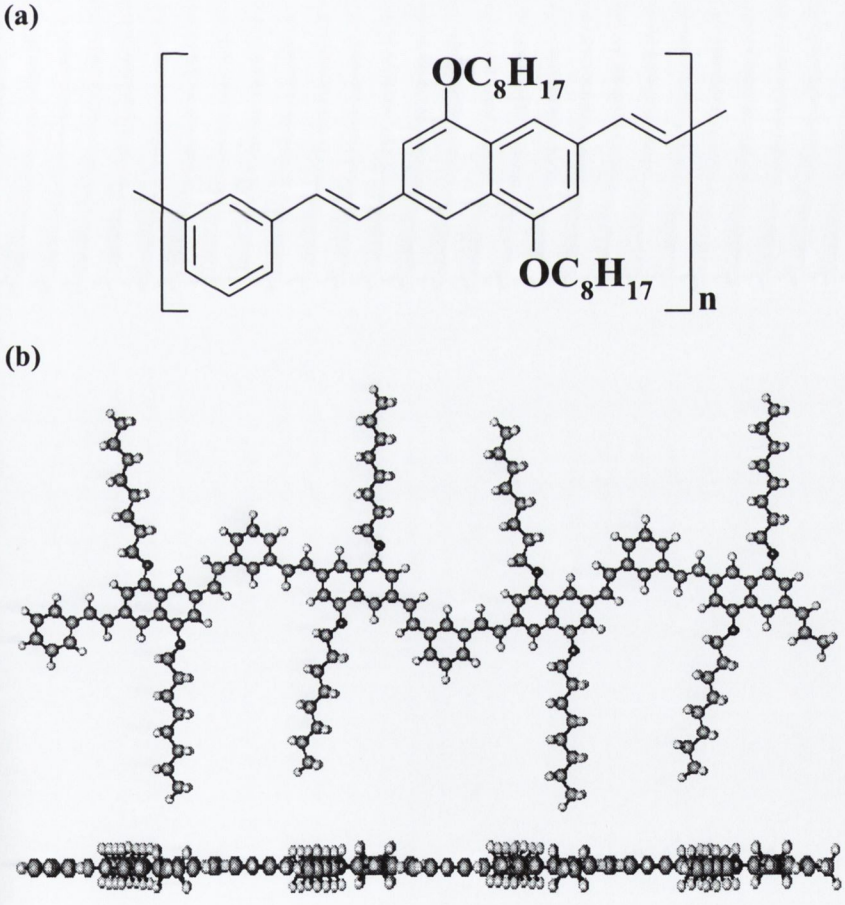

Figure 6.2 **(a)** Chemical structure of poly(*m*-phenylene-co-(1,5-dioctyloxy-2,6-naphthylene vinylene)) (*m*-PNV). **(b)** Optimised structure of *m*-PNV calculated over four repeat units of the polymer using the AM1 Hamiltonian, halted at an energy gradient less than 0.1 kcal $Å^{-1}$ mol^{-1}. The optimised polymer structure shows that it is relatively planar.

structure calculated over four repeat units of the polymer is presented in Figure 6.2b. The optimised structure of the polymer shows that it is relatively planar.

The composite dispersions were prepared in almost exactly the same way as the composites were prepared in the previous chapter. The polymer was dissolved in spectroscopic grade chloroform. To this solution a mass of SWNT soot equal to total mass of the polymer in that solution was added. This was ultrasonically agitated using a high power sonic tip (120 W) over 60 s. As overexposure to ultrasound can damage the nanotubes the sample was then transferred to a low power sonic bath (60 W) where it was gently agitated for a number of hours. The solution was then diluted with pure chloroform to produce a range of concentrations. These concentrations are quoted in Table 6.1, where the concentrations are measured as the partial concentration of SWNT in the dispersion. One therefore has to double this value for the total mass (polymer + nanotubes) concentration of the dispersion. The samples were then left to stand undisturbed for twenty four hours to allow the dispersions reach thermal dynamic equilibrium.

6.3 Review of Investigations of polymer-SWNT system

Recently Coleman *et al.*[11] and Fleming *et al.*[12] have modelled and performed measurements on a system consisting of polymer-single walled carbon nanotubes dispersed in solution as a function of concentration, and a summary of the results will be provided here. Consider a system where composites are prepared with the polymer and nanotube mass in equal proportions, as described in the preceeding section. In such a system the level of polymer coating the carbon nanotubes, or carbon nanotube bundles, will be low. Certain amounts of the polymer will bind to the nanotube and the remaining polymer will explore the solution through thermal diffusion. At equilibrium this system will undergo continuous transitions of adsorption and desorption of the polymer to the nanotubes or nanotube bundles. The polymer bound to the nanotubes will not fluoresce whereas the free polymer will. Thus if one measures the photoluminescence intensity of two polymer solutions at equivalent concentrations, one with SWNTs and the other without, the ratio of these photoluminescence intensities is a measure of the fraction of free polymer in the solution.

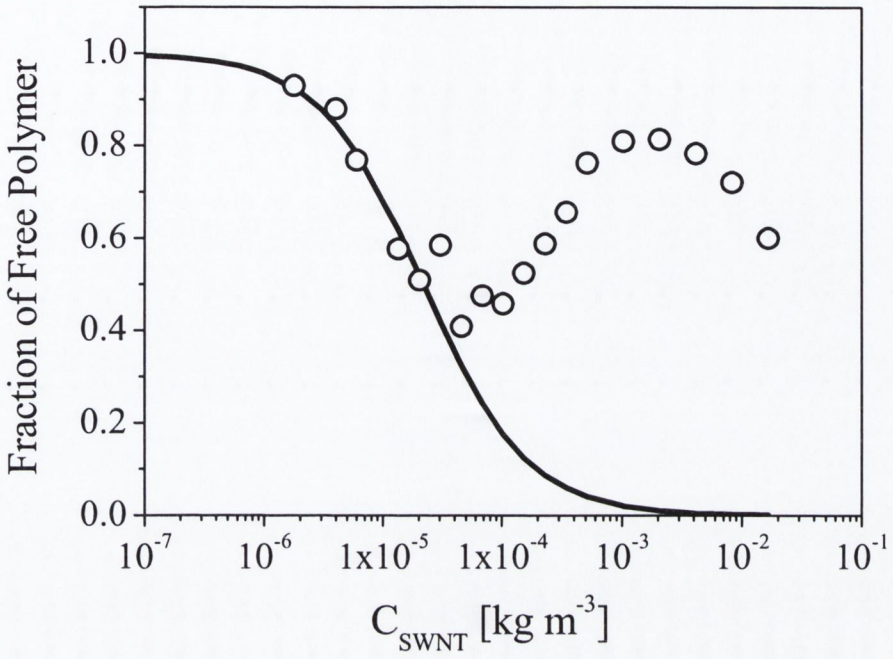

Figure 6.3 Plot of fraction of free polymer against concentration, determined from photoluminescence studies.[13] The fraction of free polymer was calculated from the ratio of the photoluminescence intensity for a composite solution to the photoluminescence intensity for the equivalent polymer solution. Note that for all concentrations the partial nanotube concentration, c_{SWNT}, equals the partial polymer concentration. The solid line is a fit in the low concentration regime.

Fleming *et al.*[12] have reported such a study where they measured fraction of free polymer as a function of concentration for 1:1 polymer to SWNTs by mass for (*m*-PNV)-SWNT composite dispersions. The partial concentrations of nanotubes, c_{SWNT}, of their samples spanned from 10^{-2} to 10^{-7} g L^{-1}. This plot of fraction of free polymer against concentration has been recreated in Figure 6.3, and it can be noted that the samples with the eleven highest concentrations are identical to the samples that will be explored further in this chapter. It can clearly be seen that this plot is highly nonlinear implying complicated behaviour of the adsorption-desorption process as a function of concentration.

Coleman *et al.*[11] modelled this behaviour. They considered that at thermal equilibrium the adsorption rate of polymer to the nanotube should be equal to the desorption rate, to maintain that equilibrium. However, the adsorption rate is primarily dependent upon spatial considerations, for example how likely is a free polymer molecule to encounter a dispersed SWNT bundle, while the desorption rate is dependent upon the van der Waals binding energy of the polymer molecule to the

carbon nanotube. This allowed the following diffusion equation to be considered:

$$\frac{16DR}{\pi}\frac{N_F}{V}f = \nu\frac{N_B}{V}V_{NT}\exp\left[-\frac{E_B}{k_BT}\right] \tag{6.1}$$

where for the adsorption term on the LHS; D is the diffusion coefficient, R is the nanotube radius, N_F is the total number of free molecules in arbitrary volume V and f is the a triple integral over space that was solved to be of order 800 for the concentration region that was under investigation. For desorption term on the RHS; ν is a constant describing the rate at which a molecule attempts to desorb, N_B is the total number of bound molecules per nanotube, V_{NT} is the spatial volume per nanotube, and in the Boltzmann factor E_B is the binding energy of polymer to nanotube, k_B is the Boltzmann constant and T is the temperature. Equation (6.1) can be rearranged to yield,

$$\frac{N_F}{N_T} = \frac{1}{1+\phi c_{SWNT}} \tag{6.2}$$

where $N_T = N_F + N_B$ is the total number of polymer molecules in arbitrary volume V, and

$$\phi = \frac{16DRf}{\pi\nu\rho A\exp\left[-\frac{E_B}{k_BT}\right]} \tag{6.3}$$

where in this case ρ is the density of the nanotubes and A is the total surface area of the nanotubes or nanotube bundle.

If one considers Equation (6.3) it can be seen that all terms on the RHS are constant with the exception of A under the assumption that the bundles dissociate at low concentration. Thus ϕ under this assumption would not be expected to be constant over all concentrations either. Equation (6.2) can be rearranged to give:

$$\phi = \frac{1}{c_{SWNT}}\left(\frac{N_T}{N_F}-1\right) \tag{6.4}$$

where N_T/N_F is simply the inverse of the fraction of free polymer. This was applied to the data depicted in Figure 6.3 and resulted in ϕ growing as a function of decreasing concentration exhibiting saturated behaviour at lowest concentrations with a numerical value of $\phi \approx 4.57\text{e}4$ m^3 kg.

If one considers Equation (6.3) it can be seen that large ϕ implies small total

surface area, A, as would be expected in a regime with isolated single nanotubes. As the dimensions of individual SWNTs are known, the binding energy was estimated by fitting the lower concentration section of Figure 6.3 with Equation (6.2) where l_{NT} was set to 300 nm, R was set to 1 nm and ϕ was set to 4.57×10^{4} m^3 kg^{-1} as determined from the previous fitting. The result yielded binding energy in the region $E_B \approx 1.06$ eV per molecule.

Recently, theoretical investigations into the interaction between conjugated polymers and carbon nanotubes have been reported.[14] Their calculations indicated an extremely strong noncovalent binding energy of $\approx$ 80 meV per carbon atom of PmPV (see Chapter 5, Figure 5.1a) bound to a SWNT. If one considers this atomic binding energy with the binding energy per molecule determined in the last paragraph this implies that approximately 14 carbon atoms per polymer molecule are binding to the nanotube.[11] Given that the optimised structure of the polymer exhibits a rigid straight backbone, one would expect then that the polymer crosses the nanotube allowing the electrostatic bonding of the 14 or so atoms, and the remaining sections of the polymer

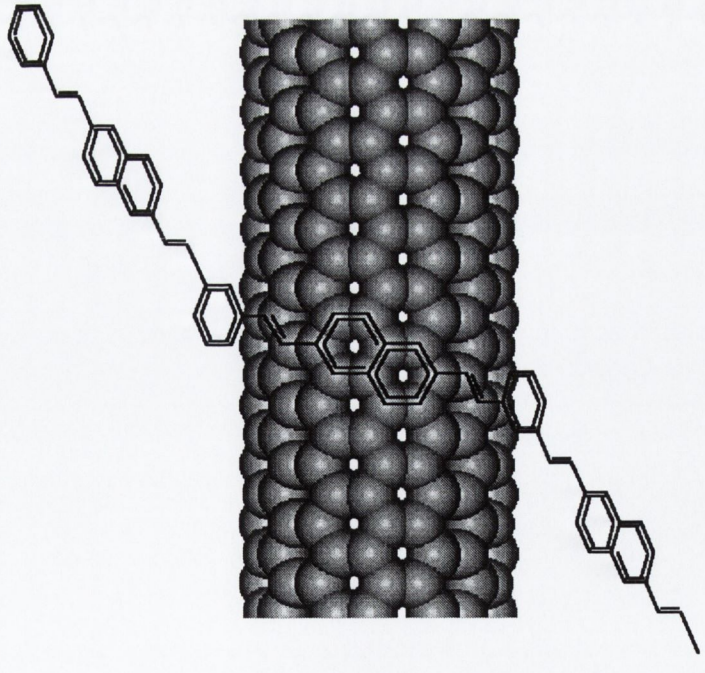

Figure 6.4 Schematic of the bonding of the *m*-PNV backbone to a SWNT. The SWNT in the figure is a (7, 7) nanotube and the dioctyloxy sidegroups have been removed from the polymer sketch for clarity.

chain reside in the solution where they are free to form solvation shells to successfully disperse the nanotube. As the polymer is rigid and relatively planar it must see the nanotube essentially as graphene and the backbone is distorted slightly to account for the curvature of the nanotube. The potential induced by this distortion must be less that the binding energy for the dispersion to be stable. This is shown schematically in Figure 6.4 where the nanotube in this case is a (7, 7) armchair nanotube and the dioctyloxy sidegroups have been removed from the polymer sketch for clarity.

6.4 Linear Optical Properties

The linear optical absorption spectra for each of the (*m*-PNV)-SWNT composite dispersions are depicted in Figure 6.5. The region spanning 400 nm to 600 nm is depicted in Figure 6.5a. It can be seen that at 532 nm the spectra in all cases are reasonably flat. It can be seen that at partial cabon nanotube concentrations (c_{SWNT}) of $\approx 5.2\times10^{-4}$ g L^{-1} the spectrum has become 'noisy' due to the low amounts of material interacting with the light. All spectra collected from lower concentration samples were not included in the plot, as they had become so 'noisy' that they were clearly unreliable. In Figure 6.5b the region from 320 nm to 440 nm representing the polymer peaks has been expanded to allow a closer view of the polymer absorption behaviour.

Certain features of the electronic structure of the SWNTs are visible in the linear absorption spectra on closer inspection. In Figure 6.6 the linear absorption, spectrum for the (*m*-PNV)-SWNT composite dispersion with highest concentration for wavelengths spanning 500-1000 nm has been plotted. In the inset to this figure the plot has been reproduced with the wavelength axis converted to photonic energy. In the inset the background π-plasmon resonance baseline has been subtracted from the data to highlight the peaks. The features in these plots were also exhibited by the all composites of lower concentrations. Petit *et al.*[15] reported on the electronic structure of SWNTs using linear absorption spectroscopy as their experimental tool. They measured features in the region of 0.5 - 2.5 eV exhibited by pristine SWNTs and SWNTs that they had exposed to naphthalene-lithium. They reported three principle peaks at 0.68, 1.2 and 1.7 eV, and from previous theoretical

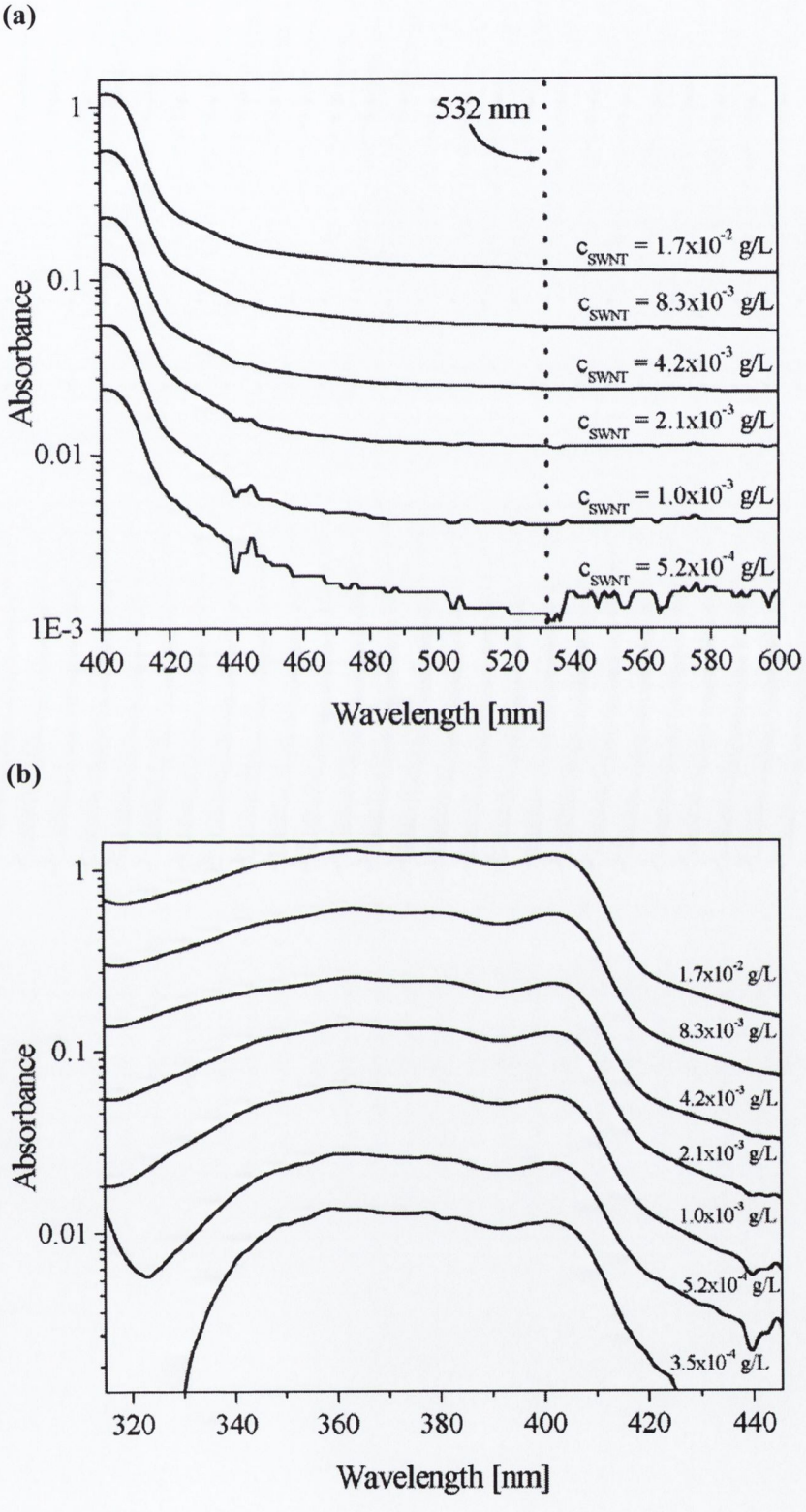

Figure 6.5 UV-Visible spectra for the (*m*-PNV)-SWNT composite dispersions where **(a)** details the spectra in the region of 532 nm, and **(b)** details the region from 320 nm to 440 nm.

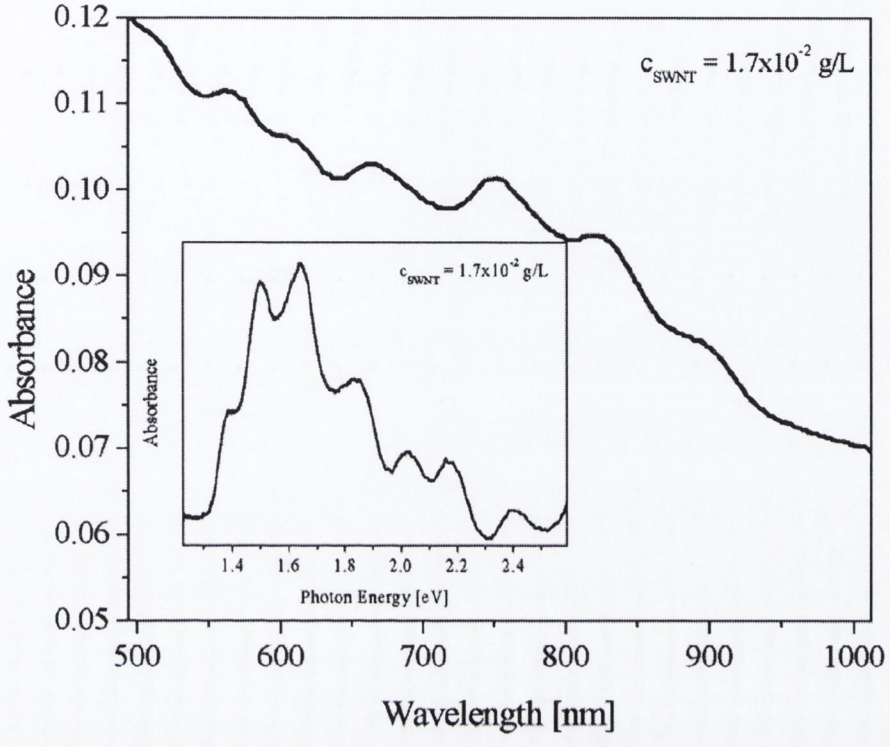

Figure 6.6 UV-Visible spectrum for the (*m*-PNV)-SWNT composite dispersion with highest concentration for wavelengths spanning 500-1000 nm. In the inset the plot has been reproduced with the wavelength axis converted to photonic energy and also the background π-plasmon resonance baseline has been subtracted from the data to highlight the peaks. The features in these plots were exhibited by the composites of all other concentrations also.

calculations[16-18] they assigned the first two of these to optical band-gap transitions in semiconducting tubes and the third to metallic tubes. In the inset of Figure 6.6, there is a feature at energy just above 1.6 eV, in reasonable agreement with the aforementioned peak reported at 1.7 eV. The peaks in these spectra most likely correspond to singularities or 'spikes' in the density of states know as Van Hove singularities, and the broadening of these 'spikes' into peaks as observed in the spectra is due to the superposition of narrower absorption bands corresponding to the response of individual SWNTs of different chiral indices and also possibly of different diameters. Singularities in the density of states for SWNTs are expected and have been theoretically modelled and predicted.[18-20]

The linear absorption coefficients of the composite dispersions are plotted against their concentration in Figure 6.7. Only the data points taken from the spectra

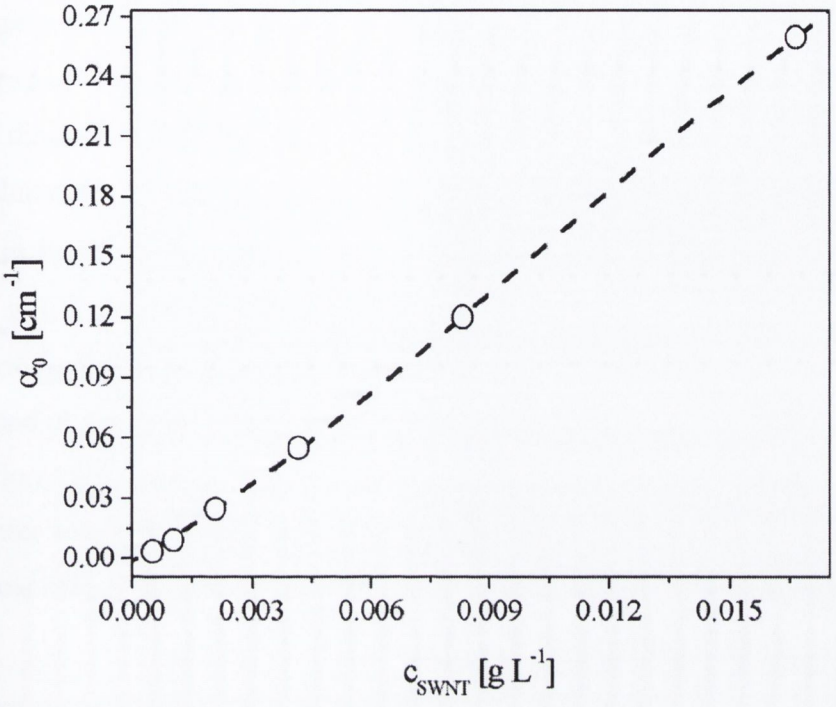

Figure 6.7 Plot of linear absorption coefficient α_0 as a function of partial nanotube concentration c_{SWNT} for the (m-PNV)-SWNT composite dispersions excited at 532 nm. The dashed line is intended as a guide to the eye.

depicted in Figure 6.5a are included in this figure. It can be seen that the data increases smoothly as a function of the concentration and the trend is approximated with a dashed line in the figure. This dashed line is intended merely as a guide to view the data. The linear absorption coefficients are included in Table 6.1. In this table the linear absorption coefficients with c_{SWNT} concentrations of 3.47×10^{-4} g L^{-1} and lower are shown in italics to indicate that these are extrapolated values and not measured properties. These absorption coefficients were extrapolated from Figure 6.7 as the measured spectra were excessively noisy and impossible to interpret.

6.5 Open Aperture Z-scan Response

The open aperture z-scans performed in this study were, due to the relatively low concentration, all performed in 1 cm quarts cells. In this chapter the results collected for on focal intensity $I_0 \approx 0.46$ GW cm^{-2} are discussed. This corresponded to laser pulses with energy of order 0.08 mJ. The samples with partial nanotube concentration c_{SWNT} going from 1.67×10^{-2} to 1.54×10^{-4} g L^{-1} all exhibited a reduction

in transmission about the focus of the lens for all samples typical of positive optical limiting. For the remaining two samples of lowest partial nanotube concentration, and also pure polymer samples at any concentration no response at the excitation intensity was observed. Sample open aperture z-scan spectra for the (*m*-PNV)-SWNT composite dispersions are depicted in Figure 6.8. The composites with partial SWNT concentrations of 4.17×10^{-3} g L^{-1} are presented in Figure 6.8a, with 1.04×10^{-3} g L^{-1} are presented in Figure 6.8b, with 3.47×10^{-4} g L^{-1} are presented in Figure 6.8c and with 2.32×10^{-4} g L^{-1} are presented in Figure 6.8d. It can be seen that the minimum transmission in Figure 6.8d is lower than that in Figure 6.8c even though the samples are irradiated at the same optical intensities and the sample in Figure 6.8c is of higher concentration than that of Figure 6.8d. At a superficial level this result would appear to be counter intuitive showing that as the concentration decreases the magnitude of the nonlinear effect actually increases.

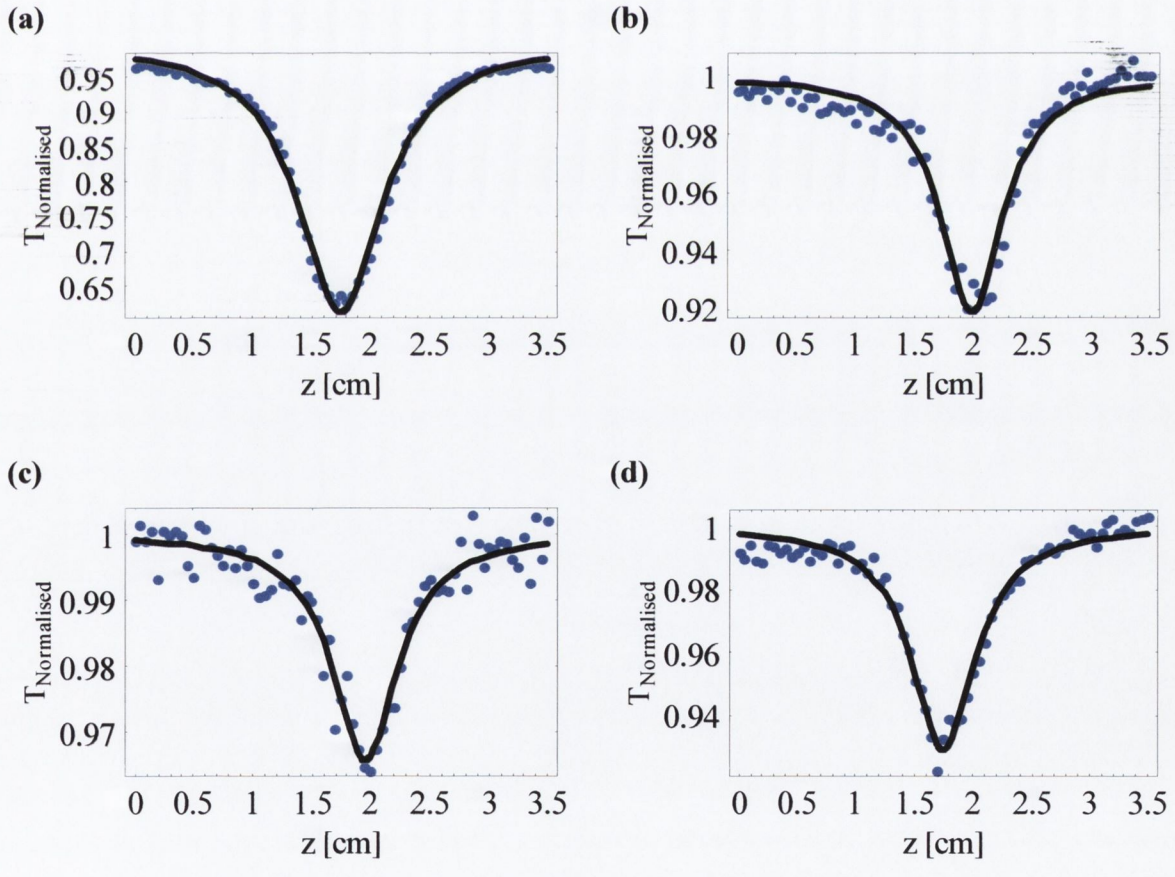

Figure 6.8 Sample open aperture z-scan spectra for the (*m*-PNV)-SWNT composite dispersions with partial SWNT concentrations of **(a)** 4.17×10^{-3} g L^{-1} **(b)** 1.04×10^{-3} g L^{-1} **(c)** 3.47×10^{-4} g L^{-1} and **(d)** 2.32×10^{-4} g L^{-1}. The on focus intensity irradiation was $\approx$ 0.46 GW cm^{-2} in all cases.

In Figure 6.9a a plot of the normalised on focus transmission as a function of the partial SWNT concentration, c_{SWNT} is depicted. It can be seen that in the region of $c_{SWNT} \approx 2.3\times10^{-4}$ g L^{-1} the transmission begins to reduce even though the concentration is decreasing, this is directly from the z-scans as discussed in the previous paragraph. In Figure 6.9b a plot of the effective nonlinear absorption coefficient β_{eff} determined from fitting of the open aperture spectra as a function of c_{SWNT} is presented. The β_{eff} coefficient can be seen to increase in the region of 2.3×10^{-4} g L^{-1} again even though the concentration is decreasing in accordance with the behaviour of the transmission minimum as a function of concentration.

It is therefore clear that the nonlinear response exhibited by the system iscomplicated, almost certainly due to the breaking up of carbon nanotube bundles in the system. It is impressive that nonlinear optical attenuation measurements in the ns regime are capable of detecting these nanoscale changes.

c_{SWNT} [g L^{-1}]	α_0 [cm^{-1}]	I_0 [GW cm^{-2}]	β_{eff} [cm W^{-1}]	β_{eff}/c_{SWNT} [cm L g^{-1} W^{-1}]
1.67×10^{-2}	2.6×10^{-1}	0.46	$(1.1 \pm 0.2)\times10^{-8}$	$(6.3 \pm 1.2)\times10^{-7}$
8.33×10^{-3}	1.2×10^{-1}	0.46	$(5.8 \pm 1.2)\times10^{-9}$	$(6.9 \pm 1.4)\times10^{-7}$
4.17×10^{-3}	5.5×10^{-2}	0.46	$(3.2 \pm 0.6)\times10^{-9}$	$(7.8 \pm 1.6)\times10^{-7}$
2.08×10^{-3}	2.5×10^{-2}	0.46	$(2.3 \pm 0.5)\times10^{-9}$	$(1.0 \pm 0.2)\times10^{-6}$
1.04×10^{-3}	9.0×10^{-3}	0.46	$(3.8 \pm 0.8)\times10^{-10}$	$(3.7 \pm 0.7)\times10^{-7}$
5.20×10^{-4}	3.2×10^{-3}	0.46	$(1.2 \pm 0.2)\times10^{-10}$	$(2.3 \pm 0.5)\times10^{-7}$
3.47×10^{-4}	*2.2×10^{-3}*	0.46	$(1.7 \pm 0.3)\times10^{-10}$	$(4.8 \pm 0.9)\times10^{-7}$
2.32×10^{-4}	*1.5×10^{-3}*	0.46	$(3.4 \pm 0.7)\times10^{-10}$	$(1.5 \pm 0.3)\times10^{-6}$
1.54×10^{-4}	*9.5×10^{-4}*	0.46	$(1.8 \pm 0.4)\times10^{-10}$	$(1.1 \pm 0.2)\times10^{-6}$
1.03×10^{-4}	*8.2×10^{-4}*	0.46	---	---
6.86×10^{-5}	*4.2×10^{-4}*	0.46	---	---

Table 6.1 Concentrations and linear and nonlinear optical coefficients for the (*m*-PNV)-SWNT composite dispersions. The linear absorption coefficients with c_{SWNT} partial concentrations of 3.47×10^{-4} g L^{-1} and lower are shown in italics to indicate that these are extrapolated values and not measured properties.

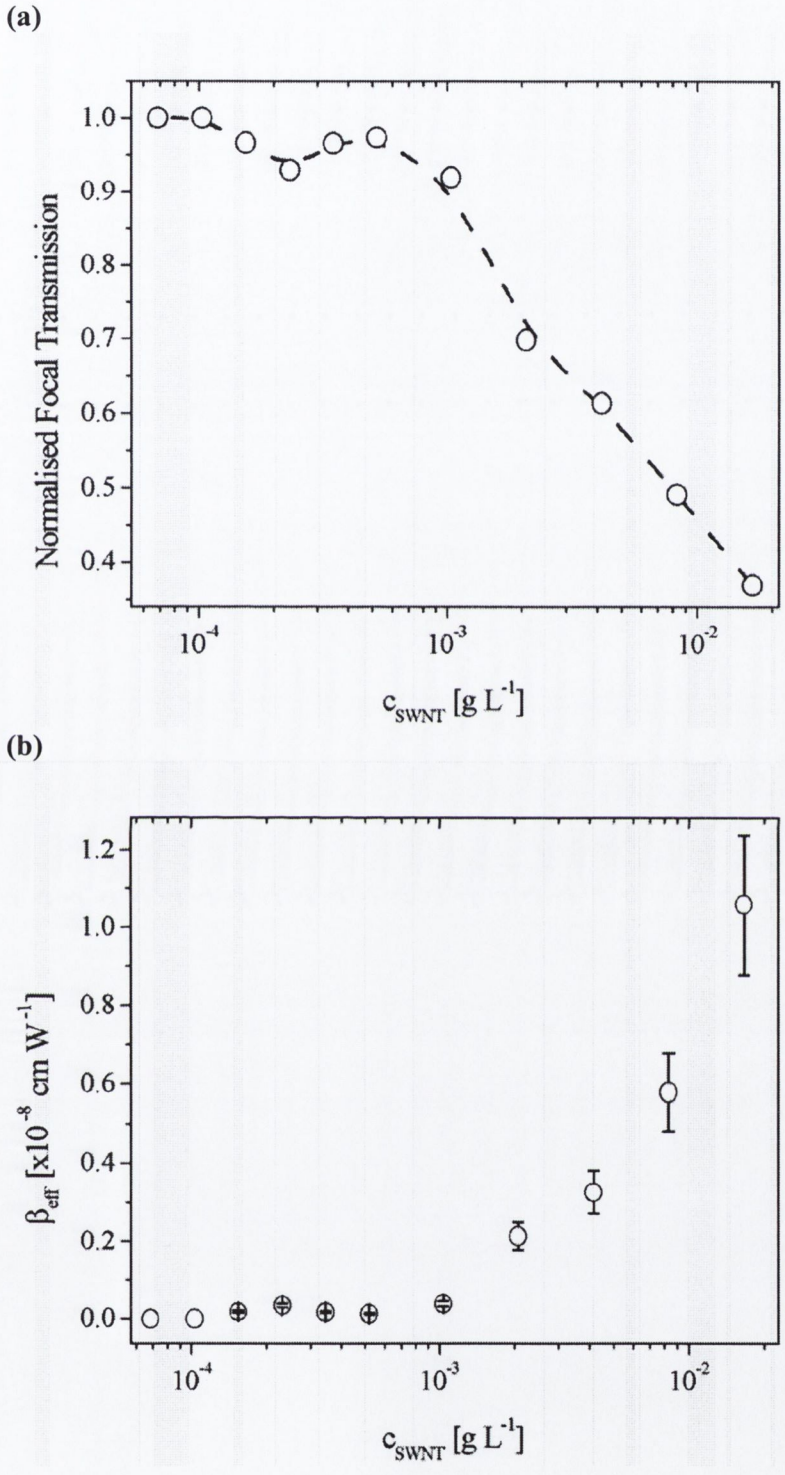

Figure 6.9 **(a)** Plot of the normalised on focus transmission as a function of the partial SWNT concemtration, c_{SWNT}. It can be seen that in the region of $c_{SWNT} \approx 2.3\times10^{-4}$ *g* L^{-1} the transmission begins to reduce even though the concentration is decreasing. The dashed line is intended as a guide to the eye. **(b)** Plot of effective nonlinear absorption coefficient β_{eff} as a function of c_{SWNT}. The β_{eff} coefficient can be seen to increase in the region of 2.3×10^{-4} g L^{-1} again even though the concentration is decreasing.

6.6 Discussion

It was demonstrated in the previous chapter that MWNTs certainly optical limit through a scattering process, although one cannot discount the possibility of nonlinear absorption also. It was discussed in the introduction to that chapter that other authors reported much the same effects as to the causality of optical limiting exhibited by SWNT dispersions. If it is assumed that the scattering is proportional to the number of scattering centres per unit volume then, at a superficial level at least, considering Figure 6.9a and 6.9b it is evident that at partial SWNT concentrations of order $c_{SWNT} \approx 2.3\times10^{-4}$ g L^{-1} there are more nonlinearly optically active entities per unit volume than at concentrations higher than this. This would then imply that, as the partial SWNT concentration is decreased the bundles must break yielding more scattering centres per unit volume than the higher aggregated systems at higher partial mass concentrations of the SWNTs. In this case open aperture z-scan spectroscopy has been successfully applied to monitor the concentration dependent kinetic behaviour of SWNT bundles. The technique showed that the bundles tend to break at lower

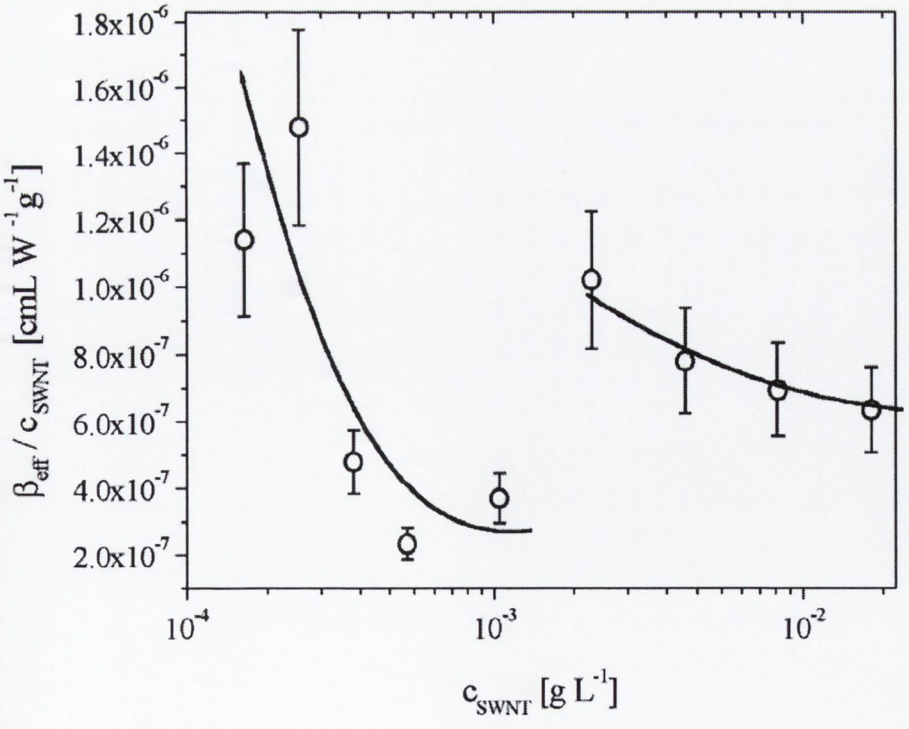

Figure 6.10 Plot of effective nonlinear absorption per concentration, β_{eff} / c_{SWNT}, as a function of concentration. The solid lines in the figure are sketched as guides to view the data.

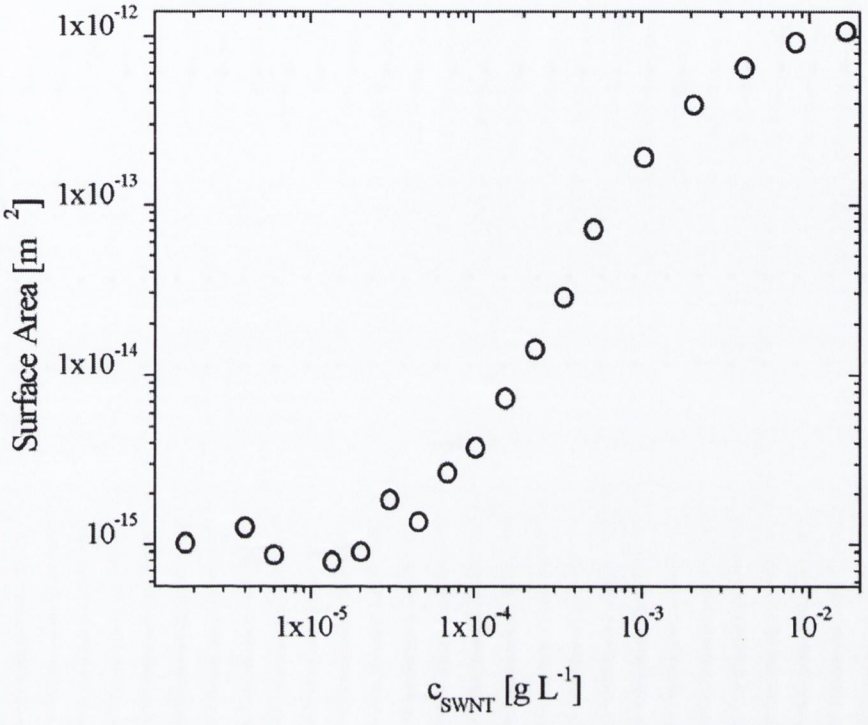

Figure 6.11 Plot of the calculated surface are of the SWNT bundle as a function of its partial mass concentration in solution. It can be seen that the value saturates at low concentrations possibly indicating isolated SWNTs, although these concentrations are lower than the concentrations investigated in this thesis.[21]

concentrations through thermally induced diffusion without the need for any chemically induced processes to aid the dissociation. A conjugated polymer at an equivalent partial mass concentration of the SWNTs is necessary, to allow probably monolayer coating of the nanotubes or bundles, to provide stability to the dispersion. However, it cannot be determined from this data what the sizes of the bundles are, and more importantly if isolated SWNTs were observed. As the partial concentration of SWNT was too low at concentrations of 8.2×10^{-4} g L^{-1} and lower for any nonlinearity to be detected it was not possible to go to lower concentrations, and it should also be noted that the polymer exhibited no response of its own.

In an attempt to gain further insight into the nature of the effective nonlinear absorption coefficients presented in Figure 6.10 a plot of effective nonlinear absorption per concentration, β_{eff} / c_{SWNT}, as a function of concentration has been prepared in Figure 6.11. The solid lines in the figure are sketched as guides to view the data. This figure seems to imply that the nonlinear attenuation per concentration

operates in one of two different regimes. The samples with the four highest partial SWNT concentrations, c_{SWNT} spanning from 1.67×10^{-2} g L^{-1} to 2.08×10^{-3} g L^{-1}, exhibit behaviour where the β_{eff}/c_{SWNT} ratio increases slowly with reducing partial concentration. Then as c_{SWNT} is reduced to 1.04×10^{-3} g L^{-1} the β_{eff}/c_{SWNT} ratio breaks the trend and is reduced by approximately a factor of two. As the samples tend further toward lower concentrations the β_{eff}/c_{SWNT} ratio then exhibit a second trend that increases again with reducing concentration.

If it is assumed that thermally induced scattering, as reported in the literature[22-24], is responsible for a significant proportion of the nonlinear optical attenuation then it can be noted that the total surface area of the optically active entities may be a parameter of interest. Carbon nanotubes are excellent thermal conductors[25] and therefore as the nanotubes get 'hot' from the laser pulses they will heat the solvent about the total surface area of the nanotube or the nanotube bundle. The total surface area per SWNT bundle as function of concentration can be obtained using the results outlined in Section 6.3 and by manipulation of Equation (6.3). This is plotted in Figure 6.11. It can be seen that the total surface area per concentration saturates at partial SWNT concentrations below 10^{-5} g L^{-1}, presumably in the regime where the nanotube bundles have completely dissociated and are individual and isolated. It should be noted that these concentrations at which the surface area per bundle saturates are lower than the concentrations of the samples that were measured here.

The effective nonlinear absorption coefficient has been plotted against the calculated total surface are per unit volume in Figure 6.12, where the plot has been presented on Log-Log scales. The data reveals that two regimes, similar to that observed in Figure 6.10, are again evident here. It can be seen that at higher partial concentrations, spanning the region $c_{SWNT} = 1.67\times10^{-2}$ - 2.08×10^{-3} g L^{-1} the data follows a trend where the β_{eff} and the total surface per unit volume are linearly related to each other, and a linear fit over this section of the curve yields a slope of approximately 1.0 ± 0.1. This is in good agreement with the idea that the total surface area of the bundle being responsible for the nonlinear response, as discussed above. However, below this concentration, $c_{SWNT} < 2.08\times10^{-3}$ g L^{-1}, the data changes and follows a second linear trend of steeper slope, approximately equal to 4.2 ± 0.8.

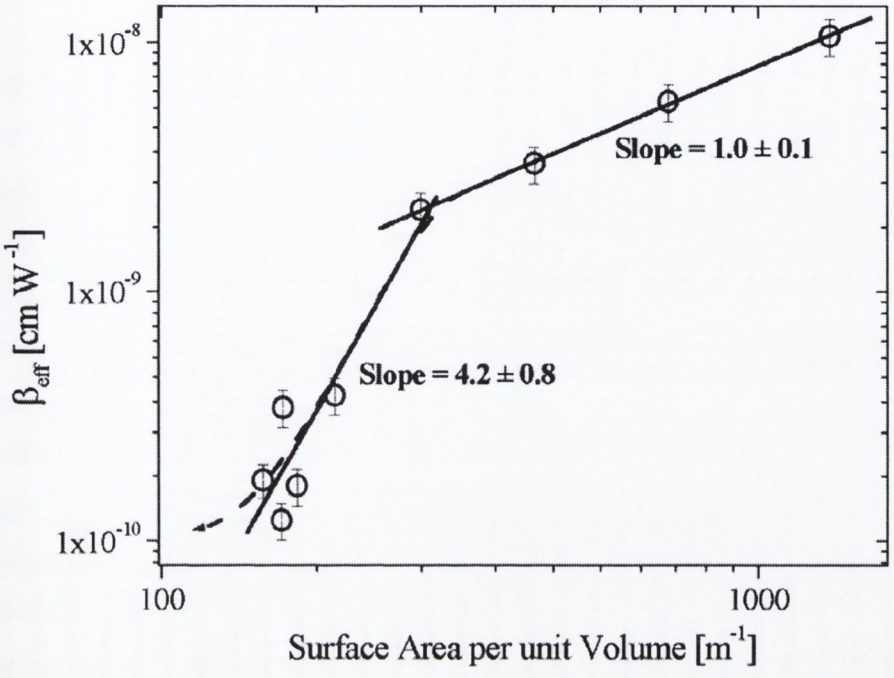

Figure 6.12 Plot of the effective nonlinear absorption coefficient β_{eff} against the calculated surface are of the SWNT bundle per unit volume, plotted on Log-Log scales. These β_{eff} coefficients are those presented in Figure 6.9b for their respective partial mass concentrations. These scaling laws exhibiting power law dependence operate in two regimes and are clearly visible in the figure and linear functions are fitted to these regions. The dashed line is a sketch representing another possible curve that may fit the lower concentration data.

These are experimentally determined scaling laws that show that the total surface area per unit volume in a SWNT bundle is related to the effective nonlinear absorption coefficient β_{eff} with power law dependence. These scaling laws assert that at higher concentrations ($c_{SWNT} > 2.08\times10^{-3}$ g L^{-1}) β_{eff} is approximately proportional to the total surface area per unit volume and at lower concentrations ($c_{SWNT} < 2.08\times10^{-3}$ g L^{-1}) β_{eff} is approximately proportional to the total surface area per unit volume raised to the power of 4.2. The dashed line in Figure 6.12 line is a sketch representing another possible curve that may fit the lower concentration data although this will not be pursued further in the discussions here.

If one considers that the SWNT bundles progressively reduce in size through thermal dissociation as the concentration is decreased then this may yield useful insight into the observed effect. It is possible that below partial SWNT concentrations of 2.08×10^{-3} g L^{-1} that the bundles become so small that size related

quantum mechanical size effects may be responsible for the regime change.

Scaling laws such as those observed above are not a new concept in the field of nonlinear optics and they have been both observed experimentally and predicted theoretically in the literature. Flytzanis, a pioneer of scaling laws and their uses in nonlinear optics, reviewed his work on the dimensionally dependent scaling laws of nonlinear susceptibilities in carbon chains and other single dimensional systems such as polymers in 1987.[26] He believed that the simple functional dependence of macroscopic quantities (such as nonlinear susceptibilities) on an effective simple parameters, as opposed to the complicated dependence of such quantities on the different microscopic parameters that define the quantum nature of the interaction of light and matter, was in many respects far more useful. However he realised that the choice of the effective parameter used to investigate the system had to be intuitively pertinent to the physical phenomenon and also amenable to a rigorous definition within a quantum mechanical description of the process under review. He also stated that the parameter must reflect the range of validity of a certain approach or model, as quite often size effects become crucial to the extent that drastic changes can occur both in the energy spectrum and wave functions and in the quantum mechanical quantities that enter the expressions of the macroscopic physical properties.

Scaling laws were obtained for all odd order susceptibilities in one-dimensional systems where the nonlinear susceptibilities were found to be related by simple power laws to the electron delocalisation length.[27] The delocalisation length is the 'space' available to an electron in a system with infinite extension and in general extends over several unit cells in a material. It can also be envisaged as the minimum 'box' within which an electron can be squeezed without its states and its response to external fields being affected by size effects. Flytzanis[27] then proposed two regimes the small-size and infinite-extension regime and showed that the relevant parameter to consider was the field induced dipole moment and the induced dipole density respectively. For zero-dimensional systems he demonstrated that for carbon chains without bond alternation the third order polarisability was related to the fifth power of the chain length. For chains with bond alternation he showed that the third order polarisability was proportional to the sixth power of the delocalisation length, when the delocalisation length was comparable or greater than the molecular length. When the delocalisation length was less than the molecular length they

stated and experimentally demonstrated that the scaling law was independent of the molecular length.[28]

Subsequently the scaling of nonlinear polarisabilities with molecular size drew much attention both theoretically[29-33] and experimentally[34-36] for different systems such as conjugated polymers of varying chain length and oligomers of varying sizes. In general it was found that the scaling of optical polarisabilities with the number of carbon atoms in the system N was usually described with power law dependence where the polarisability was proportional to N^k. For small sizes (those comparable or smaller than the delocalisation length) the numerical value for k was found to vary between 3 and 8 depending on the system and model. For the larger sizes (infinitely extended systems where the molecular length was in excess of the delocalisation length) it was found that k was expected to saturate to unity, since the polarisability then became an extensive property. These general results are interesting when compared with Figure 6.12. The nonlinear absorption coefficient is directly proportional to the imaginary nonlinear susceptibility in a material where the nonlinearity is due to parametric processes. If one considers, as mentioned earlier, that the external atoms in the carbon nanotube bundle are the only ones to contribute to the thermally induced nonlinearity then clearly the surface area per unit volume is directly proportional to the number of optically active carbon atoms in the system. However it is interesting that the slope in the lower concentration region, where one would expect the bundles to be smallest, is within the range of the small-size regime power law as predicted in the literature for the relationship between the parametric hyper-polarisability and the number of carbon atoms in the system. It is also most interesting that the relationship saturates to unity for the larger bundles as was reported and predicted for large-size infinitely extended regime hyper-polarisability to number of carbon atoms dependence. It has to be noted at this point that despite the agreement between the literature and the plot presented here the same theory does not hold. As nonlinear optical attenuation in carbon nanotube systems is a least partially, and in many cases perhaps principally, due to light scattering the effective nonlinear absorption coefficient in Figure 6.12 is not due to the parametric third order imaginary polarisability.

Recently Benoit *et al.*[37] reported the low-field and high-field transport properties of polymer-SWNT thin films for varying concentrations of the SWNT

content in the films. Their results showed that transport was essentially due to delocalised charge carriers with characteristic delocalisation lengths of 8-28 nm due to the bundle boundaries. This can be considered in terms of Figure 6.12 once again, where at the critical concentration where the regime change was observed the bundles were expected to have a diameter of order 10 nm.[11] In this region, and tending to lower concentrations the π-electrons on the surface of the bundle are therefore completely delocalised about the circumference of the bundle, this is the effective small-size regime. At higher concentrations it is likely that the bundles circumference is such that the electrons are not completely delocalised about the circumference of the bundle and it is proposed that this is the effective infinitely extended regime. Therefore it appears that once the circumference of the bundle is lower than the delocalisation length then the power law dependence has exponent 4.2 ± 0.8 and after the circumference exceeds the delocalisation length the power law exponent reduces to 1.0 ± 0.1.

It is also possible that the nature of the nonlinearity is not constant accompanying the regime changes from small-size to infinitely extended. Future studies using time dependent pump-probe spectroscopy would be an invaluable approach to investigate this.

6.7 Conclusion

The principle aim of this chapter was to investigate if the open aperture z-scan technique could be used to detect the thermally induced kinetic behaviour of SWNT bundles. It was demonstrated that it was in fact possible to use standard optical limiting measurements to observe the bundle dissociation. However, it was not possible to detect isolated SWNTs as the concentration required to reach this regime was so low that the optical nonlinearity was undetectable. The trends in the plot of the effective nonlinear absorption coefficient β_{eff} against the calculated surface are of the SWNT bundle per unit volume, plotted on Log-Log scales, yielded interesting novel scaling laws for the SWNT system. Two regimes are clearly visible in the figure and linear functions are fitted to these regions, resulting in a slope of approximately 1.0 ± 0.1 for the higher partial nanotube concentrations and 4.2 ± 0.8 for the lower. This effect is interesting and requires further research to understand. Further studies should use dynamic light scattering experiments to experimentally

determine the bundle size in the dispersion over the entire c_{SWNT} range. These studies would certainly allow for the possibility to account for size related quantum mechanical confinement effects, which is one possible phenomenon discussed above that may cause this regime change. Time dependent spectroscopy of these samples would also be of particular interest, as the nature of the nonlinearity in each regime should be investigated.

As carbon nanotube research and applications tend toward more 'real life' marketable uses the manipulation of defect free individual SWNTs will be of paramount importance. It is impressive that SWNT bundles suspended using a conjugated polymer dissociate in a common organic solvent (chloroform in this case) at reduced concentrations. Further research proving that the bundles actually dissociate to a regime where the polymer disperses individual SWNTs would be a simple but powerful method of isolating nanotubes without the need for chemical modifications.

References

[1] R. H. Baughman, A. A. Zakhidov, and W. A. de Heer, Science **287,** 787-792 (2002).

[2] A. Thess, R. Lee, P. Nikolaev, H. Dai, P. Petit, J. Robert, C. Xu, Y. H. Lee, S. G. Kim, A. G. Rinzler, D. T. Colbert, G. E. Scuseria, D. Tomanek, J. E. Fischer, and R. E. Smalley, Science **273,** 483-487 (1996).

[3] http://www.ruf.rice.edu/~smalleyg/image_gallery.htm

[4] R. S. Lee, H. J. Kim, J. E. Fischer, A. Thess, and R. E. Smalley, Nature **388,** 255-257 (1997).

[5] J. E. Fischer, H. Dai, A. Thess, R. Lee, N. M. Hanjani, D. L. Dehaas, and R. E. Smalley, Physical Review B **55,** R4921-R4924 (1997).

[6] G. T. Kim, E. S. Choi, D. C. Kim, D. S. Suh, Y. W. Park, K. Liu, G. Duesberg, and S. Roth, Physical Review B **58,** 16064-16069 (1998).

[7] J. Hone, I. Ellwood, M. Muno, A. Mizel, M. L. Cohen, A. Zettl, A. G. Rinzler, and R. E. Smalley, Physical Review Letters **80,** 1042-1045 (1998).

[8] M. L. Tian, F. Q. Li, L. Chen, Z. Q. Mao, and Y. H. Zhang, Physical Review B **58,** 1166-1168 (1998).

[9] Y.-K. Kwon and D. Tomanek, Physical Review Letters **84,** 1483-1486 (2000).

[10] Y.-K. Kwon, S. Saito, and D. Tomanek, Physical Review B **58,** R13314 (1998).

[11] J. N. Coleman et al., A Fleming, S Maier, S O'Flaherty, A Minett, MS Ferreira, S Hutzler, WJ Blau, Submitted to J. Phys. Chem. B (2003).

[12] A. J. Fleming et al., In Preparation (2003).

[13] A. J. Fleming, Personal Communication.

[14] M. I. H. Panhuis, A. Maiti, A. B. Dalton, A. van den Noort, J. N. Coleman, B. McCarthy, and W. J. Blau, Journal of Physical Chemistry B **107,** 478-482 (2003).

[15] P. Petit, C. Mathis, C. Journet, and P. Bernier, Chemical Physics Letters **305,** 370-374 (1999).

[16] J. W. Mintmire and C. T. White, Synthetic Metals **77,** 231-234 (1999).

[17] J. W. Mintmire and C. T. White, Carbon **33,** 893-902 (1995).

[18] J. W. Mintmire, B. I. Dunlap, and T. C. White, Physical Review Letters **68,** 631 (1992).

[19] N. Hamada, S.-I. Sawada, and A. Oshiyama, Physical Review Letters **68,** 1579 (1992).

[20] Y. I. Prylutskyy, S. S. Durov, O. V. Ogloblya, E. V. Buzaneva, and P. Scharff, Computational Materials Science **17,** 352-355 (2000).

[21] J. N. Coleman, Personal Communication.

[22] L. Vivien, D. Riehl, J. F. Delouis, J. A. Delaire, F. Hache, and E. Anglaret, Journal of the Optical Society of America B-Optical Physics **19,** 208-214 (2002).

[23] L. Vivien, D. Riehl, P. Lancon, F. Hache, and E. Anglaret, Optics Letters **26,** 223-225 (2001).

[24] L. Vivien, E. Anglaret, D. Riehl, F. Hache, F. Bacou, M. Andrieux, F. Lafonta, C. Journet, C. Goze, M. Brunet, and P. Bernier, Optics Communications **174,** 271-275 (2000).

[25] M. S. Dresselhaus, G. Dresselhaus, and P. C. Eklund, *Science of Fullerenes and Carbon Nanotubes* (Academic Press, New York, 1996).

[26] D. S. Chemla and J. Zyss, *Nonlinear Optical Properties of Organic Molecules*

and Crystals (Academic Press, Orlando, 1987), Chapter III-4, Volume II.
[27] C. Flytzanis, ACS Symposium Series **233,** 167 (1983).
[28] G. P. Agrawal and C. Flytzanis, Chemical Physics Letters **44,** 366 (1976).
[29] S. Mukamel, A. Takahashi, H. X. Wang, and G. Chen, Science **266** (1994).
[30] S. R. Marder, Science **265,** 632 (1994).
[31] B. Pierce, Journal of Chemical Physics **91,** 791 (1989).
[32] F. C. Spano and A. G. Soos, Journal of Chemical Physics **99,** 9265-9271 (1993).
[33] S. Tretiak, V. Chernyak, and S. Mukamel, Physical Review Letters **77,** 4656-4659 (1996).
[34] I. D. Samuel, I. Ledoux, C. Dhenaut, J. Zyss, H. H. Fox, R. R. Schrock, and R. J. Silbey, Science **265,** 1070 (1994).
[35] C. Bubeck, *Nonlinear Optical Material: Principles and Applications* (IOS Press, Amsterdam, 1995).
[36] A. Mathy, K. Ueberhofen, R. Schenk, H. Gregorius, R. Garay, K. Muellen, and C. Bubeck, Physical Review B **53,** 4367-4376 (1996).
[37] J. M. Benoit, B. Corraze, and O. Chauvet, Physical Review B **65,** 241405(R) (2000).

Chapter 7

Concluding Comments

Optical limiting investigations exhibited by phthalocyanine and carbon nanotube systems was the central underlying theme throughout the entire body of this work.

The nonlinear response of 41 structurally different phthalocyanine compounds was investigated. The results were fitted using a five level model that was effectively reduced to a three level system due to the lengthy pulse duration relative to all other lifetimes in the system. The model, although not generally spectroscopically correct, fitted the data well and produced reasonable results verified by other authors using similar compounds. It was found that putting nickel or cobalt into the central phthalocyanine cavity reduced the magnitude of the nonlinear absorption compared to that of similar phthalocyanines without a metal in the central cavity. The chloroindium phthalocyanine monomer (Chapter 4, compound **6**) exhibiting the largest ratio of excited to ground state absorption cross sections κ while the palladium phthalocyanine (Chapter 4, compound **10**) was found to exhibit the largest nonlinear absorption coefficient.

It was found that the ratio of the ground to excited state absorption cross sections κ did not exhibit a clear dependence on the atomic mass of the central metal. However, it did appear to show a more stable dependence on the linear absorption coefficient, especially after removing the contributions from cobalt, nickel and

peripherally bridged dimer phthalocyanines. As cobalt and nickel were found not to be useful as optical limiters, it is interesting that the 'good' materials follow such a trend. However, it was disappointing that the peripherally bridged dimers broke this trend as they do show promise when one would require low saturation energy densities, F_{Sat}. They exhibited some of the lowest F_{Sat} values in this study. The apparent linearity in the relationship between κ and α_0, on Log-Log scales, is a phenomenological result that appears to represent an experimental molecular engineering design rule.

Preliminary investigations of a polymerised phthalocyanine and phthalocyanine monomers embedded in a polymer were also undertaken. Polymerising the phthalocyanines, or embedding the phthalocyanines as inclusions in a polymer host to form a composite material is of interest because this allows traditional methods such as spin casting to be employed to produce suitable films for solid state applications. Phthalocyanines offer a tremendous degree of design flexibility that they may be employed to fabricate practical organic passive optical limiters.

A systematically varied series of PmPV-MWNT and PFO-carbon nanostructure composites by nanostructure content was fabricated, materially investigated and characterised with regards to optical limiting, or nonlinear extinction. Scattering measurements exhibited a clear nanostructure content dependence of perfectly elastically scattered light. The nanostructured composition of the materials was clearly distinguishable in the scattering data, suggesting that this method has potential for application in measuring polymer-MWNT composite purity.

These types of materials have the advantage that they are easily fabricated, the raw material is readily available and there is much potential for further optimisation. The polymer-MWNT composite is attractive compared to some of the other alternatives for optical limiting applications as the optically active entities (the nanotubes) are already embedded in a polymer host that can be used for solid-state casting. In addition many potential host polymers remain to be tested.

Future work in this area would inevitably involve variation of both nanostructured guest and polymer host to improve dispersion properties and increase optical limiting efficiency towards real world applications. It would also be advantageous to undertake an empirical study of the angular scattering profiles from

'loaded' composite. First purified MWNTs from PmPV based composites would be obtained. These would then be dispersed in PFO, and to this range of PFO-purified MWNT samples carbon black spheres would be loaded into the polymer-MWNT dispersion in various proportions. Thus the ratio of MWNT to spherical particles would be known. The scattering lobes could then be empirically fitted to provide a calibration for the measure of composite purity.

Optical limiters fabricated from the polymer-MWNT composite system also have other advantages. This system is essentially a conductive plastic[1], and therefore in addition to its use as an optical limiter this composite would be antistatic, electrostatic dissipative and electromagnetic shielding.[2] For example, electromagnetic shielding, is essential in electronic equipment such as laptop computers, mobile phones and other portable electronic devices. There is no suitable plastic for this task and at present metal in one form or another is usually used to provide the shielding. Thus, a device protected by a coating of an optically limiting polymer-nanotube composite from laser irradiation would also be electromagnetically shielded given the conductive nature of the composite. Optical limiting coatings would essentially be encasing the target within Gaussian surface. This would be enormously beneficial for military applications.

The future exploitation of carbon nanotubes in electronic and magnetic application relies on the spatial manipulation of single isolated SWNTs of known electronic properties. However in the preparation phase SWNTs aggregate into bundles. In Chapter 6 it was investigated if the open aperture z-scan technique could be used to detect the dissociation SWNT bundles. It was demonstrated that it was in fact possible to use standard optical limiting measurements to observe the bundle dissociation. However, it was not possible to detect isolated SWNTs as the concentration required to reach this regime was so low that the optical nonlinearity was undetectable.

The trends in the plot of the effective nonlinear absorption coefficient β_{eff} against the calculated surface are of the SWNT bundle per unit volume, plotted on Log-Log scales, yielded interesting results. Scaling laws defining two distinctly different regimes were clearly visible and linear functions fitted to these regions, resulted in a slope of approximately 1.0 ± 0.1 for the higher partial nanotube concentrations and 4.2 ± 0.8 for the lower concentrations. This effect is interesting

and requires further research to understand. Further studies should use dynamic light scattering experiments to experimentally determine the bundle size in the dispersion over the entire c_{SWNT} range. These studies would certainly allow for the possibility to account for size related quantum mechanical confinement effects, which is one possible phenomenon that may cause the regime change. Time dependent spectroscopy of these samples would also be of particular interest, as the nature of the nonlinearity in each regime should be investigated. As carbon nanotube research and applications tend toward more 'real life' marketable uses the manipulation of defect free individual SWNTs will be of undeniable importance. It is impressive that SWNT bundles suspended using a conjugated polymer dissociate in a common organic solvent (chloroform in this case) at reduced concentrations.

If photonic technologies are the future then the use of lasers as the driving force of information processing is inevitable. The protecting of targets, the most important being the eye, via optical limiting is a task of paramount importance. This thesis has demonstrated that phthalocyanine and carbon nanotube systems may be useful for such applications. It has been demonstrated that the use of optical limiting as a spectroscopic tool also has many other possibilities to be used for material characterisation.

References

[1] R. H. Baughman, A. A. Zakhidov, and W. A. de Heer, Science **287,** 787-792 (2002).

[2] D. T. Colbert, Plastics Additives & Compounding, January/February, (2003).

Appendix I: SI and esu Unit Systems

If one assesses the literature dealing with the subject of Nonlinear Optics, it is evident that it is separated in two systems of units. Some authors have adopted the more modern MKS system of SI units but the majority of scientific authors predominantly adopt the more archaic electrostatic units (esu) or gaussian systems of units. In this thesis the nonlinear susceptibilities and hyperpolarisabilities were in all cases quoted in esu units and the conversion between the two systems will be detailed in the following paragraphs.

In the gaussian formalism the nonlinear polarisation is defined using the following expanding series

$$P(t) = \chi^{(1)}\underline{E}(t) + \chi^{(2)}\underline{E}(t)\underline{E}(t) + \chi^{(3)}\underline{E}(t)\underline{E}(t)\underline{E}(t) + \ldots \qquad \text{(A.1)}$$

In this system the $\underline{E}$, $\underline{B}$, $\underline{D}$, $\underline{P}$ etc. have the same units of statvolt cm^{-1}, where 1 statvolt is the equivalent of 300 V. Hence the susceptibilities have the following dimensions in Gaussian units.

$$\chi^{(n)} = \left(\frac{cm}{statvolt}\right)^{(n-1)} \qquad \text{(A.2)}$$

When one quotes values of the susceptibilities in this formalism one does not generally quote the units given in Equation (A.2) but simply refers to them as being electrostatic units (esu) for all susceptibilities. The SI formalism (MKS) defines the nonlinear polarisation according to:

$$P(t) = \varepsilon_0\left[\chi^{(1)}\underline{E}(t) + \chi^{(2)}\underline{E}(t)\underline{E}(t) + \chi^{(3)}\underline{E}(t)\underline{E}(t)\underline{E}(t) + \ldots\right] \qquad \text{(A.3)}$$

where ε_0 is the dielectric permittivity and has a numerical value of 8.8e-12 F m^{-1}. For conversion between the two formalisms one can cast Equations (A.1) and (A.2) in the following form:

$$\underline{P}(t) = \chi^{(1)}\underline{E}(t)\left[1 + \frac{\chi^{(2)}\underline{E}(t)}{\chi^{(1)}} + \frac{\chi^{(3)}\underline{E}(t)\underline{E}(t)}{\chi^{(1)}} + \ldots\right] \qquad \text{(A.4)}$$

$$\underline{P}(t) = \varepsilon_0\chi^{(1)}\underline{E}(t)\left[1 + \frac{\chi^{(2)}\underline{E}(t)}{\chi^{(1)}} + \frac{\chi^{(3)}\underline{E}(t)\underline{E}(t)}{\chi^{(1)}} + \ldots\right] \qquad \text{(A.5)}$$

The quantity in parenthesis in both Equations (A.4) and (A.5) are in this case identical although the individual values of both the susceptibilities and the electric fields are different. They are related in their respective formalisms through:

$$\underline{E}(MKS) = 3\times10^{4}\,\underline{E}(gaussian) \tag{A.6}$$

$$\chi^{(1)}(MKS) = 4\pi\chi^{(1)}(gaussian) \tag{A.7}$$

Combination of the relationships governed by Equations (A.4)-(A.7) allows one to form the following conversion relations between the SI formalism and the Gaussian formalism:

$$\chi^{(2)}(MKS) = \frac{4\pi}{3\times10^{4}}\chi^{(2)}(gaussian) \tag{A.8}$$

$$\chi^{(3)}(MKS) = \frac{4\pi}{\left(3\times10^{4}\right)^{2}}\chi^{(2)}(gaussian) \tag{A.9}$$

This can be easily expanded to higher order susceptibilities. The numerical factor on the *RHS* of Equation (A.9) is equal to 1.4e-8. A similar factor is involved in moving between the formalisms when considering the molecular hyperpolarisabilities. For example, for the second order hyperpolarisabilities, which was used in Chapter 3, the factor is equal to 1.4e-14.

Appendix II: Publications List

Published

SM O'Flaherty, SV Hold, M Cadek, A Drury, JN Coleman, WJ Blau
Nonlinear Optical Response of Multi Walled Carbon Nanotube Dispersions
Journal of the Optical Society of America B ***20***, 1, 49-58, (2003).

SM O'Flaherty, SV Hold, M Cadek, A Drury, JN Coleman, WJ Blau
Nonlinear Optical Response of Multi Walled Carbon Nanotube Dispersions (Selected Re-publication)
Virtual Journal of Ultrafast Science – Condensed Matter Physics ***2***, 1, (2003).

SM O'Flaherty, SV Hold, M Cadek, A Drury, JN Coleman, WJ Blau
Nonlinear Optical Response of Multi Walled Carbon Nanotube Dispersions (Selected Re-publication)
Virtual Journal of Nanoscale Science & Technology – Carbon Nanotubes, C_{60}, and Related Studies ***7***, 4, (2003).

SM O'Flaherty, R Murphy, SV Hold, M Cadek, JN Coleman, WJ Blau
Material Investigation and Optical Limiting Properties of Carbon Nanotube and Nanoparticle Dispersions
Journal of Physical Chemistry B ***107***, 4, 958-964, (2003).

SM O'Flaherty, SV Hold, MJ Cook, T Torres, Y Chen, M Hanack, WJ Blau
Molecular Engineering of Peripherally and Axially Modified Phthalocyanines for Optical Limiting and Nonlinear Optics
Advanced Materials ***15***, 1, 19-32, (2003).

SM O'Flaherty and WJ Blau
Molecular Engineering for Laser Protection
The Irish Scientist Year Book ***10***, 196, (2002).

SM O'Flaherty, SV Hold, M Cadek, A Drury, JN Coleman, WJ Blau
Nanosecond Nonlinear Optical Extinction in Dispersed Multi Walled Carbon Nanotubes Excited at 532 nm
Proceedings of SPIE 'Opto-Ireland 2002' ***4876***, 750-758, (2002).

SM O'Flaherty, R Murphy, SV Hold, M Cadek, A Drury, JN Coleman, WJ Blau
Optical Limiting Properties of Carbon Nanostructure and Polymer Dispersions
Proceedings of SPIE 'Photonics West 2003' ***4991***, 194-204, (2003).

SM O'Flaherty, SV Hold, Y Chen, M Hanack, WJ Blau
Reverse Saturable Absorption Based Optical Limiting Properties of Indium and Gallium Phthalocyanines and Naphthalocyanines
Proceedings of SPIE 'Photonics West 2003' ***4991***, 183-194, (2003).

EM García-Frutos, SM O'Flaherty, SV Hold, G de la Torre, S Maier ,P Vázquez, W Blau, T Torres
Non-linear Absorption of Alkylsulfonyl Metallophthalocyanines
Synthetic Metals ***137***, 1479-1480, (2003).

Y Chen, M Hanack, S O'Flaherty, G Bernd, A Zeug, B Roeder, and WJ Blau
An Axially Grafted Charm Bracelet Type Indium Phthalocyanine Copolymer
Macromolecules ***6***, 11, 3786-3788 (2003).

A Auger, WJ Blau, I Chambrier, MJ Cook, B Isare, F Nekelson, SM O'Flaherty
Nonlinear Absorption Properties of some 1,4,8,11,15,18,22,25-octa-alkyl Phthalocyanines
Journal of Materials Chemistry ***13***, 1042-1047, (2003).

Y Chen, M Fujitsuka, SM O'Flaherty, M Hanack, O Ito, WJ Blau
Strong Optical Limiting of Soluble Axially Substituted Gallium and Indium Phthalocyanines
Advanced Materials ***15,*** 11, 899-902 (2003).

EM García Frutos, SM O'Flaherty, EM Maya, G de la Torre, W Blau, P Vázquez, T Torres
Alkynyl Substituted Phthalocyanine Derivatives as Targets for Optical Limiting
Journal of Materials Chemistry ***13***, 749-753, (2003).

Y Chen, S O'Flaherty, LR Subramanian, WJ Blau, M Hanack
Synthesis, Characterization and Optical Limiting Properties of Axially Substituted Gallium(III) Naphthalocyanines
Chemistry of Materials ***14***, 5163-5168, (2002).

Y Chen, LR Subramanian, M Fujitsuka, O Ito, S O'Flaherty, WJ Blau, T Schneider, D Dini, M Hanack
Synthesis and Optical Limiting Properties of Axially Bridged Phthalocyanines: $[tBu_4PcGa]_2O$ and $[tBu_4PcIn]_2O$
European Journal of Organic Chemistry ***8***, 18, 4248-4254, (2002).

M Kröll, SM O'Flaherty, WJ Blau
Optical Properties of Silver Nanowires in Nanoporous Alumina Membranes
Proceedings of SPIE 'Opto-Ireland 2002' ***4876***, 641-649, (2002).

R Murphy, JN Coleman, SM O'Flaherty, M Cadek, B McCarthy, A Drury, RC Barklie, WJ Blau
Comparative Study of Two Polymer Carbon Nanotube Composites using Electron Paramagnetic Resonance and Transmission Electron Microscopy
Proceedings of SPIE 'Opto-Ireland 2002' **4876**, 659-667, (2002).

K Ryan, SM Lipson, SM O'Flaherty, V Barron, M Cadek, A Drury, HJ Byrne, RP Wool, WJ Blau, JN Coleman
Photoluminescence Quenching and Degradation Studies to Determine the Effect of Nanotube Inclusions on Polymer Morphology in Conjugated Polymer-carbon Nanotube Composites
Proceedings of SPIE 'Opto-Ireland 2002' ***4876***, 361-369, (2002).

KG Ryder, SM Lipson, A Drury, SM O'Flaherty, WJ Blau
Model Study in Molecular Engineering for Nonlinear Photonic Devices: poly (arylene ethynylene) and poly (arylene vinylene) Copolymers
Proceedings of SPIE 'Annual Meeting San Diego 2001' ***4461***, 246-259, (2001).

C Nitschke, SM O'Flaherty, M Kroell, A Strevens, S Maier, MG Rüther, WJ Blau
Preparation and Nonlinear Optical Properties of Phthalocyanine Nanocrystals
Proceedings of SPIE 'Photonics West 2003' ***4991***, 124-132, (2003).

Submitted

SM O'Flaherty, R Murphy, SV Hold, A Drury, M Cadek, JN Coleman, WJ Blau
Polymer and Carbon Nanostructure Dispersions for Optical Limiting
Proceedings of IWEPNM, Kirchberg/Tirol, Austria, American Institute of Physics, submitted April 2003.

C Nitschke, SM O'Flaherty, M Kroell, WJ Blau
Linear and Nonlinear Optical Properties of Zinc Phthalocyanine Nanoparticles
Chemical Physics Letters, submitted May 2003.

C Nitschke, SM O'Flaherty, M Kroell, WJ Blau
Material Investigations and Optical Properties of Phthalocyanine Nanoparticles
Journal of Physical Chemistry B, submitted June 2003.

Y Chen, SM O'Flaherty, V Krishnan, M Hanack, MP Feth, H Bertagnolli, WJ Blau
Synthesis, characterization and optical limiting properties of a gallium phthalocyanine dimer with gallium-gallium bond
European Journal of Organic Chemistry, submitted May 2003.

SM O'Flaherty, AJ Fleming, S Maier, AI Minett, JN Coleman, WJ Blau
Scaling of the Optical Nonlinearity with Single Walled Carbon Nanotube Size
Chemical Physics Letters, submitted September 2003.

JN Coleman, A Fleming, S Maier, S O'Flaherty, A Minett, MS Ferreira, S Hutzler, WJ Blau
Binding Kinetics and Spontaneous SWNT Bundle Dissociation in Low Concentration Polymer-Nanotube Solutions
Journal of Physical Chemistry B, Submitted July 2003.